SUPERCONDUCTING VORTEX MATTER UNDER TEMPORAL AND SPATIAL PERTURBATIONS

by

CAMILLA BUHL LARSEN

A thesis submitted to
The University of Birmingham
for the degree of
DOCTOR OF PHILOSOPHY

School of Metallurgy and Materials
College of Engineering and Physical Sciences
The University of Birmingham
August 2019

ABSTRACT

Understanding the behaviour of the flux line lattice (FLL) of type-II superconductors under external perturbations is crucial for the development of superconducting technologies. By employing time-resolved small angle neutron scattering (SANS), we investigate the niobium FLL when perturbed by an external AC field. Our dynamic investigation is carried out along a fourfold $\langle 100 \rangle$ crystallographic direction, which affects the observed characteristic time constants significantly. We investigate the dynamic behaviour across different structural vortex phase transitions and observe no softening of the lattice close to the transitions. Non-elastic features are also observed.

SANS is also used to investigate an impure vanadium sample. We explore the well-known Bragg glass and the more elusive vortex glass. Measurements of longitudinal correlation lengths indicate that the vortex glass in vanadium is dominated by short-range order correlations. Muon spin rotational measurements show that the skew of the local field distribution becomes negative in the vortex glass phase. The negative skew distributions are further investigated with time-dependent Ginzburg-Landau simulations (TDGL), showing that negative skew can be achieved through positional disorder or vortex core deformations. We illustrate the potential of applying the TDGL simulations in Monte Carlo optimization procedures.

ACKNOWLEDGEMENTS

I would like to express my thanks to my supervisor, Dr. Mark Laver, for taking me on this project and making it possible for me to attend experiments, conferences, workshops, and a training school as part of my scientific training. I am grateful for his guidance during experiments, advice and insights into theoretical aspects of my research, and most of all for introducing me to the field of superconducting flux line lattices.

Special thanks go out to my colleagues Stavros Samothrakitis, Rob Arnold, and Ellie Tekin for their continuous support and friendship. Your help during experiments and my write-up period has been invaluable. Likewise, I thank everyone else who inhabited the B20 office of the Metallurgy and Materials department during my PhD time for a pleasant working environment and plentiful interesting coffee breaks.

I would also like to express my thanks to the scientific staff, who helped out with my experiments; Dominic Fortes (ISIS), André Heinemann (FRM-II), Uwe Keiderling (HZB), André Sokolowski (HZB), and Robert Cubitt (ILL).

Finally and most importantly, I would like to thank my family for always being there for me and supporting me through my studies.

Contents

LIST OF ABBREVIATIONS

AC	**A**lternating **C**urrent
BCS	**B**ardeen **C**ooper **S**chrieffer
DFT	**D**ensity **F**unctional **T**heory
FLL	**F**lux **L**ine **L**attice
FRM-II	**F**orschungs**r**eaktor **M**ünchen **II**
FWHM	**F**ull **W**idth at **H**alf **M**aximum
GL	**G**inzburg-**L**andau
HTSC	**H**igh-$\mathbf{T}_c$ **S**uper**C**onductor
HZB	**H**elmholtz-**Z**entrum **B**erlin
ILL	**I**nstitut **L**aue-**L**angevin
IMS	**I**ntermediate **M**ixed **S**tate
LF	**L**ongitudinal **F**ield
MD	**M**olecular **D**ynamics
μSR	**M**uon **S**pin **R**otation (**R**elaxation, **R**esonance)
P2P	**P**eak to **P**eak
RRR	**R**esidual **R**esistivity **R**atio
SANS	**S**mall **A**ngle **N**eutron **S**cattering
SQUID	**S**upderconducting **Q**uantum **I**nterference **D**evice
STM	**S**anning **T**unneling **M**icroscope
TDGL	**T**ime **D**ependent **G**inzburg-**L**andau
TF	**T**ransverse **F**ield
ZF	**Z**ero **F**ield

DIFFRACTION SPOT NOMENCLATURE

BLL	**B**ottom **L**eft **L**eft
BLR	**B**ottom **L**eft **R**ight
BM	**B**ottom **M**iddle
BRL	**B**ottom **R**ight **L**eft
BRR	**B**ottom **R**ight **R**ight
LL	**L**ower **L**eft
LR	**L**ower **R**ight
ML	**M**iddle **L**eft
MR	**M**iddle **R**ight
TL	**T**op **L**eft
TLL	**T**op **L**eft **L**eft
TLR	**T**op **L**eft **R**ight
TM	**T**op **M**iddle
TR	**T**op **R**ight
TRL	**T**op **R**ight **L**eft
TRR	**T**op **R**ight **R**ight
UL	**U**pper **L**eft
UR	**U**pper **R**ight

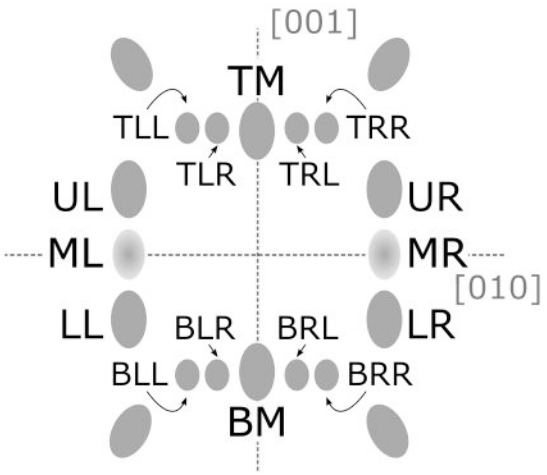

Figure 1: Schematic of the flux line lattice diffraction spots and their labels. The diffraction spots illustrate those obtained in the scalene phase with a static applied field along the [1 0 0] direction. ML and MR refer to areas of weak scattering appearing in between the main diffraction spots. Unlabelled spots are higher order diffraction spots. The labels will be utilized for the analysis of experimental neutron scattering investigations of the flux line lattice in chapter 4 and 5.

INTRODUCTION

Superconductivity has now been studied for more than a century, starting from the early discovery of elemental [1] and binary alloy [2] superconductors and up to the currently in vogue cuprates [3] and iron pnictides [4]. Despite being very different systems, both cuprates and iron pnictides exhibit high critical temperatures at ambient pressure. While Bardeen, Cooper and Schrieffer managed to explain the mechanism of low-T_c superconductivity via electron-phonon mediated Cooper pairs [5], a similar understanding of high-T_c superconductivity eludes the physics community. The fascination with these superconductors is deepened by the wealth of different ordering phenomena, including antiferromagnetic fluctuations, stripe spin order and charge order, which occur when their parent compounds are doped with either holes or electrons [6, 7].

In view of such exotic materials with promising properties and intricate phase diagrams, one may question the motivation to study the old "conventional" elemental superconductors, which exhibit limited critical temperatures. The case for investigating superconductors such as niobium and vanadium is that they are some of the few elemental superconductors of the type-II classification. As a result, vortices of supercurrent can form inside them when exposed to a magnetic field. These vortices can form a structured lattice, *the flux line lattice*, which is also observed in high-T_c superconductors. The properties of the flux line lattice have important implications for the implementation of superconductors in technological applications, which typically have to be designed so as to limit the movement of the vortices. Niobium and vanadium provide excellent, simple model systems for studying the flux line lattice experimentally, especially because they

provide a much stronger neutron scattering signal than high-T_c superconductors. The motivation for studying the flux line lattice in vanadium and niobium can be broken down into three main points:

(i) Insight into the microscopic state of superconductors. Despite their *apparent* simplicity and conventional nature, niobium and vanadium both display non-trivial behaviour. Small angle neutron scattering has revealed that their vortex morphologies depend on the magnetic field orientation with respect to the underlying crystal axes and that different structural transitions can be induced via temperature and field changes [8]. Microscopic information regarding vortex pinning properties and elastic constants can be deduced by observing the dynamic behaviour near these transitions.

(ii) The flux line lattice as a general condensed matter testing ground. The flux line lattice is not only interesting as a subject of superconductivity studies but can also act as a general condensed matter model system. Studies of disordered vortex states can for example help improve our understanding of glassy systems.

(iii) Exploring Ginzburg-Landau theory. An extensive literature exists on the phenomenological Ginzburg-Landau equations and the different properties that have been calculated for the flux line lattice [9]. Detailed experimental measurements of the flux line lattice make it possible to test the Ginzburg-Landau results.

This thesis aims to investigate the flux line lattice as it is perturbed from its equilibrium state. In doing so, we incorporate the three main points from above. One of our primary goals is to investigate the dynamical response of the flux line lattice in a niobium sample and see how well Ginzburg-Landau theory describe the experimental situation. Furthermore, we aim to investigate the vortex states of an impure vanadium sample through experimental and numerical means.

Overview of thesis

Below is a brief description of the contents of the different chapters as well as a list of the experiments relevant to each chapter. Underlined experiments have been carried out without the author in attendance. Instead I have merely carried out the data analysis.

Chapter 1: Superconductivity: Conventional superconductivity theory is outlined alongside a more detailed description of the the flux line lattice. Two different, but complementary, theoretical approaches to the out-of-equilibrium behaviour of the flux line lattice are described, namely elastic and critical state theory.

Chapter 2: Prior characterizations of the flux line lattice: Based on past experimental and numerical studies, vortex states with different levels of disorder are described.

Chapter 3: Neutron scattering and muon spin rotation: This chapter introduces the essential neutron scattering theory needed for understanding the analysis of the experimental data. Muon spin rotation theory is also briefly introduced to provide context for Chapters 5 and 6.

Chapter 4: Dynamic properties of the flux line lattice in niobium: Stroboscopic small angle neutron scattering is used to observe how the flux line lattice responds to a temporally changing magnetic field. Our experiment is compared with conventional GL elasticity theory.

Experiments: (Stroboscopic SANS investigation of niobium; Maxwell setup; V4; HZB; 2017), (Stroboscopic SANS investigation of niobium; Helmholtz setup; V4, HZB; 2017), (Stroboscopic SANS investigation of vanadium; Helmholtz setup; V4; HZB; 2015; E. Tekin, M. Laver)

Chapter 5: Metastable states in vanadium: Experimental studies of impure vanadium samples make it possible to investigate how small amounts of disorder affect a

crystalline system. We investigate the Bragg glass with small angle neutron scattering and see how orientational order can be restored via a perpendicular oscillating field. We investigate the more disordered states with μSR and establish a vortex phase diagram for our sample.

Experiment: (SANS investigation of vanadium cylinder with oscillating field; SANS-1; FRM-II; 2016), (SANS investigation of vanadium disk with oscillating field; D33, ILL; 2017), (μSR investigation of vanadium; GPS; PSI; S. Samothrakitis; R. Toft-Petersen; M. Laver), Stroboscopic SANS investigation of vanadium; Helmholtz setup; V4; HZB; 2015; E.Tekin, M. Laver)

Chapter 6: Ginzburg-Landau simulations of the vortex lattice: The time-dependent Ginzburg-Landau equations are used to numerically investigate the field distribution of the flux line lattice under different conditions. Comparisons are made to experimental μSR data in an attempt at understanding the implications of negative skew distributions.

CHAPTER 1

SUPERCONDUCTIVITY

This chapter focus on the theories of superconductivity pertaining to conventional elemental superconductors. A brief description of the general phenomenology of superconductors is first given in Section 1.1. The Ginzburg-Landau equations constitute the main theoretical framework of this thesis and are introduced in detail in Section 1.2. Section 1.3 then reviews elastic flux line lattice theories, which are effectively two-dimensional and built on the assumption of perfectly straight flux lines. This assumption will not hold in the presence of impurities, which induce spatial perturbations. As an alternative to elastic theory, critical state models are therefore introduced in Section 1.4, wherein the behaviour of the flux line lattice in a sample with strong pinning forces is described.

1.1 Theories of superconductivity

In 1911 Kamerlingh Onnes observed that the resistivity of mercury abruptly drops to zero when cooled below a critical temperature of $T_c \approx 4.2\,\mathrm{K}$. The appearance of perfect conductance signalled a transition to an entirely new state of matter, today known as the *superconducting state*. A few decades after this initial discovery, Meissner and Ochsenfeld recognized that the superconducting state is not only characterized by perfect conductance but also by perfect diamagnetism [10]. Thus at low applied fields, a superconductor will exist in the Meissner-(Ochsenfeld) state, where magnetic flux is expelled from the bulk

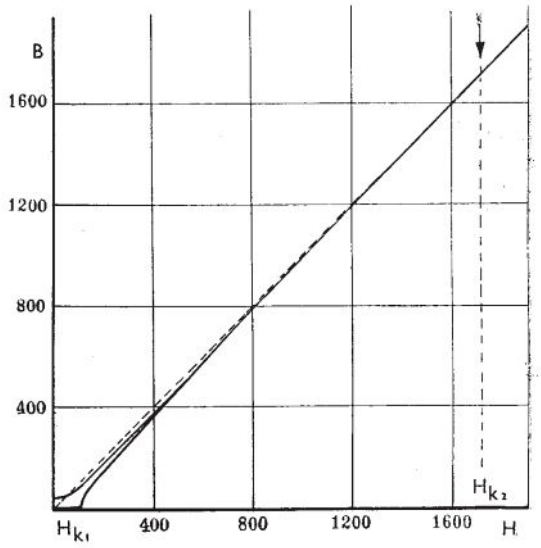

Figure 1.1: The induced field in $PbTl_2$ at 2.11 K as a function of the applied field. Below the lower critical field, H_{c1} (H_{k1} on the plot), the induced field is zero as for type-I superconductors. In between the lower critical field and upper critical field, H_{c2} (H_{k2} on the plot), the induced field increases steadily until it reaches the normal state flux density at H_{c2}. A hysteresis effect is observed as the applied field is decreased again from H_{c2} and residual flux appears trapped below H_{c1}. From Ref. 11.

of the sample. Shortly after this discovery, Rjabinin and Shubnikov observed a peculiar behaviour of the induced field curve of the superconducting alloy $PbTl_2$ [11] (cf. Fig. 1.1). Below a critical field, H_{c1}, the flux density was observed to be nearly zero, as expected from a superconductor existing in the Meissner state. Yet above this critical field, the flux density increased proportionally with the applied field until superconductivity broke down at an upper critical field, H_{c2}. This motivated the distinction between two different types of superconductors: Type-I superconductors, which exhibit a complete Meissner effect in the entire superconducting region, and type-II superconductors, which exhibit an incomplete Meissner effect between H_{c1} and H_{c2}.

The discovery of superconductivity prompted the development of new theories to explain the behaviour of this new state of matter. In 1935, the London brothers presented a set of phenomenological electromagnetic equations that were able to explain the Meissner effect [12]. However, while powerful in its relative simplicity and ability to reproduce some experimental observations, the London model has limited applicability due to it only being valid in the limit of weak applied fields and superconducting currents. Later in 1950, Ginzburg and Landau presented the new phenomenological Ginzburg-Landau (GL) theory [13]. An important outcome of this theory was Abrikosov's realization of the existence of the *flux line lattice* (FLL) [14]. The FLL is a solution to the equations of GL

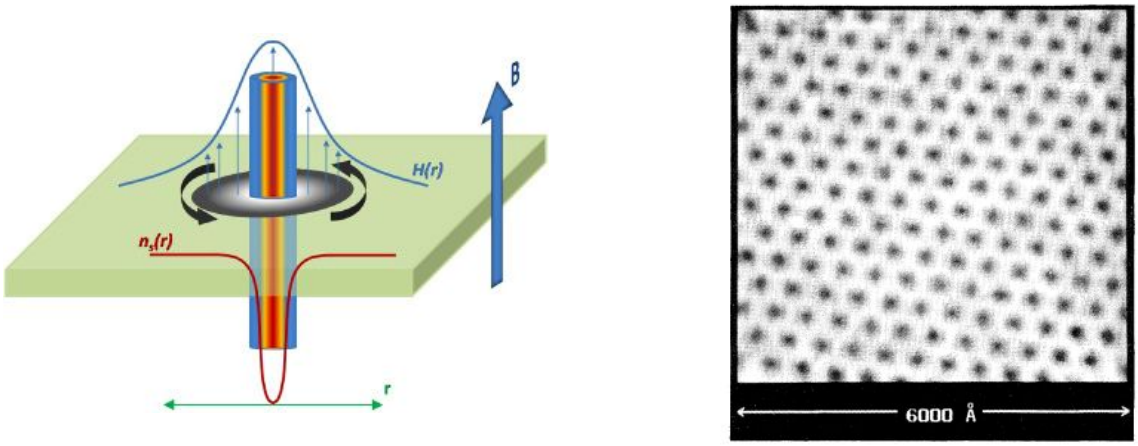

Figure 1.2: Left: Schematic of a single superconducting vortex. The induced magnetic field (order parameter) attains its maximum (minimum) value at the vortex core and gradually tapers off (recovers) away from it. In the image, the order parameter is labelled by $n_s(r)$, while the magnetic field is labelled by $H(r)$. Each vortex core is circulated by the supercurrent, $\mathbf{j}_s(\mathbf{r})$. Reprinted from Ref. 15. **Right:** Scanning Tunneling Microscope (STM) image of the vortex lattice of $NbSe_2$ obtained with a magnetic field of 1 T and a temperature of 1.8 K. The magnetic field was applied along the long axis of $NbSe_2$, which has a layered, hexagonal crystal structure. Dark areas in the image corresponds to vortex cores. From Ref. 16.

theory in which magnetic flux quanta penetrate the bulk of the superconductor and, in the absence of impurities, form a periodic lattice. Superconducting current, also known as the supercurrent, circulate around each flux line, which accordingly is also referred to as a vortex. Thus, the FLL explains the increasing flux density observed by Rjabinin and Shubnikov in type-II superconductors, and superconductors penetrated by flux lines are therefore said to be in the *mixed* or, equivalently, *Shubnikov* state. An illustration of a single flux line of a type-II superconductor is depicted in the left panel of Fig. 1.2, while the right panel shows a real-space image of an ordered FLL. In GL theory, the distinction between type-I and type-II superconductors can be made via the GL parameter, $\kappa = \lambda/\xi$, which defines the ratio of the penetration depth of the magnetic field, λ, to the superconducting coherence length, ξ. Superconductors with $\kappa < 1/\sqrt{2}$ are type-I, while superconductors with $\kappa > 1//\sqrt{2}$ are type-II.

Though very successful in explaining some macroscopic properties of superconductivity,

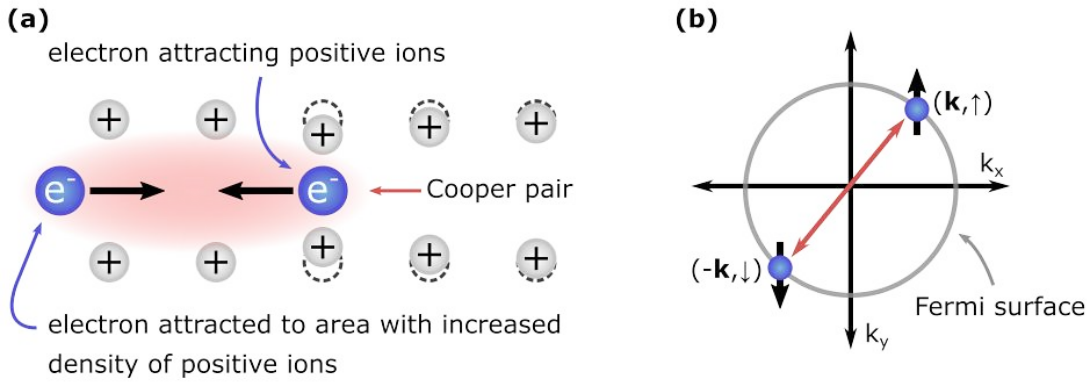

Figure 1.3: Schematics of Cooper pair formation in BCS theory. **(a)** A net attraction between two oppositely moving electrons is created from the dislocations of positive ions. **(b)** A BCS Cooper pair is formed from electrons with opposite spins and wave vectors, resulting in a zero momentum state.

GL theory still did not give a microscopic explanation of the phenomena. This was instead provided by the Bardeen-Cooper-Schrieffer (BCS) theory of superconductivity [5], cf. Fig. 1.3 for a schematic of the electron-phonon mechanism. The high-temperature copper-oxides [17] and the iron-pnictides [18] do not adhere to BCS theory and have therefore been classified as unconventional. The exact nature of the pairing mechanism of these superconductors is still under heavy investigation, though it is known to display inherent anisotropic properties [19, 20]. The otherwise conventional elemental superconductors, niobium and vanadium, are also known to exhibit anisotropic behaviours. In this thesis, they are used as simple model systems for investigating anisotropy effects in superconductors and for understanding vortex matter in general.

There are general differences between the vortex states of the elemental superconductors and different unconventional ones. High-T_c superconductors (HTSC) have large penetration depths and small coherence lengths, translating into large GL parameters and slowly varying magnetic fields. An important aspect of HTSCs is their layered structure resulting in the superconductivity taking place in two-dimensional planes. In the case of the cuprate superconductor Bi-2212 ($Bi_2Sr_2CaCuO_{8-\delta}$), the anisotropic structure results in the observation of unique two-dimensional pancake vortices [21]. As a result, Bi-2212 is a widely studied system (see Ref. 22 for a recent example). The conventional type-II super-

conductors, on the other hand, have underlying cubic crystal structures. Their anisotropic properties predominantly originate from the anisotropic nature of their Fermi surfaces. Nevertheless, in all cases the anisotropy expresses itself in the FLL of the superconductor, resulting in exotic vortex morphologies that are not observed in isotropic superconductors. This chapter will provide a brief outline of some parts of conventional superconductivity theory, which are necessary for illuminating this topic. Special attention will be paid to Ginzburg-Landau theory due to its importance in our numerical investigation and analysis of our experimental results.

1.1.1 London Theory

The London equation couples the magnetic field $\mathbf{B}$ and electric field $\mathbf{E}$ to the supercurrent $\mathbf{j}_s(\mathbf{r})$. A thorough derivation of the equations can be found in the textbook by de Gennes, cf. Ref. 23. Here, we state the first London equation [23]:

$$\mathbf{B} + \lambda^2[\nabla \times \nabla \times \mathbf{B}] = 0 \tag{1.1}$$

A simple way of demonstrating the Meissner effect is to solve the above London equation in one dimension, where a magnetic field is applied tangential to a superconductor surface. One then obtains the solution:

$$B(x) = B(0)\mathrm{e}^{-x/\lambda} \tag{1.2}$$

where x is the distance in the bulk from the surface of the superconductor. Thus the internal field decreases exponentially and will eventually approximate zero as one moves into the bulk of a macroscopic superconductor, cf. Fig. 1.4. From this one-dimensional solution, it is also evident that the parameter λ defines the field penetration depth.

Unlike GL theory, the existence of the FLL is not a result that automatically follows from the London equations. One can however insert vortices manually at positions $\mathbf{r}_\nu$ by

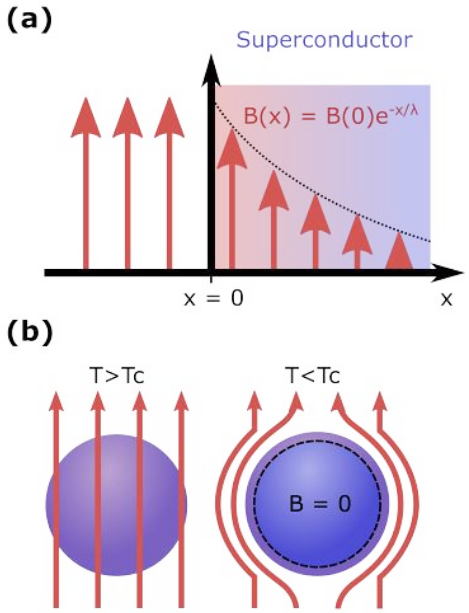

Figure 1.4: The behaviour of a superconductor in a static magnetic field as originally described by London theory. **(a)** Inside the bulk of a superconductor the field strength decays exponentially with a rate decided by the field penetration depth, λ. **(b)** Consequently, magnetic field lines are able penetrate a superconductor above T_c, while the induced field will tend to 0 in the bulk of the superconductor below T_c.

modifying the London equation to [9]:

$$\mathbf{B}(\mathbf{r}) + \lambda^2[\nabla \times \nabla \times \mathbf{B}(\mathbf{r})] = \mathbf{z}\Phi_0 \sum_{\nu} \delta_2(\mathbf{r} - \mathbf{r}_\nu) \tag{1.3}$$

here Φ_0 is known as the flux quantum, which defines the amount of flux going through each vortex core, and $\mathbf{z}$ is a unit vector defining the direction of the field. Meanwhile $\delta_2(\mathbf{r})$ is a 2-dimensional delta function, which defines the position of the vortex cores, where the superconductor is in the normal state. In this description, the vortex lines along the third dimension are thought to be completely straight and parallel. An advantage of the London model is that one can derive exact analytic expressions. From the modified London equation, the internal field profile of an array of isolated flux lines is found as [24]:

$$\mathbf{B}(\mathbf{r}) = \hat{\mathbf{z}} \frac{\Phi_0}{2\pi\lambda^2} \sum_{\nu} K_0 \left(\frac{|\mathbf{r} - \mathbf{r}_\nu|}{\lambda} \right) \tag{1.4}$$

where $|\mathbf{r} - \mathbf{r}_\nu|$ is the distance from a vortex core centre and K_0 is a modified Bessel function. The solution unphysically diverges at the vortex core positions, $\mathbf{r} = \mathbf{r}_\nu$. This is an artefact of manually inserting the vortices via a delta function, which naturally implies that the vortex cores have no finite width. To achieve a more realistic solution, one can

manually insert finite core widths by redefining the length $|\mathbf{r}-\mathbf{r}_\nu|$ as $(|\mathbf{r}-\mathbf{r}_\nu|^2+2\xi^2)^{1/2}$ [24]. This renormalization expression originates from Clem's description of a single vortex line in GL theory [25].

In general, the London description of the FLL has limited applicability to elemental superconductors, because it is only valid for weakly changing fields and for superconductors with a GL parameter of $\kappa >> 1$. This is not the case for niobium and vanadium, which are both just barely type-II. The restriction on κ is introduced by the use of Maxwell's equation $\nabla \times \mathbf{B}(\mathbf{r}) = \mu_0 \mathbf{j}_s(\mathbf{r})$ in the derivation of the conventional theory, since this implies a local relationship between the field and the supercurrent. This can only be true if the vortex cores are small, in other words meaning that the field penetration depth should be large compared to the superconducting order parameter coherence length. This section has only introduced London theory in its most simple form. The London model has since then been extended further, see for example the non-local generalization of the London model by Pippard [26] and the anisotropic London theory by Kogan [27].

1.2 Ginzburg-Landau theory

1.2.1 The time-independent Ginzburg-Landau equations

The basic premise of GL theory is that the transition from a superconducting to a normal state is characterized by an order parameter that continuously goes to zero, as is the defining behaviour of second-order transitions in general Landau theory. In the case of GL theory, the order parameter was originally identified as a macroscopically coherent wave function, $\psi(\mathbf{r}) = |\psi(\mathbf{r})|e^{i\theta(\mathbf{r})}$. It was not until 1959 that Gor'kov was able to connect GL theory with the by then developed BCS theory and determine that the GL order parameter is related to the density of Cooper pairs and thus to the gap function [28], $\psi(\mathbf{r}) \propto \Delta(\mathbf{r})$. With this order parameter in mind, the free energy expansion of a spatially

inhomogeneous superconductor in an applied field can be defined as:

$$F = F_n + a_{\mathrm{GL}}(T)|\psi(\mathbf{r})|^2 + \frac{b_{\mathrm{GL}}}{2}|\psi(\mathbf{r})|^4 + \frac{\hbar^2}{2m^*}\left|\left(\nabla - \frac{ie^*\mathbf{A}}{\hbar}\right)\psi(\mathbf{r})\right|^2 + \frac{B^2}{2\mu_0} \tag{1.5}$$

where F_n is the free energy of the superconductor in the normal state, a_{GL} and b_{GL} are phenomenological parameters, $\mathbf{A}$ is the vector potential, $\mathbf{B} = \nabla \times \mathbf{A}$ is the internal field, $m^* = 2m_e$ and $e^* = 2q$ are the mass and charge of a Cooper pair, and μ_0 is the vacuum permeability. The role of the vector potential is to ensure that the gradient term, $\frac{\hbar^2}{2m^*}\left|\left(\nabla - \frac{ie^*\mathbf{A}}{\hbar}\right)\psi(\mathbf{r})\right|^2$, is invariant under gauge transformations. The parameter b_{GL} is fixed to always be positive to ensure that the free energy always exhibit minima at finite $\psi(\mathbf{r})$. Meanwhile, the parameter $a_{\mathrm{GL}}(T) = a_{\mathrm{GL0}}(T - T_c)$, $a_{\mathrm{GL0}} > 0$, is defined such that it is positive above T_c and negative below. In the case of a spatially homogeneous superconductor with no applied field, the order parameter minimizer is:

$$|\psi_0|^2 = \begin{cases} 0, & \text{for } T > T_c \\ -\frac{a_{\mathrm{GL}}(T)}{b_{\mathrm{GL}}}, & \text{for } T < T_c \end{cases} \tag{1.6}$$

In the more general case, the equilibrium state of the spatially inhomogneous superconductor in an applied field is determined by minimizing the free energy of the entire sample, $\int F d\Omega$, with respect to $\psi^*(\mathbf{r})$ and $\mathbf{A}(\mathbf{r})$:

$$\begin{aligned} \delta F = &\int d\mathbf{r}\left\{\delta\psi^*\left[a_{\mathrm{GL}}\psi + b_{\mathrm{GL}}|\psi|^2\psi + \frac{\hbar^2}{2m^*}\left(\nabla - \frac{ie^*\mathbf{A}}{\hbar}\right)^2\psi\right] + \text{ C.C.}\right\} \\ &+ \int d\mathbf{r}\delta\mathbf{A}\left\{\frac{1}{\mu_0}\nabla\times\mathbf{B}_i - \frac{ie^*\hbar}{2m^*}\left[\psi^*\left(\nabla - \frac{ie^*\mathbf{A}}{\hbar}\right)\psi + \text{ C.C.}\right]\right\} \end{aligned} \tag{1.7}$$

In this way, one arrives at the Ginzburg-Landau equations:

$$0 = a_{\mathrm{GL}}\psi + b_{\mathrm{GL}}|\psi|^2\psi + \frac{\hbar}{2m^*}\left(\nabla - \frac{ie^*\mathbf{A}}{\hbar}\right)^2\psi \tag{1.8}$$

$$\mathbf{j}_s = \frac{i\hbar e^*}{2m^*}\left(\psi^*\nabla\psi - \psi\nabla\psi^*\right) - \frac{(e^*)^2}{m^*}|\psi|^2\mathbf{A} \tag{1.9}$$

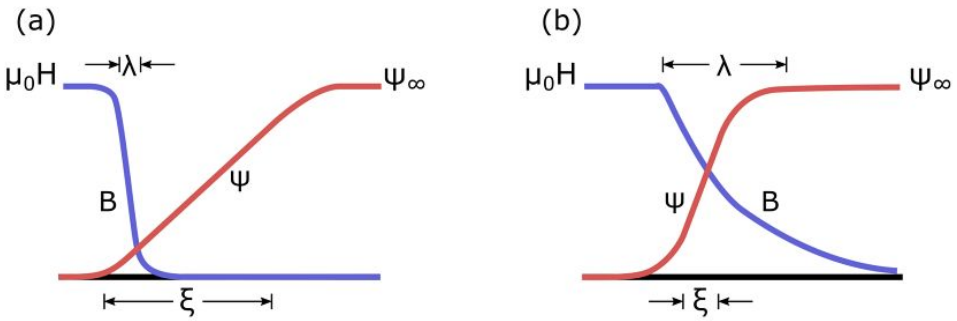

Figure 1.5: Behaviour of the induced field, B, and order parameter, ψ, near a normal state to superconductor surface for a type-I (**a**) and type-II (**b**) superconductor. In the normal state, the induced field attains the applied field value, $\mu_0 H$. Adapted from Ref. 29.

here $\mathbf{j}_s$ is the supercurrent density, $\mathbf{j}_s = \frac{1}{\mu_0}\nabla \times \nabla \times \mathbf{A}$. As was mentioned in the introduction, the GL equations are characterized by two characteristic length scales, the field penetration depth, λ, and coherence length, ξ. The ratio between these two define the GL parameter:

$$\kappa = \frac{\lambda(T)}{\xi(T)} \tag{1.10}$$

The GL parameter determines the behaviour of the superconductor near superconducting to normal state domain walls, see Fig. 1.5. In the case of $\kappa < 1/\sqrt{2}$ (type-I superconductors), the domain wall energy is positive, meaning that the ground state configuration minimizes the number of domain walls and therefore expels all magnetic field [29]. When $\kappa > 1/\sqrt{2}$ (type-II superconductors) the domain wall energy is negative and it therefore becomes energetically favorable to let the magnetic field penetrate the superconductor in the form of flux lines. The thermodynamic critical field, B_c, is in GL theory found from the difference between the normal and superconducting state:

$$F - F_n = \frac{B_c^2}{2\mu_0} = \frac{a_{\mathrm{GL}}^2}{2b_{\mathrm{GL}}} \tag{1.11}$$

where the minimizer from Eq. (1.6) has been used to realize the second equation. The GL expression for the upper critical field, B_{c2}, is derived by first linearising Eq. (1.8) by excluding the term $|\psi|^2\psi$, which becomes infinitesimally small as the upper critical field

is approached [30]:

$$0 = a_{\mathrm{GL}}\psi + \frac{\hbar}{2m^*}\left(\nabla - \frac{ie^*\mathbf{A}}{\hbar}\right)^2 \psi \tag{1.12}$$

which is similar to the linear Schrödinger equation for a charged particle moving in a magnetic field. Employing the Landau gauge and the lowest Landau level approximation, the following expression for B_{c2} is identified [30]:

$$B_{c2} = \frac{\Phi_0}{2\pi\xi^2} = \sqrt{2}\kappa B_c \tag{1.13}$$

where Φ_0 is still the flux quantum. Calculations of the lower critical field, B_{c2}, requires one to identify the field at which the free energy of the Meissner state is unaffected by the addition of one flux line. This calculation requires a consideration of the energy of a single flux line, eventually resulting in [9]:

$$B_{c1} = \frac{\Phi_0}{4\pi\lambda^2}\left(\ln\kappa + 0.5\right) \tag{1.14}$$

If the applied field is increased from B_{c1}/μ_0, more flux lines enter the superconductor, resulting an an increased flux density. With increasing applied field, the vortex cores will tend to increasingly overlap until they completely fill out the volume of the superconductor at the upper critical field.

1.2.2 The Abrikosov lattice

The flux line lattice was first theoretically described by Abrikosov in Ref. 14, wherein he finds a periodic solution to the GL equations. Abrikosov first constructs a two-dimensional trial solution to the first GL equation in the lowest Landau level approximation, Eq. (1.12), as:

$$\psi(x,y) = \sum_{n=-\infty}^{\infty} C_n \exp(inky)\exp\left(-\frac{1}{2}\kappa^2\left[x - \frac{nk}{\kappa^2}\right]^2\right) \tag{1.15}$$

where C_n and k are dependent on the geometry of the two-dimensional arrangement of vortices. This trial function also turns out to be appropriate for the general GL equation with the nonlinear $|\psi|^2\psi$ term included. To ensure periodicity along the x-direction, the normalization constants C_n need to be periodic themselves, $C_{N+n} = C_n$. The parameters C_n and k of the equilibrium flux line lattice are found by minimizing the free energy. Abrikosov writes the GL free energy of the flux line lattice as [14]:

$$F(B) = \frac{B^2}{2\mu_0} - \frac{(B_{c2} - B)^2}{2\mu_0(2\kappa^2 - 1)\beta_A} \tag{1.16}$$

where $\beta_A = \langle|\bar{\psi}|^4\rangle / \langle|\bar{\psi}|^2\rangle^2$ is the Abrikosov parameter, which depends on the morphology of the two-dimensional vortex lattice. In his original derivation, Abrikosov found that the free energy was minimized when all the normalization constants C_n where equal, corresponding to a periodicity of $N = 1$. This resulted in a square vortex arrangement, with an Abrikosov parameter of $\beta_A = 1.18$. Kleiner *et al.* later showed that this solution is in fact unstable towards a hexagonal vortex solution, as depicted in Fig. 1.6, which has an Abrikosov parameter of $\beta_A = 1.16$ and $N = 2$ [31]. The hexagonal equilibrium state provides maximal distance between all vortex cores and thus implies a repulsive interaction between vortices in the mixed state. The small difference in the Abrikosov parameter between the square and hexagonal vortex lattice illustrates how structural transitions can easily be induced via, for example, extra anisotropy terms in the free energy [32].

1.2.3 The intermediate mixed state

Type-II superconductors can be further sub-classified into type-IIa and type-IIb depending on the presence of an *intermediate mixed state* (IMS) in the phase diagram [33]. The IMS exists as a transitional state between the Meissner state and mixed Shubnikov state in type-IIa superconductors, where domains of Abrikosov vortices coexist with the Meissner state (cf. Fig. 1.7a). The observed domain formation is caused by concomitant short-range

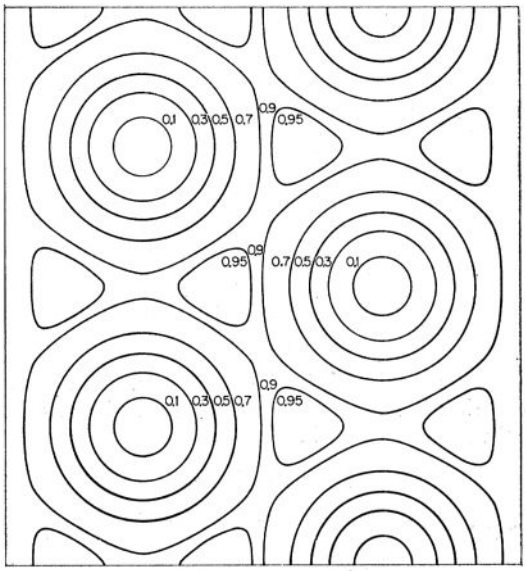

Figure 1.6: A contour diagram of the near-H_{c2} order parameter, $|\psi|^2$, as calculated by W. H. Kleiner et al. In the minimum-energy state, the vortices arrange themselves in a hexagonal pattern to maximize the distance between them. From Ref. 31.

repulsive *and* long-range attractive components of the vortex-vortex interaction. Thus, type-IIa superconductors exhibit characteristics of both type-I and type-II at low applied fields, which is a result of their low-κ values of ~ 1 [33].

The field-dependent behaviour of the intensity and reciprocal lattice vectors of a type-IIa superconductor, as measured with neutron scattering, is depicted in Fig. 1.7b. At low applied fields, the superconductor is in the Meissner state and contains no vortices, causing no measured intensity or detected lattice spacing. The lower field at which the Meissner phase disintegrates is determined by the sample shape. An infinitely long cylindrical sample has a demagnetization factor of $D = \frac{1}{2}$, when the field is applied along the long axis of the cylinder. A spherical sample has a demagnetization factor of $D = \frac{1}{3}$. Thus, the IMS appears at an applied field of $\mu_0 H'_{c1} = (1-D)\mu_0 H_{c1} = \frac{1}{2}\mu_0 H_{c1}$ in long cylindrical samples [35] and at $\mu_0 H'_{c1} = \frac{2}{3}\mu_0 H_{c1}$ in spherical samples [36]. In the IMS, the gradual appearance of vortices as a function of field causes the integrated scattering intensity to increase, while the flux density in the Abrikosov domains remains at a finite constant value, B_0. At applied fields of $\frac{1}{2}\mu_0 H_{c1} + \frac{1}{2}B_0$ for cylindrical samples and $\frac{2}{3}\mu_0 H_{c1} + \frac{1}{3\mu_0}B_0$ for spherical samples, a transition to the mixed state occurs. Here, the scattering intensity decreases as a function of higher fields due to the decreasing form factor, while the reciprocal lattice vector, and thus flux density, gradually increases. The intensity curve

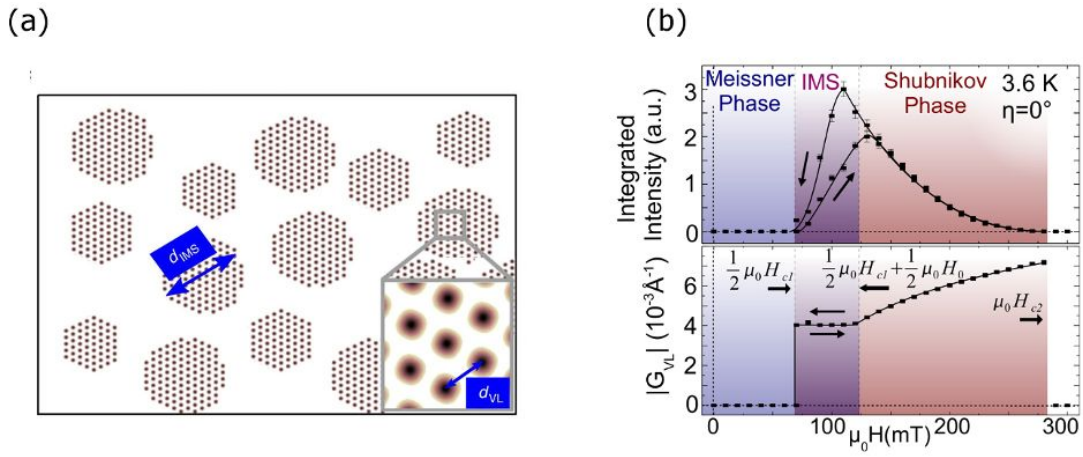

Figure 1.7: **(a)** Schematic of the intermediate mixed state, where islands of Abrikosov vortices (red dots) are surrounded by Meissner state. Reprinted from Ref. 34. **(b)** The intensity and reciprocal lattice spacing of a type-IIa superconductor, as determined from neutron scattering of a cylindrical niobium sample. Figure from Ref. 35.

of Fig. 1.7b display hysteretic behaviour in the IMS, which is interpreted as a sign of different IMS vortex morphologies upon increasing and decreasing fields [35]. Decreasing fields is thought to result in the island-like domains depicted in Fig. 1.7a, while increasing fields result in dendritic domains [37].

1.2.4 The time-dependent Ginzburg-Landau equations

Describing out-of-equilibrium behaviour of the FLL necessitates time-dependent GL equations. Such a set of equations was first written down by Landau and Khalatnikov in Ref. 38, where they investigated relaxation processes in superfluid ^{4}He. The basic premise of their time-dependent GL theory was the following transport equation:

$$\frac{\partial|\psi|}{\partial t} = -\gamma\frac{\partial F}{\partial|\psi|} \tag{1.17}$$

which implies that the order parameter will relax towards a free energy minimum with a rate of change proportional to the slope of F. The parameter γ is a proportionality constant. To make this equation applicable to superconductors, whose elementary particles are charged, one needs to make sure that the time-derivative is gauge-invariant,

$\partial/\partial t \rightarrow \partial/\partial t + ie^*/\hbar\phi$, where ϕ is the electric potential [39]. As such, the following time-dependent GL equations can be defined [40, 41]:

$$\frac{\hbar^2}{2m^* D}\left(\frac{\partial}{\partial t} + i\frac{e^*}{\hbar}\phi\right)\psi = \frac{\hbar^2}{2m^*}\left(\nabla - i\frac{e^*}{\hbar}\mathbf{A}\right)^2\psi + |a_{\mathrm{GL}}|\psi - b_{\mathrm{GL}}|\psi|^2\psi \tag{1.18}$$

$$\sigma\left(\nabla\phi + \frac{\partial \mathbf{A}}{\partial t}\right) = \frac{\hbar e^*}{2m^* i}\left(\psi^*\nabla\psi - \psi\nabla\psi^*\right) - \frac{(e^*)^2}{m^*}|\psi|^2\mathbf{A} - \frac{1}{\mu_0}\nabla\times\nabla\times\mathbf{A} \tag{1.19}$$

where D is a phenomenological diffusion constant and σ is a field relaxation parameter. The relaxation rate of the vector potential, Eq. (1.19), is realized by adding a normal current of non-superconducting electrons to Eq. (1.9) [41].

The validity of the TDGL equations as given in Eqs. (1.18)–(1.19) remains controversial, because they do not appear to be derivable from microscopic theory like their static counterparts [42]. This is proven in Ref. 43, where Frank *et al.* provide a mathematical rigorous argument for the incompatibility of the TDGL equations and the microscopic time-dependent Bogoliubov–de–Gennes equations. Frank *et al.* state that this incompatibility does not necessarily invalidate the TDGL equations, seeing as physics beyond BCS theory may contribute to their formulation. They make this point because the TDGL equations for years have been employed in a wide range of studies, see for example Ref. 40 where TDGL results compare favorably to experimental resistivity measurements of $Nb_{0.5}Ta_{0.5}$ and $Nb_{0.1}Ta_{0.9}$, and Ref. 44 where the numerical results are positively compared to terahertz spectroscopy measurements of NbN. In Ref. 40, good agreement between TDGL theory and experimental measurements is observed when the reduced temperature, T/T_c, is above 0.6.

1.3 Elasticity theory

The microscopic nature of the superconducting state is reflected in the response of the FLL to external perturbations [45]. Each individual vortex line can be described as

an elastic string with an associated line tension [9]. The dynamical response of the entire FLL is affected by the line tension of each individual vortex line, their repulsive interaction potential in the mixed state, thermal fluctuations, and pinning effects. For small distortions, the flux lines are expected to behave elastically and can accordingly be treated like a solid media that bends akin to a crystal lattice. In this description, the overall elastic properties are fully characterized by the elastic moduli, which have been derived for the FLL in great detail by e.g. Labusch [46, 47] and Brandt [9, 48, 49]. The derivation of the elastic constants of arbitrary three-dimensional systems is a complex endeavour and a number of simplifying assumptions are therefore typically made to facilitate the calculations. Assuming the applied field, and thereby the flux lines, are aligned along $\hat{\mathbf{z}}$, the elastic energy of the FLL can according to continuum theory be written as [9]:

$$F_{\mathrm{el}} = \frac{1}{2}\int_{\mathrm{BZ}} \frac{d\mathbf{k}}{(2\pi)^3}\mathbf{u}_\alpha(\mathbf{k})\Phi_{\alpha\beta}\mathbf{u}^*_\beta(\mathbf{k}) \tag{1.20}$$

where $(\alpha, \beta) = (x, y)$, $\Phi_{\alpha\beta}$ is the elastic matrix, and $\mathbf{u}(\mathbf{k})$ are the Fourier components of the displacement vectors of the flux lines:

$$\mathbf{u}(\mathbf{k}) = \frac{\Phi_0}{B}\sum_i \int dz \mathbf{u}_i e^{-i\mathbf{k}\cdot\mathbf{R}_i}, \qquad \mathbf{u}_i = \int_{\mathrm{BZ}} \frac{d\mathbf{k}}{(2\pi)^3}\mathbf{u}(\mathbf{k})e^{i\mathbf{k}\cdot\mathbf{R}_i} \tag{1.21}$$

where the sum is performed over over all vortices, i. The real-space displacement vectors, $\mathbf{u}_i = \mathbf{r}_i - \mathbf{R} = (u_{ix}, u_{iy}, 0)$, are defined as the difference between their distorted position, $\mathbf{r}_i$, and the ideal lattice positions, $\mathbf{R}_i$. The elements of the elastic matrix elements are defined as:

$$\Phi_{xx} = c_{11}k_x^2 + c_{66}k_y^2 + c_{44}k_z^2 \tag{1.22}$$

$$\Phi_{yy} = c_{66}k_x^2 + c_{11}k_y^2 + c_{44}k_z^2 \tag{1.23}$$

$$\Phi_{xy} = \Phi_{yx} = (c_{11} - c_{66})k_x k_y \tag{1.24}$$

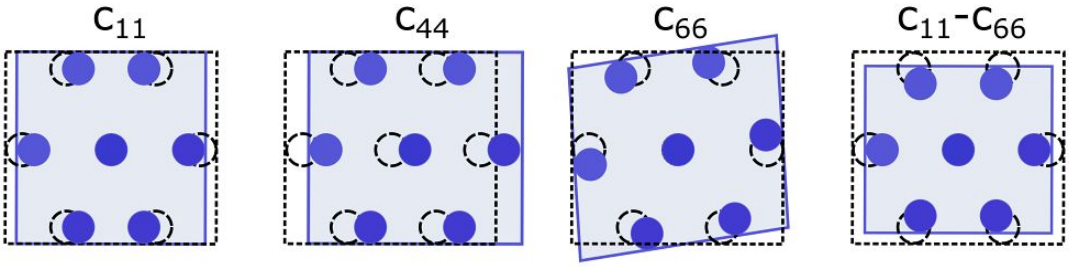

Figure 1.8: Schematics of different elastic deformations of an isotropic FLL. The deformations associated with the compression modulus, c_{11}, tilt modulus, c_{44}, shear modulus, c_{66} and the shape-preserving $c_{11} - c_{66}$ compression are shown from left to right. The triangular equilibrium lattice positions are marked with dashed circles, while the distorted positions are marked with blue spheres. Bounding boxes are used to show how the unit cell area is preserved for the c_{44} and c_{66} distortions, but not the c_{11} and $c_{11}-c_{66}$ distortions.

where k_x and k_y are components of the vector $\mathbf{k}$, and c_{11}, c_{44} and c_{66} are the compression, tilt and shear moduli, which describe three independent elastic modes of the FLL. The Labusch parameter, $\alpha_L(\mathbf{k})$, is added to the diagonal elements to account for elastic pinning interactions with impurities [50]. A k-independent Labusch parameter is used when the vortices are pinned individually, while a k-dependence of the parameter is indicative of collective pinning [9]. In the weak collective pinning regime, $\alpha_L(\mathbf{k})$ is reduced when $k_\perp > R_c^{-1}$ or $k_z > L_c^{-1}$, where radius R_c and length L_c characterize the size of the coherent short range ordered regions of the pinned FLL [9].

1.3.1 Isotropic elasticity theory

In Ref. 47 Labusch provides simple derivations of the elastic properties of an isotropic, hexagonal FLL with straight lines. Labusch reasons that any three linearly independent combination of c_{11}, c_{44}, and c_{66} will characterize all the elastic properties of the FLL under consideration. This motivates the derivations of the three moduli, c_{44}, c_{66} and $c_L = c_{11} - c_{66}$. The c_L modulus is in general elasticity theory known as the *hydrostatic compression* modulus and is chosen because, unlike the pure c_{11} compression modulus, it preserves the shape of the FLL [51]. The in-plane effect of elastic deformations characterized by the different elastic moduli is illustrated in Fig. 1.8. The compression and tilt moduli

are determined from simple thermodynamic arguments, where one considers how the free energy is affected by a volume-changing unit cell and how much work is done when the lattice is tilted. The resulting expressions for the moduli are [47]:

$$c_L = B^2 \frac{\partial H}{\partial B}, \qquad c_{44} = BH \tag{1.25}$$

On the other hand, the derivation of the shear modulus necessitates that one considers the FLL unit cell more concretely. Labusch used the trial function from Eq. (1.15) and could thereby derive [47]:

$$c_{66} = \frac{H_c^2}{2\mu_0} \frac{\kappa^2(2\kappa^2 - 1)}{[1 + (2\kappa^2 - 1)\beta_A]^2} \times 0.48 \left(1 - \frac{B}{H_{c2}}\right)^2 \tag{1.26}$$

According to this expression, the shear modulus goes to zero at H_{c2}, indicating that the vortex lattice becomes liquid-like at high fields.

1.3.2 Anisotropic and nonlocal elasticity

The straightforward expressions of the previous section break down if the FLL evinces any kind of anisotropic or nonlocal behaviour, which introduces a k-dependence in the elastic moduli. Nonlocal behaviour ($k \neq 0$) can either be intrinsic to the superconductor or induced via large deformations of the FLL. The continuum description of the elastic matrix elements, Eqs. (1.22) to (1.24), does not hold once the size of the deformation in the xy-plane approaches the size of the Brillouin zone, $k_x^2 + k_y^2 \approx k_{BZ}^2$ [9]. This is because the assumed periodicity of the matrix elements, $\Phi_{\alpha\beta}(\mathbf{k}) = \Phi_{\alpha\beta}(\mathbf{k} + \mathbf{K})$, with $\mathbf{K}$ being the reciprocal lattice vectors of the FLL, ceases to hold true. In Ref. 48, Brandt calculates the nonlocal elastic constants for large inductions, where the GL equations can be linearized. In Ref. 49 he derives the nonlocal elastic constants at low inductions, where London theory applies. Despite being qualitatively different theories, Brandt obtains similar results from the two derivations; In both cases the shear modulus is found to be dispersionless,

while the FLL softens with respect to the dispersive tilt and compression moduli. Larkin and Ovchinnikov rederived the nonlocal elastic constant from the microscopic theory of Gorkov [52], and obtained the following, slightly corrected results, which have since been simplified by Brandt [53]:

$$c_{66} \approx \frac{B_{c2}^2}{\mu_0}\frac{b_M(1-b_M)^2}{8\kappa^2}\left(1-\frac{1}{2\kappa^2}\right)(1-0.58b_M+0.29b_M^2) \tag{1.27}$$

$$c_{11}(k) = \frac{B_{c2}^2}{\mu_0}\left(1-\frac{1}{2\kappa^2}\right)\left(1+\frac{k^2\lambda^2}{1-b_M}\right)^{-1}\left(1+\frac{k^2\xi^2}{2-2b_M}\right)^{-1} \tag{1.28}$$

$$c_{44}(k) = \frac{B_{c2}^2}{\mu_0}\left[\left(1+\frac{k^2\lambda^2}{1-b_M}\right)^{-1}+\frac{\xi^2(1-b_M)}{2b_M\lambda}\right] \tag{1.29}$$

where $b_M = B/B_{c2}$ is the reduced field. The above equations are valid in the field range $(2\kappa^2)^{-1} < b_M < 1$.

Anisotropy modifications of the traditional GL [54] and London equations [27] are well studied due to the inherent anisotropy of the high-T_c cuprate superconductors, owing from their tetragonal, layered structure. In both theories, anisotropy is introduced in the free energy via an effective mass tensor. The anisotropy can also be characterized by the varying field penetration depth along different crystal directions. For a tetragonal superconductor, with a basal plane penetration depth of λ_{ab}, a long axis penetration depth of λ_c, and the field $\mathbf{B} \parallel \hat{\mathbf{z}}$ oriented along the c-axis, the following set of elastic constants has been derived from anisotropic London theory [9]:

$$c_{11}(\mathbf{k}) = \frac{B^2}{\mu_0}\frac{1+\lambda_c^2k^2}{(1+\lambda_{ab}k^2)(1+\lambda_c^2k_\perp^2+\lambda_{ab}^2k_z^2)} \tag{1.30}$$

$$c_{44}(\mathbf{k}) = \frac{B^2}{\mu_0}\left[\frac{1}{1+\lambda_c^2k_\perp^2+\lambda_{ab}^2k_z^2}+\frac{f(k_z)}{\lambda_{ab}^2k_{BZ}^2}\right] \tag{1.31}$$

$$f(k_z) = \frac{1}{\Gamma^2}\ln\frac{\xi_c^{-2}}{\lambda_{ab}^{-2}+k_z^2+\Gamma^2k_0^2}+\frac{\ln\left[1+k_z^2/(\lambda_{ab}^{-2}+k_0^2)\right]}{2k_z^2\lambda_{ab}^2} \tag{1.32}$$

which is only valid at low inductions, $b_M < 0.25$ and with $\kappa = \lambda_{ab}/\xi_{ab} > 2$. Γ is the anisotropy ratio, λ_{ab}/λ_c, and $k_0 \approx k_{BZ}$ is a cutoff. A derivation based on the same system

has been performed by Houghton *et al.* [55], employing anisotropic GL theory:

$$c_{11}(\mathbf{k}) = \frac{B^2}{\mu_0}\frac{(1-b_M)}{2b_M\kappa}\left(\frac{k^2+\Gamma m_\lambda^2}{(k^2+m_\lambda^2)(k_\perp^2+\Gamma k_z^2+\Gamma m_\lambda^2)} - \frac{1}{k_\perp^2+\Gamma k_z^2+m_\xi^2}\right) \tag{1.33}$$

$$c_{44}(\mathbf{k}) = \frac{B^2}{\mu_0}\frac{(1-b_M)}{2b_M\kappa^2}\Gamma\left(\frac{1}{k_\perp^2+\Gamma(k_z^2+m_\lambda^2)}+1\right) \tag{1.34}$$

$$m_\lambda^2 = \frac{1-b_M}{2b_M\kappa^2}, \qquad m_\xi^2 = \frac{1-b_M}{b_M} \tag{1.35}$$

These equations are valid at high inductions, where the fields of the flux lines overlap, $\frac{1}{2}\kappa^2 < b_M < 1$. We do not reprint the shearing modulus, since it is similar to the nonlocal case. A common thread shared among the results presented in this section is that any deviance from the purely local, isotropic elastic description results in a softening of the FLL with respect to tilt and compression modes. The dispersive anisotropic GL elastic constants, Eqs. (1.33) and (1.34), and the dispersive nonlocal elastic constants derived from microscopic theory, Eqs. (1.28) and (1.29), behave similarly at increasing fields. In both cases we see that the tilt and compression moduli goes to zero at the upper critical field. This same behaviour is not explicitly observed in the London elastic constants, Eqs. (1.30) and (1.31). However, by inserting the effective field penetration depth, $\lambda(B) = \lambda(0)/\sqrt{1-b_M}$, one recovers a similar field-dependent behaviour [9].

1.4 Critical state models of superconductivity

The elastic description of Section 1.3 provides thermodynamic arguments for how the vortices are distorted under small perturbations. Critical state models are instead grounded in the electromagnetic description of current flows and processes, and are used to determine how flux enters and propagate through the bulk of a superconductor. The first and most well-known critical state model is that of Bean [56], which describes the irreversible magnetization states observed in superconductors, cf. Fig. 1.1. If one applies an external current, $\mathbf{J}_{ext}$, to a superconductor with a FLL, the flux lines will be affected by a Lorentz

force:

$$\mathbf{F}_L = \mathbf{J}_{ext} \times \Phi_0 \tag{1.36}$$

The Lorentz force will cause the flux lines to move with a constant velocity $\mathbf{v}$ in a direction perpendicular to $\mathbf{J}_{ext}$, which in turn will induce an electromotive force, $\mathbf{E} = \mathbf{B} \times \mathbf{v}$, causing dissipative processes [57]. The movement of vortices can be stopped by pinning phenomena, which play a crucial role Bean's critical state model. Lattice defects or impurities in a superconductor can locally reduce the superconducting order parameter and thereby attract and pin nearby vortex cores in place. In Bean's critical state model, a stationary vortex state is obtained when the Lorentz force is exactly balanced by the pinning force, $\mathbf{F}_p$:

$$\mathbf{F}_p + \mathbf{F}_L = 0 \tag{1.37}$$

In some cases a damping force is also included [57]. The critical current, $\mathbf{J}_c$, is defined as the largest possible current one can apply without destabilizing the stationary state. A defining feature of a critical state model is the field and temperature dependence of the critical current [39]. In Bean's original model [56], the critical current was field and temperature independent. Later Kim *et al.* suggested the following model based on experimental data:

$$\mathbf{J}_c(T, B) = \frac{J_0}{1 + B/B_0} \tag{1.38}$$

where J_0 is a constant. These two models constitute the two most well-known critical state models, though several different formulations exist [58, 59].

Knowing the basic premise of the theory, the concept of irreversible magnetization phenomena in a superconducting slab can be understood as illustrated in Fig. 1.9. If one increases the field of a cooled superconductor above H_{c1} (ignoring barrier effects), vortices will initially enter the superconductor and be stopped by pins. Increasing the field further will cause more vortices to amass at the border of the sample, which will cause a flux gradient in the superconductor. Maxwell's equations state that the field gradient

will induce a current $\nabla \times \mathbf{B} = \mu_0 \mathbf{J}_c$, encouraging the vortices to move further into the bulk of the sample. According to Bean's theory, the induced current will always be equal to the critical current, $\mathbf{J}_c$, regardless of the flux gradient. If the applied field is lowered again, an equal critical current will be induced in the other direction, eventually leading to flux being trapped as the applied field reaches zero.

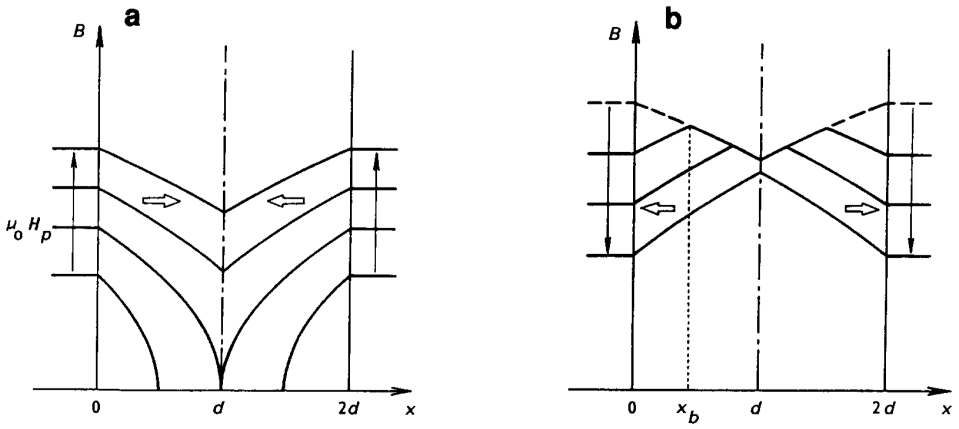

Figure 1.9: Example of an irreversible process in a superconductor as understood through Bean's model. In panel (a) the applied field $\mu_0 H_p$ is gradually increased from zero, which results in a field gradient in the material. The applied field is decreased again in panel (b), where it is evident that some flux will be trapped. Reprinted from Ref. 57.

1.4.1 Flux cutting

Unusual critical states are theoretically predicted if the critical current is not perpendicular to the local magnetic induction [61]. Depending on the ratio of the perpendicular to parallel critical current components with respect to the local field, flux line cutting is

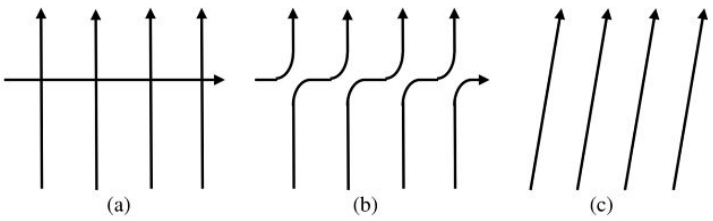

Figure 1.10: **(a)** An extreme example of flux cutting in which a horizontal flux line cuts through a vertical array of flux lines. **(b)** The flux lines join and **(c)** eventually form a diagonal array. Reprinted from Ref. 60.

thought to occur. Flux line cutting describes a situation in which flux lines are able to break and reform, thereby effectively making it possible for other flux lines to pass through them, cf. Fig. 1.10. In Ref. 62 Brandt *et al.* calculate an approximate GL interaction energy, $E(\theta_f, s)$, and repulsive force, $F_f(\theta_f, s)$, between two adjacent flux lines, which are separated by a distance s and tilted with respect to one another by an angle θ_f:

$$E(\theta_f, s) = A_f \frac{\Phi_0^2}{2\mu_0 \lambda \sin\theta_f} \left[\cos\theta_f \exp\left(-\frac{S}{\lambda}\right) - \frac{1}{\sqrt{2}\kappa} \exp\left(-\frac{S\sqrt{2}}{\xi}\right) \right] \tag{1.39}$$

$$F_f(\theta_f, s) = -\frac{\partial E}{\partial s} = A_f \frac{\Phi_0^2}{2\mu_0 \lambda^2 \sin\theta_f} \left[\cos\theta_f \exp\left(-\frac{S}{\lambda}\right) - \exp\left(-\frac{S\sqrt{2}}{\xi}\right) \frac{s}{S} \right] \tag{1.40}$$

where

$$S = \sqrt{s^2 + \xi_v^2} \tag{1.41}$$

$$A_f = \frac{\lambda}{\xi_v} K_1\left(\frac{\xi_v}{\lambda}\right) \tag{1.42}$$

$$\kappa = \sqrt{2}\frac{\lambda}{\xi_v} \sqrt{\frac{1 - K_0^2(\xi_v/\lambda)}{K_1^2(\xi_v/\lambda)}} \tag{1.43}$$

where Eq. (1.43) is used to determine the variational core parameter ξ_v. The results are approximate because the flux lines have been assumed to be non-bending. The interaction energy consists of two different interaction terms. The first is the electromagnetic interaction, which is repulsive when $\theta_f < \pi/2$ and which decays over a scale determined by λ. The second energy term is the attractive core interaction, which decays over a length scale determined by ξ. The maximal repulsive force is according to Eq. (1.40) correlated with κ, indicating that flux cutting should be more likely to happen in low-κ superconductors.

CHAPTER 2

PRIOR CHARACTERIZATIONS OF THE FLUX LINE LATTICE

In this chapter, we aim to provide a brief overview of the extensive literature that exists on the flux line lattice. Section 2.1 describes the different types of static vortex states that have been theoretically predicted and experimentally observed in superconducting samples. Section 2.2 outlines the massive effort that has gone into understanding the FLL via simulations, while Section 2.3 describes previous FLL transport investigations that have been undertaken with experimental and numerical means.

2.1 Vortex states of an impure superconductor

An exciting aspect of the FLL is its similarity to ordinary matter; it exhibits both a crystalline order with defined elastic energy as well as a melting transition that sets in upon increasing temperature fluctuations [63]. Impurities induce spatial perturbations in the FLL, thereby affecting the overall ordering behaviour and inducing new vortex states such as the Bragg glass, which has also been observed in non-superconducting matter like smectic liquid crystals [64]. The FLL therefore makes an excellent general model system for understanding the impact of disorder on two- or quasi-two-dimensional crystalline systems and for studying order-to-disorder transitions across glassy states of matter [65]. Unlike other crystalline systems, the relative strength of the FLL disorder

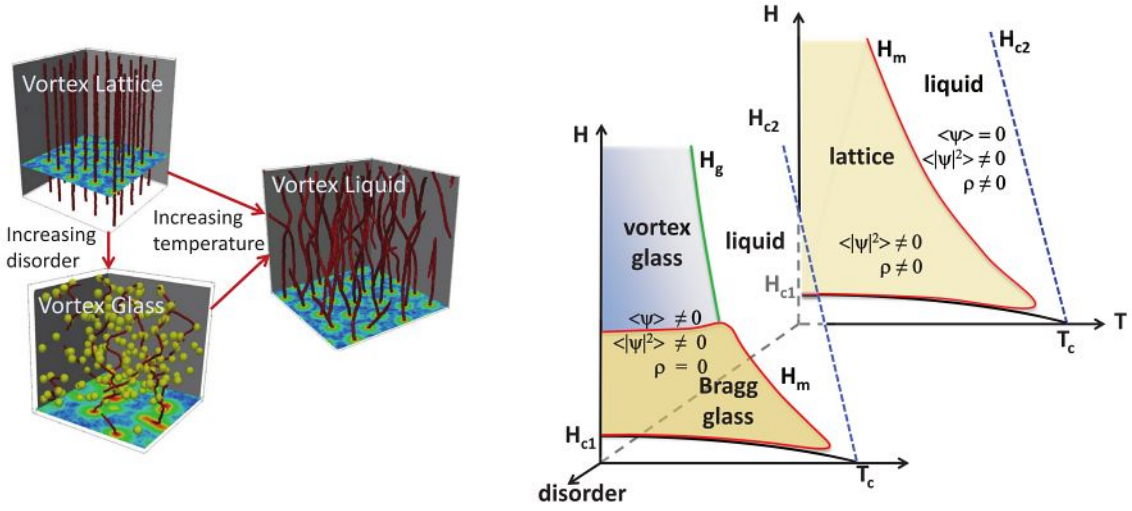

Figure 2.1: Left: 3D representations of the ordered vortex lattice and the disordered vortex glass and vortex liquid. Flux lines are modelled as red tubes, while the planes show a cross section of the squared order parameter, $|\psi|^2$. The yellow spheres represent atomic defects, which drive the transition to the vortex glass phase. The plots have been generated with the 3D time-dependent Ginzburg-Landau equations. **Right**: Examples of vortex phase diagrams and how they are affected by the introduction of impurities in the superconductor. The parameter ρ is the resistivity of the vortex matter. Reprinted from Ref. 67.

potential is tuneable via the sample temperature and the applied magnetic field. The overall inherent disorder across all temperature and field ranges can also be enhanced by, for example, inducing more crystal lattice defects through irradiation treatments [66]. The FLL is profoundly affected by the presence of impurities [67]. The superconducting order parameter is reduced in their vicinity, resulting in them acting as pinning sites and disturbing the equilibrium vortex morphology. Fig. 2.1 depicts examples of different static vortex states as well as the effect of impurities on a typical phase diagram of a type-II superconductor. In an entirely isotropic superconductor, the flux lines would be straight and the vortex cores arranged with hexagonal symmetry. Impurities cause the flux lines to bend and disturb the spatial translational order, thus inducing a quasi-long-range ordered Bragg glass phase [68, 69] or a short-range ordered vortex glass phase [70].

2.1.1 Quasi-long-range ordered FLL: The Bragg glass

In an initial attempt to answer what happens to a crystalline system upon added disorder, Larkin used a perturbative approach [71]. By assuming that the vortices are only weakly displaced from their equilibrium position, the disorder potential, $U(\mathbf{u}(r), r)$ can be Taylor expanded in terms of the displacement, $\mathbf{u}(r)$ [72]:

$$U(\mathbf{u}(r), r) \approx U(0, r) - f(r) \cdot \mathbf{u}(r) \tag{2.1}$$

where $f(r)$ is a random Gaussian variable used to model the randomly displaced vortex positions and r is the vortex separation. Translational order can be quantified via the translational correlation function, $C_{\mathbf{G}_0}(r)$ and the displacement correlation function $b(r)$ [73]:

$$C_{\mathbf{G}_0}(r) = \langle e^{i\mathbf{G}_0 \cdot [\mathbf{u}(r) - \mathbf{u}(0)]} \rangle, \qquad b(r) = \langle |\mathbf{u}(r) - \mathbf{u}(0)|^2 \rangle \tag{2.2}$$

where $\mathbf{G}_0$ is a first-order reciprocal lattice vector of the perfect lattice and $\langle \cdots \rangle$ denotes a thermodynamic average over all vortices. The Larkin model results in the correlation function $C_{\mathbf{G}_0}(r) \sim \mathrm{e}^{-r^{4-d}}$, where d is the dimension of the system. According to this result, the addition of any amount of arbitrarily weak disorder to a system below four dimensions will always result in the complete destruction of long-range order. Another way of stating the same result is through the displacement correlation function, which was found to grow linearly with the vortex displacement. In this same framework, Larkin was able to calculate the critical current based on the Larkin-Ovchinnikov length, R_c, which defines the scale of the pinning potential [52, 74]. Typically, this length scale will correspond to the size of the vortex cores as given by the superconducting coherence length, ξ.

The lack of long-range order in the Larkin model implies that the FLL should not be observable in scattering experiments. This is however not the case, seeing as peaks have been observed in the structure factors of numerous scattering experiments, see for example Refs. 75 and 76 for investigations on conventional superconductors. As it turns

out, the Larkin model is only appropriate when the displacements are smaller than the Larkin-Ovchinnikov length. Beyond the Larkin regime, $|\mathbf{u}(r)| > R_c$, the approximation of Eq. (2.1) overestimates the effect of disorder and is no longer appropriate, because the vortices start to compete for pinning sites. Instead, the FLL enters the *random manifold regime*, where the displacements are of the order $R_c < |\mathbf{u}(\mathrm{r})| < a_0$, with $a_0 = (2\Phi_0/\sqrt{3}B)^{1/2}$ being the equilibrium spacing between flux lines. Thus, the displacements are large enough that the FLL can exhibit glassy behaviours [73, 77, 78]. In this regime, the displacement correlation function ceases to grow linearly and instead exhibits a non-trivial algebraic growth $b(\mathbf{r}) \propto r^{2\eta}$, where η is a lattice roughness constant. Going to even larger length scales, $|\mathbf{u}(\mathrm{r})| > a_0$, where one also has to consider the periodicity of the lattice, the displacement correlation function grows logarithmically and the translational correlation function decays as a power law [73]. Thus, some translational order remains at large length scales, explaining the observability of the FLL in scattering experiments. A vortex state exhibiting this kind of quasi-long-range order is known as a *Bragg glass* [68, 73]. By now, the Bragg glass has been experimentally observed in several materials. Fig. 2.2A shows real-space images of the Bragg glass as obtained with Scanning Tunneling Microscopy (STM) of a $SnMo_6S_8$ sample [79]. From the Delaunay triangulation, it is evident that some disorder is present at 2 T and 400 mK, though the overall vortex morphology is similar to the hexagonal equilibrium state. It should, however, be noted that while the pictures of Fig. 2.2A exemplify typical behaviours of different kinds of vortex states, a true characterization can only be made by looking at large length scales to ensure the proper scaling behaviour of the correlation functions. In Ref. 69, the Bragg glass was observed in superconducting niobium via SANS measurements. Signatures of the Bragg glass phase was in this case unravelled by employing a Reverse Monte-Carlo (RMC) procedure to extract correlations from rocking curves. Fig. 2.2B depicts a schematic of a neutron scattering Bragg glass peak shape, where the power-law decay of the intensity is evident. The RMC method has also been used to prove the existence of the Bragg glass phase in vanadium [76].

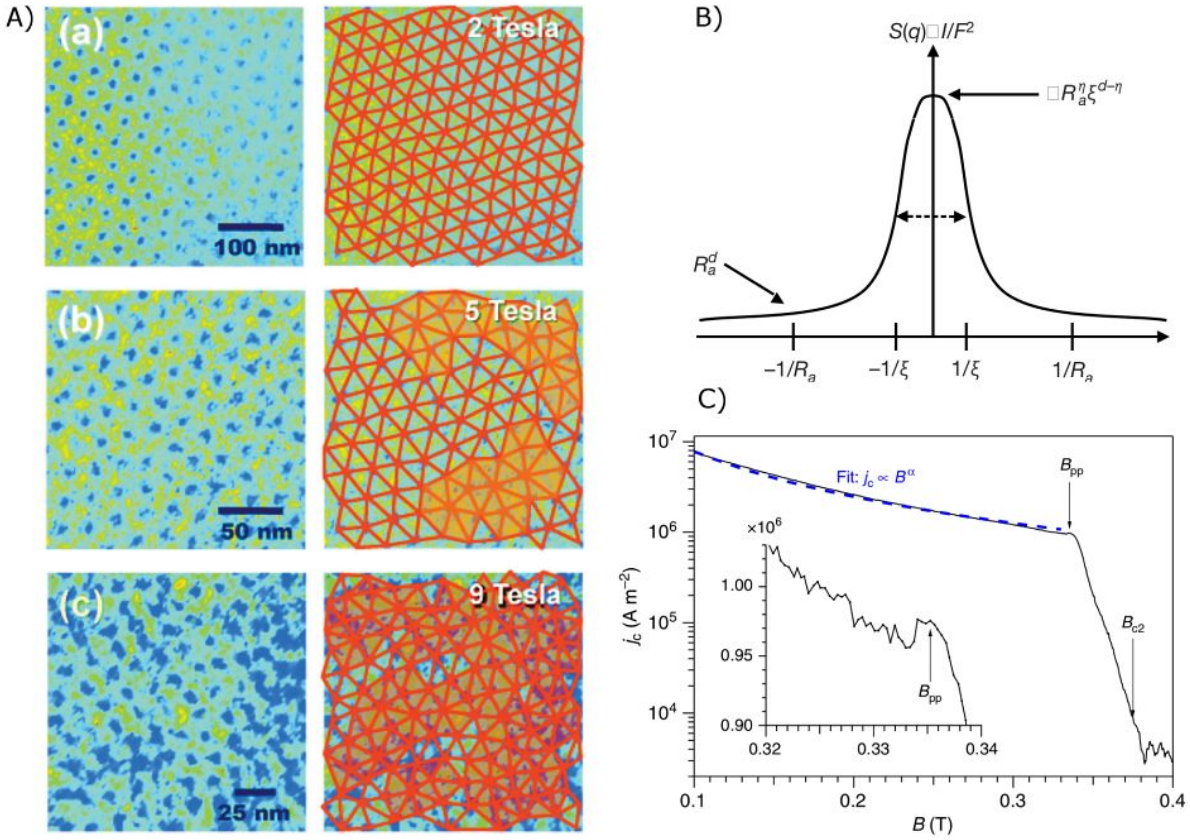

Figure 2.2: Different aspects of vortex matter. **A)** STM images of the vortex lattice in $SnMo_6S_8$ obtained at a temperature of 400 mK. In the right column, the vortex lattices have been superimposed with Delaunay triangulations to highlight nearest neighbours and topological defects (orange zones). The 2 T and 9 T data depict a Bragg glass and vortex glass, respectively. The figure is reprinted from Ref. 79. **B)** The angular dependence of the neutron structure factor $S(\mathbf{q})$ as according to the Bragg glass model. The peak has an intensity of $R_a\xi^{d-n}$, which decays to R_a^d at the position R_a. The parameter R_a is a characteristic length scale of the system and ξ is, in this plot, defined as the experimental resolution. The figure is reprinted from Ref. 68. **C)** A measurement of the critical current, j_c, as a function of the induced field B in an impure vanadium sample. The inset shows the peak effect close to B_{c2}. This figure is from Ref. 76.

2.1.2 Short-range ordered FLL: The vortex glass

The pinning energy becomes more pronounced with increased temperature and applied magnetic field [80]. As a result, the FLL can transition from the quasi-long-range ordered Bragg glass to a short-range ordered *vortex glass*. In this phase, it becomes energetically favourable for the vortices to distort themselves far away from their equilibrium position to occupy pinning sites, while still trying to minimize the overall elastic energy of the FLL [81]. The vortex glass phase is therefore inhabited by an increasing amount of dislocations as the disorder potential becomes more pronounced, cf. the last row of Fig. 2.2A. The structural properties of the vortex glass is in general not well understood due to the limitations of scattering experiments. In Ref. 82, Chudnovsky carries out a theoretical study of a flux line system, where the flux lines are affected by a large concentration of weak pinning sites, the so-called collective pinning regime. Using elastic theory, he finds that in such a system the translational order is destroyed while orientational order remains, resulting in a hexatic vortex glass. The amount of orientational order is estimated by the correlation function [83]:

$$g_6(\mathbf{r}) = \langle e^{i6[\theta(\mathbf{r})-\theta(\mathbf{0})]} \rangle \tag{2.3}$$

where $\theta(\mathbf{r})$ is the local orientation of the FLL. Other descriptions of the disordered FLL include amorphous [84] and multidomain [85] vortex glasses.

The vortex glass can be experimentally characterized by μSR measurements, which are especially useful for mapping out the vortex phase diagram [86, 87]. Phase diagrams of this type can typically be generated by calculating the skew, α, of the field distributions:

$$\alpha = \frac{\langle \Delta B^3 \rangle^{1/3}}{\langle \Delta B^2 \rangle^{1/2}}, \qquad \langle \Delta B^m \rangle = \frac{\sum_j n(B_j)(B_j - \langle B \rangle)^m}{\sum_j n(B_j)} \tag{2.4}$$

where $n(B_j)$ is the distribution of the local fields B_j. An ideal isotropic hexagonal lattice

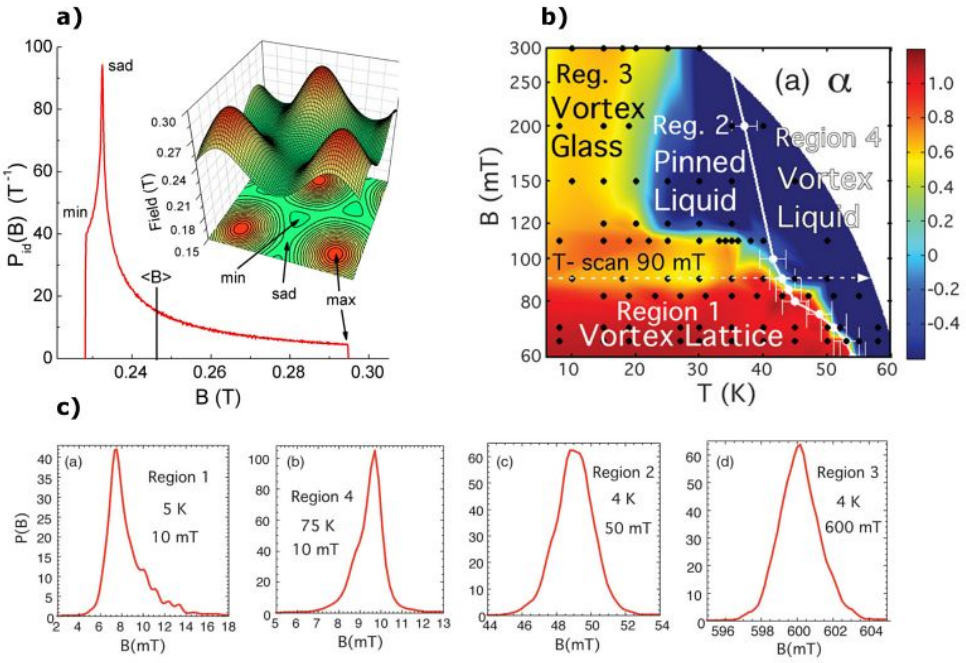

Figure 2.3: **a)** The field distribution of a hexagonal vortex lattice. The figure is from Ref. 88. **b)** Example of a vortex phase diagram of $Bi_2Sr_2CaCu_2O_{8+\delta}$ as determined from the skew of the μSR field distributions. **c)** The typical shape of the field distributions from the different regions of the phase diagram in b). Both figure b) and c) is from Ref. 87.

results in a very characteristic field distribution as depicted in Fig. 2.3a. The minimum induced field is found at the equidistant position between three neighbouring vortices, while the maximum field is found at the vortex cores. The low probability assigned to the higher fields is an indication of the relatively small size of the vortex cores. The most commonly observed field is found at the saddle points between the vortices. Fig. 2.3b depicts the vortex phase diagram of $Bi_2Sr_2CaCu_2O_{8+\delta}$ resulting from the experimental field distributions, given in Fig. 2.3c. Field distributions obtained from μSR do typically not have straight-forward interpretations in terms of what overall vortex phases they represent. In the presented μSR-based vortex phase diagram, negative skew distributions have been interpreted as being evocative of pinned liquid or liquid vortex phases. This stems from the understanding that negative skew distributions lean towards the higher fields, implying an increased distortion of the vortex cores.

A curious effect perhaps presumptuously associated with the Bragg glass-to-vortex glass

transition, sometimes also denominated as the order-to-disorder transition, is the peak effect [89]. The peak effect is a sudden enhancement of the critical current, j_c, as a function of either applied field or current. In conventional superconductors, the peak effect is typically observed close to the upper critical field line, cf. Fig. 2.2C. This is of technological importance because it defines an area of the phase diagram where the superconducting state can endure unusually high external currents. Currently, the microscopic origin of the peak effect is not fully understood. Many investigations have coupled it to the proliferation of dislocations in the vortex glass phase [89, 90, 91]. However, in Ref. 76, Toft-Petersen *et al.* report magnetometry *and* SANS measurements on a vanadium sample, showing that the peak effect occurs well above the order-to-disorder transition. Similar studies on niobium report a peak effect occurring below the transition line [92] and coincident with it [93]. The overall experimental picture is therefore not very clear and is further muddled by the metastable nature of the vortex glass phase, which results in the observed location of the order-to-disorder transition to be dependent on the way the FLL was prepared.

2.1.3 Melting of the FLL

While impurities and dislocations are the cause of static disorder in the FLL via pinning sites, thermal fluctuations introduce dynamic disorder. The thermal disorder counteracts the pinning disorder by making it possible for the FLL to jump past pinning energy barriers and sample different metastable states. Effectively, this smooths out the disorder potential and lowers the critical current [83]. At high enough temperatures, the vortices fully depin and move freely, indicating a transition to a vortex liquid. The melting of the FLL has been experimentally observed in high-T_c superconductors, such as $YBa_2Cu_3O_{7-\delta}$ and $Bi_{2.15}Sr_{1.95}CaCu_2O_{8+x}$, through a combination of resistivity [94], magnetisation [95, 96], specific heat [97], and neutron scattering experiments [63]. The melting transition is associated with sharp drops in the measured resistivity, magnetization jumps, peaks in the specific heat, and decreased neutron scattering intensity. Similar studies have been carried out for low-T_c superconductors, such as Nb_3Sn [98], Nb [99] and V [76], though the

experimental situation is in this case complicated by the fact that thermal fluctuations play a much smaller role in these systems.

The size of thermal fluctuations in a superconductor can be estimated via the Ginzburg number, $Gi \approx (\mu_0 k_B T_c \kappa^2 / 2\xi^3 B_{c2}^2)^2$. This number is introduced into the following expression for the melting transition field, $B_m(T)$, relative to the upper critical field [89, 100]:

$$\frac{B_{c2}(T) - B_m(T)}{B_{c2}(0)} \approx 0.43 c_L^{-4/3} Gi^{1/3} t^{2/3} (1 - t^2)^{2/3} \tag{2.5}$$

where $t = T/T_c$ is the reduced temperature and c_L is the Lindemann number. According to the Lindemann criterion, melting occurs when the thermal vortex displacements, u, are of the same order as a fraction, c_L, of the lattice spacing, a_0. In other words $\langle u^2 \rangle \approx c_L^2 a_0^2$ [101]. From Eq. (2.5), it is evident that the field range of the vortex liquid phase is strongly dependent on T_c and ξ and that high-T_c superconductors, which display low ξ, will possess much more wide-spanning liquid phases than low T_c superconductors. The phase diagrams of Fig. 2.1 are hence typical of high-T_c superconductors. In Ref. 76, a vanadium sample with Ginzburg number of $G_i \approx 6 \times 10^{-10}$ is investigated. With a Lindemann number of $c_L = 0.2$, they find that the melting transition line at 0.3 T lies within just 8 mK of the upper critical field.

2.2 Numerical methods for investigating the FLL

This section will briefly introduce the molecular dynamics (MD) and time-dependent Ginzburg-Landau approaches to simulating the FLL. Other numerical methods exist, such as the elegant iterative GL method introduced by Brandt [102], which can reproduce the field profiles from experimental μSR measurements of a vanadium sample in the clean limit [103]. Nonetheless, the focus will remain on the MD and TDGL methods because they are capable of dealing with the intricate pinning landscapes that may occur in impure

samples.

2.2.1 Molecular dynamics simulations

Molecular dynamics simulations treat the superconducting vortices as either elastic strings or point-like particles and model their movement with the overdamped Langevin equation [104]:

$$\mathbf{F}_i = \eta \frac{d\mathbf{r}_i}{dt} = \sum_j^{N_v} \mathbf{F}^{vv}(\mathbf{r}_i - \mathbf{r}_j) + \sum_k^{N_p} \mathbf{F}^{vp}(\mathbf{r}_i - \mathbf{r}_k^p) + \mathbf{F}^L \tag{2.6}$$

where η is the vortex viscosity, often described as the Bardeen-Stephen friction coefficient [105], and $\mathbf{r}_i$ is the position of the vortex being described by the equation. N_v and N_p are the total number of vortices and pinning sites in the system, which are placed at the positions $\mathbf{r}_j$ and $\mathbf{r}_k^p$, respectively. The first term models interactions between vortices, while the second term describes the interaction between the vortices and the pinning sites of the system. The last term is a driving force, which models the effect of, for example, an external current or perpendicular magnetic field. The exact formulation and implementation of the Langevin equation can vary between different MD studies to, for example, include different geometries [106] or temperature fluctuations [107]. However, different implementations will, at the very least, contain the vortex-vortex and pinning interactions, seeing as these are fundamental to the free energy landscape of the vortex lattice. The vortex-vortex interaction can be modelled as [104, 108]:

$$\mathbf{F}^{vv}(r) = \frac{\Phi_0^2 s}{2\pi\mu_0\lambda^3}\left[\frac{\lambda}{r} - q_{\text{int}} \exp\left(\frac{r}{\xi}\right)\right] \tag{2.7}$$

where r is the length between two vortices, Φ_0 is the flux quantum, s is the vortex length, μ_0 is the permeability of free space, and λ and ξ are the field penetration depth and coherence length of the superconductor, respectively. The first term describes the repulsive interaction between vortices, which dominates in the Shubnikov state, while the second term describes a short-ranged attraction, which can cause the formation of

domains as is observed in the IMS. The parameter q_{int} quantifies the relative strength between the repulsive and attractive interaction. The influence of the attractive pinning sites is often modelled using a Gaussian approximation [109]:

$$\mathbf{F}^{vp}(\mathbf{r}_k^p) = -A^p \exp\left[-\left(\frac{|\mathbf{r}_i - \mathbf{r}_k^p|}{\xi}\right)^2\right], \quad A^p = \sigma_e \frac{B_{c2}^2}{16\pi\kappa^2}(1 - b_M)\pi\xi^2 \tag{2.8}$$

where σ_e is the flux line core condensation energy, $\kappa = \lambda/\xi$ is the GL parameter, and $b_M = B/B_{c2}$ is the reduced field. MD simulations are excellent for investigating transport properties and dynamical phase diagrams of vortex systems [104]. The point-particle description means that the simulations can be performed with a large number of vortices, often up to 1000 or more, and the simulations are therefore capable of describing complex vortex structures with domain formations [104].

2.2.2 Ginzburg-Landau simulations

Finite-element, finite-difference, and finite-volume simulations based on the TDGL equations resolve vortex structures via a spatial mesh instead of treating the vortices like particles or strings. These calculations provide direct access to the local field distributions, though it comes at the cost of being computationally intensive. The time-dependent equations are both useful for studying dynamics and for approaching the stationary equilibrium solution from an initial out of equilibrium state. Frequently, the focus of TDGL studies is high-T_c superconductors due to their potential in applications. In such cases, where κ is large, the behaviour of the FLL can be adequately described by the infinite-λ limit of the TDGL equations [110]:

$$\left(\frac{\partial\psi}{\partial t} + i\phi\right)\psi = \epsilon(\mathbf{r})\psi - |\psi|^2\psi + (\nabla + i\mathbf{A})^2\psi + \zeta_T(\mathbf{r}, t) \tag{2.9}$$

which here is presented in a nondimensionalized form. In this approximation, a single equation is sufficient to simulate the magnetic behaviour of the superconductor. The pa-

rameter ϕ is the electric field and $\zeta_T(\mathbf{r}, t)$ is a Langevin noise term that simulates thermal fluctuations. In Eq. (2.9) pinning effects are included via spatial variations in the critical temperature, also known as δT_c pinning, which results in a local reduction of the order parameter ψ. The function $\epsilon(\mathbf{r}) = [T_c(\mathbf{r}) - T]/[T_c^S - T]$ quantifies the strength of the δT_c pinning [110, 111]. Here, T is the temperature of the sample, $T_c(\mathbf{r})$ is the spatially varying critical temperature and T_c^S is the critical temperature of the bulk. The δT_c pinning potential is employed both in the modelling of pinning effects in high-T_c superconductors, such as Dy-doped $YBa_2Cu_3O_{7-\delta}$ [112], as well as low-κ superconductors [41]. Pinning effects can also be induced by variations in the mean free path of charge carriers, also known as δl pinning, which typically originates from crystal lattice defects [113].

In Ref. 114 defects are modelled by assigning the order parameter to be 0 at the pinning site positions $\mathbf{r}^p$, $\psi(\mathbf{r}^p) = 0$. This corresponds to a strong pinning implementation of the normal inclusion pinning scheme described by Du in Ref. 115.

2.3 FLL transport behaviours

Knowledge of the dynamical properties of superconducting vortices is of great importance for the design of electronic superconducting technologies [116]. Applying an external magnetic field, current, or even just tilting a superconductor with respect to the main applied field can via Lorentz forces induce dissipative processes, which adversely impact the superconducting state. The occurrence of flux creep or flux flow is intimately tied to pinning properties since impurities under certain conditions can pin vortices into place. The ease with which the vortices depin is strongly dependent on the elastic properties of the FLL, typically characterized by the elastic moduli.

2.3.1 Experimental transport studies

Traditionally, experimental investigations of dynamical features of the FLL have been carried out with macroscopic bulk techniques, such as current-voltage (IV) characterizations, which for examples have been employed to indirectly investigate the dynamical behaviour of vortices in niobium films with asymmetric pinning arrays [117] and in channel geometries in bilayer films consisting of layers of weak-pinning a-NbGe and strong-pinning NbN [118]. Microscopy techniques such as Lorentz Transmission Electron Microcsopy (TEM) have also been used, see Refs. 119 and 120 for two examples of such investigations on niobium thin films.

In Ref. 121, IV-measurements have been used to identify different dynamical behaviours in the anisotropic superconductor 2H-$NbSe_2$ with weak pinning. Elastic flow is understood as coherent depinning of the vortices from their equilibrium position, while plastic flow occurs at larger driving forces and is characterized by an onset of inhomogeneous filamentary motion of the vortices. Fluid flow occurs at even larger driving forces when the pinning potentials comparatively become insignificant and the vortices, therefore, can move together coherently. Fig. 2.4 depicts the results from further investigations of 2H-$NbSe_2$, where transport measurements are combined with SANS measurements of the FLL structure [122]. The FWHM of the neutron scattering rocking curve peaks in the plastic flow region and drastically decreases in the fluid flow region, the onset of which is detected by a sudden steep increase in the IV-curve. Plastic flow has also been observed in $YBa_2Cu_3O_{7-x}$ crystals via AC susceptibility measurements [123] and magnetic relaxation measurements [124]. The phase diagram in the right panel of Fig. 2.4 depicts the elastic, plastic, liquid and normal regimes as determined based on experimental investigations of $YBa_2Cu_3O_{7-x}$. The two referenced samples, 2H-$NbSe_2$ and $YBa_2Cu_3O_{7-x}$, are quite different and the observed dynamical phases described in Fig. 2.4 therefore appear to be universal to type-II superconductors. The relative sizes of the different domains of a dynamical vortex phase diagram may vary dependent on the sample properties. Differences between low-T_c superconductors (LTSC), high-T_c superconductors (HTSC) such

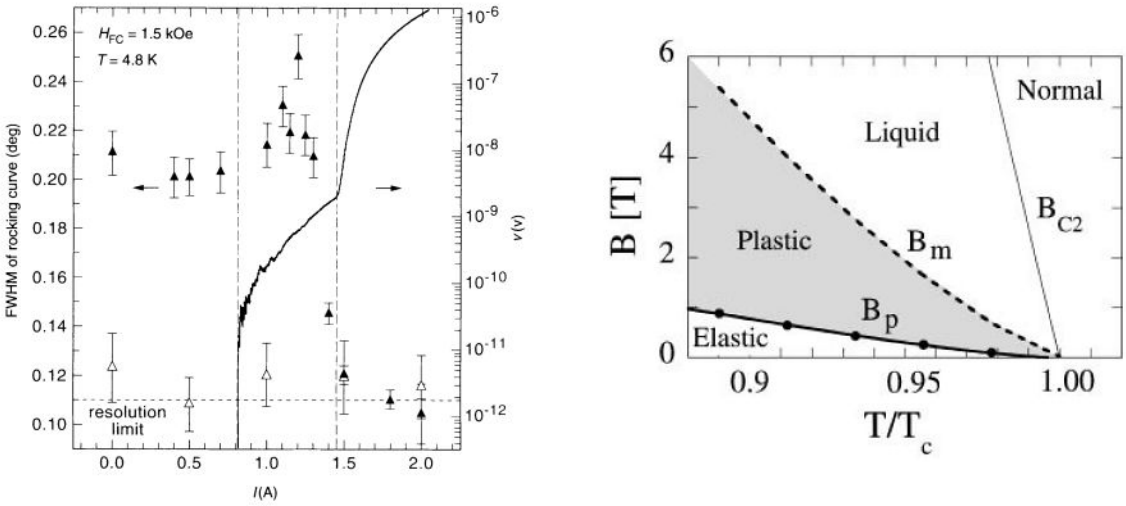

Figure 2.4: Left: Dynamical investigations of the vortex lattice of 2H-$NbSe_2$, performed with a field of 1.5 kOe and at a temperature of 4.8 K. The solid line is the voltage as a function of current, while the triangles are the FWHM of the rocking curves measured upon increasing (black triangles) and decreasing (white triangles) current. The dashed lines separate the plot into three different regimes. At low applied currents, no voltage is measured as the vortices are pinned into place. At intermediate currents, the measured voltage increases and the FWHM of the SANS rocking curve increases, indicating a loss of coherence as one would expect in the plastic regime. A kink is observed in the IV-curve at $I = 1.5$ A, signifying a transition to a coherent vortex flow state. This is corroborated by the SANS FWHM, which is seen to drop significantly in this regime. From Ref. 122. **Right:** A vortex-creep phase diagram of $YBa_2Cu_3O_{7-x}$. From Ref. 124.

as $YBa_2Cu_3O_{7-x}$, and 2H-$NbSe_2$ are summarized by Higgins *et al.* in Ref. 121. Here typical Ginzburg numbers are reported as 10^{-2}, 10^{-4}, and 10^{-8} for HTSCs, 2H-$NbSe_2$, and LTSCs, respectively. Compared to $YBa_2Cu_3O_{7-x}$ and 2H-$NbSe_2$, temperature fluctuations are hence less important for LTSCs such as vanadium and niobium, and a larger applied current is needed to achieve a free flux flow state.

2.3.2 Numerical studies of dynamical phases

Theoretically, small perturbations from the equilibrium FLL are well described by London and GL-based elasticity theory [9, 73]. At even larger driving forces, analytical treatments become difficult and MD simulations are often employed instead, see Refs. 104, 125, 126, 127 and 128 for examples thereof. Fig. 2.5 shows MD results for low-κ superconductors based on the overdamped Langevin equations with varying levels of driving forces. With

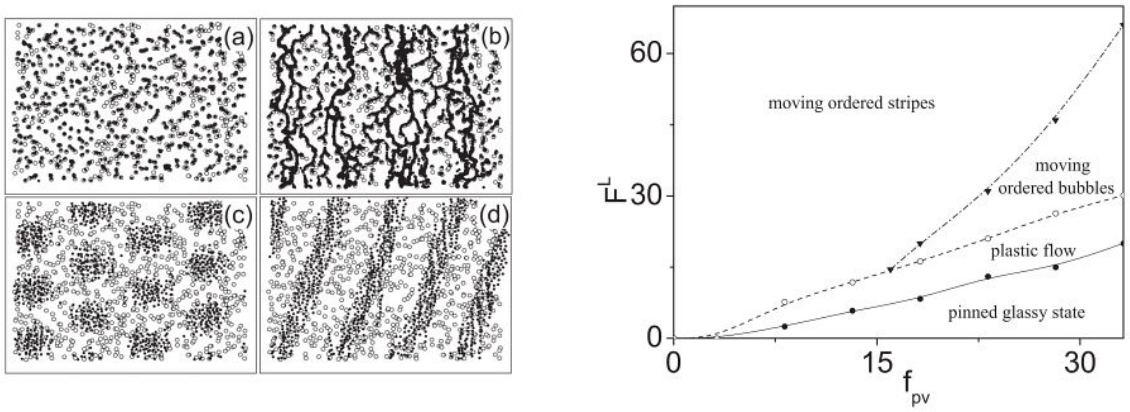

Figure 2.5: Left: Different 2D vortex configuration as determined from molecular dynamics simulations based on the Langevin equations. Solid circles represent vortices, while the open circles show the pinning centre positions. The simulations have been carried out with an applied field of $B = 0.65B_{c2}$, a pinning strength of $f_{pv} = 28.2f_0$ and driving forces of a) $0f_0$, b) $20f_0$, c) 40 f_0 and d) 100 f_0. The parameter f_0 is a normalization constant. **Right:** A dynamic phase diagram describing the vortex behaviour as a function of the pinning strength f_{pv} and the driving force F^L at $B = 0.65B_{c2}$. Both figures are from Ref. 104.

no external driving force, the vortices are trapped by the pinning potentials. Panel (b) displays the plastic flow state, where some vortices are pinned in place, while others move in preferred channels. At even higher driving forces, the vortices are seen to fully depin and can eventually form bubble- or stripe-like domains, depending on how the attractive and repulse components of the vortex-vortex interaction are balanced [104, 129]. The phase diagram of the right panel illustrates the different dynamical phases identified from the simulation. In accordance with experimental observations, elastic, plastic, and fluid flow regimes are detected.

CHAPTER 3

NEUTRON SCATTERING AND MUON SPIN ROTATION EXPERIMENTAL TECHNIQUES

Fundamental aspects of the small angle neutron scattering (SANS) and muon spin rotation (μSR) experimental techniques are described in this chapter. Neutrons and muons both possess magnetic moments, which enable them to interact with and scatter from magnetic potentials and thereby to act as probes for investigating magnetic matter. Neutrons can be prepared in states with wavelengths and energies comparable to lattice spacings and excitation levels of magnetic materials [130]. As such, neutron scattering is a useful tool for investigating the FLL of superconductors and is the primary experimental technique that was employed for the work presented in this thesis. As an ancillary method, μSR was used to gather detailed information about local field distributions.

3.1 Small angle neutron scattering

A scattering experiment is based on the fundamental premise that particles scatter coherently from structures in so far the Bragg condition is fulfilled:

$$2d \sin \theta_B = \lambda_n n \tag{3.1}$$

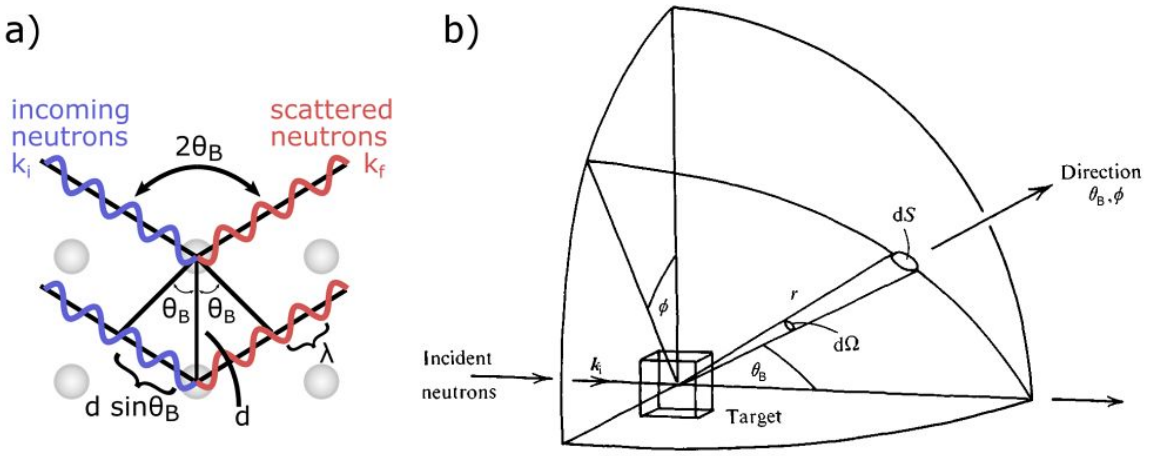

Figure 3.1: a): Visual representation of Braggs law showing neutron waves interacting with planes of scattering objects placed a distance d apart. The lower wave has to travel an extra distance of $2d \sin\theta_B$, which explains the scattering coherence criteria given in Eq. (3.1). **Right:** Geometry of a scattering experiment. Incoming particles with incident wave vectors $\mathbf{k}_i$ interact with the target material and are scattered into the solid angle $d\Omega$. The figure is from Ref. 130.

where λ_n is the wavelength of the scattered particle and will henceforth be referred to as the neutron wavelength. The parameter d is the real space distance between Bragg peaks, n is a positive integer describing the order of the reflection, and θ_B is defined as the Bragg angle. The scattering angle, $2\theta_B$, is defined as the angle between the incoming wave vector, $\mathbf{k}_i$, and outgoing wave vector, $\mathbf{k}_f$, as given in Fig. 3.1a. In Fig. 3.1b, the general geometry of a scattering experiment is depicted. The magnitude of the scattering vector, $\mathbf{q} = \mathbf{k}_i - \mathbf{k}_f$, is related to the Bragg angle as:

$$|\mathbf{q}| = q = \frac{4\pi}{\lambda_n} \sin\theta_B \tag{3.2}$$

In small angle neutron scattering, the small angle approximation can be used to simplify Eq. (3.2) to $q \approx \frac{4\pi\theta_B}{\lambda_n}$. Feasible scattering angles of a SANS setup depend on the instrumental settings such as the sample to detector distance. Typical scattering angles from our experiments are in the range of 0.1° to 1°. With an assumed neutron wavelength of 6 Å, this angle range is equivalent to a q-range of 0.002 Å^{-1} to 0.02 Å^{-1}, corresponding to probing structures of sizes ranging from 3000 Å and down to 300 Å. The spacing

of vortices in superconductors is dependent on the induced magnetic field and is many times larger than the underlying crystal lattice but still well within the scope of SANS experiments.

3.1.1 Elastic scattering from an array of vortices

The essential property measured during a SANS experiment is the differential scattering cross section, $\mathrm{d}\sigma/\,\mathrm{d}\Omega$, which describes the probability of an incoming neutron being scattered into the solid angle $\mathrm{d}\Omega$. Unlike the partial differential scattering cross section investigated with inelastic neutron scattering, $\mathrm{d}^2\sigma/(\,\mathrm{d}\Omega\,\mathrm{d}E)$, the differential scattering cross section does not depend on the energy of the outgoing neutrons and is instead built on the assumption of elastic scattering, $|\mathbf{k}_i| = |\mathbf{k}_f|$. Hence, SANS experiments are aimed at probing structures and not excitations. To calculate a theoretical expression for the differential scattering cross section originating from magnetic potentials, one needs to know how the magnetic structure of a material affects the wave function of the incoming neutrons. This can be modelled by assuming a magnetic interaction potential of the form:

$$V_M = -\sum_j^N \hat{\boldsymbol{\mu}}_n \cdot \mathbf{B}(\mathbf{r} - \mathbf{R}_j) \tag{3.3}$$

where the sum is performed over N scatterers positioned at $\mathbf{R}_j$, $\mathbf{B}$ is the local field induction, and $\hat{\boldsymbol{\mu}}_n$ is the magnetic moment operator. This operator is defined in terms of the neutron gyromagnetic ratio, γ_n, the nuclear magneton, μ_N, and the Pauli spin matrix, $\hat{\boldsymbol{\sigma}}$, as $\hat{\boldsymbol{\mu}}_n = -\gamma_n \mu_N \hat{\boldsymbol{\sigma}}$. In scattering theory, it is typically assumed that the magnetic interaction potential is weak compared to the kinetic energy of the neutrons. As such, $V_M(\mathbf{r})$ can be treated as a perturbation and the first Born approximation can be applied. The probability of a neutron with incoming wave vector $\mathbf{k}_i$ interacting with the magnetic potential and being scattered with an outgoing wave vector $\mathbf{k}_f$ is then found

using Fermi's golden rule. The resulting differential cross section then becomes [130]:

$$\frac{\mathrm{d}\sigma}{\mathrm{d}\Omega} = \left(\frac{m_n}{2\pi\hbar^2}\right)^2 \left| \int V_M e^{i\mathbf{q}\cdot\mathbf{r}} \,\mathrm{d}\mathbf{r} \right|^2 \tag{3.4}$$

Inserting the magnetic potential from Eq. (3.3), one gets:

$$\frac{\mathrm{d}\sigma}{\mathrm{d}\Omega} = \left(\frac{m_n}{2\pi\hbar^2}\right)^2 \left| \int \hat{\boldsymbol{\mu}}_n \cdot \mathbf{B}(\mathbf{r}) e^{i\mathbf{q}\cdot\mathbf{r}} \,\mathrm{d}\mathbf{r} \sum_j^N e^{i\mathbf{q}\cdot\mathbf{R}_j} \right|^2 \tag{3.5}$$

This expression can be split into the structure factor, $S(\mathbf{q})$, and the form factor, $F(\mathbf{q})$, defined as:

$$S(\mathbf{q}) = \left| \sum_j^N e^{i\mathbf{q}\cdot\mathbf{R}_j} \right|^2, \qquad F(\mathbf{q}) = \frac{m_n}{2\pi\hbar^2} \int \hat{\boldsymbol{\mu}}_n \cdot \mathbf{B}(\mathbf{r}) e^{i\mathbf{q}\cdot\mathbf{r}} \,\mathrm{d}\mathbf{r} \tag{3.6}$$

The two expressions in Eq. (3.6) can be simplified if an ideal FLL with no translational disorder is assumed. If the FLL is constructed from the basis vectors $\mathbf{a}_1$, $\mathbf{a}_2$, and $\mathbf{a}_3$, the corresponding reciprocal lattice vectors are [131]:

$$\mathbf{b}_1 = 2\pi \frac{\mathbf{a}_2 \times \mathbf{a}_3}{\mathbf{a}_1 \cdot (\mathbf{a}_2 \times \mathbf{a}_3)}, \qquad \mathbf{b}_2 = 2\pi \frac{\mathbf{a}_3 \times \mathbf{a}_1}{\mathbf{a}_1 \cdot (\mathbf{a}_2 \times \mathbf{a}_3)}, \qquad \mathbf{b}_3 = 2\pi \frac{\mathbf{a}_1 \times \mathbf{a}_2}{\mathbf{a}_1 \cdot (\mathbf{a}_2 \times \mathbf{a}_3)} \tag{3.7}$$

The reciprocal lattice has been constructed such that $\mathbf{b}_i \cdot \mathbf{a}_j = 2\pi\delta_{ij}$, which means that the structure factor is reduced to [130]:

$$S(\mathbf{q}) = \left| \frac{(2\pi)^3 N}{V} \sum_{\mathbf{G}} \delta_2(\mathbf{q} - \mathbf{G}) \right|^2 = \frac{(2\pi)^6 N^2}{V^2} \sum_{\mathbf{G}} \delta_2(\mathbf{q} - \mathbf{G}) \tag{3.8}$$

where V is the volume of the sample and the vector $\mathbf{G}$, defined as $\mathbf{G} = h\mathbf{b}_1 + k\mathbf{b}_2 + l\mathbf{b}_3, \{h, k, l\} \in \mathcal{Z}$, is a reciprocal lattice vector. The two-dimensional delta-function, $\delta_2(\mathbf{q} - \mathbf{G})$, defines the well-known Laue scattering condition, $\mathbf{q} = \mathbf{k}_i - \mathbf{k}_f = \mathbf{G}$, which is best illustrated with the Ewald sphere construction (cf. Fig. 3.2). The Ewald sphere can be centred at an arbitrary place in reciprocal space and has a radius equal to the length of the

wave vectors $|\mathbf{k}_i| = |\mathbf{k}_f|$, underlining the elastic nature of the scattering. If the incoming wave vector is drawn such that it ends at a reciprocal lattice point, then scattering can only occur if the outgoing wave vector in a similar fashion starts from the locus of the Ewald sphere and has an end point that coincides with one of the reciprocal lattice points touching the surface of the sphere. By observing the constructed triangle, it is evident that the Laue scattering condition is equivalent to the Bragg scattering condition given in Eqs. (3.1) and (3.2). Due to extinction of specific reflections in certain lattice types, scattering may not always occur even if the scattering conditions are fulfilled.

In the ideal vortex lattice picture, the field distribution must be a well-behaved periodic function and can therefore be written as a Fourier series, $\mathbf{B}(\mathbf{r}) = \frac{1}{V}\sum_{\mathbf{G}} \mathbf{B}_{\mathbf{G}} \exp(i\mathbf{G}\cdot\mathbf{r})$ with $\mathbf{B}_{\mathbf{G}} = \int_V \mathrm{d}\mathbf{r}\mathbf{B}(\mathbf{r}) \exp(-i\mathbf{G}\cdot\mathbf{r})$. The form factor can in this case be rewritten as [130]:

$$F(\mathbf{q}) = \frac{\gamma_n}{4\Phi_0 V}\int \sum_{\mathbf{G}} B_{\mathbf{G}} e^{i(\mathbf{q}-\mathbf{G})\cdot\mathbf{r}}\,\mathrm{d}\mathbf{r} = \frac{\gamma_n}{4\Phi_0}\sum_{\mathbf{G}} B_{\mathbf{G}}\delta_2(\mathbf{q}-\mathbf{G}) \tag{3.9}$$

where the prefactor of the form factor has been rewritten using $\mu_N = \frac{e\hbar}{2m_p} \approx \frac{e\hbar}{2m_n}$ and inserting the definition of the flux quantum $\Phi_0 \equiv \frac{h}{2e}$. Hence, the form factor ends up including the same scattering condition that is observed in the simplified expression for the structure factor. In the above equations, the magnetic interaction has been rearranged under the assumption that the incoming neutrons are unpolarized, $\hat{\boldsymbol{\mu}}_n \cdot \mathbf{B}(\mathbf{r}) = \gamma_n m_N B(\mathbf{r})$. Combining Eqs. (3.8) and (3.9), the final scattering cross section for the approximation with no disorder can then be combined to be [130]:

$$\frac{\mathrm{d}\sigma}{\mathrm{d}\Omega}(\mathbf{q}) = S(\mathbf{q})|F\mathbf{q}|^2 = \frac{(2\pi)^6 N^2}{V^2}\left(\frac{\gamma_n}{4\Phi_0}\right)^2 \sum_{\mathbf{G}} |B_{\mathbf{G}}|^2 \delta_2(\mathbf{q}-\mathbf{G}) \tag{3.10}$$

Based on the above equation, magnetic structure information can be gathered by measuring the intensities at the Bragg peaks. However, sample mosaicity and finite instrumental resolution both cause the scattering condition, $\delta_2(\mathbf{q}-\mathbf{G})$, to have a spread, which is further broadened by any kind of disorder of the FLL. Therefore a typical SANS measurement procedure is to rotate the sample with the purpose of *rocking* through the Bragg

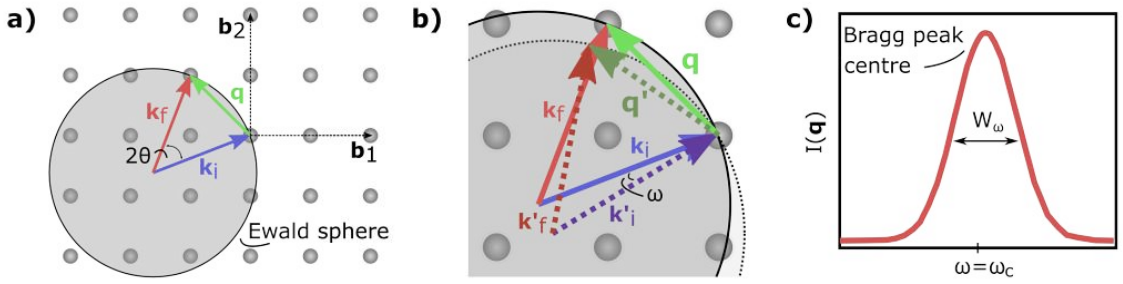

Figure 3.2: **a)** The Ewald sphere illustrates the Bragg condition in reciprocal space. Coherent scattering and thereby the appearance of a Bragg peak can only occur when the scattering vector connects reciprocal lattice points. **b)** Rotating the crystal lattice by ω corresponds to changing the scattering locus. **c**) A rocking curve can be obtained by scanning through the Bragg condition during a SANS measurement.

condition (cf. Fig. 3.2). Characteristics, such as width and intensity, of a measured *rocking curve* can be used to extrapolate information regarding the overall ordering of the FLL lattice. The integrated rocking curve intensity for a specific reciprocal vector $\mathbf{G}$ is, as expected, dependent on neutron flux, the solid angle, measurement time, and the range of the rocking scan [130]:

$$I_{\mathbf{G}} = \phi_0 \int \mathrm{d}\Omega \int \mathrm{d}t \frac{\mathrm{d}\sigma}{\mathrm{d}\Omega} \tag{3.11}$$

where ϕ_0 is the incoming neutron flux. In Ref. 132, the integrated intensity of a Bragg peak reflection is reported as:

$$I_{\mathbf{G}} = \left(\frac{\gamma_n}{4}\right)^2 \frac{\lambda_n^3 t}{\Phi_0^2 \sin 2\theta_B} \frac{|B_{\mathbf{G}}|^2}{S_0^2} \tag{3.12}$$

where t is the sample thickness, θ_B is the Bragg angle, and S_0^2 is the area of the FLL unit cell. Rocking curve scans are extensively used for the scope of the current work to extract dynamic properties and to get a general insight into the ordering of the FLL. A decrease in the rocking curve intensity can be a sign of loss of order in the FLL. However, as is evident from Eq. (3.12), the intensity is also dependent on the local field induction, $I \propto B^{-1/2}$ [75].

A more specific expression for the magnetic Fourier components can be gained by employing the modified London equation, Eq. (1.3). Fourier transforming this expression results

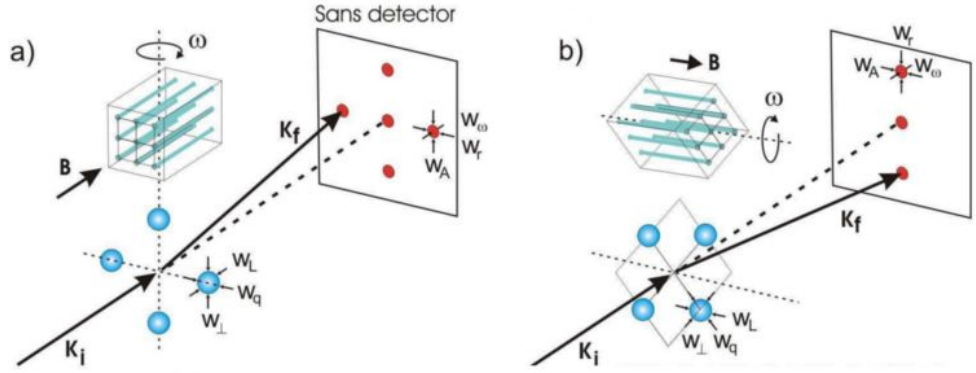

Figure 3.3: Parallel (**a**) and perpendicular (**b**) scattering geometries of a FLL SANS experiment. The real-space FLL is in the figure illustrated as a square lattice, which gives rise to a square array of spots in reciprocal space, as is seen on the detector. The figure is from Ref. 36.

in:

$$\mathbf{B_G} = \frac{\bar{B}}{1 + \lambda^2 |\mathbf{G}|^2} \tag{3.13}$$

where λ is the London penetration depth and $\bar{B}$ is the average magnetic induction. Referring back to the expression for the differential cross section, Eq. (3.10), it is evident that this rough estimation indicates that the rocking curve intensity has a strong λ^{-4} dependence. This means that low-κ superconductors, such as niobium and vanadium, provide much stronger scattering signals than high-κ superconductors, making them excellent testing grounds for general investigations of vortex matter.

3.1.2 Parallel and perpendicular SANS set-ups

One of the major geometric considerations during a SANS investigation of the FLL is how to align the external magnetic field with respect to the incoming neutron beam. Usually, one of two main orientations is used; parallel or perpendicular. The difference between the two configurations is shown in Fig. 3.3. The field direction affects the orientation of the flux lines and thus what kind of correlations are measured with the rocking curve widths. In the parallel setup, the rocking curve width probes correlations along the flux lines. In contrast, correlations in the plane of the vortices are measured in the perpendicular setup. From a rocking curve scan, three different Bragg peak widths can be obtained from

each diffraction spot. The width W_ω refers to the width of the rocking curve as shown in Fig. 3.2, while the two remaining widths, the azimuthal width W_A and the radial width W_r, can be extracted from the 2D-integrated image of the rocking scan by performing 2D-gaussian fits to one of the FLL domain spots. The measured widths can be related to the reciprocal widths of the diffraction spots, $W_\mathbf{q}$, W_L, and $W_\perp$ (cf. Fig. 3.3). Here $W_\mathbf{q} = \Delta\mathbf{G}/\mathbf{G}$ describes the variation in the scattering vector, while W_L and $W_\perp$ are the reciprocal widths parallel and perpendicular to the main field direction.

Regardless of the geometrical setup, the rocking curve width can be expressed as [133]:

$$W_\omega^2 = a^2 + b^2 + c^2 \tag{3.14}$$

where a is the angular spread of the incoming beam, and b is dependent on the correlations giving rise to the reciprocal space width W_L in the parallel setup and the width $W_\perp$ in the perpendicular setup. The parameter c is related to the wavelength spread and $W_\mathbf{q}$ as $c^2/\theta_B^2 = \Delta\lambda_n^2/\lambda_n^2 + W_\mathbf{q}^2$ [133], where θ_B again denotes the Bragg angle. Typically, a is the largest contributor to the total rocking curve width, which is why long collimation lengths are typically preferable in an attempt to decrease the angular spread of the beam. The radial width of the detector spots can likewise be calculated based on the defined parameters [133]:

$$W_r^2 = \frac{a^2c^2 + a^2b^2 + 4b^2c^2}{a^2 + b^2 + c^2} \tag{3.15}$$

The angular spread a can be estimated from the instrumental setup, ie. by knowing the collimation length and sample aperture dimensions. The parameters b and c can subsequently be estimated by combining Eqs. (3.14) and (3.15).

3.2 Muon spin rotation

The basic premise of μSR experiments is to utilize the short free lifetime and asymmetric decay profile of muons to gain information about condensed matter systems. Polarized muons are first implanted into a material, where their polarization is affected by the local magnetic field, and the direction of the emitted decay particles are subsequently analyzed with the intent of extracting magnetic field profiles.

3.2.1 Muon decay characteristics

At facilities like the Paul Scherrer Institut (PSI), muons are produced by first letting accelerated protons collide with a graphite target, resulting in the creation of pions. These pions eventually decay and emit, among other particles, muons. Both negatively and positively muons can be created in this fashion, though positive muons are typically used for FLL experiments because they are less susceptible to nuclear capture. The parity violation of muon decay means that only positrons with positive helicity are observed in nature. The probability of a muon emitting a positron in a given direction, θ_μ, is given by [134]:

$$W(\theta_\mu) \propto 1 + A\cos\theta_\mu \tag{3.16}$$

where θ_μ is the angle between the spin of the muon and the direction of the positron, and A is an energy-dependent asymmetry parameter. From a theoretical perspective, the asymmetry parameter takes a value of 1/3 when averaged over all possible muon energies. Based on Eq. (3.16), it is evident that positrons are more likely to be emitted along the direction of the muon polarization.

3.2.2 Muon experiment geometries

Two typical muon spin geometries are shown in Fig. 3.4, depicting transverse field (TF) and longitudinal field (LF) setups, respectively. The main difference between the two is

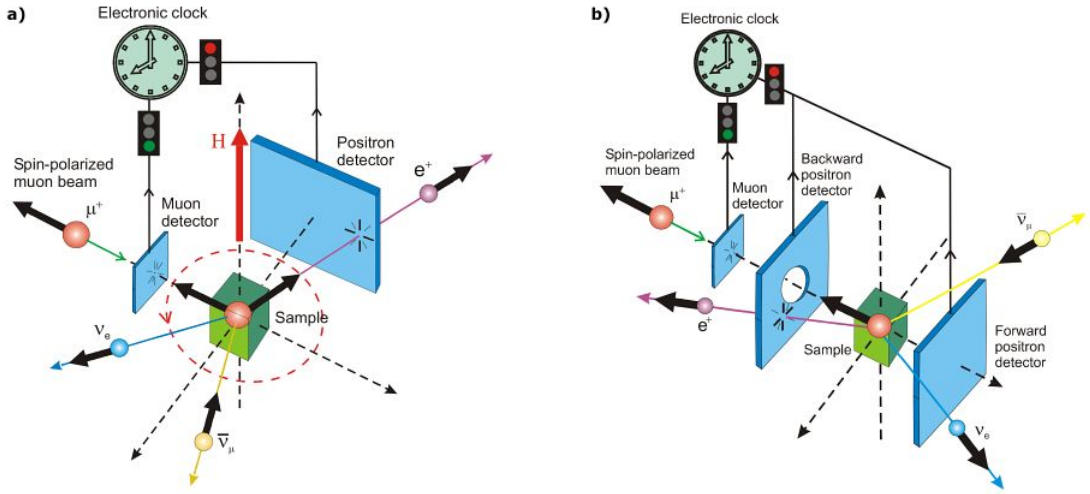

Figure 3.4: a) Illustration of the transverse field μSR setup, where an external field is applied perpendicular to the incoming muon direction. The spin of the muons precess around the external field direction with a frequency that is related to the local internal field. **b)** In the longitudinal field (zero field) setup, a field (no field) is applied along the muon momentum, allowing for precise measurements of weak internal fields. The figures are from Ref. 135.

the direction in which the external magnetic field is applied with respect to the muon momentum. When a muon is implanted in a sample, the component of the muon spin perpendicular to the local magnetic flux will experience a torque, $\Gamma = \frac{d\mathbf{S}}{dt} = -\mu_0 e/(2m)(\mathbf{S} \times \mathbf{B})$, which will cause the muon spin to precess around the field direction with a Larmor frequency $\omega_L = \gamma_\mu \mathbf{B}$. In the LF setup, the external field is applied along the muon polarization direction and the muon spins are therefore not usually expected to perform signifcant precessions. In contrast, the TF setup is used to probe the muon spin polarization and consequently the local field distribution of e.g. type-II superconductors. This setup is used for parts of the experimental work presented in Chapter 5.

During a TF experiment, each positron detector will record a time-dependent histogram of the number of detected positrons [134]:

$$N(t) = N_0 e^{-t/\tau_\mu}[1 + A_0 g(t)] + Bg, \qquad g(t) = \int n(B)P(t;B)d\mathbf{B} \tag{3.17}$$

where N_0 and A_0 are constants, $P(t, B)$ is the muon polarization function, $n(\mathbf{B})$ is the

magnetic field distribution, and Bg is a background term. Thus an experimental magnetic field distribution can be extracted from Eq. (3.17) by inverting it via a Fourier transform [136] or using maximum entropy methods [137].

CHAPTER 4

DYNAMIC PROPERTIES OF THE HIGH PURITY NIOBIUM FLUX LINE LATTICE

4.1 Introduction

This chapter details experimental time-resolved SANS investigations of the FLL in niobium when exposed to temporal perturbations. Our main motivation was to understand whether the dynamic behaviour of the FLL can be accurately described by elastic models. We performed this investigation by applying a small oscillating magnetic field to pull the vortices away from their equilibrium positions. Understanding the response of superconducting vortices to external perturbations is of importance to technical applications of type-II superconductors, seeing as dissipative processes can greatly diminish their current-carrying capabilities.

Our experimental investigations were inspired by an earlier study [45], wherein the static magnetic field was applied along a two-fold crystallographic direction of a niobium sample. Our study differed from this by instead applying higher static fields along a crystallographic fourfold direction. The higher fields were used to ensure that we stayed outside the complicated intermediate mixed state and firmly inside the mixed state, which would make it easier to compare our results to model predictions. The fourfold axis was chosen because it would give us the opportunity to evaluate the possible elasticity of the FLL of

different vortex morphologies and also to explore the possibility of softening at VL phase transitions.

Our main finding was that the FLL in our case did not behave elastically, as was evidenced by a clear frequency dependence of the characteristic time constants of the flux lines. The field and temperature dependence of these time constants also exhibited the exact opposite behaviour than earlier observed in the two-fold study [45] and as predicted from elastic GL theory [138]. We observed a difference between time constants extracted from different vortex domains in the scalene phase, indicating that the vortices do not deform uniformly when the oscillating field is applied.

A similar time-resolved SANS investigation of a vanadium sample with the static field applied along a threefold crystallographic direction exhibited time constants with similar behaviour to the two-fold study and not our current fourfold study. This indicates that the anisotropic nature of the niobium FLL along the fourfold direction influences its dynamic behaviour.

Overall, Section 4.2.1 contains the current understanding of the static configurations of the niobium FLL and Section 4.2.2 describes the recent attempt at characterizing its dynamic properties with time-resolved SANS along a two-fold axis. The remainder of the chapter, Sections 4.3 and 4.4, are then dedicated to presenting the setup and results of new dynamic SANS measurements performed for the scope of this thesis.

4.2 The flux line lattice of niobium

Niobium has a long history of being the subject of SANS investigations and was even employed in the first experimental observation of the Abrikosov FLL [75]. Since then, the FLL of niobium has warranted further investigations due to a rich phase diagram consist-

ing of a multitude of different vortex morphologies [8, 139, 140]. The variety of attainable vortex structures is highly dependent on the orientation of the applied magnetic field with respect to the crystal axes, as is observed from the two different niobium phase diagrams in Fig. 4.1. When the external field is rotated close to ⟨111⟩, hexagonal vortex patterns are observed in accordance with the typical close-packed structure one would expect from an isotropic superconductor. However, applying the field *along* a fourfold axis results in a number of different geometries. This indicates an underlying anisotropy of the electronic properties of niobium. Square vortex phases are observed at low and high magnetic fields at low temperatures, an isosceles phase is predominantly observed at high temperatures, and a scalene phase is seen at intermediate field and temperature values. The specified triangular structures are in reciprocal space constructed from the scattering centre and two diffraction spots. They thus make up half a unit cell. Each unit cell must contain exactly one flux quantum. The right panel of Fig. 4.1 shows integrated SANS detector images of the different vortex morphologies. Several coexisting FLL domains appear in each detector image, which is indicative of the symmetry-breaking nature of the FLL unit cells. Diffraction spots belonging to different domains should all exhibit the same intensity when the fourfold direction is aligned exactly along the field direction. Therefore, spots belonging to the same domain can be identified by rotating the sample with respect to the magnetic field and observing the relative intensity changes [139].

Structural FLL transitions are not unique to niobium and are observed in other type-II superconductors such as PbTl [141], the borocarbides RNi_2B_2C (R = Lu, Y, Er, Tm) [142, 143, 144, 145], V_3Si [146], the heavy-fermion superconductor $CeCoIn_5$ [147], Sr_2RuO_4 [148], and the high-T_c cuprate $La_{1.83}Sr_{0.17}CuO_{4+\delta}$ [149]. This selection of systems encompasses both conventional and unconventional superconductors, which all possess an underlying crystal structure with fourfold symmetry and exhibit field-dependent isosceles-to-square FLL transitions. An unprecedented aspect of the anisotropic niobium FLL is that the vortex structures *all* break some underlying symmetry with respect to

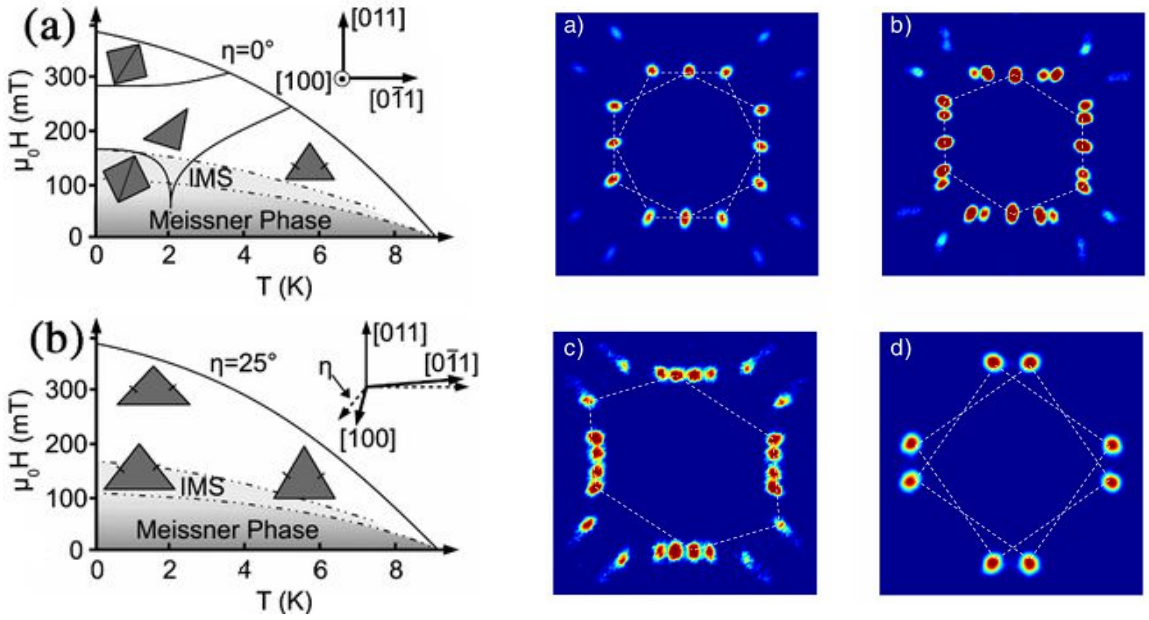

Figure 4.1: Left: Vortex phase diagram of ultrapure niobium ($RRR \approx 1000$) when the aligned field is applied (a) along a $\langle 100 \rangle$ direction, and (b) 25° away from a $\langle 100 \rangle$ direction. The figure was adapted from Ref. 140. **Right:** The niobium FLL at different applied fields and temperatures as obtained by integrating SANS detector images. The detector images show examples of the (a) isosceles, (b) low-field scalene, (c) high-field scalene, and (d) high-field square phases. Reprinted from Ref. 8.

the underlying crystallographic structure [139]. Unlike the square unit cells observed in the FLLs of the other superconductors, the square unit cell of niobium is misaligned with respect to the cubic crystal axes. The niobium unit cell is found to be rotated with an angle of 14.7° and 10.9° with respect to $\langle 100 \rangle$ in the case of the low-field and high-field square phases, respectively [139]. The scalene phase is another unique vortex phase of the niobium FLL that breaks both rotational and reflection symmetry of the cubic crystalline structure and thus results in the four simultaneous domains in the integrated SANS detector images [139].

4.2.1 Origin of FLL structural transitions

The complexity of the niobium FLL phase diagram can at first seem surprising, given the otherwise conventional nature of niobium as a superconductor. Despite its well-known anisotropic magnetic properties, such as the morphology of the FLL and the temperature

dependence of the upper critical field, niobium is mostly characterized as an s-wave superconductor and thus displays an isotropic superconducting gap. Detailed measurements of the upper critical field of niobium samples of various purity levels have been provided by Weber *et al.* in 1991 [150], who were able to show that the field-orientation dependence of the upper critical field can be explained from the very pronounced anisotropy of the niobium Fermi velocity and from the much less pronounced anisotropy of the electron-phonon interaction.

Early theoretical investigations of vortex morphologies pointed out that non-standard vortex structures can be obtained from phenomenological theories, such as GL theory, by adding higher-order anisotropy terms to the free energy [32]. It was demonstrated by Nakai *et al.* [151] that square and isosceles FLL structures can be stabilized by including anisotropic behaviour in the functions describing the superconducting gap and Fermi velocity. The left panel of Fig. 4.2 shows the cross section of these two functions, when they are modelled as $|\Delta(\mathbf{r},\theta)|^2 = |\Delta(\mathbf{r},\frac{\pi}{8})|^2(1+\alpha_d\cos 4\theta)$ and $v_f(\theta) = v_f(\frac{\pi}{8})(1+\beta_v\cos 4\theta)$, with θ being the polar angle, and α_d and β_v being anisotropy parameters. By incorporating these models into the quasiclassical Eilenberger equations, it is possible to show that for certain values of the anisotropy parameters, the square vortex phase can be stabilized. As is depicted in the figure, the orientations of the square phases are decided by the minima of the $v_f(\theta)$ and $|\Delta(\mathbf{r},\theta)|^2$ functions. A square phase driven by the anisotropy of the superconducting gap will have its nearest neighbours aligned along $\langle 100\rangle$, while a square phase driven by the Fermi velocity anisotropy will have its nearest neighbours aligned along $\langle 110\rangle$. The competing effects of the Fermi velocity and superconducting gap anisotropies can, for the right values of α_d and β_v, lead to rich vortex phase diagrams with re-entrant isosceles-to-square-to-isosceles transitions [151]. Higher-order $\cos 8\theta$ anisotropy terms would allow the minima of $v_f(\theta)$ and $|\Delta(\mathbf{r},\theta)|^2$ to be orientated away from the $\langle 100\rangle$ and $\langle 110\rangle$ axes and can thus provide a phenomenological explanation for the square niobium FLL phases [139].

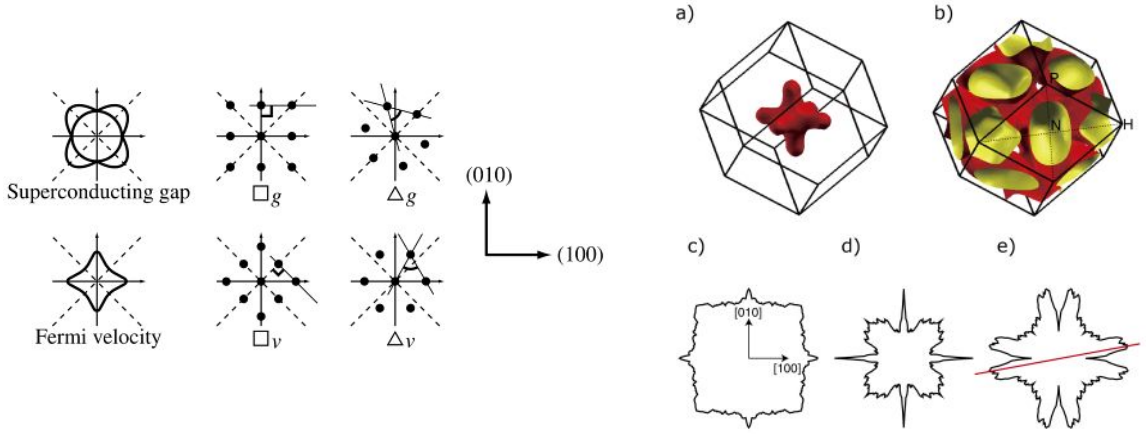

Figure 4.2: Left: Illustration of how the orientation of rhombic and square FLL unit cells with respect to a fourfold axis can be affected by anisotropies of the superconducting gap and Fermi velocity functions. The solid black dots signify the vortex spots. Figure from Ref. 151. **Right:** Subplot a) and b) show the closed and extended Fermi surfaces of niobium, as calculated via DFT. The remaining subplots illustrate cross sections taken perpendicular to the field direction of the c) Fermi velocity, d) angle-resolved density of states (AR-DOS), and e) inverse AR-DOS. The red line is used to indicate broken mirror symmetry in the inverse density of states function. Figure from Ref. 152.

A proper microscopic explanation for the symmetry-breaking nature of the niobium FLL was recently given by Adachi *et al.* [152], who combined density functional theory (DFT) calculations of the Fermi surface of niobium with the same quasiclassical Eilenberger equations previously employed by Nakai. As expected from the earlier characterizations of the anisotropic properties of niobium, the symmetry-breaking vortex morphologies are related to the highly anisotropic nature of the Fermi velocity. The right panel of Fig. 4.2 depicts the Fermi surface, the Fermi velocity and the angle-resolved density of states (AR-DOS) of niobium. It is found that the scalene phase in niobium occurs because of the absence of mirror symmetry about the Fermi velocity maximum direction, as is indicated in the cross section of the inverse AR-DOS function.

4.2.2 Characterizations of the elastic nature of the niobium FLL

An important precursor to the work presented in this chapter is the initial time-resolved SANS measurements of the niobium FLL performed by Mühlbauer *et al.* [45]. Compared

to macroscopic measurements, scattering techniques such as SANS makes it possible to directly probe the microscopic information of the bulk of the FLL and thus reduce the influence of surface pinning. The time-resolved aspect of the measurements also means that dynamic properties, such as the elastic matrix, can be accessed directly. The basic premises of the experimental measurements presented in Ref. [45] are shown in Fig. 4.3. A static magnetic field induces the main vortex lattice structure, while a smaller oscillatory field perpendicular to the static one is used to periodically push the vortices away from their equilibrium position. Elastic properties can then be extracted by observing the characteristic time-scale of the FLL response to the oscillatory field. The basic premise of the Mühlbauer analysis is that the FLL response can be described by a diffusion model:

$$\frac{du}{dt} = D\frac{d^2u}{dx^2}, \qquad D = \frac{c_{44}}{\eta} \tag{4.1}$$

where $u(x,t)$ is the tilt distortion as a function of position x and time t, D is a diffusion constant, η is the vortex viscosity, and c_{44} is the tilt modulus as defined in Fig. 4.3. The model in Eq. (4.1) assumes that the deformation is uniquely quantified by the tilt modulus and that the vortices therefore move uniformly in a direction perpendicular to the static applied field. In the right panel of Fig. 4.3, dispersion plots of the elastic energy of the tilt, compression and shear waves are presented. Their strong k-dependence underlines the importance of the assumption of local deformation. The vortex viscosity can be calculated from the induced field B and flux flow resistivity ρ_{FF}, or estimated from the conductivity of the superconductor in the normal state, ρ_n:

$$\eta = \frac{B^2}{\rho_{\mathrm{FF}}} \approx \frac{BB_{c2}}{\rho_n} \tag{4.2}$$

The coupling between the experimentally accessed relaxation time τ and the diffusion constant is thus made by solving the diffusion equation. The following expression is valid for a cylinder with a radius r:

$$\tau \approx \frac{r^2}{(2.405)^2 D} \tag{4.3}$$

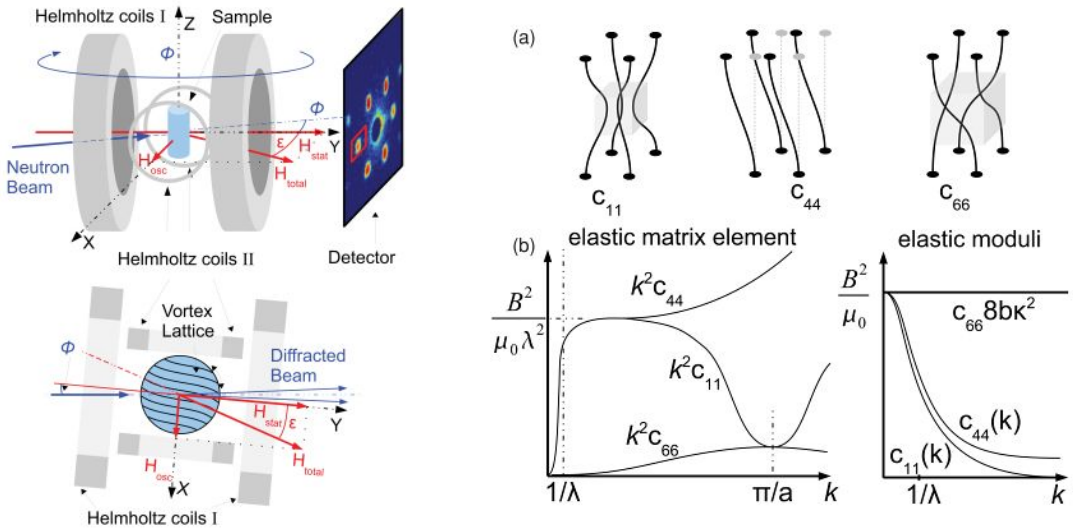

Figure 4.3: Left: The setup employed by Mühlbauer *et al.* [45] to measure the elastic c_{44} modulus of the niobium FLL using time-resolved stroboscopic SANS. The first set of Helmholtz coils is used to induce the main static magnetic field along the neutron beam direction, $\mathbf{H_{stat}}$, while a second set of Helmholtz coils induces a smaller, perpendicular oscillatory field, $\mathbf{H_{osc}}$. Rocking scan measurements are performed by rotating the sample through a range of ϕ-angles. **Right:** a) Schematic representation of the uniaxial compression modulus, c_{11}, tilt modulus, c_{44}, and shear modulus, c_{66}. b) The k-dependence of the elastic matrix elements and elastic moduli calculated by Brandt. From Ref. 45.

where the specific number 2.405 comes from the first node of the Bessel function $J_0(x)$. Thus, the tilt modulus is expressed in terms of the FLL relaxation time in the following way:

$$c_{44} \approx D\eta \approx \frac{BB_{c2}r^2}{\rho_n(2.405)^2\tau} \tag{4.4}$$

The final results of Mühlbauer *et al.* are summarized in panel a) and b) of Fig. 4.4. They are compared to the model predictions of the isotropic elastic theory of Brandt, who estimated that the tilt modulus in the local limit can be approximated as $c_{44} \approx BH$, where B is the induced field and H the applied field [9]. According to this theory, c_{44} is expected to exhibit the same temperature dependence as the induced field, meaning that it is only expected to be weakly temperature dependent. Comparing the experimental results of panel b) with the theoretical predictions of panel c), one sees that the temperature and field dependence are roughly similar. However, in general the experimental tilt moduli are

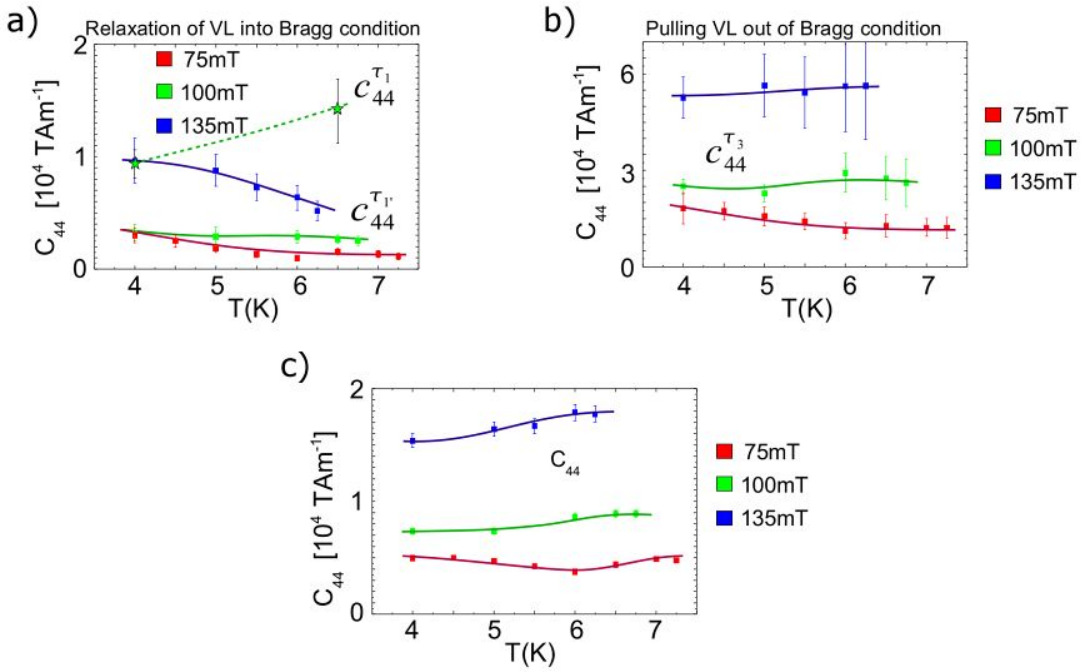

Figure 4.4: a) and **b)** Tilt moduli, c_{44}, as extracted from stroboscopic SANS measurements of niobium when it is relaxing into and being pulled out of the Bragg condition. **c)** The tilt moduli as predicted from the local elastic theory of Brandt [9]. All plots are reprinted from Ref. 45.

more than twice the value of the corresponding theoretical predictions. Comparing panels a) and b), it is also worth noticing that there is a significant difference in elastic constants that have been estimated from either observing the vortex lattice relaxing into or being pulled out of the Bragg condition. This asymmetry is not expected from a simple elastic model. A complicating aspect of the Mühlbauer data analysis is that the measurements were carried out with low applied fields and therefore measured the dynamic behaviour of the FLL in or close to the intermediate mixed state (IMS). The domain-like nature of the IMS means that the vortex lattice may not be perturbed by just one collective elastic mode, which may explain the discrepancy between the experimental c_{44} results and Brandt's theory. Mühlbauer *et al.* additionally pointed out that the discrepancy may be related to uncertainties in the estimated normal conducting resistivity, $\rho_n(T)$.

4.3 Stroboscopic SANS setup

Stroboscopic small angle neutron scattering was carried out at the V4 instrument of the BER-II reactor at Helmholtz-Zentrum Berlin (HZB), Germany [153]. Employing the list-mode data acquisition option of V4, every neutron arriving at the detector is time-stamped, which makes an exploration of the dynamic properties of the FLL possible [154]. Experiments were performed with the parallel scattering geometry, as described in Section 3.1.2. The static main field was aligned along a fourfold [100] direction of a niobium sample. The incoming neutron beam direction was also aligned roughly along the same [100] direction. During rocking scans, the sample was rotated with respect to the neutron beam. The stroboscopic SANS data were collected over two separate HZB beam times with the same spherical single-crystal niobium sample but different coil geometries, as specified in the next section. During both experiments, we employed a sample aperture with a diameter of 5 mm to ensure that we were probing the bulk of the sample. We employed neutrons with wavelengths of 14 Å and a wavelength resolution of $\Delta\lambda/\lambda = 0.1$ as well as a collimation distance, and corresponding sample-to-detector distance, of 16 m. V4 has a source aperture of size $50 \times 30\,\mathrm{mm}^2$, resulting in an angular resolution function with an approximate width of $a \approx r_s/L_c \approx 0.2°$, where r_s is the size of the source aperture and L_c is the collimation length [155].

The niobium sample is more than 30 years old and was cut from a single crystal rod grown via a floating zone process. The sample was subsequently etched to remove damage from the spark cutting and annealed at 2200°C under vacuum for 50 hours. As a final step the sample was heated in an 400°C oxygen atmosphere for five minutes [156], because this is known to reduce surface pinning effects without affecting the purity of the sample [157]. The treatment results in oxygen atoms diffusing into the bulk of the sample, which locally lowers H_{c1} in the diffusion layer and thereby also lowers the Bean-Livingston surface barrier [158]. The residual resistivity ratio was measured to have a value of $RRR = \rho(295K)/\rho(10K) = 450$ and a GL parameter of $\kappa = 0.7$ [156].

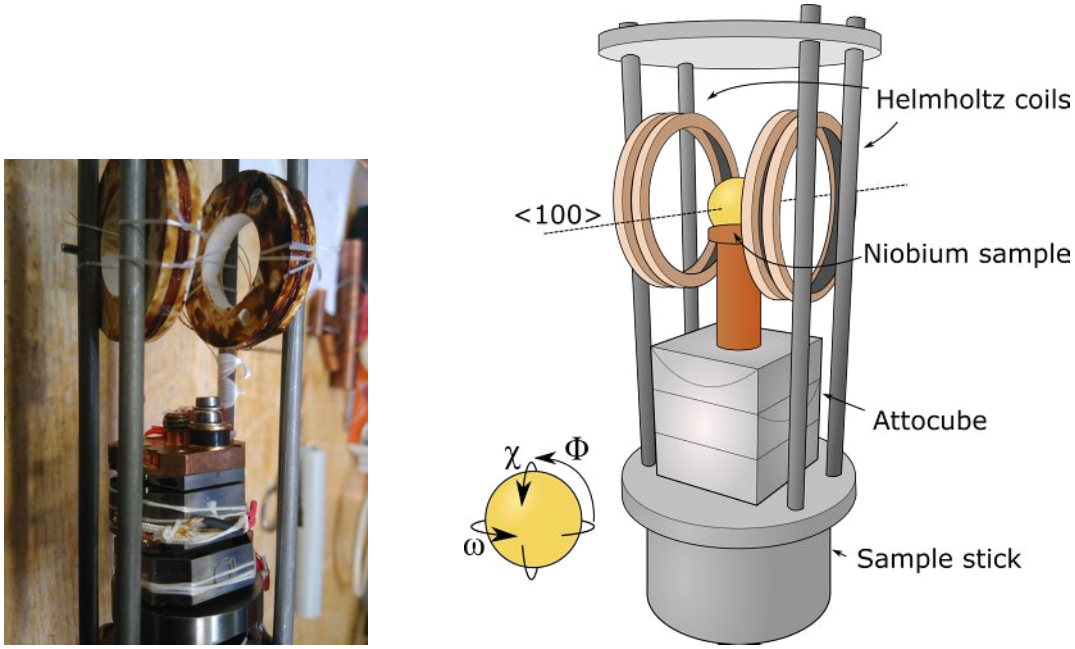

Figure 4.5: The coil setup used to induce an oscillatory field during the experiment. **Left:** Picture of the Helmholtz coils attached to the coil cage and the attocube used during the second experiment. **Right:** Schematic of the same setup, showing how the sample was placed at the centre of the coils. The inset in the lower left corner defines the different rotations, with the ω-rotation being the one employed for rocking scans.

4.3.1 Coil specifications

Similarly to the Mühlbauer experiment, a small, oscillatory field was used to temporarily pull vortices away from their equilibrium positions. In both experiments, the AC field was aligned perpendicular to the static field direction. The AC field was induced using a sample stick setup developed by André Sokolowski at HZB prior to our experiments, where a small cage with a set of coils was attached to the end of the stick (Fig. 4.5). Two different kinds of coil setups were attempted: A constant gradient field Maxwell coil setup (experiment M) and a uniform field Helmholtz coil setup (experiment H). The Maxwell coil setup was attempted together with a micro goniometer, while the Helmholtz coils were used with an attocube.

During the analysis and discussion, the main focus will be on the Helmholtz coil experiment, which employed the same setup to perturb the FLL as in Ref. 45. If the flux

lines perturb elastically and uniformly, the Helmholtz setup should make it possible to probe the c_{44} elastic constant of the FLL. The Maxwell coil setup was attempted to see if a different dynamic behaviour would be observed with a spatially non-uniform oscillating field. The dynamic results from the non-uniform Maxwell setup are therefore not as easy to compare to earlier experiments, but are for sake of completeness reported in Appendix A.

According to the Biot-Savart law, the magnetic field produced by one coil with n windings and a radius R is:

$$B(x) = \frac{\mu_0 n I R^2}{2(R^2 + x^2)^{3/2}} \tag{4.5}$$

where μ_0 is the permeability of free space, I is the current in the coils, and x is the perpendicular distance from the plane of the coils. If one has two coils instead, each placed at a distance $r/2$ from a centre position, the total field will be:

$$B_{\text{tot}}(x) = \frac{\mu_0 n I R^2}{2(R^2 + [x - r/2]^2)^{3/2}} \pm \frac{\mu_0 n I R^2}{2(R^2 + [x + r/2]^2)^{3/2}} \tag{4.6}$$

Adding the two terms together corresponds to the description of the total magnetic field of a Helmholtz coil setup, where a uniform field is achieved in a region between centres of the coils if $R = r$. If the second term is instead subtracted from the first, one achieves a constant gradient field Maxwell setup, where the magnetic field is close to 0 in the centre between the two coils. Given the asymmetric nature of the Maxwell field profile, one would only expect to be able to measure dynamic behaviour in the rocking curve shifts if the sample was not fully centred between the two coils. During the actual experiment, the dimensions of the coil cage were limited by the size of the cryostat, which meant the radii of the coils did not equal the distance between them. Magnetic field profiles based on the measured coil dimensions are presented in Fig. 4.6, where it is evident that the realized magnetic field is not completely uniform in the Helmholtz case.

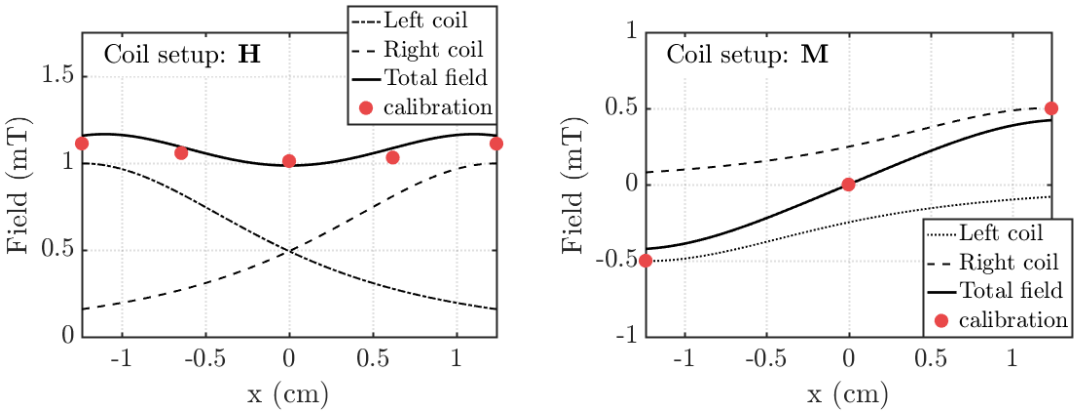

Figure 4.6: Left: Magnetic field profile of the Helmholtz coils, with the coils placed at $x = \pm 1.24\,\text{cm}$. The dashed lines are the calculated curves of the fields induced by each of the two coils, while the solid line is the sum of the two. The red points show calibration measurements performed with a Gauss meter and an applied current of 0.4 A. All theoretical curves have been calculated with a winding number of $n = 64$, a current of $I = 0.4\,\text{A}$, a coil radius of $R = 1.60\,\text{cm}$, and a distance between the coils of $r = 2.48\,\text{cm}$. These values were measured from the actual experimental setup and have errors of 0.05 cm. **Right:** Magnetic field profile of a Maxwell coil setup with coils of the same physical dimensions. A current of 0.2 A was used to calculate the theoretical curves and perform the experimental calibration.

A rectangular pulse shape was employed for the input signal. Fig. 4.7 shows oscilloscope measurements of the incoming and outgoing signals from the coils, which makes it clear that there is an inherent electronic delay of about 100 μs. This time scale is much shorter than the relaxation times of the FLL reported by Mühlbauer [45], affirming that the electronic delay should not affect the dynamic FLL measurements. The critical parameters of the coils are reported in the caption of Fig. 4.6. During the calibration of the Helmholtz setup, applying a 100 mHz 40 mV_{p2p} signal was seen to result in a measured current of 0.4 A and a magnetic field, measured with a Gauss meter at the sample position and reported as the peak to peak value, of 1.04 mT. Hence, the voltage needed for a specific AC field was estimated through the ratio 38 $\text{mV}_{\text{p2p}}/\text{mT}$. Conversely, the signal generator could resolve the given input voltage down to 1 mV_{p2p}, corresponding to an AC field resolution of 0.03 mT.

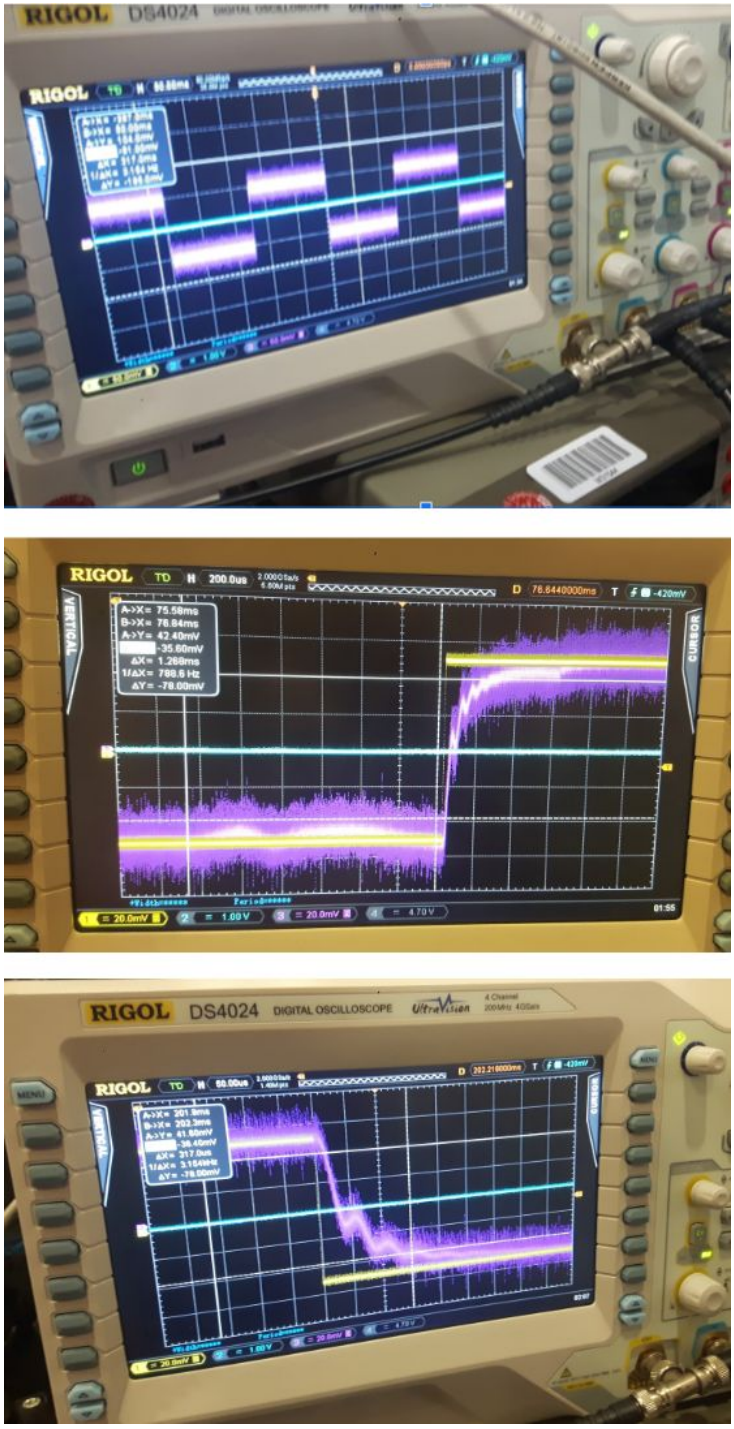

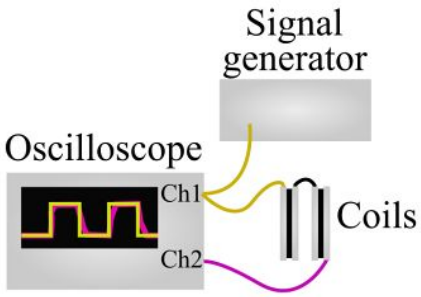

Figure 4.7: Left: Pictures of the oscilloscope used to measure the square signal generating the perpendicular oscillating field. In the top picture, the square shape of the pulses are evident. The two lower pictures show zoom-ins of the pulse edges with time resolutions of 200 μs and 50 μs per square. The yellow line is the input from the signal generator, while the purple line is the signal after it has passed through the coils. The pictures were taken during experiment H, while running a test with a 4 Hz 100 $\mathrm{mV_{p2p}}$ signal. **Right:** Simplified schematic of the connections between the oscilloscope, signal generator and coils.

4.3.2 Alignment of the sample

The sample mounts were chosen so as to ease the alignment process, since any major differences between the static field and the $\langle 100 \rangle$ crystallographic directions would make it impossible to observe the desired vortex morphologies, such as the particularly sensitive high-field square phase [36]. During the first experiment, the sample was glued to a micro goniometer, kindly borrowed from the HZB Quantum Materials Lab. In this way, the sample could be pre-aligned with an X-ray Laue camera without having to worry about the sample shifting during a later glueing process. Furthermore, any misalignment detected during the experiment could be corrected by pulling the sample stick out of the cryostat and making the necessary adjustments to the goniometer. A major downside to this procedure was the time wasted every time the sample stick had to be pulled out and reinserted into the cryostat. Even though the Laue camera makes it possible to pre-identify a $\langle 100 \rangle$ direction to within a tenth of a degree, the final alignment observed during the actual measurements may still be off due to bends in the sample stick. It is therefore not possible to prevent the need for readjustments with a good pre-alignment of the sample. For the second experiment with the Helmholtz coils, the sample was attached to an attocube, which via piezoelectric motors made it possible to make in-situ adjustments of the crystallographic orientation. The schematic inset in Fig. 4.5 illustrates the sample rotation axes. It is evident that in the parallel setup, the ω- and χ-rotations are most relevant for the FLL alignment. The ω-alignment corresponds to a rotation of the sample stick with respect to the applied field and can easily be performed at any point during the experiment by rotating the stick manually or by driving it with a motor. The χ-alignment, however, can only be performed via the micro goniometer or attocube, because the motors of the V4 instrument are unable to rotate the sample and the magnet independently from one another in this direction.

At the beginning of both experiments, the in-situ neutron alignment was initiated by performing an ω_X-scan, where ω_X defines a rotation in the ω-direction independently from the

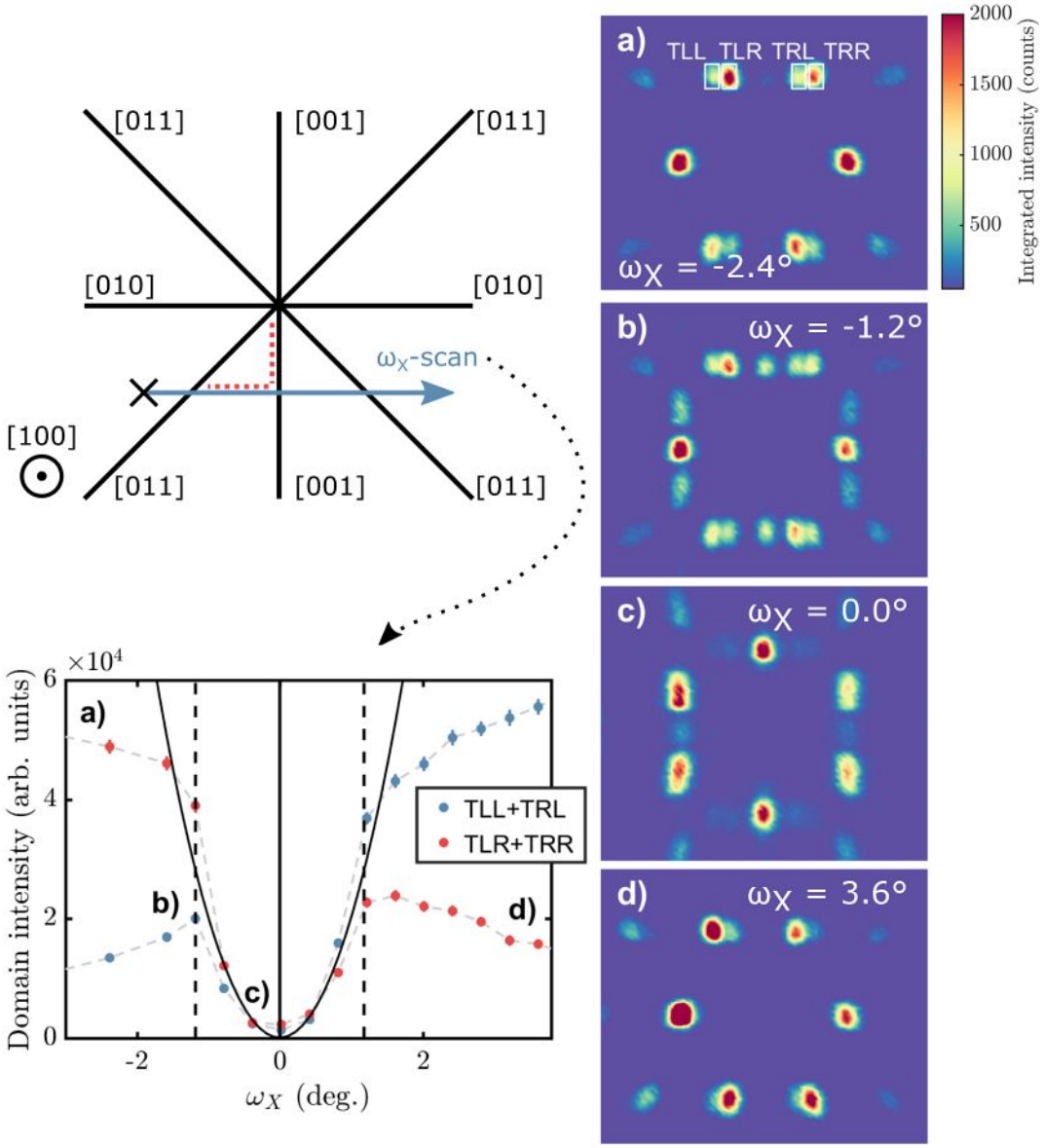

Figure 4.8: Depiction of the alignment process of a field-cooled FLL, performed with a field of 200 mT and a sample temperature of 1.6 K. The top left drawing illustrates the crystallographic directions of the sample, when the [100] direction is pointing out of the plane. The sample is aligned by first performing an ω_X-scan across three symmetry directions. The lower left plot illustrates how the domain population of two coexisting domains change as the sample is rotated. The solid parabolic line is a quadratic fit to the data points within the vertical dashed lines, which represent the points at which the scan crosses the diagonal symmetry axes. The solid vertical lines denotes the point where the scan crosses the vertical symmetry axis. Integrated rocking scan detector images from various points of the alignment scan are shown in the left plots. The same linear colour scale is used for all four detector plots. Data from experiment M.

static field. This is not to be confused with the rocking curve ω-scans, where the sample and the applied field are rotated together. At each specified ω_X-angle, a full rocking scan was measured along both the $\omega-$ and $\chi-$ rotation axes. By observing symmetry changes in the integrated rocking curve images, one could determine the point at which the field is aligned along a high-symmetry crystallographic direction. The main concept behind the sample alignment is depicted in Fig. 4.8. During both experiments, the alignment was performed with an applied field of 200 mT and a temperature of 1.6 K, since this should place us firmly in the Shubnikov regime with a scalene vortex arrangement. The ω_X-scan made it possible to align the sample in the ω-direction and additionally informed us as to how far off the alignment is in the χ-direction due to the cubic nature of the sample. The two dotted red lines in the top left panel of Fig. 4.8 show that the horizontal distance from the diagonal symmetry axis to the vertical symmetry axis is the same as the vertical distance to the horizontal symmetry axis.

The detector image from Fig. 4.8a shows a vortex structure with a non-symmetric intensity distribution among the domains, indicating that the field at this sample rotation is far away from any symmetry direction. Two coexisting domains can be identified based on the relative intensities of the diffraction spots. The top spots have been labelled as the top left left (TLL), top left right (TLR), top right left (TRL), and top right right (TRR) spots. It is evident the bright TLR and TRR spots belong to one vortex domain, while the less bright TLL and TRL spots belong to a separate domain. As the sample is rotated, the scalene phase emerges, as is seen in detector image b). The vortex lattice close to the optimal ω_X-alignment is shown in c). If one keeps rotating away from this point, one will eventually get back to the originally observed vortex structures, as shown in d), though the majority of the intensity has now shifted to the other domain.

The lower left panel of Fig. 4.8 quantifies the alignment process by showing how the intensities of the TLL+TRL and TLR+TRR domains changes as a function of the sample rotation. The intensities have been obtained by fitting 2D Gaussian functions to the

Table 4.1: Summary of the experimental differences between experiment H and M. The spherical niobium sample is shown mounted on tap of a copper mount and the micro goniometer. The white cross marks the [100] direction. The structural transitions, which we managed to probe with dynamic measurements, are also listed for each setup.

Experiment label	**H**	**M**
Coil setup	Helmholtz (uniform)	Maxwell (constant gradient)
Sample mount	Copper mount on attocube	Copper ring on micro goniometer
	 	
[100] alignment	$< 0.1°$	$\approx 1.1°$ off
Structural transitions	Scalene $\rightarrow$ isosceles	Scalene $\rightarrow$ isosceles
	Scalene $\rightarrow$ high-field square phase	-
Cooling procedure unless otherwise stated	Field cooling	Field cooling

integrated detector images using the GRASP Matlab extension [159]. It is evident that the optimal alignment, where all four top vortex spots are of equal intensity, is achieved at the minima of the fitted quadratic equation in the figure. Approximately $\pm 1.1°$ away from this point, kinks are observed in the intensity data, indicating a crossover of a diagonal symmetry axis. We can, therefore, conclude that the χ-alignment is off by about 1.1°. The presented data were obtained during experiment M, where the micro goniometer was used as a sample mount. Due to time constraints, it was not possible to further readjust χ at this point, and the final alignment used for the actual measurements therefore ended up being off by about 1.1°. The same approach was used during our later Helmholtz experiment, though the improved experimental setup with the attocube made it possible to attain an alignment within 0.1° of the fourfold direction. A summary of the differences between the two experiments is listed in Table 4.1.

4.3.3 Observed structural vortex transitions

Before addressing the dynamic aspect of the data analysis, the relevant structural vortex transitions should be identified. During both experiments, temperature and field scans were performed in an attempt to characterize the behaviour near the scalene-to-isosceles and the scalene-to-high-field square phase transitions. In Fig. 4.9, time- and angle-integrated detector images from a temperature scan across the scalene-to-isosceles transition at an applied field of 200 mT are depicted. At each field and temperature condition, a full ω rocking curve was measured. The depicted data were obtained during experiment H, with field cooled samples and a perpendicular AC field applied. The AC field should not affect the static analysis and was only applied in order to get an idea of how much heating the AC field induces at various cryostat set point temperatures. A similar temperature scan was also carried out with the Maxwell configuration (Experiment M) and the resulting detector images are shown in Appendix A. From the depicted detector plots, it is evident that the transition can be quantified by the change of the vertical FWHM of the upper left (UL) and upper right (UR) spots, see Fig. 4.10. A linear

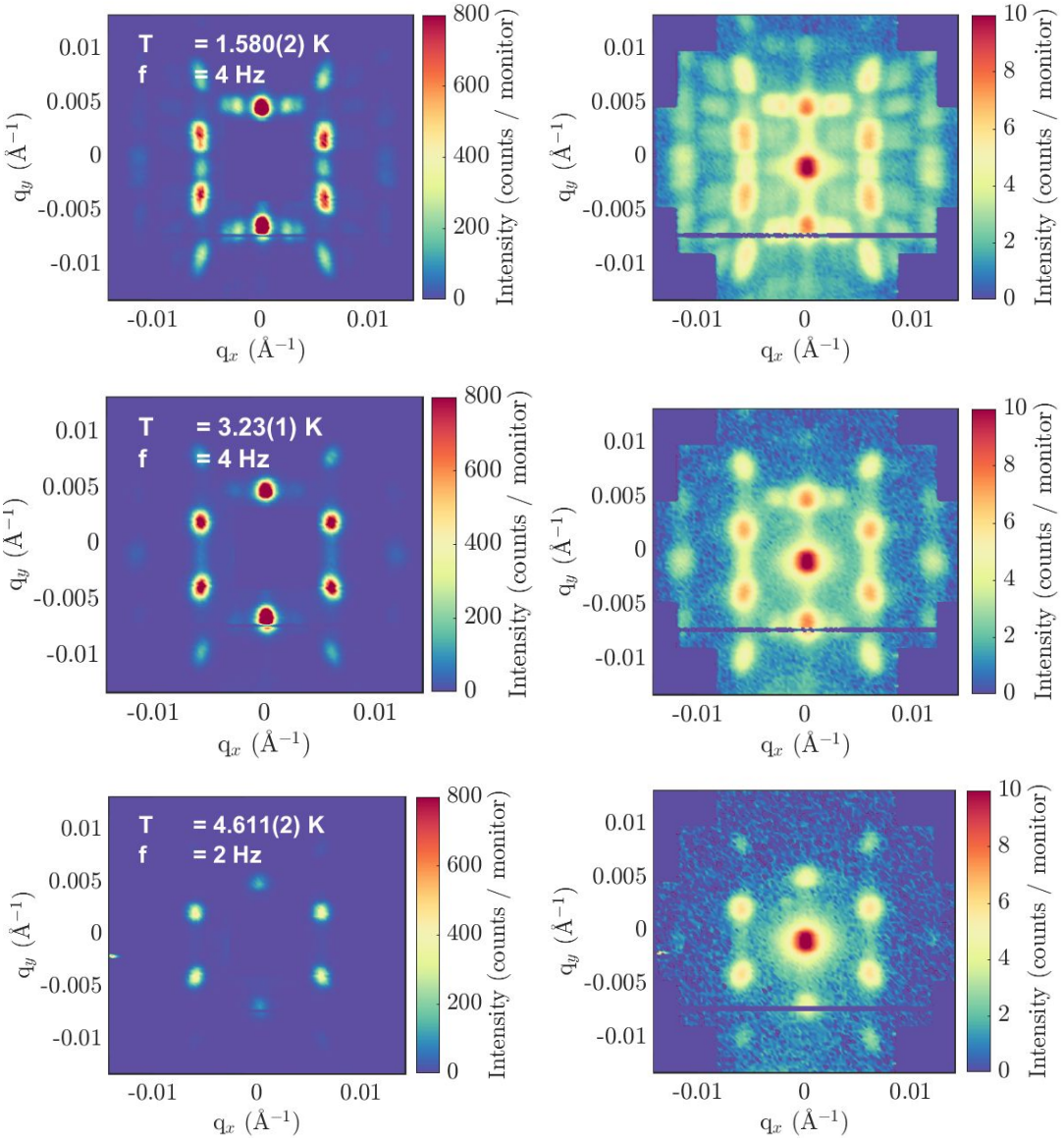

Figure 4.9: Integrated detector images obtained from rocking scans performed at different temperatures, with a static field of 200 mT and an oscillatory field of 1.3% of the main field. The images to the left have a linear colour scale, while the images to the right show the same data with a logarithmic colour scale. The beam centres have been masked out of the plots in the left column for the sake of getting a better view of the diffraction spots. The dark horizontal line at the bottom half of the detector is caused by a broken detector tube. The data were obtained from experiment H.

function with a background term was fitted to both the Helmholtz and the Maxwell data, resulting in an average transition temperature of 3.4(1) K. This agrees with the niobium phase diagram of Ref. 139. The data from the two experiments are not completely overlapping, which may be related to their different coil configurations, since the AC field can affect the quality of the FLL and thus the observed spot widths [160]. The slight difference in sample orientation might also affect the exact location of the scalene-to-isosceles transition. From the flux density plot of the right panel of Fig. 4.10, it is evident that the induced fields measured during the two experiments exhibit the same temperature dependence. The magnetic induction was estimated from each time-and-angle-integrated rocking curve detector image by fitting 2D Gaussian functions to the diffraction peaks. Based on the position of the peaks, the size of the unit cell and therefore the magnetic induction could be calculated. For each temperature and field condition, a minimum of four peaks were fitted in order to get at least two independent estimates of the magnetic induction, which then were averaged to obtain the left plot of Fig. 4.10. For the sake of estimating the critical temperature at 200 mT, the square root of the intensity of the UL and UR spots have been plotted as a function of temperature in Fig. 4.11. According to GL theory, the square root of the neutron intensity should decrease linearly close to T_c. From a linear fit, the critical temperature is estimated as $T_c = 5.5(3)\,K$, which again agrees with the phase diagram of Ref. 139.

Detector images from a static field scan are presented in Fig. 4.12. The depicted data were obtained from experiment H, with a static field alignment within 0.1° of a fourfold direction and no AC field applied. One sees that the scalene phase with four visible domains gradually transitions into a square phase with two visible domains. By fitting 2D Gaussian functions to the domain spots, the spot centres were extracted and the exact angles of the unit cells calculated. These results are shown in the left panel of Fig. 4.13. At an applied field of $\mu_0 H = 330\,\mathrm{mT}$, the angle α_a deviates from 90° by 5 standard errors. When $\mu_0 H = 340\,\mathrm{mT}$, α_a deviates by less than one standard error, giving a first

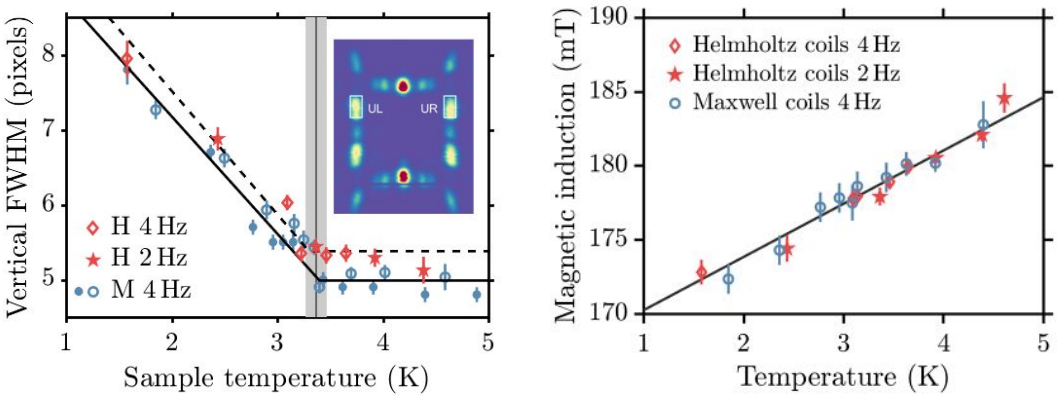

Figure 4.10: Left: The scalene to isosceles structural transition quantified by the vertical FWHM of the UL and UR spots. The inset shows a detector image of the scalene phase measured with an applied field of 200 mT and at a temperature of 1.6(1) K. The vortex spots used for the structural analysis are highlighted with white boxes. The solid and dashed lines are linear fits with a constant term defined above the transition to the isosceles phase. The vertical solid line depicts the position of the phase transition determined from the fits, while the gray area corresponds to ±1 standard error. The AC fields were generated with 100 mV_{p2p} and 150 mV_{p2p} voltages in the Helmholtz and Maxwell experiments, respectively. The filled blue circles are results obtained by counting just 10 seconds per angle in the rocking curve, while the empty blue circles originate from data where each angle has been counted for at least 120 seconds. In the case of the Helmholtz data, all measurements were obtained with counting times of at least 120 seconds per angle. **Right:** The temperature dependence of the induction at an applied field of 200 mT. The black line is a linear fit with coefficients $B(T) = 3.6(2)\,\mathrm{mT/K}\cdot T + 167(1)\,\mathrm{mT}$.

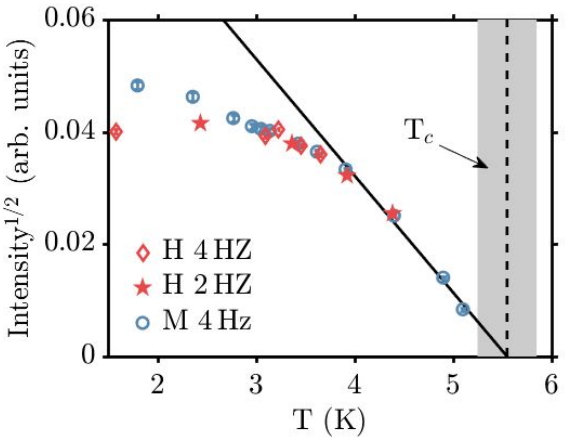

Figure 4.11: The square root of the Bragg peak intensity as a function of temperature. The intensity was obtained by fitting a 2D Gaussian with a background term to the UL and UR spots and calculating a weighted mean. The data were obtained with an applied static field of 200 mT and perpendicular oscillating fields with input voltages of 100 mV_{p2p} and 150 mV_{p2p} for experiment H and M, respectively. A linear function has been fitted to the data points above 4 K. The dashed line marks the critical temperature, and the shaded area indicate the standard error.

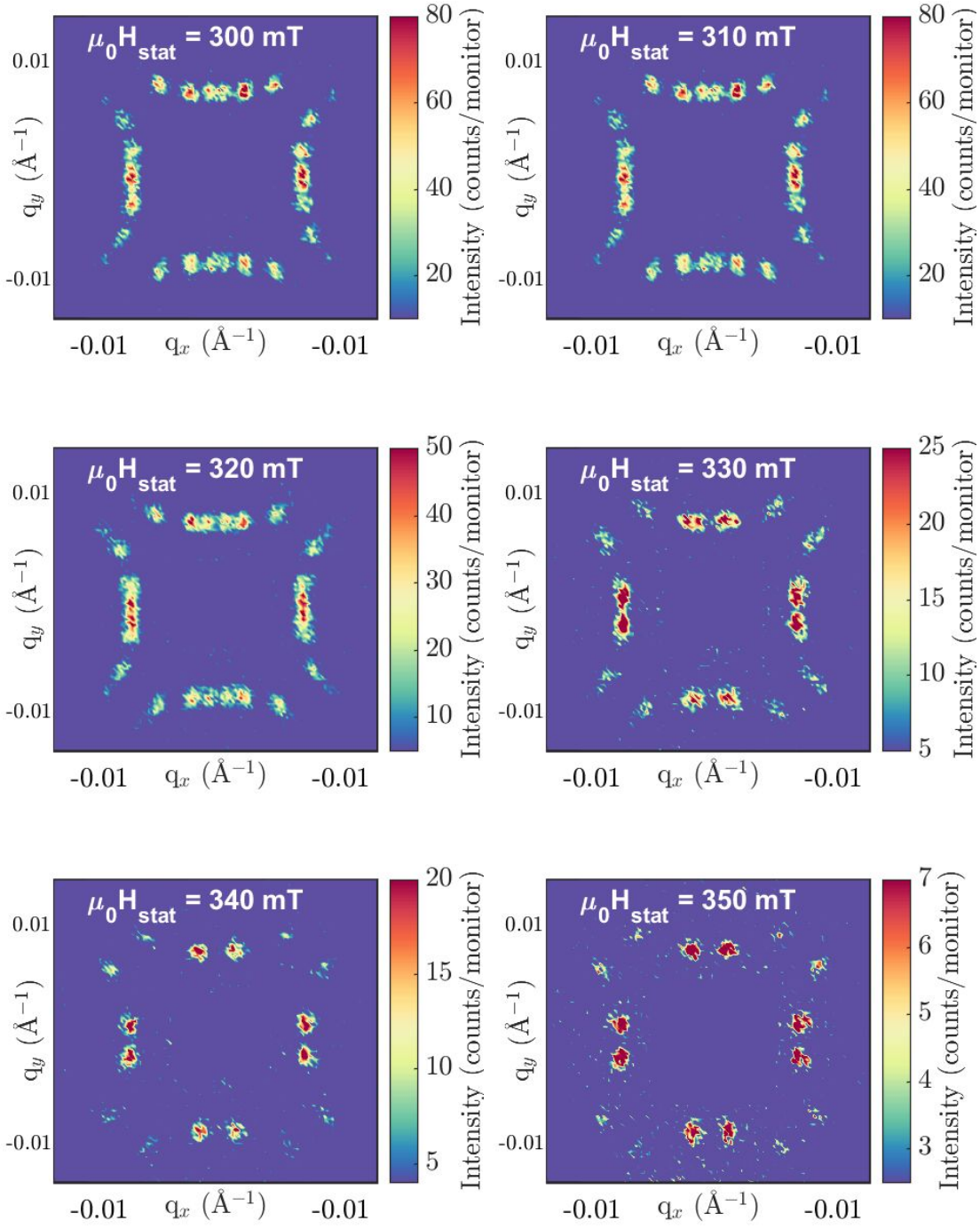

Figure 4.12: Images obtained from integrated rocking scans measured at a temperature of 1.55(1) K and varying static fields. A background measurement performed at a temperature of 10 K and a static field of 200 mT was subtracted from the data. Poisson noise at the centres of the detector images was masked out. The depicted data were collected at experiment H.

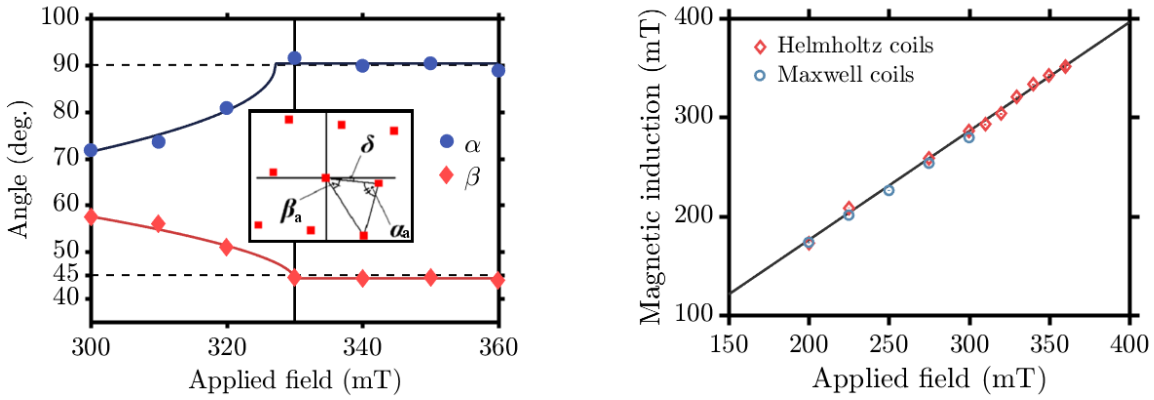

Figure 4.13: Left: The scalene to high-field square structural transition as depicted through the angles α_a and β_a. The angles are defined in the inset figure. The inset is from Ref. 139. The coloured solid lines are fits, as defined in Eq. (4.7). The vertical solid line marks the transition from the scalene to high-field square phase. **Right:** The magnetic induction as a function of the applied field. The solid line is a linear fit, $B(H) = 1.10(2)\mu_0 H - 44(6)\,\mathrm{mT}$. In both plots, the error bars are smaller than the used plot markers.

indication that the high-field square phase locks in between 330 and 340 mT. For the sake of determining the transition field, we fitted the following power law functions to our data:

$$\alpha_a(H),\ \beta_a(H) = \begin{cases} A_a + C_a \cdot (H_s - H)^{\gamma_a} & H < H_s \\ A_a & H > H_s \end{cases} \tag{4.7}$$

where H_s, A_a, C_a, and γ_a are fitting parameters. The transition field to the high-field square phase, H_s, was determined as 327(3) mT based on the α_a angles and 330.0(1) mT based on the β_a angles, resulting in an weighted mean value of $H_s = 330.0(1)$ mT. The exponents of the two fits were determined as 0.47(3) and 0.6(1). In the right panel of Fig. 4.13, the induction increases linearly with the applied field. This confirms that we are exploring a part of the niobium phase diagram which is firmly outside the IMS, where the induction is constant as a function of the applied field [140].

It should be noted that the 327(3) mT transition field determined from the data in Fig. 4.13 is highly dependent on how well one can tell different diffraction peaks apart. In some cases, diffraction spots can appear elongated, indicating that it is actually made

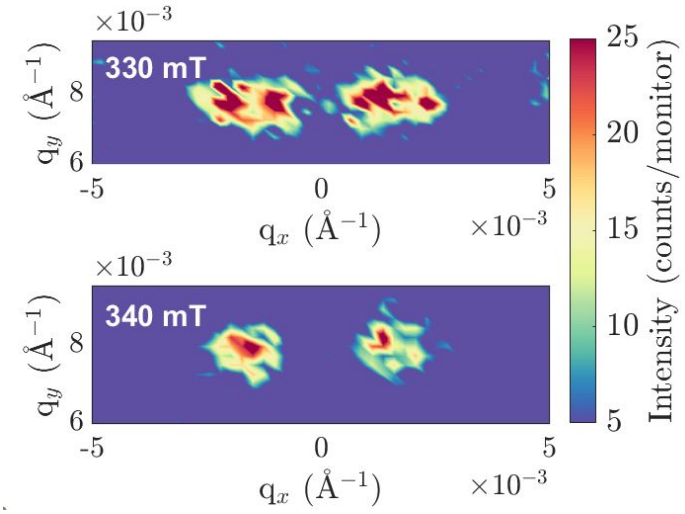

Figure 4.14: Zoomed-in views of the TLL, TLR, TRL and TRR spots from the 330 mT and 340 mT detector images from the static field scan of Fig. 4.12. A 10 K background measurement has been subtracted from the data, and the two plots share a common linear colour bar. The depicted data was collected during experiment H.

up of several vortex domains, which the detector resolution is too poor to resolve. This causes some ambiguity in the determination of the phase transition, as the decision to fit one or two Gaussian functions to a given spot introduces an implicit assumption about the symmetry of the FLL and affects the determined spot position(s) and subsequent calculated angles. The shape of the top spots at applied fields of 330 and 340 mT are shown clearly in Fig. 4.14. Here it is evident that the 330 mT spots are elongated compared to the rounder 340 mT spots. It is therefore likely that the transition field in reality is higher than the earlier determined value of 327(3) mT and instead resides somewhere between 330-340 mT.

4.3.4 Stroboscopic measurement procedure

The stroboscopic measurements were performed by field cooling the niobium sample, applying the perpendicular oscillating field, and performing an ω-rocking scan through the Bragg conditions of the vortex domains. The essence of the extraction of dynamical features is summarized in Fig. 4.15. Each vortex domain has varying intensities through the ω-rock and achieves maximal intensity exactly at the domain Bragg condition. The change in direction of the applied field means that the vortex positions, and correspondingly the Bragg condition, shift as a function of time. Due to the time-stamping of the neutrons, the obtained ω-rocking curves can be split into a number of time channels, as is

shown in the surface plots. In this case, 100 time bins were used for each measurement, corresponding to bin sizes of 5 ms for a frequency of 2 Hz.

The change in the Bragg condition is identified by tracking the changing centres of the rocking curves. In the middle panels of Fig. 4.15, rocking curves from five selected time channels are shown. It is evident that the whole curve shifts as a function of time and that each rocking curve seems to be characterized by two length scales. Namely, we observe a long range order making up the bulk of the peak as well as a short range order contributing to the shoulders of the rocking curves. The middle row plots of Fig. 4.15 show that the rocking curve profiles change as a function of time, indicating that the two distributions do not move coherently and that the overall order of the FLL therefore changes as a function of time. In the 4.4 K data a two-peaked rocking curve is observed at 20.4 ms after the initial angle shift. This supports the view that two independent distributions, and not just a single asymmetric Pearson-type distribution, are needed to fit each rocking curve profile. Therefore, the centres of the two distributions are obtained by fitting the sum of two Gaussian functions:

$$I(\omega) = BG + \frac{s_1}{\sigma_1\sqrt{2\pi}} \exp\left(-\frac{(\omega-\omega_{c1})^2}{2\sigma_1^2}\right) + \frac{s_2}{\sigma_2\sqrt{2\pi}} \exp\left(-\frac{(\omega-\omega_{c2})^2}{2\sigma_2^2}\right) \tag{4.8}$$

where ω_{c1} and ω_{c2} are the two centres of the rocking curve, s_1 and s_2 are the scaling factors of each respective Gaussian, and σ_1 and σ_2 are the two different widths. The parameter BG is a background term, which is needed if a background measurement has not been subtracted from the data. The long-range rocking curve centres are shown as a function of time in the bottom panel of Fig. 4.15, which can be used to extract the relaxation time of the FLL at the given conditions. The relaxation time is found by fitting the following exponential function:

$$\omega_c(t) = \begin{cases} \omega_0 + A\exp\left(-\frac{t+t_h-t_s}{\tau_d}\right), & t < t_s \\ \omega_0 + A\left(1-\exp\left(-\frac{t-t_s}{\tau_u}\right)\right), & t_s \le t < t_s + t_h \\ \omega_0 + A\exp\left(-\frac{t-t_h-t_s}{\tau_u}\right), & t \ge t_h + t_s \end{cases} \tag{4.9}$$

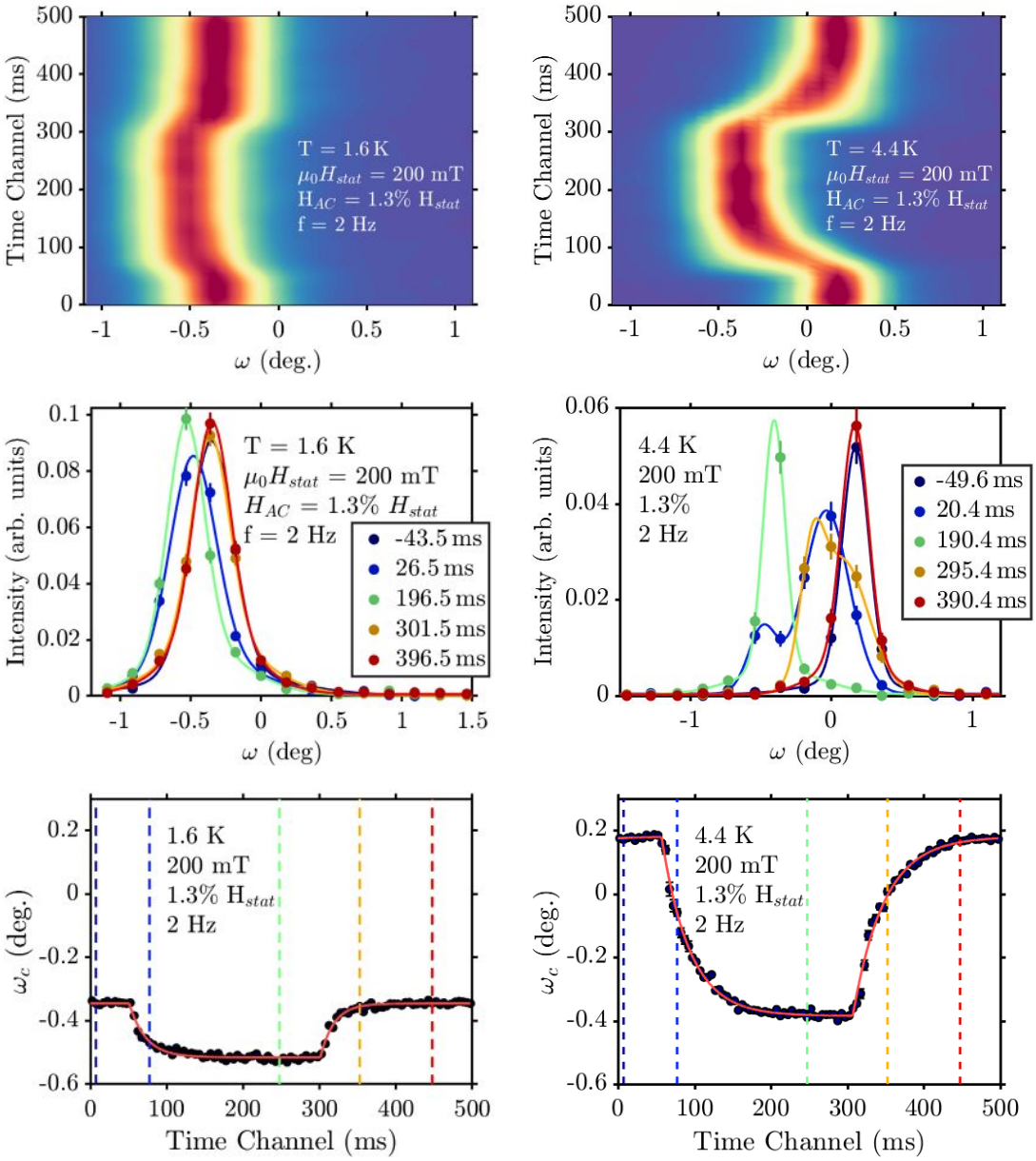

Figure 4.15: Top row: The angle- and time dependence of the neutron intensity obtained from rocking curves measured at temperatures of 1.6 K and 4.4 K. The intensities were collected from the UL diffraction spot. **Middle row:** Rocking curves from selected time channels from the two different temperature measurements. The solid line is a double-Gaussian fit, as defined in Eq. (4.8). The times in the legends refer to offsets from the start of the angle shift as determined from fits in the bottom row. **Bottom row:** The change of rocking curve centres as a function of time. The red solid line corresponds to a fit based on Eq. (4.9). All data in this figure are from experiment H. The vertical dashed lines mark the times at which the rocking curves from the previous row where extracted.

The fit-function describes the behaviour before the start of the pulse, in the middle of it, and after the FLL has relaxed back to the equilibrium. The parameter ω_0 is the background term corresponding to the unperturbed Bragg condition. The parameter A describes how far the Bragg condition has been pulled in degrees, which gives an indication of the softening of the lattice. The parameters t_h and t_s define the duration of the pulse and beginning time of the angle shift, respectively. The start of the angle shift is found by having t_s as a free fitting parameter, while t_h is calculated in seconds from the equation $t_h = \frac{1}{2f}$, where f is the frequency of the AC field.

4.4 Dynamical properties extracted from SANS

4.4.1 Temperature scan across the scalene to isosceles transition

Characteristic time scales

Fig. 4.16 depicts the temperature dependence of the characteristic time scales of the niobium FLL measured with both coil configurations and a static field of 200 mT. The analysis is based on the rocking curves of the UL and UR spots, as defined in Fig. 1. AC voltages of 100 $\mathrm{mV_{p2p}}$ and 150 $\mathrm{mV_{p2p}}$ were used for the Helmholtz and Maxwell setups, respectively, and AC frequencies of 2 and 4 Hz were employed. The data was in all cases binned into 25 bins, corresponding to bin sizes of 20 and 10 ms, respectively. In the case of the Helmholtz setup, the 100 $\mathrm{mV_{p2p}}$ voltage generates a magnetic field with an amplitude of 2.6 mT, corresponding to 1.3 % of the static field. The Maxwell coil setup will, provided the sample is fully centred, generate no field at the centre between the coils. The sample should, however, experience a constant field gradient of about 0.4 mT/cm. As is listed in Table 4.1, the best alignment achieved with the Maxwell setup was within 1.1° of a $\langle 100 \rangle$ direction. With the Helmholtz setup we achieved a better alignment of 0.1° of $\langle 100 \rangle$. However, in order to get more comparable to results between the two experiments,

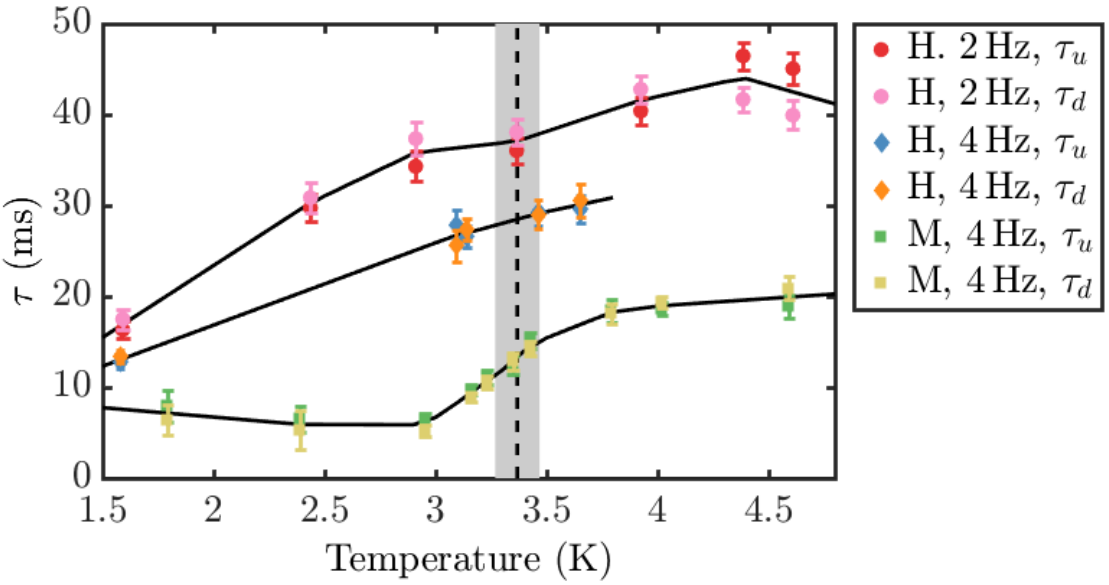

Figure 4.16: The characteristic time scales extracted from temperature scans at an applied field of 200 mT and with different AC coil configurations. The time constants τ_d and τ_u were found by fitting the function in Eq (4.8) to the experimental data. The solid lines are linear interpolations and have been inserted to guide the eye.

the attocube was used to rotate the sample such that the alignment was roughly 1° off during the temperature scans of the Helmholtz experiment too.

The time scales related to pulling the vortices out and letting them relax back into their equilibrium positions, τ_u and τ_d, are the same within errors. This is unlike what was observed in the Mühlbauer experiment, where the time scales associated with pulling the vortices out of their equilibrium position were found to be much shorter (~ 50 ms) than the time scales related to letting them relax back (~ 500 ms). It is worth considering whether this discrepancy is caused by different experimental parameters or inherent different sample characteristics. The niobium sample investigated in the Mühlbauer experiment is of higher purity ($RRR \approx 1000$) [45] than our niobium sample ($RRR \approx 450$). In terms of the experimental setup, Mühlbauer applied the static field along a twofold $\langle 110 \rangle$ axis compared to our fourfold $\langle 100 \rangle$ axis. Both experiments employ a perpendicular AC field, however Mühlbauer used a larger amplitude of 5 mT and a much lower frequency of 0.2 Hz. The lower repetition rate leaves longer time for the FLL to relax into an equi-

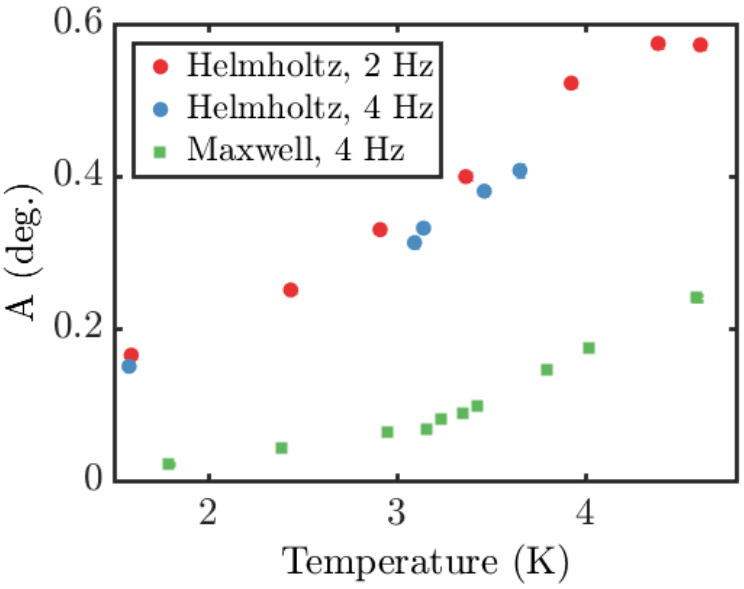

Figure 4.17: The absolute magnitude of the shift of the long-range rocking curve centres as a function of the sample temperature, as extracted with the fit function defined in Eq. (4.9). The error bars are smaller than the symbol size.

librium position. In the case of our experiments, frequencies of 2 and 4 Hz corresponds to time periods of 250 and 125 ms between each field change in the perpendicular AC field. Hence it is effectively impossible to measure the reported relaxation rates of ~ 500 ms with our experimental parameters. However, our angle shift curves, such as the ones shown in the bottom panels of Fig. 4.15, do appear to be fully relaxed before each new measurement cycle begins, and we can therefore assume that our measured time constants are not limited by the frequency. The 2 Hz 1.6 K curve (left panels of Fig. 4.15) exhibits some of the faster dynamics we measured and therefore has the best conditions for reaching a fully relaxed state, and even in this case we see that τ_u and τ_d are the same within errors.

Another discrepancy between the two studies is the overall temperature-dependence of the time constants (Fig. 4.16). Our time constants are seen to increase monotonically with temperature across both coil configurations and all frequency settings, which is the exact opposite behaviour observed experimentally in the study of Mühlbauer. Thus the Mühlbauer results indicate that the FLL gets stiffer at higher temperatures, which is in line with the uniform ($\mathbf{k} = 0$) elasticity description, $c_{44} \approx BH$ [9]. Our results, contrarily indicate that the lattice gets softer. This is corroborated by Fig. 4.17, which shows that the rocking curve centres shift with increasingly larger amplitudes as the temperature

increases.

Time-dependent behaviour of rocking curves

We now look more carefully at the parameters of the rocking curves. An interesting aspect of the temperature data, which was already evident in the example analysis plots of Fig. 4.15, is the shape and intensity behaviour of the ω-rocking curves as a function of time. As was pointed out, the rocking curves do not maintain a constant shape, which is also shown in the plots of Fig. 4.18. The time-averaged intensities of the long-range order peak, s_1, decrease with increasing temperature, as is expected as one approaches T_c. As a function of time, s_1 drops at the onset and end of each angle shift. Simultaneously, the long-range order peak width, σ_1, is seen to increase, suggesting a loss of order. The reduction of the long-range order can be caused by surface currents opposing the changing field [161] or by flux cutting phenomena (cf. Section 1.4.1). The latter is possible if the deformation of the FLL is non-local ($\mathbf{k} \neq 0$), meaning that all flux lines are not pushed an equal amount and therefore could end up at an angle with respect to one another. The peak intensity and width of the short-range order, s_2 and σ_{c2}, is seen to show the inverse time-dependent behaviour of the same properties of the long-range order peak. When adding s_1 and s_2 together, one achieves a roughly constant scattering intensity as a function of time for the different temperatures (cf. Fig. 4.19). This implies that we have a constant amount of scatterers as a function of time, making flux cutting annihilation events more unlikely. The final two panels of Fig. 4.18 show that both the long-range and short-range order peak positions exhibit dynamic behaviour. In the previous section the time constants were extracted based on the changing ω_c values of the long-range order peak. If one tries to fit the ω_c-curve of both the long- and short-range order at 4.4 K, one gets respective average time constants of 44(1) ms and 32(4) ms.

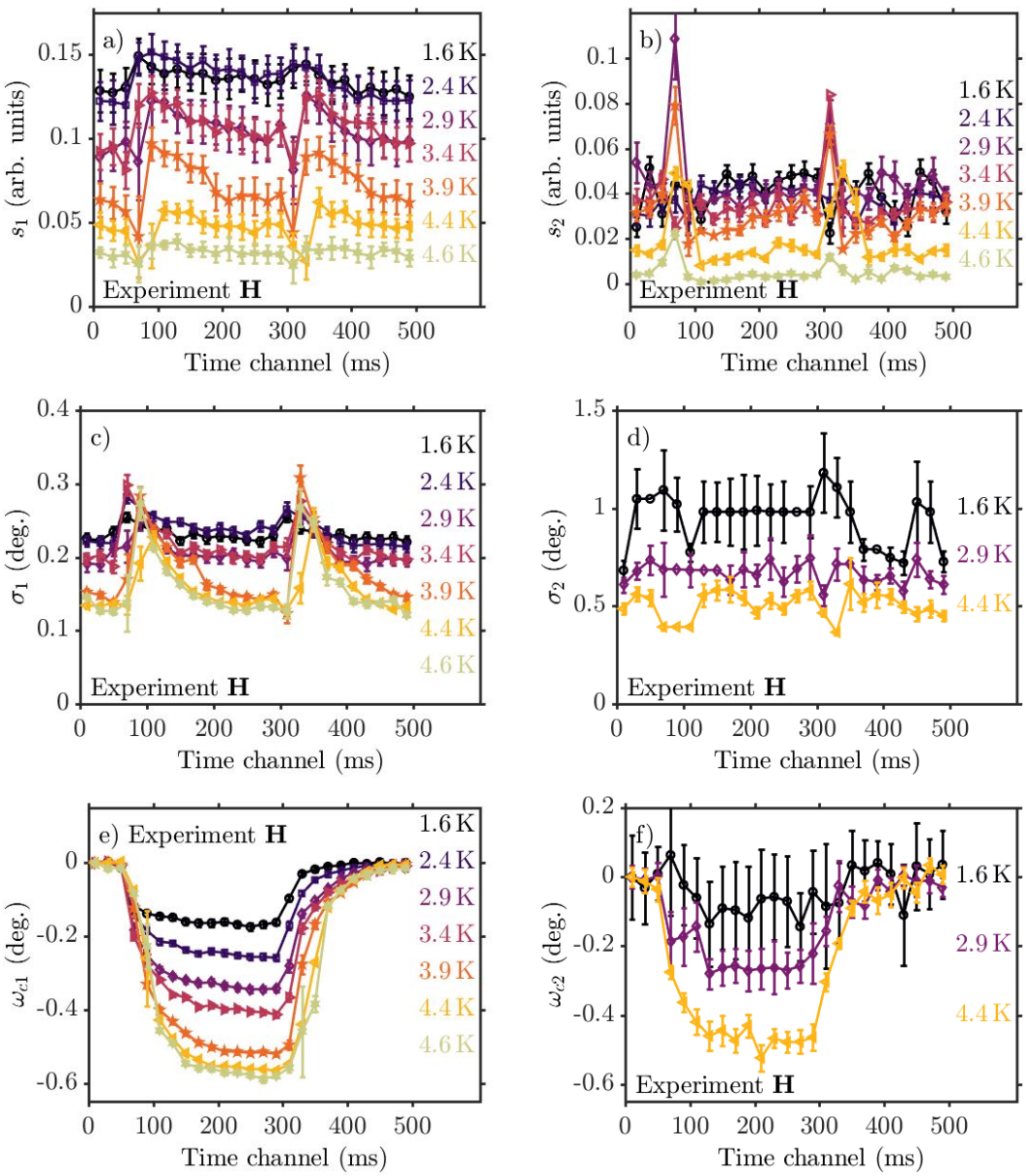

Figure 4.18: Time-dependent information extracted from fitting Eq. (4.8) to the rocking curves of the Helmholtz coils temperature scan. The plots display **a)** intensity s_1 of the long-range Gaussian peak, **b)** intensity s_2 of the short-range Gaussian peak, **c)** peak width σ_1 of the long-range peak, **d)** peak width σ_2 of the short-range peak, **e)** peak position of the long-range ordered peak, and **f)** peak position of the short-range ordered peak. In subplot **d)** and **f)**, only three curves are shown for clarity.

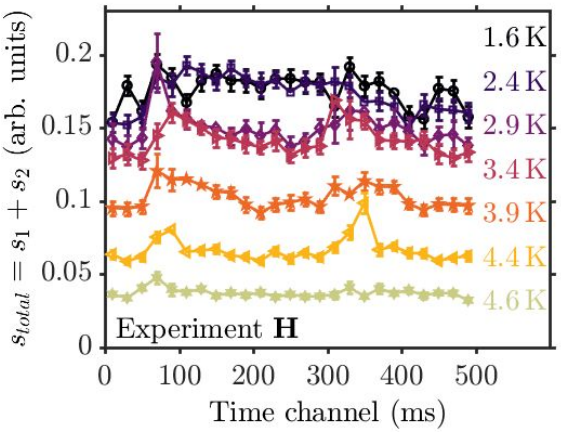

Figure 4.19: The total scattering intensity extracted from the rocking curves of the UL and UR diffraction spots when adding the long-range order intensity and short-range order intensity together. Obtained from measurements with the Helmholtz configuration, a 200 mT applied field, and a 2 Hz 100 $\mathrm{mV_{p2p}}$ AC field.

Correlation lengths

The rocking curve standard deviations given in Fig. 4.18 have not been corrected for the instrumental resolution and are therefore not a true reflection of the amount of disorder along the flux lines. To account for the detector resolution, one needs to refer back to the theoretical expressions for the rocking curve width, W_ω, and radial spot width, W_r, given in terms of the parameters a, b, and c in Section 3.1.2. Here, a refers to the angular spread of the beam and c is related to the wavelength spread and the width $W_\mathbf{q} = \Delta\mathbf{G}/\mathbf{G}$ as $c^2/\theta_B^2 = \Delta\lambda_n^2/\lambda_n^2 + W_\mathbf{q}^2$. In the parallel scattering geometry, the parameter b expresses the disorder along the flux lines. The parameter a is based on the experimental geometry described in Section 4.3 and is calculated to have a width of $a \approx 0.05\,\mathrm{m}/16\,\mathrm{m} = 0.003125\,\mathrm{rad} = 0.179°$. The two other parameters, b and c, can then be determined by solving the system of two equations containing the expression for W_ω, Eq. (3.14), and W_r, Eq. (3.15). The rocking curve FWHM is related to the standard deviations of Fig. 4.18 as $W_{\omega_i} = 2\sqrt{2\ln 2}\sigma_i$. For every temperature, the radial width was determined by summing the intensities in each time slice over all angles and fitting a 2D Gaussian to the TM spot. The vertical FWHM of the TM spot then corresponds to the radial width, which is shown as a function of time and temperature in Fig. 4.20. Overall, one sees no clear time dependence, which may be an effect of the lower in-plane resolution in the parallel geometry. The horizontal lines of the figure have been calculated from Eq. (3.15) assuming no spread in the scattering vector, $W_\mathbf{q} = 0$, and extracting the

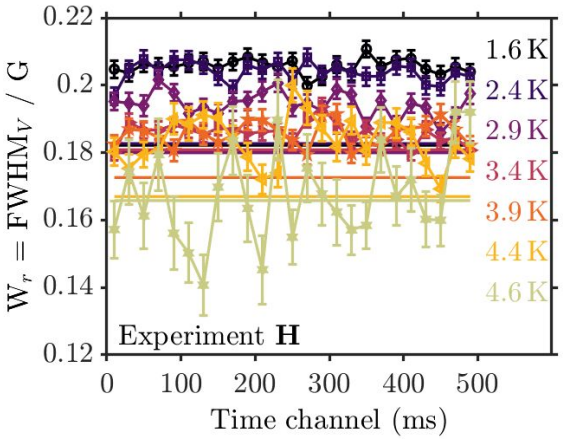

Figure 4.20: The radial width of the TM diffraction spot (vertical FWHM) as a function of temperature. The data was collected with the Helmholtz coil setup with a static applied field of 200 mT and an oscillating field with a frequency of 2 Hz and an amplitude of of 1.3% of the static field. The horizontal lines are the expected static values for W_r calculated from Eq. (3.15) assuming $W_{\mathbf{q}} = 0$.

parameter b from the rocking curve widths. The high temperature radial widths are seen to have the same magnitude as the $W_{\mathbf{q}} = 0$ lines, indicating that it will be impossible to extract the correlation lengths in the direction of $\mathbf{q}$ for these temperatures. Only the radial widths measured at 1.6 K and 2.4 K appear significantly larger than their corresponding $W_{\mathbf{q}} = 0$ lines, meaning that the spot widths in these cases are not dominated by the instrumental contributions. The time-integrated radial width is at 1.6 K found to be 0.184(2)°, 0.206(2)°, and 0.205(3)° for measurements collected with no AC field, a 1.3% 2 Hz AC field and a 1.3% 4 Hz AC field, respectively. Thus, a slight widening of the radial peak width is observed as a result of the oscillatory field.

The resolution corrected rocking curve widths are shown in the top row of Fig. 4.21. One should note that the same radial widths have been used to solve the system of equations for the long and short range order, given that it is not possible to separate their contributions to the diffraction spot widths. This may therefore affect the accuracy of the corrected rocking curve widths. In general, as was observed in Fig. 4.18, the long-range order widths spike at times corresponding to changes in the angle shifts as induced by the AC field. The correlation lengths along the flux lines are calculated as $\xi_{L_i} = 1/(b_i q)$, where q is the length of the scattering vector [162]. In studies where the experimental rocking curve width is extracted from a Lorentzian width, the correlation length is instead calculated as $\xi_L = 2/(bq)$ [122]. Our correlation lengths are shown as calculated from the

long and short-range order Gaussian widths in the bottom row of Fig. 4.21. On average, longer correlation lengths are observed for both the long- and short-range order at higher temperatures in the isosceles phase. However, the high-temperature data also show more distinct time-dependent behaviour, most likely as a result of the lattice softening that was already documented in Fig. 4.17.

The resolution corrected spot width in the direction of the scattering vector, $W_{\mathbf{q}}$, is found via:

$$W_{\mathbf{q}} = \frac{\Delta \mathbf{G}}{\mathbf{G}} = \sqrt{\frac{c^2}{\theta_B^2} - \frac{\Delta \lambda_n^2}{\lambda_n^2}} \tag{4.10}$$

where c was found by solving the system of equations defined by the expressions for W_r and W_{ω_1}, $\Delta\lambda_n/\lambda_n = 10\%$ and θ_B is the Bragg angle. The resulting corrected widths, which provide a measure for the correlation lengths in the direction of $\mathbf{q}$, are shown in Fig. 4.22. The $W_{\mathbf{q}}$ widths are for all temperatures above 2.4 K seen to be rather noisy and in some case zero within error bars. It should be noted that the errors of $W_{\mathbf{q}}$ have been calculated based on the experimental errors of the rocking curve widths, W_w, and radial widths, W_r, but do not include any potential variation in the instrumental parameters such as the wavelength spread $\Delta\lambda_n/\lambda_n$ or angular spread, a. Given that $W_{\mathbf{q}}$ is very sensitive to these instrumental parameters, the errors of Fig. 4.22 are most likely underestimated and the $W_{\mathbf{q}}$ values may be inaccurate. Hence, this section illustrates how the parallel scattering geometry is sub-optimal for analyzing the in-plane correlations.

4.4.2 Field scan across the scalene to high-field square transition

The time constants extracted from field scans performed at temperatures of 1.6 K are shown in Fig. 4.23. The voltage of the AC field was changed during the Helmholtz field scan such that the amplitude of the AC field was kept at a fixed percentage of 1.1% of the applied static field. For the investigated applied static fields of 200 mT, 275 mT, 320 mT,

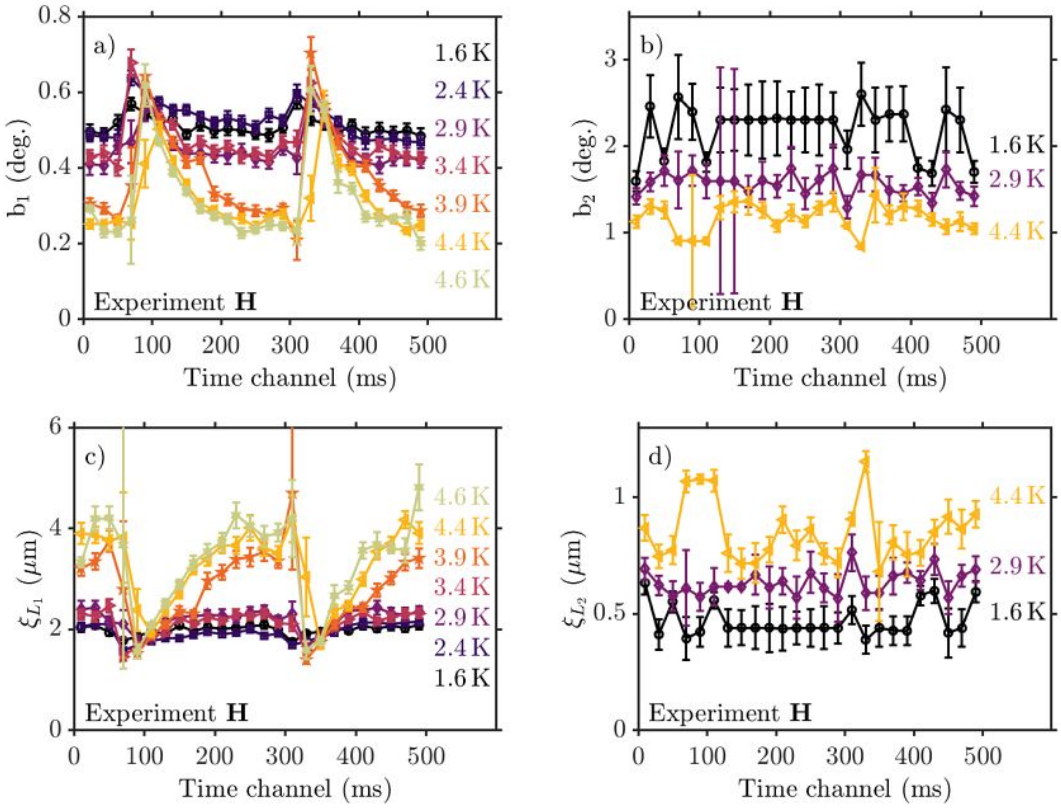

Figure 4.21: **a)** and **b)** The resolution corrected rocking curve widths of the the long and short-range order. **c** and **d)** The correlation lengths along the flux lines as calculated from the corrected rocking curve widths. Correlation lengths were only calculated for the measurements obtained at 1.6 K and 2.4 K, because only these data set had reasonable errors.

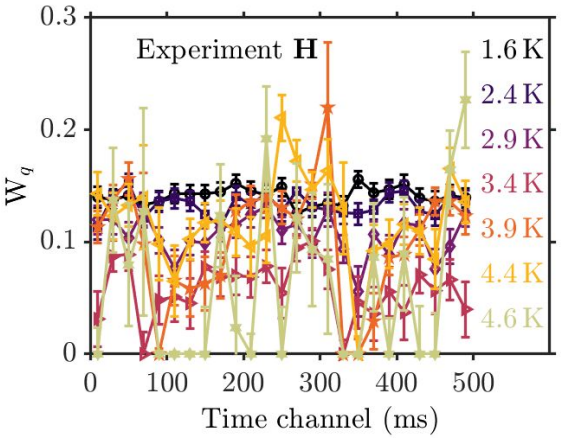

Figure 4.22: The width in the direction of scattering, $W_{\mathbf{q}}$, obtained by correcting the radial width, W_r, for the instrumental resolution as a function of time. This width is a measure for the correlations along the same direction.

325 mT, 330 mT, and 350 mT we employed respective voltages of 86 mV_{p2p}, 120mV_{p2p}, 137mV_{p2p}, 139mV_{p2p}, 141mV_{p2p}, 150mV_{p2p} with a 1 Hz frequency. For the Maxwell setup, we used a constant voltage of 150mV_{p2p} and a frequency of 6 Hz for all applied fields in the field scan. The Helmholtz results were obtained with an alignment of 0.1° within a ⟨100⟩ direction, while the Maxwell data was 1.1° off. The two time-scales, τ_u and τ_d, agreed within errors for each measurement condition, and a weighted average has therefore been taken to improve the precision of the results. Because of the sub-par sample alignment, the high-field square phase was not observable with the Maxwell coil setup, and the corresponding field scan was therefore limited to a static field of 300 mT. At increasing induced fields the counts in the rocking curves decrease because of the decreasing magnetic form factor, which explains the large error bars observed at large inductions. As a result of the decreasing form factor, we only had time to carry out a single dynamic measurement in the high-field square phase, which took around 6 hours to measure in total. This single point does not diverge significantly from the previous measurements in the high-field scalene phase and does therefore not indicate any unique dynamic behaviour in the square phase. Fig. 4.24 shows that the amplitude of the angle shift linearly increases across the phase transition.

As was the case for the temperature data, the general trend of the field scan data goes directly against what has been observed by Mühlbauer *et al.* [45], who found that the time scales of the niobium FLL decrease as a function of time. Thus our results do also not agree with the predictions of uniform elasticity theory, $c_{44} = BH$ [9], given that the elastic moduli is inversely correlated to the time constants (cf. Eq. (4.4)). Theoretically, one can find increasing time constants with increasing fields through the anisotropic elasticity description, cf. Sec. 1.3.2. According to this description, the c_{44} and c_{66} elastic moduli should decrease at higher inductions, translating into longer relaxation times as was observed in our results. However, the anisotropic elasticity description still does not account for the frequency dependence observed in the dynamic temperature scan of Section 4.4.1.

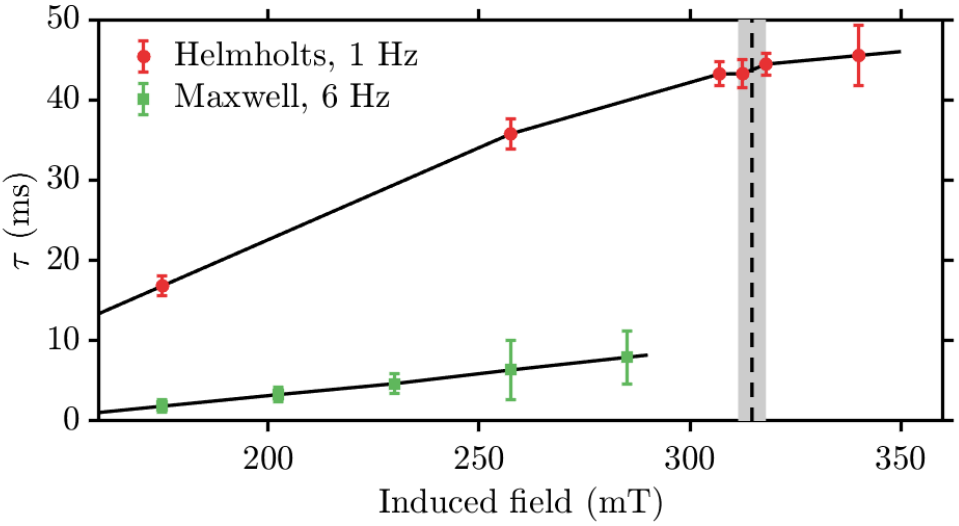

Figure 4.23: Characteristic time scales extracted from field scans at 1.6 K. The presented time constants are the weighted means of τ_u and τ_d as determined from the UL and UR diffraction spots. The Helmholtz field scan was performed with a 1 Hz perpendicular AC field, which had a magnitude of 1.1% of the main field. The values of the induced field in the sample are based on the data in the right panel of Fig. 4.13. The shaded grey area denote the location of the isosceles-to-high-field square transition within ±1 standard error. As was noted based on the detector images of Fig. 4.14 the actual transition may lie at slightly higher field values. The solid black lines serve as visual guides.

To support the idea that the discrepancy between our results and uniform elasticity theory is a result of anisotropy effects along the fourfold axis, we compare our results to a similar unpublished dynamic study of a cylindrical vanadium sample. The experiment was carried out at the V4 instrument by E. Tekin and M. Laver. The static field was in this case applied along a threefold $\langle 111 \rangle$ crystallographic direction, while the oscillating field was induced by Helmholtz coils and applied along $\langle 1\bar{1}0 \rangle$. A collimation and sample-to-detector distance of 16 m was used along with a neutron wavelength of $\lambda_n = 10$ Å. The investigated vanadium sample is the same sample investigated in Ref. 76 and is presented in more detail in Chapter 5. The *RRR* of the sample is estimated to be in the range of 50-100 making it more impure than both our own and the Mühlbauer niobium sample. An example detector image from this experiment is shown in Fig. 4.25, where a single vortex domain is observed with an equilateral triangular half-unit cell. The vortex unit

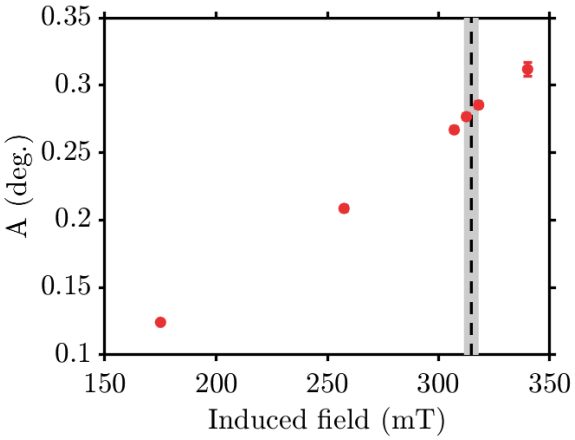

Figure 4.24: Absolute magnitude of the shift of the rocking curve centre as a function of the sample induction. The induction values at a given applied field, B(H), has been calculated as according to the calibration in Fig. 4.13. The grey area denotes the structural transition from a scalene to a high-field square phase.

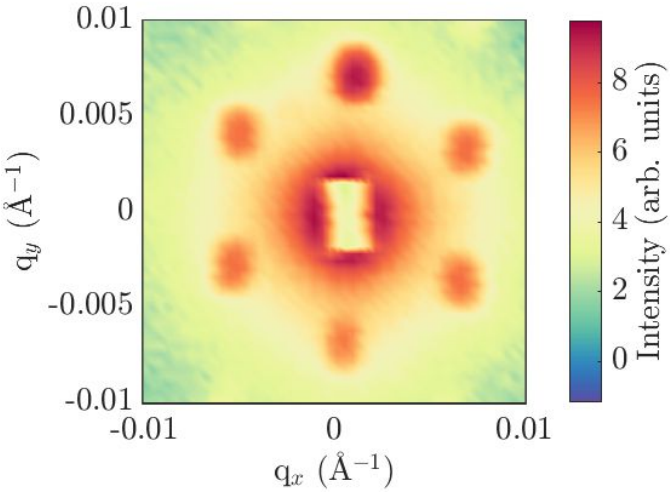

Figure 4.25: Integrated rocking curve detector image measured with the vanadium sample, a sample temperature of 1.6 K and an applied field of 200 mT along a ⟨111⟩ crystallographic direction. The colour scale is logarithmic.

cell was not observed to change shape during the vanadium experiment. The same hexagonal vortex morphology has previously been observed in niobium at all temperatures and field values, provided the field is parallel to a ⟨111⟩ direction [8].

A comparison between the dynamic behaviour observed during the niobium $H_{stat} \parallel \langle 100 \rangle$ experiment and the vanadium $H_{stat} \parallel \langle 111 \rangle$ experiment is carried out in Fig. 4.26. During both experiments, the amplitude of the angle shift increases with the applied field, while the evolution of the time constants show opposing behavior. The time constants measured during the vanadium experiment are shown as a function of the induced field in Fig. 4.27. Here, it is seen that the vanadium time constants decrease as a function of increasing field, similarly to the behaviour observed during the Mühlbauer experiment. Hence, the field and temperature trends observed in Figs. 4.16 and 4.23 during our experiment

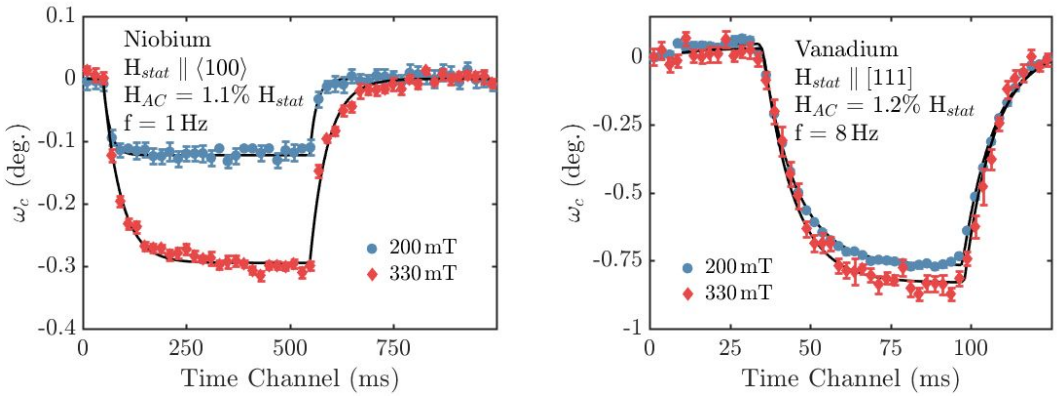

Figure 4.26: Comparison between the dynamic behaviour of the FLL in niobium with the static field applied along ⟨100⟩ and the FLL in vanadium with the static field applied along ⟨111⟩. A Helmholtz coil setup has been employed for both experiments and all measurements were carried out at an temperature of 1.6(1) K.

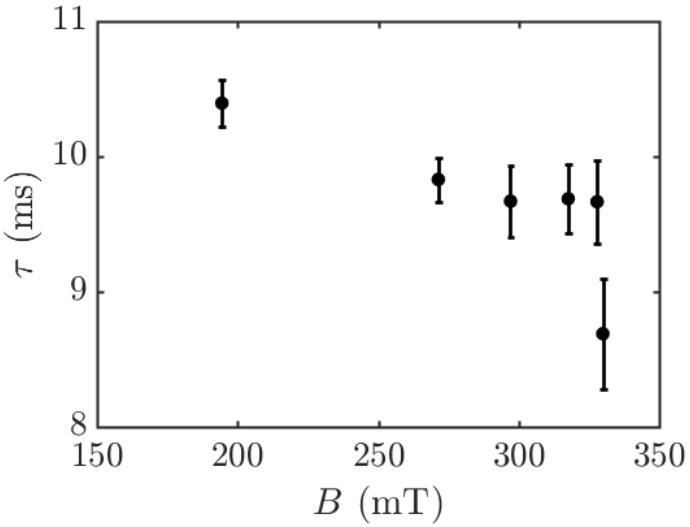

Figure 4.27: The time constants extracted from the vanadium data as a function of the induced field. The presented time constants were averaged over τ_u and τ_d extracted from the UL and UR spots. The field scan was carried out at a temperature of 1.6 K with an oscillating field amplitude of 1.2(1)% of the static field and a frequency of 8 Hz.

appear to be unique to crystallographic directions where anisotropic behaviours are most apparent, such as ⟨100⟩ directions. The time constants related to either pulling the vortices out or letting them relax back into the Bragg condition were observed to be the same within errors during both the fourfold niobium and threefold vanadium experiments. The asymmetry in the Mühlbauer time constants can therefore most likely be asserted to be an effect of the intermediate mixed state explored during that experiment.

4.4.3 Non-local behaviour of the FLL

In this section, we investigate the "non-local" properties of the niobium FLL. By non-local we here mean whether different domains display differing time-dependent behaviour. In the detector plot of Fig. 4.28, different areas of the detector image are marked, wherein the intensity has been integrated as a function of time and ω-angle. The time-dependent behaviour of the corresponding rocking curve centres are shown in the same figure along with a table of the extracted time constants. The boxes split the UL and UR diffraction spots into several domains, which would have been more visible with a better resolution, cf. Fig. 4.1. As is evident from the relative intensities, box 1 and 4 cover spots from one domain, while box 2 and 3 cover spots belonging to another.

Diffraction spots from different domains are seen to exhibit differing time constants. Meanwhile, diffraction spots belonging to the same domain but appearing at different **q**-vectors are seen to have time constants that agree within errors, indicating that a Lorentz rescaling cannot account for the observed differences. To fully rule out the possibility of a Lorentz factor affecting the time-dependent analysis, 2D Gaussian functions have been fitted to the different diffraction spots as a function of time, cf. Fig. 4.29. A Lorentz factor can only affect the time-dependent analysis if the spot position on the detector change as a function of time, but Fig. 4.29 shows that this is not the case.

Box 5 and 6 cover diffraction spots further out on the detector plane. The rocking curves extracted from these spots are seen to result in much larger time constants than what has been seen from the first four spots. The lack of uniformity in the time constants supports the notion from the previous sections, which concluded that the vortices do not move in a coherent elastic way. Instead we here see indications of different parts of the FLL in the sample moving with different characteristic time scales.

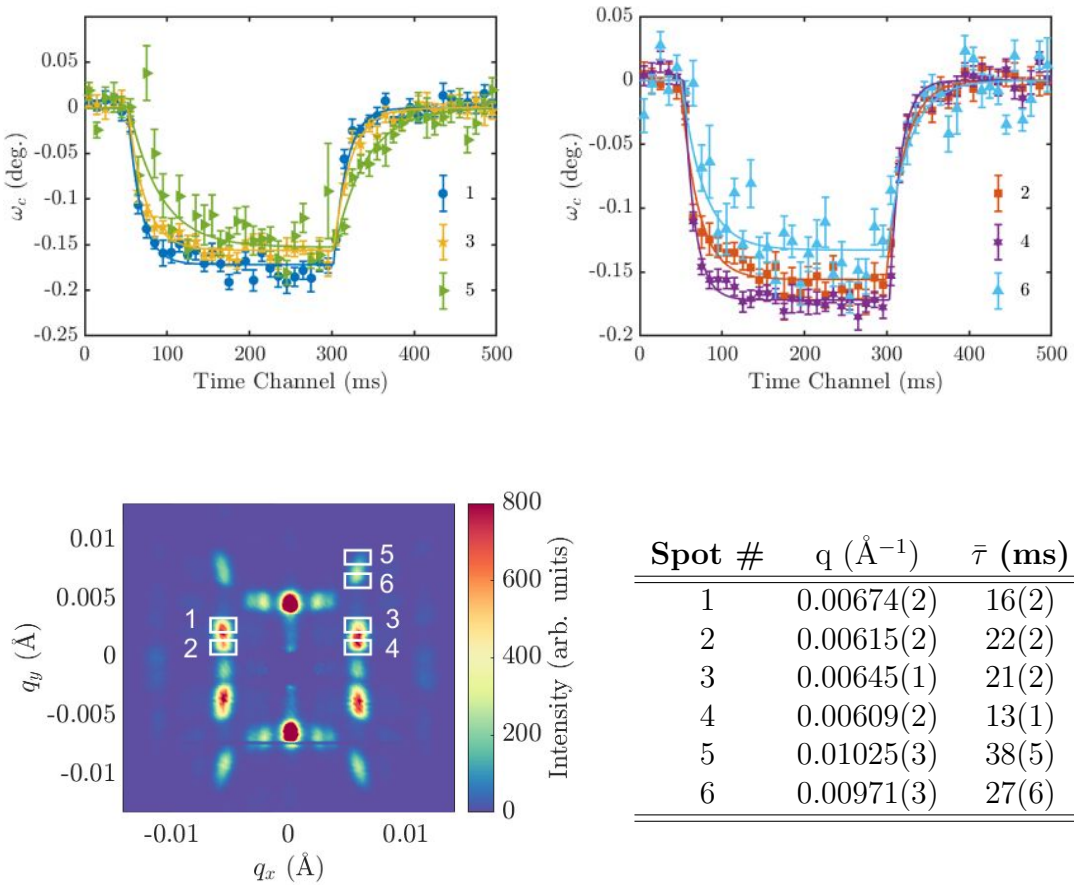

Spot #	q (Å^{-1})	$\bar{\tau}$ **(ms)**
1	0.00674(2)	16(2)
2	0.00615(2)	22(2)
3	0.00645(1)	21(2)
4	0.00609(2)	13(1)
5	0.01025(3)	38(5)
6	0.00971(3)	27(6)

Figure 4.28: Investigation of whether the extracted time constants are sensitive to specific vortex domains or the position of a diffraction spot on the 2D detector. This analysis is based on data collected with a 200 mT applied field, a sample temperature of 1.6 K, and a perpendicular oscillatory field with a frequency of 4 Hz and an amplitude of 1.3% with the Helmholtz coil setup. The sample alignment was during this measurement 1.1° off a fourfold direction. The top panels show the time evolution of the rocking curve centres, ω_c, based on different areas of the detector. The figure on the lower left panel depicts and labels the areas on the detector that has been integrated as a function of time. The table in the lower right panel depicts the resulting time constants (averaged over τ_u and τ_d, which in all cases where the same within errors) for the different areas as well as the length of the q-vector for each spot, as determined from a 2D Gaussian fit.

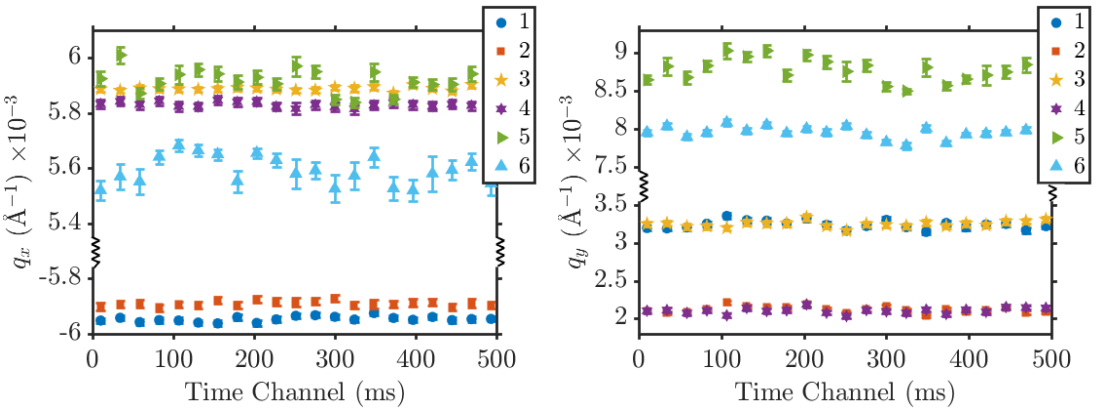

Figure 4.29: The coordinates (q_x, q_y) of the difraction spot centres as a function of time. The coordinates have been determined by fitting 2D Gaussian functions to the angle-integrated time-slices of the diffraction spots marked with boxes in Fig. 4.28.

4.4.4 Diffuse scattering

Indications of different kinds of diffuse scattering are observed in our data. The first kind is the appearance of the extra short-range order in the rocking curves of the first order diffraction peaks, as has been discussed in Section 4.4.1. Comparisons between rocking curves obtained with and without an AC field are made in Fig. 4.30, where only the curves with the AC field are seen to exhibit a short-range order. In general, the AC curves are seen to be broader, indicating an increased disorder of the FLL. At the same time, however, the AC curves are observed to have an overall larger integrated intensity. This extra intensity may be a result of the oscillating field improving the long-range inter-vortex order, an effect which will be further explored in Chapter 5. The appearance of a short-range order in experimental rocking curves was previously reported in Ref. 122, where the extra weight in the tails of the rocking curves was interpreted as a sign of the 2H-$NbSe_2$ sample having entered the plastic regime after applying an external DC current.

The second kind of apparent diffuse scattering referred to in this text is the vertical diffuse streaks observed in the detector planes during both the Helmholtz and Maxwell experiment. Fig. 4.31 shows that the diffuse streaks are enhanced by the AC field. Unlike the first kind of diffuse scattering, which appears at the approximately same **q**-vectors as the

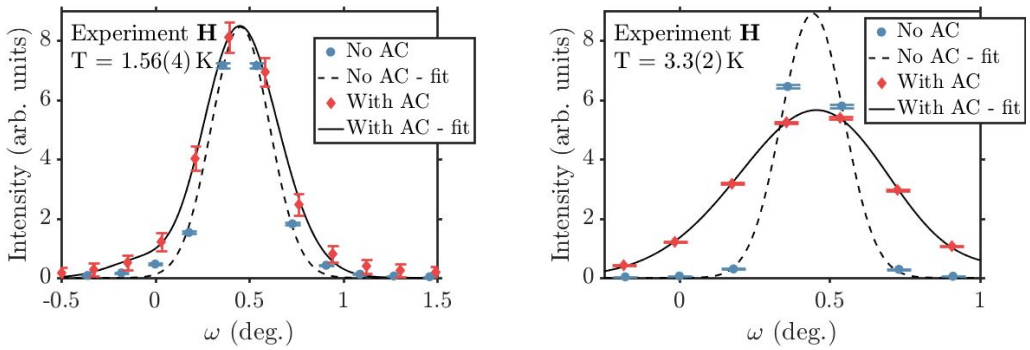

Figure 4.30: Depiction of the first kind of diffuse scattering discussed in the text. Time-integrated UR rocking curves obtained with and without a 2 Hz 100 mV_{p2p} AC field show that the AC field contributes to the observed extra weight in the tails of the AC rocking curve peak. The solid lines are single (double) Gaussian functions fitted to each rocking curve without (with) an AC field applied.

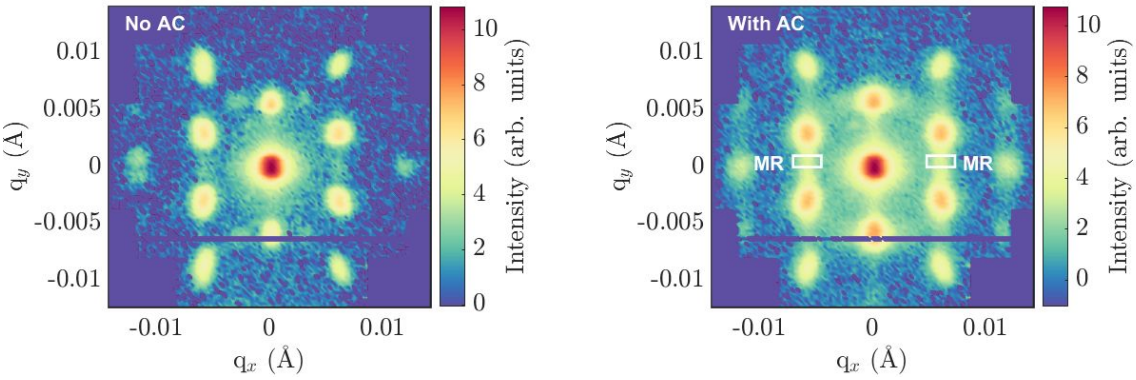

Figure 4.31: Depiction of the second kind of diffuse scattering discussed in the text. **Left**: Integrated rocking curve detector image obtained with a static field of 200 mT, a sample temperature of 3.5 K and no AC field. **Right:** Integrated detector image obtained at the same static field and temperature conditions, but now with a 1% 4 Hz AC field applied. The depicted data are from experiment H.

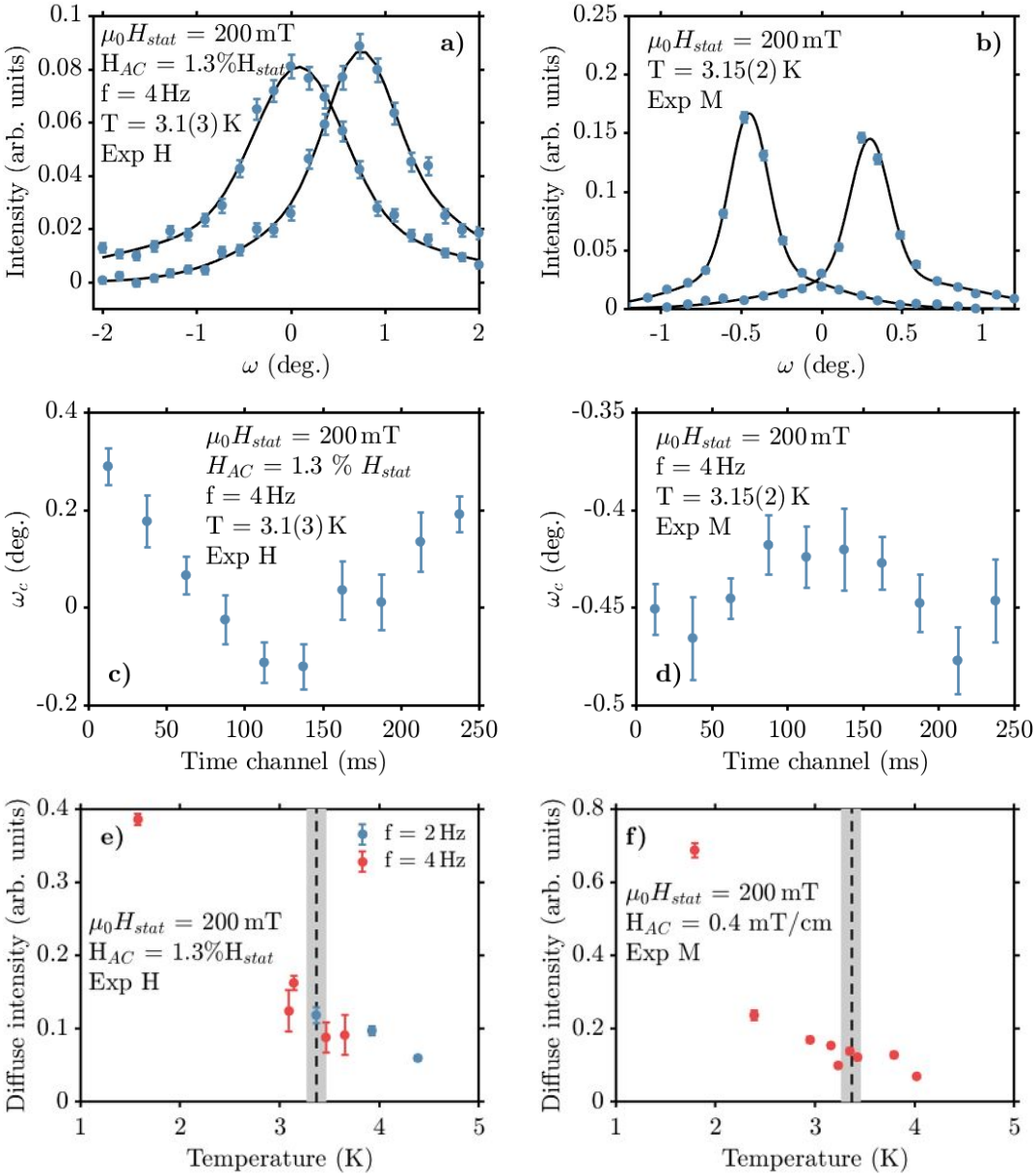

Figure 4.32: Characteristics of the diffuse vertical stripes appearing between the vortex diffraction spots in both experiment M and H. **a)-b)** Examples of time-integrated rocking curves of the ML and MR areas. All rocking curves have been fit with a double Gaussian, as according to Eq. (4.8). **c)-d)** The change in the long-range peak position of selected data sets as a function of time.**e)-f)** The time-integrated rocking curve intensity as a function of temperature.

vortex spots and therefore has the approximately same underlying structure, the diffuse streaks exhibit a range of different scattering **q**-vectors and may therefore be the result of a different lattice structure. Fig. 4.32 depicts an investigation of the general behaviour of the diffuse streaks, where they are seen to exhibit rocking behaviour as well as a time-dependent behaviour similar to the short- and long-range order of the Bragg peaks. In many ways, the apparent stripey diffuse scattering therefore appears to behave dynamically like the UL and UR peaks. It is hence possible that the extra intensity between the peaks is not a result of diffuse scattering, but is rather the signature of a minority domain that becomes more visible when the lattice is pulled away from the fourfold axis. In Fig. 4.33 this idea is tested by seeing how the intensity of the ML and MR areas change as a function of angle in the alignment ω_X scans. In a dynamic measurement performed at 200 mT and a temperature of 3.3(2) K, the integrated intensity in the ML and MR areas was found to be 2.9(1) times higher than in the static case. If the perpendicular 1.3% field was static, one would expect a shift in the flux lines of 0.7° from the fourfold axis. According to to the analysis of the ML and MR intensities in Fig. 4.32, one can expect an angle shift of about 0.4° with an oscillating field at temperatures around 3 K. This shift is consistent with the shift extracted from the UL and UR peaks in Fig. 4.17, where a shift of about 0.38(1)° is expected at a temperature of 3.3 K. Inserting this data point in Fig. 4.33, one sees that it fits within the 95% confidence interval of the ω_X-scan fit. It is therefore possible that the pulling of the AC field contributes to the intensity in this region.

The static rocking curves of Fig. 4.32 have been fit with the same double Gaussian function as the other rocking curves of this chapter, Eq. (4.8). For the Helmholtz data, the averaged widths of the static 3.1(3) K rocking curves are $\sigma_1 = 0.47(3)^\circ$ and $\sigma_2 = 2.2(4)^\circ$. These widths are significantly larger than the widths reported for the UL and UR spots in Fig. 4.18 and therefore indicate that the structure associated with the ML and MR intensities has shorter correlation lengths than the main vortex lattice structure. The stripey nature of the scattering on the detector image makes it impossible to fit a 2D

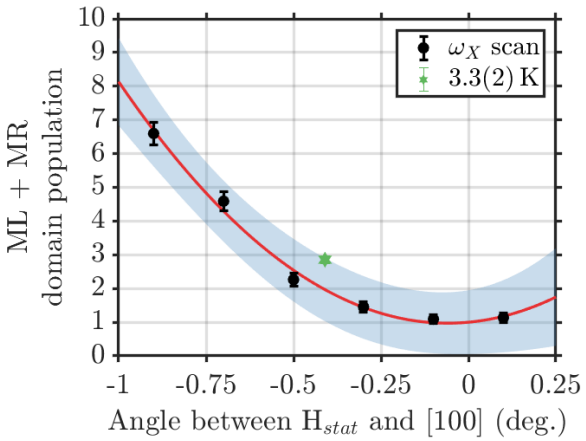

Figure 4.33: The integrated intensities of the ML and MR boxes marked in Fig. 4.31 as a function of the angle shift from a four-fold axis. The black point are data obtained from a static ω_X-scan performed at an temperature of 1.6 K and with the χ_X alignment being 1° off $\langle 100 \rangle$. The red line is a second order polynomial fit and the shaded area corresponds to a 95% confidence interval. The green star is the ratio between the dynamic and static measurements of the ML and MR intensities, as obtained at an applied field of 200 mT and a temperature of 3.3(2) K. The dynamic data was obtained with the Helmholtz coils and an AC field with a frequency of 4 Hz and an amplitude of 1.3%.

Gaussian function to extract an in-plane width. As such, it is not possible to correct for the instrument resolution in the same way it was for the UL and UR temperature scan data in Section 4.4.1. Using the uncorrected widths, a rough estimate for the long-range correlations of the ML and MR spots is $\xi_L = 1/(b_1 q) = 0.9(1)\,\mu$m, where $b_1 = 2\sqrt{2\ln 2}\sigma_1$ and $q = 0.0059(1)\,\text{Å}^{-1}$ is the mean distance to the centre of the stripey regions. The estimated longitudinal long-range correlation length of the ML and MR regions is thus shorter than the longitudinal short-range correlations reported for the UL and UR spots in Fig. 4.21. The estimated short-range correlation length of the ML and MR regions can similarly be estimated to be $0.19(3)\,\mu$m. While some added intensity could result from a minority domain, the correlation length analysis shows that the ML and MR intensities additionally posses some disordered, diffuse nature, likely being the result of a shearing of the lattice. In addition to the stripes of scattering observed between the UL and LL spots, a similar stripe of scattering is also observed between the TM and BM spots. This stripe cannot stem from minority domain, confirming that some of the intensity of the stripe features must come from other sources.

4.5 Summary

The dynamic behaviour of a pure ($RRR \approx 450$) niobium sample along a fourfold $\langle 100 \rangle$ symmetry axis was investigated via time-resolved SANS. From a static analysis, a number of structural vortex transitions resulting from the anisotropic Fermi surface of niobium was first identified. We identified a scalene-to-high-field square transition at an applied field of 327(3) mT from a field scan at 1.6 K, as well as a scalene-to-isosceles transition at 3.4(1) K from a temperature scan at 200 mT. Afterwards, dynamic SANS measurements were carried out across the structural transitions.

A small perpendicular AC field was used to push the vortices away from their equilibrium position, making it possible to measure the characteristic time scales of the FLL every time the field changed. Both a Helmholtz and a Maxwell coil configuration were used to induce the AC field. The dynamic behaviour observed via both coil configurations was found to be dramatically different from previous investigations of the niobium FLL [45]. This discrepancy was partially explained by employing anisotropic elasticity theory instead of the uniform ($\mathbf{k} = 0$) elasticity used to interpret the results of Ref. 45. However, our results also showed indications of non-elastic behaviour given the observed frequency dependence in the temperature scan. Another interesting phenomena was observed due to the numerous domains, which are present in niobium when the field is aligned along the fourfold direction. The different domains were observed to have differing time constants, with the majority domains possessing faster time scales than the minority domains. This again goes against a simple elastic picture where the all flux lines of the entire FLL is moving coherently together and instead indicates that flux lines in different parts of the samples are moving with different time scales.

A main goal of our investigations was to see whether the vortex lattice softened near structural phase transitions. Our data showed no indication of this. Instead the extracted time constants appeared to increase continuously and monotonously across the

Table 4.2: This table summarizes the main results from the experiments discussed in this chapter. Two of the experiments were performed for the scope of this work, while experiment V was carried out before the start of this thesis. The first half of the table lists sample properties and experimental parameters, while the second half describes the dynamic behaviour of the FLL observed in each of the experiments.

Experiment	**Exp H**	**Exp M**	**Exp V**	**Mühlbauer**
Reported in	This work	This work	This work	Ref. 45
Sample type	Niobium	Niobium	Vanadium	Niobium
RRR	450	450	50 - 100	1000
$\mathbf{H}_{\mathrm{stat}}$ alignment	$\langle 100 \rangle$	$\langle 100 \rangle$	$\langle 111 \rangle$	$\langle 110 \rangle$
AC frequency (Hz)	1-4	4	8	0.2
τ **vs. T**	Increasing	Increasing	Decreasing	Decreasing
τ **vs.** $\mathbf{H}_{\mathbf{stat}}$	Increasing	Increasing	Decreasing	Decreasing
Diffuse scattering in rocking curve?	yes	yes	no	no
Diffuse vertical streaks on detector?	yes	yes	no	no

phase transitions with increasing field and temperature.

A summary of our results and comparisons to other studies can be found in Table 4.2. It is evident that the temperature- and field-dependent behaviour of the time constants is unique to our experiment and is therefore likely a result of the orientation of the static field. The same can be said the the diffuse scattering, which has also only been observed in the present dynamic SANS measurements.

CHAPTER 5

METASTABLE STATES IN VANADIUM

5.1 Introduction

In this chapter, SANS and μSR investigations of the vortex phase diagram of impure vanadium samples are presented. The main motivation was to better understand the phase diagram of impure vanadium, which serves as a model system for understanding how impurities affect crystalline order in general. Specifically, we wanted to better understand the nature of the Bragg glass and vortex glass by measuring the vortex correlations near the order-to-disorder phase transition. We also wanted to better understand the metastable nature of the vortex glass by investigating how well the order of a disordered FLL can be restored by applying a perpendicular magnetic AC field.

Through a series of rocking curve SANS measurements of the vanadium sample with varying AC amplitudes, we managed to systematically show how applying a magnetic AC field can result in increased rocking curve intensities along with decreased rocking curve widths. It was observed that the restoring effect is stronger at lower temperatures, where temperature fluctuations are less likely to help the system escape from metastable states. The longitudinal correlations of the vortices were observed to decrease as the order-to-disorder line was approached, indicating that the vortex glass is dominated by short-range correlations.

The order-to-disorder line was mapped out via a series of field and temperature scans with a perpendicular oscillatory field applied to reach the ground state of the system. Overall, we found that the experimental order-to-disorder line did not appear to be consistent with a multidomain glass description. Unfortunately, the errors of the transition temperatures were too large to decisively determine whether the vanadium phase diagram contained a tricritical point. Complementary to the SANS investigations, μSR was also used to map out the phase diagram. The field distributions extracted from the μSR measurements attained negative skews in the vortex glass phase near the melting line. The peak effect lies in the negative skew region of the phase diagram, motivating a further survey of negative skew vortex distributions. This will be presented in Chapter 6.

In this chapter, Section 5.2 describes the results of three SANS investigations performed at three different facilities and with different sample setups. In Section 5.2.2, the results from a high-resolution SANS investigation of vanadium are presented revealing indicators of the Bragg glass phase. Section 5.2.3 illustrates how the oscillatory field can restore the order of the FLL and Section 5.2.4 then contains the SANS investigation of the vanadium phase diagram. Complementary μSR results are subsequently presented in Section 5.3.

5.2 SANS investigation of impure vanadium

Small-angle neutron scattering experiments were performed at the V4 instrument of the BER-II reactor of Helmholtz-Zentrum Berlin (HZB), at the SANS-1 instrument of the FRM-II reactor of Heinz Maier-Leibnitz Zentrum (MLZ), and at the D33 instrument of the high-flux reactor of Institut Laue-Langevin (ILL). The V4 and SANS-1 experiments were carried out on a single crystal cylindrical vanadium sample, the same sample investigated in Ref. 76. This sample is reported to display a Ginzburg-Landau parameter of $\kappa = 1.3$, a London penetration depth of $\lambda(T = 0) = 35\,\mathrm{nm}$, a coherence length of $\xi(T = 0) = 26\,\mathrm{nm}$,

a mean free path of $l = 48\,\mathrm{nm}$ and an impurity parameter of $a_i = 0.84\,\mathrm{nm}$ [76]. The mean free path can be related to the residual resistivity ratio (RRR), via the expression $l = m_{\mathrm{eff}} v_F / (\rho_T n_e e^2) RRR$, where m_{eff} is the effective electron mass, v_F the Fermi velocity, ρ_T the specific resistance at room temperature, n_e the density of conduction electrons, and e the electronic charge [163]. Given that we do not have exact resistivity measurements for our sample, we instead estimate its RRR value by comparing our sample characteristics with the values reported by Ref. 164 and thereby estimate a RRR in the range of $RRR \approx 50 - 100$. Our vanadium sample is thus more affected by impurities than our niobium sample of the previous chapter (Chapter 4), though critical current measurements on the vanadium sample are still consistent with weak pinning [76]. The current understanding of the vortex phase diagram of the cylindrical sample is depicted in Fig. 5.1, where sizeable Bragg and vortex glass phases are observed. The upper critical field, B_{c2} is modelled by the empirical expression [165]:

$$B_{c2}(T) = B_{c2}(0) \frac{1 - t^2}{1 + \frac{2}{3} t^{7/4}} \tag{5.1}$$

with an upper critical field of $B_{c2}(0) = 0.44\,\mathrm{T}$ and a critical temperature of $T_c = 5.31\,\mathrm{K}$. The critical temperature of the vanadium sample is thus lower than the value $5.47\,\mathrm{K}$ reported for pure vanadium [164], which is a result of the impurities in the sample. For the D33 experiment, a disk-shaped single-crystal vanadium sample cut from the cylindrical sample was measured. The dimensions of both samples are listed in Table 5.1.

Of the three experiments, the one performed at the SANS-1 instrument was the most extensive. This experiment was carried out in the parallel geometry, cf. Chapter 3. Full sets of rocking curves were measured by rotating the sample through the Bragg condition. The rocking curves were predominantly collected at field and temperatures close to the Bragg glass to vortex glass transition. The [111] crystal direction was roughly aligned along the static field and neutron beam direction. A smaller oscillating field was in

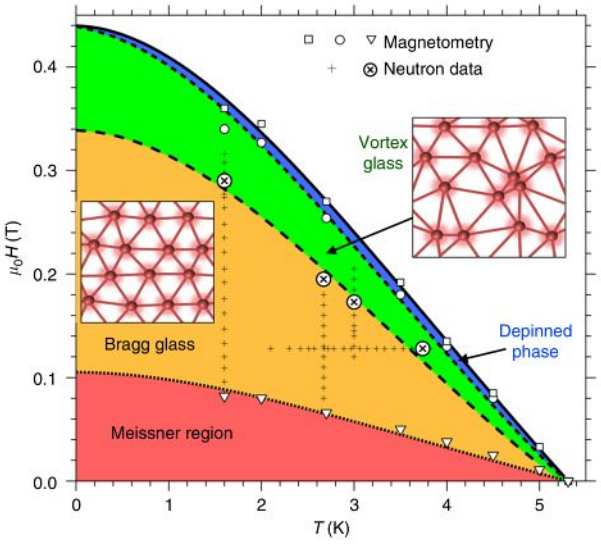

Figure 5.1: Phase diagram of the cylindrical vanadium sample from Ref. 76. The dotted and solid lines are the lower and upper critical fields, $B_{c1}(T)$ and $B_{c2}(T)$, while the two dashed lines mark the transitions to the vortex glass and vortex liquid, respectively. These two lines are fits based on the theory of Miktik and Brandt, Eq. (2.5) [89].

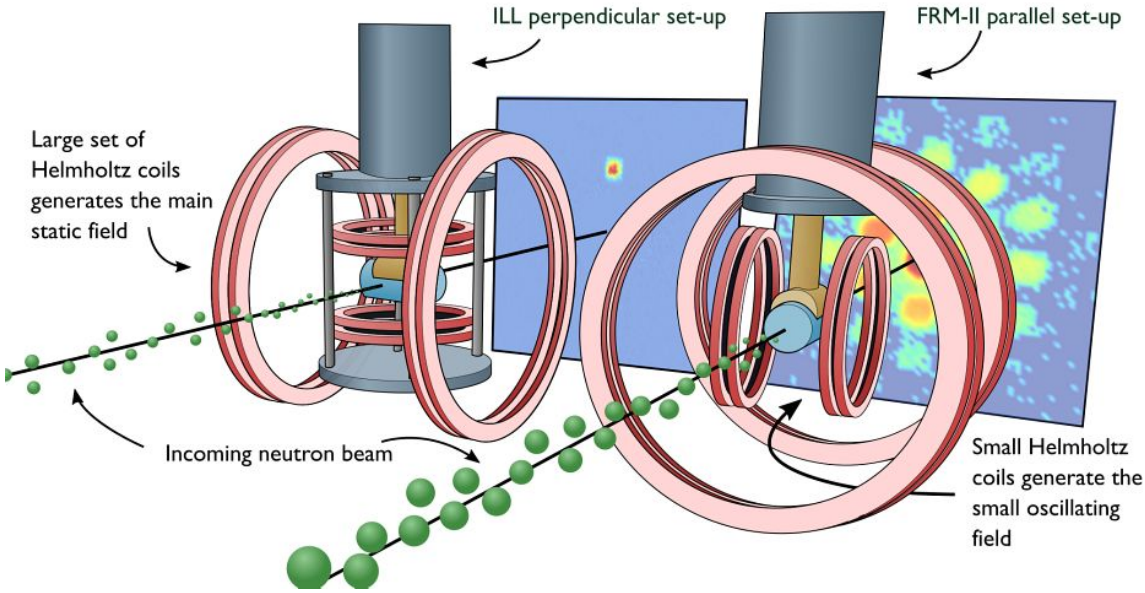

Figure 5.2: Illustration of the experimental geometries of the two main experiments performed with the ILL D33 and FRM-II SANS-1 instruments with perpendicular and parallel scattering setups, respectively. The sample is placed at the end of a sample stick, inserted into a cryomagnet and placed at the centre of two sets of Helmholtz coils; the large set of coils induce the static field that determines the direction of the vortex lines, and the smaller set of coils induces the perpendicular oscillating field. As is evident from the two representative detector images, the two different setups probe different correlations, as has been detailed in Section 3.1.2. The V4 experiment had an experimental geometry similar to the SANS-1 experiment.

some cases applied perpendicular to the main field during cooling, along the [110] crystal direction. The oscillating field was induced by applying sine-wave AC to a set of Helmholtz coils and was kept at a constant percentage of either 0.6%, 0.7%, 1.5%, or 2% of the main static field during field scans. Only a select few scans could be carried out with the 1.5% and 2% oscillating fields because these AC field strengths required manual cooling of the coils with liquid nitrogen to prevent runaway heating. The mentioned AC field amplitudes, and all following mentions of the AC amplitudes, correspond to peak to peak values. For the field scans, the sample was field cooled between each measurement in the following way. The sample was first heated to 7 K, the static magnetic field was then changed, and the AC field turned on. The sample was subsequently cooled down to the desired measurement temperature. Typically, cooling the sample from 7 K and down to a measurement temperature in the range of 0.5-4 K took about 10-20 min. The AC field was kept on while measuring, as was also done for the V4 and D33 experiments.

The setup of the V4 experiment was, in many ways, similar to the SANS-1 experiment. A [111] crystal direction was again aligned roughly along the beam and main static field direction, while a sine-wave oscillating field induced by Helmholtz coils was aligned along a [110] direction. The main difference was that different [111] directions were used for the alignment; in the SANS-1 experiment, the [111] direction along the long easy axis of the cylinder was used for the alignment, while a [111] direction in the plane of the cylinder was used for the V4 experiment. The point of the latter sample orientation was to try to achieve a similar demagnetization factor along both the static and oscillating field directions. Similar cooling rates were employed in this experiment as in the SANS-1 experiment.

Unlike the two other experiments with a parallel geometry, the D33 experiment was carried out in the perpendicular geometry. This setup is excellent for measuring the in-plane correlations of the Bragg glass, though it came at the cost of much longer counting times. The D33 setup could only fit the disk-shaped vanadium sample, which had a smaller sample volume than the cylindrical sample, thus resulting in a loss of intensity. Additionally,

the goal of the experiment was to characterize the intensity decay in the Bragg peak tails, which further warranted long counting times to gather sufficient statistics. In the two other experiments, each point of a rocking curve was counted for 30–120 s, while the D33 experiment necessitated counting times up to 20 mins. The magnetic field was in the D33 experiment still aligned along a [111] crystal direction, but perpendicular to the incoming neutron beam direction. Meanwhile, the Helmholtz-induced sine-wave oscillating field was in this case applied along the perpendicular $[11\bar{2}]$ direction. The scattering geometry is shown in Fig. 5.2 alongside the parallel scattering geometry used during the SANS-1 experiment. It generally took about 5 min to cool the sample from 7 K and down to the measurement temperature of 1.5 K, meaning that this experiment employed slightly faster cooling rates than the SANS-1 and V4 experiments.

Table 5.1 summarizes the full experimental details. During all three experiments the investigated sample was field cooled and the oscillating field, if used, was applied during the cooling. The angular resolution widths in the table have been estimated from $a \approx r_s/L_c$ [155], where r_s is the size of the source aperture and L_c is the collimation length. In the case of rectangular apertures, the larger side has been used for estimating the angular resolution. The equation gives the FWHM of the resolution in radians, while it has been converted to degrees in the table.

5.2.1 Peak shape and secondary crystallites

Despite the fact that we employed the same scattering geometry and measured the same vanadium sample at both V4 and SANS-1, the resulting rocking curve shapes differ slightly, cf. Fig. 5.3. The SANS-1 rocking curves display a clear shoulder, which is not apparent on the V4 rocking curves. The low angle-resolution of the V4 data makes it hard to ascertain whether the shoulder is a new feature or simply not resolvable. Such a feature is indicative of a secondary crystallite. It is possible that this effect was introduced in the sample due to an accidental drop at the end of the V4 experiment and prior to the SANS-1 and D33 experiments. Due to the secondary crystallite, parts of the sample may

Table 5.1: Details regarding instrument settings and sample geometries used during the SANS-1, V4 and D33 vanadium experiments. All three instruments employ 2D position sensitive detectors. The same cylindrical sample was used in the SANS-1 and V4 experiments. In the case of both samples, the [111] direction is perpendicular to the face of the sample. The final two rows list the investigated temperature and static field ranges.

Facility	**HZB**	**FRM-II**	**ILL**
Instrument	**V4**	**SANS-1**	**D33**
Year of experiment	2015	2016	2017
Scattering geometry	parallel		perpendicular
Sample shape	cylinder		disk
Sample dimensions	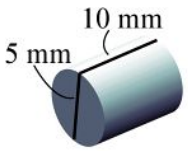		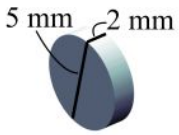
Static field orientation	[111]		[111]
AC field orientation	$[1\bar{1}0]$		$[11\bar{2}]$
Neutron wave length λ_n (Å)	10	6	8
$\Delta\lambda_n/\lambda_n$	0.1	0.1	0.1
Collimation (m)	16	20	10
Sample-to-detector distance (m)	16	20	10
Detector size (px^2)	120×112	128×128	128×128
Detector pixel size (mm^2)	8×8	8×8	5×5
Source aperture size (mm^2)	50×30	50×50	30×30
Sample aperture size	3 mm ⌀	$14 \times 9\,mm^2$	$2 \times 4\,mm^2$
Angular resolution width (deg).	0.18	0.14	0.17
Temperature range (K)	1.5	0.5 - 4.5	1.5
Field range (mT)	210-340	200 - 450	250 - 310

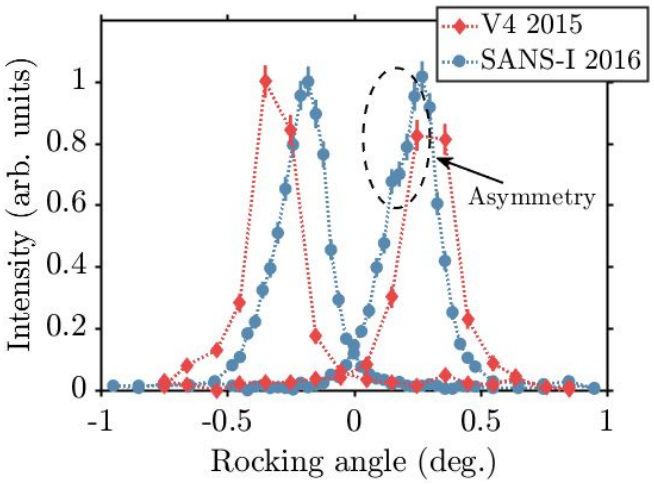

Figure 5.3: Comparison of two sets of rocking curves obtained measuring the same vanadium sample with the V4 instrument and the SANS-1 instrument. Both rocking curves were obtained with no oscillating field during field cooling and a static field of 290 mT at SANS-1 and 300 mT at V4. The sample temperature was 1.5 K and 1.6 K for the SANS-1 and V4 experiment, respectively. To ease comparison between the two sets of measurements, the intensity of all rocking curves has been normalized such that the two left rocking curves have a maximal intensity of 1.

have been out of alignment with respect to the applied field in subsequent experiments. Hence, given the anisotropic nature of vanadium [157], one should keep in mind that the drop could have affected the magnetic properties and phase diagram of the sample.

The secondary crystallite necessitates care with the rocking curve fits. In general, the SANS-1 data were taken with good enough resolution that a detailed characterization of the peak shape can be performed. Neutron and X-ray scattering investigations of samples exhibiting multiple crystallites, strain or incommensurate magnetic order often employ pseudo-Voigt functions to describe the peak shape. A Voigt function is a convolution of a Gaussian and Lorentzian function. It is used because instrumental contributions to peak broadening are usually Gaussian [155, 166] while broadening contributions from disorder and size distributions are often described by Lorentzians [167]. A pseudo-Voigt function makes it possible to approximate the Voigt function without performing the convolution. The first and most widely known pseudo-Voigt approximation is the Thompson-Cox-Hastings (TCH) profile function suggested by Thompson *et al.* [168]. According to their scheme, the Voigt function can be approximated by a linear combination of the Gaussian and Lorentzian functions:

$$V_p(x, \sigma_L, \sigma_G) = \eta L(x, \sigma_L) + (1 - \eta) G(x, \sigma_G) \tag{5.2}$$

where $G(x, \sigma_G)$ and $L(x, \sigma_L)$ are the normalized Gaussian and Lorentzian distributions:

$$G(x, \sigma_G) = \frac{1}{\sigma_G \sqrt{2\pi}} e^{-\frac{(x-x_{0G})^2}{2\sigma_G^2}}, \qquad L(x, \sigma_L) = \frac{1}{\pi} \frac{\sigma_L}{(x - x_{0L})^2 + \sigma_L^2} \tag{5.3}$$

with respective FWHMs defined as $\Gamma_G = 2\sqrt{2\ln 2}\sigma_G$ and $\Gamma_L = 2\sigma_L$. The parameters x_{0G} and x_{0L} are the centres of the distributions, and the parameter η from Eq. (5.2) is a mixing factor that determines the relative weights of the Gaussian and Lorentzian distributions. It is defined as:

$$\eta(\Gamma_G, \Gamma_L) = 1.36603 \left(\frac{\Gamma_L}{\Gamma}\right) - 0.47719 \left(\frac{\Gamma_L}{\Gamma}\right)^2 + 0.11116 \left(\frac{\Gamma_L}{\Gamma}\right)^3 \tag{5.4}$$

where Γ is the FWHM of the combined distribution, calculated as:

$$\Gamma = \left(\Gamma_G^5 + 2.69269\Gamma_G^4\Gamma_L + 2.42843\Gamma_G^4\Gamma_L^2 + 4.47163\Gamma_G^2\Gamma_L^3 + 0.07842\Gamma_G\Gamma_L^4 + \Gamma_L^5\right)^{1/5} \tag{5.5}$$

We have employed the TCH pseudo-Voigt function, as defined in Eq. (5.2) in our rocking curve fits. For the SANS-1 rocking curves, a double pseudo-Voigt was fitted to accommodate the shoulder of the peaks:

$$V_{p2}(x) = I_1 V_p(x, \sigma_G, \sigma_L) + I_2 V_p(x - x_{\text{dist}}, \sigma_G, \sigma_L) \tag{5.6}$$

where I_1 and I_2 determine the relative intensities of each pseudo-Voigt function, and x_{dist} is a parameter determining how far apart two pseudo-Voigt functions are placed, thereby quantifying the secondary crystallite offset. Fig. 5.4 shows a set of rocking curves from the SANS-1 experiment, along with fits based on double Gaussian, double Lorentzian and double pseudo-Voigt functions. It is evident that the best agreement between data and fit is achieved with the double pseudo-Voigt function. The double Gaussian fails to characterize the decay of intensity in the tail of the peak, while the double Lorentzian overestimates the intensity at the peak centre.

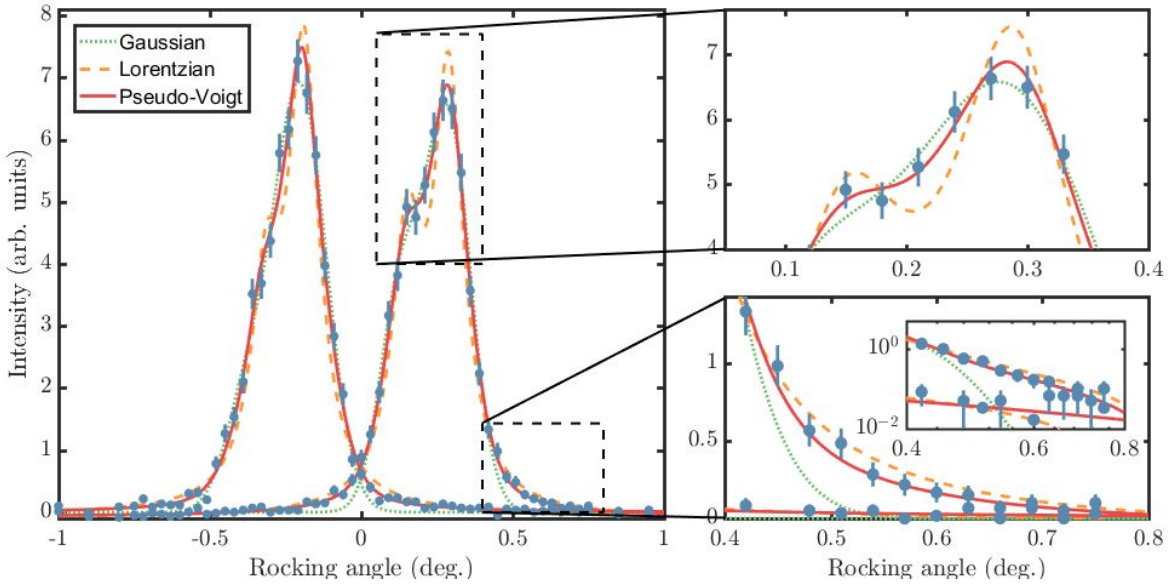

Figure 5.4: Depiction of how well different lineshapes agree with the asymmetric rocking curves obtained during the SANS-1 experiment with an applied static field of 340 mT and a temperature of 0.5 K. The different lineshapes are based on double Gaussian (dotted green lines), Lorentzian (dashed orange lines) and pseudo-Voigt (solid red lines) functions. A constant background term was included in all fits. The insets give a better view of the behaviour near the peak and tail of the right-sided rocking curve. The inset of the lower inset depicts the deacy of the intensity in the tail on a double logarithmic scale.

As one approaches the vortex glass transition, the Bragg peaks lose intensity. Fitting a multi-parameter function to low-statistics, noisy data can be difficult, as the fit easily diverges. One way of improving the fit is to limit the number of free parameters. Therefore, the widths of each pseudo-Voigt in V_{p2} have been fixed to be the same. The crystallite offset parameter x_{dist} was used as a free parameter when fitting peaks with high counts and fixed for low count peaks. In the latter case, a fixed offset of $\bar{x}_{\mathrm{dist}} = 0.143(5)^\circ$ was used, as has been determined from the two rocking curves in Fig. 5.4.

5.2.2 Bragg glass signature

Fig. 5.5 shows the high-resolution rocking curves obtained at the D33 instrument with the disk-shaped vanadium sample and applied fields of 250 and 310 mT at 1.5 K. For the sake of measuring as much of one of the tails as possible, the sample was deliberately inserted with a 3° alignment off the (112) plane from the vertical centre of the rocking

curve motor range. This limited us to just one of the two available first-order Bragg spots in the perpendicular configuration. Comparing the two rocking curves, it is evident that the intensity decreases dramatically with increased field strength. In some of the earlier SANS observations of the Bragg glass, for example in (K,Ba)BiO_3 [68], the field and temperature dependence of the rocking curve peak intensity was used as an identifier for the Bragg glass. However, as was pointed out in Ref. 69, this is at best an indirect indicator, because it was necessary to normalize the intensity data with a model-dependent form factor to make it agree with theory. Instead, one can use the peak shape as a more robust measure. In the left panel of Fig. 5.5, a power-law behaviour can be observed in the tails of the scattering peaks. This is consistent with what one would expect from a Bragg glass. Performing fits of the type, $I(\chi) = A\chi^{\zeta}$, it was possible to extract the two decay constants $\zeta = -1.9(3)$ and $-2.4(1)$ for the two applied fields. The quasi-long-range order therefore decays faster at higher fields, which is expected as the order-to-disorder line is approached. The decay constants are of the same order of magnitude as the predicted theoretical values of -2 to -1.86 [73]. Furthermore they are close to the decay constant determined for the vanadium sample of Ref. 76, where a value of -2.8 was measured using the same perpendicular scattering setup with an applied field of 180 mT and a temperature of 1.6 K. Thus, the presence of algebraic decay, and thereby the Bragg glass phase, has been evinced in the disk-shaped vanadium sample.

5.2.3 Restoring order with oscillatory fields

It is by now well-established that oscillating fields can heal the order of a FLL [169]. Oscillating fields increase interactions between vortices and thereby help them unsettle from metastable energy states. There is a large parameter space that can be explored concerning the oscillatory field, such as how the sample temperature and oscillating field amplitude affect its restorative abilities. Figs. 5.6 and 5.7 show measurements obtained at SANS-1 in the parallel geometry. Each panel consists of a set of rocking curves measured at specific applied static fields and temperatures under different oscillating field condi-

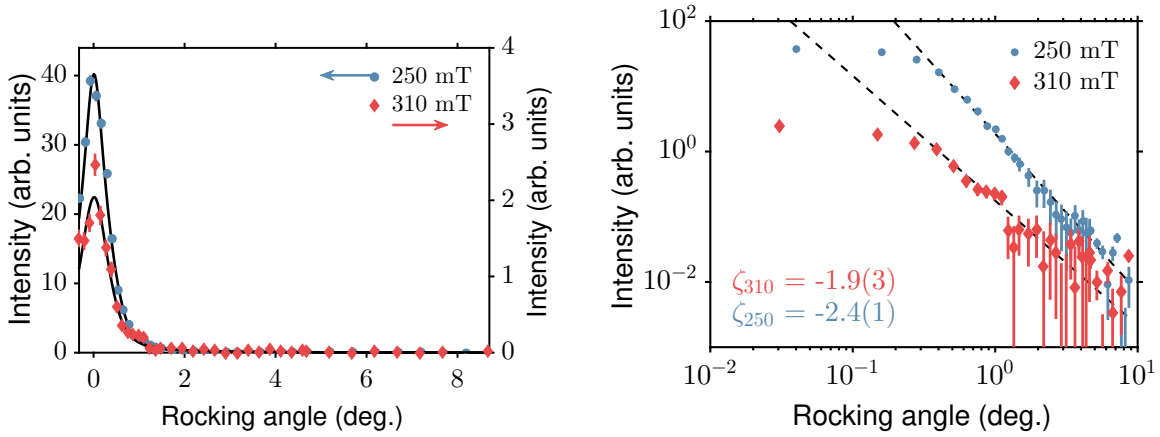

Figure 5.5: High-resolution rocking curves obtained with the perpendicular setup at D33. Both measurements were obtained at a temperature of 1.5 K and a perpendicular AC field applied. The AC frequency was 50 Hz, while the AC amplitude was 1.2% of the static field. **Left:** The rocking curves on a linear scale. Note the difference in intensity between the 250 mT (left axis) and the 310 mT (right axis) measurements. The solid lines are pseudo-Voigt fits, as defined in Eq. (5.2). **Right:** The same set of rocking curves depicted on double-logarithmic scale. The straight, dashed lines are power-law fits to the tail of the peaks. A 7 K background measurement was subtracted from both curves.

tions. It is immediately evident that the oscillatory fields help restore order in the sample, as can be observed from the overall higher peak intensity and reduced peak widths. In the panel with a sample temperature of 0.5 K and a static field of 400 mT, one does not observe any peaks in the diffraction data obtained without the oscillating field. In contrast, the diffraction data obtained with oscillating fields at 400 mT do exhibit peaks. The tails of the peaks collected with applied oscillating fields contain less spectral weight, which again implies an improved longitudinal order. We will see how the widths change later in this section.

The q-positions of the diffraction spots were determined by fittings 2D Gaussians to the integrated detector images. The q-values could subsequently be related to the Bragg angle via Eq. (3.2). The flux densities calculated based on the Bragg angles are shown in Fig. 5.8. We see that the data from field-scans performed at various temperatures all fall on one single line. A similar linear relation is seen in the V4 data, where the same sample and measurement geometry was employed, though there is a slight difference in the offset

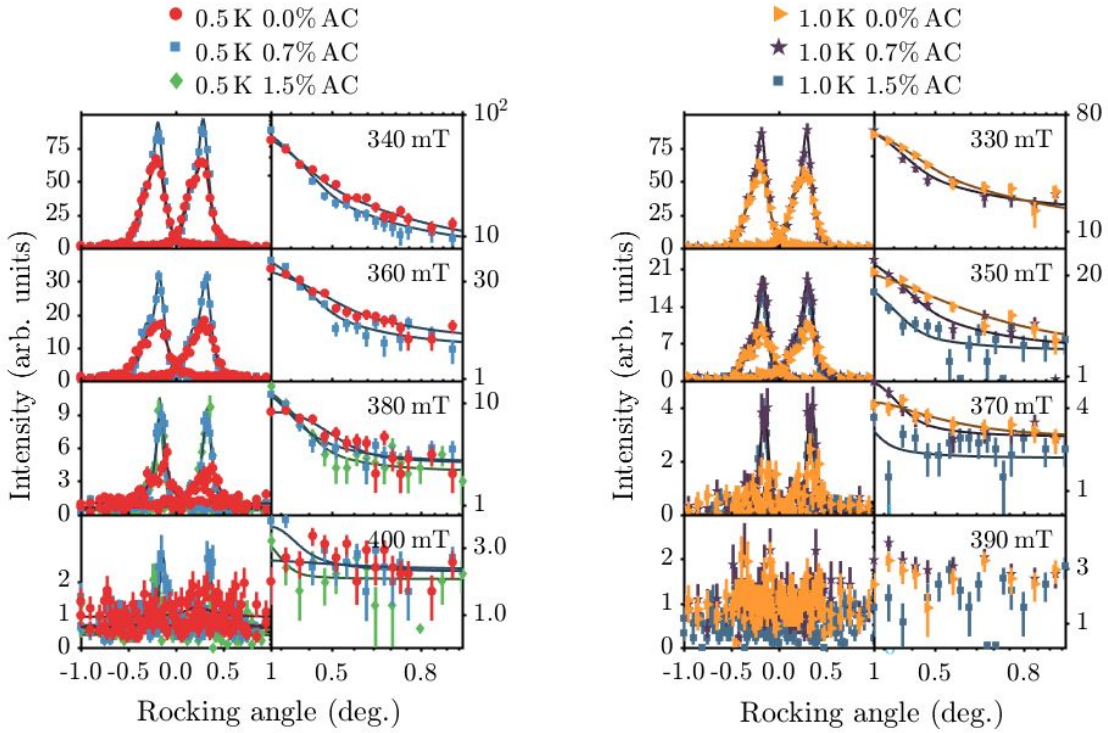

Figure 5.6: Rocking curves attained with the SANS-1 instrument in the parallel geometry with and without an oscillating field applied during the field cooling of the vanadium sample. The data in the left set of panels were collected with a sample temperature of 0.5 K and applied static fields in the range 340 mT–400 mT, while the data in the right set of panels were collected with a sample temperature of 1.0 K and fields in the range of 340 mT–390 mT. All solid lines are double pseudo-Voigt fits with added constant background terms. Adjacent panels show data for the same static field, with the left panels showing the data on a linear scale and the right panel showing the decay of the tails on a double-logarithmic scale. The legends at the top of each set of panels apply to all panels below, and the listed fields in the panels correspond to the applied field.

of the two fits.

Intensity results from a field scan is shown in Fig. 5.9. The integrated intensities of the rocking curves measured with SANS-1 were extracted via double pseudo-Voigt fits. Gaussian fits were used for the rocking curves obtained at V4 due to the limited rocking angle resolution. In both the SANS-1 and V4 data, the integrated intensity decreases with the induced field. The fitted rocking curve intensities for the SANS-1 0.0% AC field scan first become zero within errors at an induced field of 398 mT, as is also the case for the 1.5% AC data. The data collected with a 0.7% AC oscillating sine field extends the Bragg glass domain to an induced field of 418 mT, hence showing that the

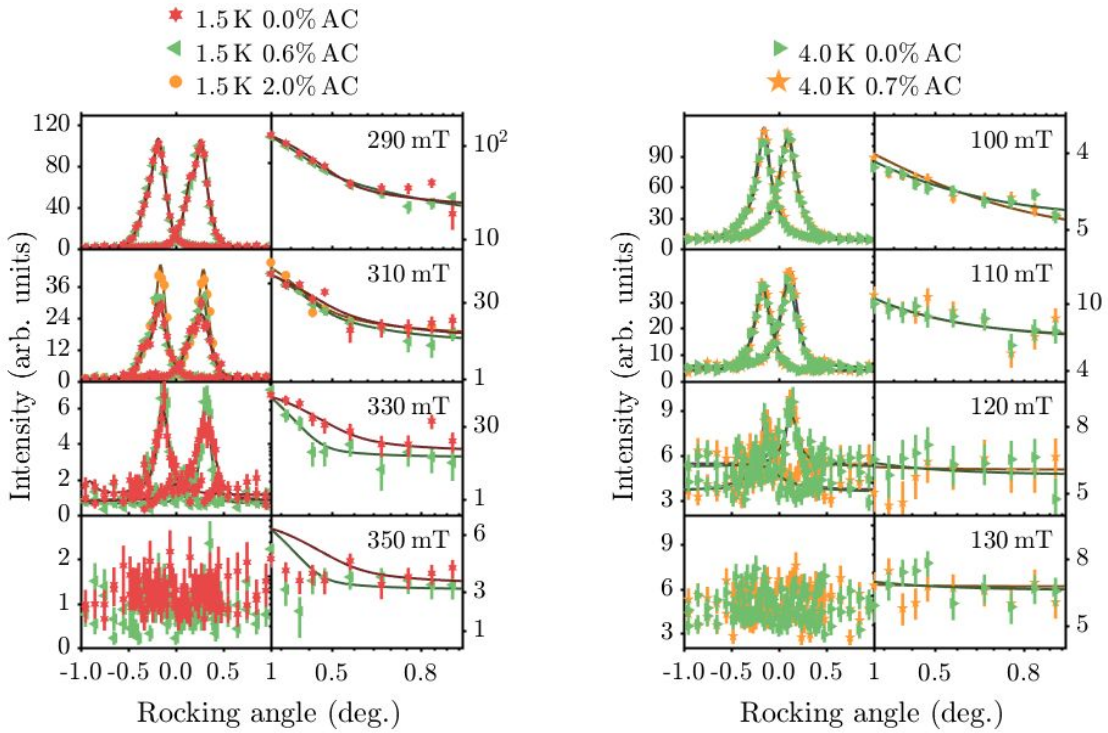

Figure 5.7: Rocking curves obtained like those in Fig. 5.6, now at sample temperatures of 1.5 K and 4 K and field ranges of 290 mT–350 mT and 100 mT–130 mT, respectively. The solid lines are double pseudo-Voigt fits with constant background terms.

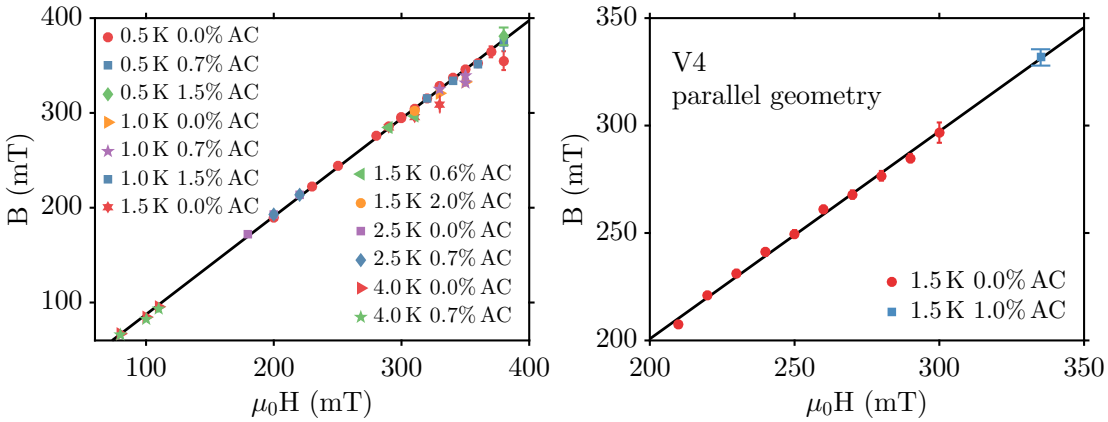

Figure 5.8: Induced field as a function of the applied field as calculated from the 2θ spot positions from the various scans of the SANS-1 (**left**) and V4 (**right**) experiments. The solid lines are linear fits to the data. The SANS-1 experiment had the relation, $B(H) = 1.034(1)\mu_0 H - 16(1)\,\mathrm{mT}$, between induced field and applied field, while the V4 experiment had the relation, $B(H) = 0.97(2)\mu_0 H + 8(6)\,\mathrm{mT}$.

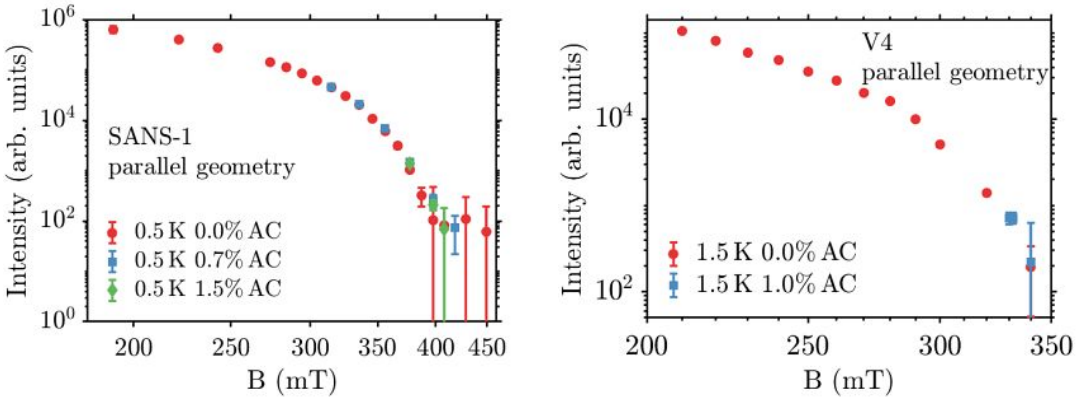

Figure 5.9: Integrated rocking curve intensities obtained with double pseudo-Voigt (left) and Gaussian (right) fits with constant background terms. The left panel shows the results of the SANS-1 experiment, while the right panel shows similar results from the V4 experiment.

AC field can improve the longitudinal order of the FLL. The V4 field scan was carried out at a slightly higher temperatures. In this case, the intensity is seen to become zero within errors at an induced field of 340 mT. The field dependence of the intensity is dependent on the SANS resolution compared to the length scale separating the random manifold regime from the Bragg glass phase. If the SANS resolution is smaller than this length scale, one expects a $B^{-1/2}$ dependence as expected for a perfect crystal. Having a SANS resolution larger than the length scale adds an extra $B^{-3/2}$ factor to the field dependence, as was observed in the first experimental investigations of the Bragg glass phase in (K,Ba)BiO_3 [68] and later in $La_{2x}Sr_xCuO_4$, ($x < 0.15$) [170]. Additionally, one needs to factor in the form factor of a single flux line [68]. This again highlights why *correlations* are better indicators for the existence of the Bragg glass, given that they are not dependent on normalizing with theoretical model-dependent expressions. In Fig. 5.9, it is seen that the field-dependence of the integrated intensities initially is linear on a double logarithmic scale for both the SANS-1 and V4 field scans. As the order-to-disorder transition is approached the intensities are observed to drop more sharply, as was also observed in Ref. 76.

Fig. 5.10 displays the spot characteristics of the SANS-1 data measured at 0.5 K. The

rocking curve width measure the correlations along the flux lines in the parallel setting. In the case of the SANS-1 rocking curves, the rocking curve width is determined as a combination of the Gaussian and Lorentzian widths, see Eq. (5.5). The widths of the 0.5 K 0% AC rocking curves already start to diverge at induced fields of 325 mT, while the oscillating fields restore longitudinal order and allow the monotonic decrease of the rocking curve width to persist for longer. The radial and azimuthal widths both increase with increased fields, indicating a collapse of translational order as the disorder transition is approached.

Fig. 5.11 depicts the radial and azimuthal spot widths extracted from the remaining field scans of the SANS-1 experiment. The induced fields have been normalized with respect to the upper critical field, as estimated from Eq. (5.1). As a result, the extracted spot widths appear to fall on one common line. The exception is the 4.0 K data, which display larger widths than other field scans at the same reduced flux densities. In general, there is no noticeable difference between the radial widths obtained with or without an AC field applied, indicating that the in-plane experimental resolution is not capable of resolving any possible improved translational order. As a result, the correlation analysis will focus on the longitudinal correlations, which the experimental geometry is optimized for.

We can estimate the longitudinal FLL correlations from the rocking curve and diffraction spot widths after they have been corrected for instrumental contributions. In the case of the SANS-1 rocking curves, the double-pseudo Voigt fits make it easy to identify the instrumental contribution to the total width, seeing as it should correspond to the Gaussian width. Meanwhile the Lorentzian width corresponds to the spread caused by the FLL. Employing the notation of Section 3.1.2, we can therefore identify the Lorentzian FWHM with b, $\Gamma_L = b$. The instrumental Gaussian rocking curve width consists of contributions from both the a and c, $\Gamma_G^2 = a^2 + c^2$. The longitudinal correlations lengths can therefore be estimated as:

$$\xi_L = \frac{2}{bq} \tag{5.7}$$

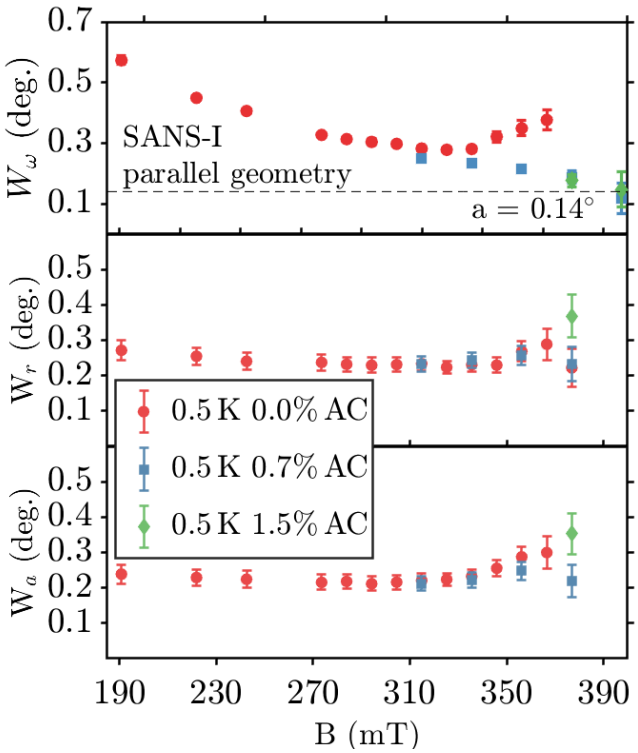

Figure 5.10: **Top**: The full rocking curve width extracted from the double-pseudo Voigt fits of the 0.5 K SANS-1 data. The rocking curve width is a combination of the Lorentzian and Gaussian widths, c.f. Eq. (5.5). **Middle** The radial width extracted from 2D Gaussian fits to the 0.5 K diffraction spots on the detector plane. **Bottom:** Azimutal widths of the diffraction spots, also obtained via 2D Gaussian fits to the 0.5 K diffraction spots.

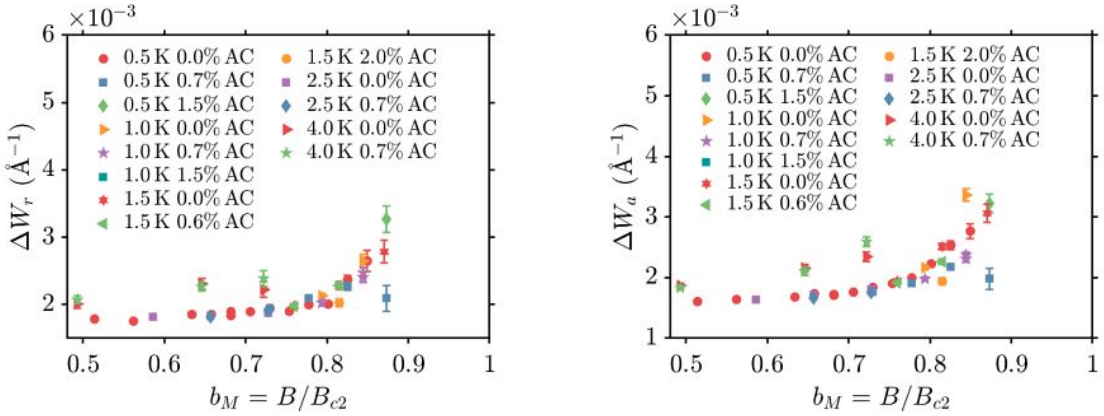

Figure 5.11: The radial and azimuthal widths of the SANS-1 diffraction spots as determined from 2D Gaussian fits to the detector integrated detector images.

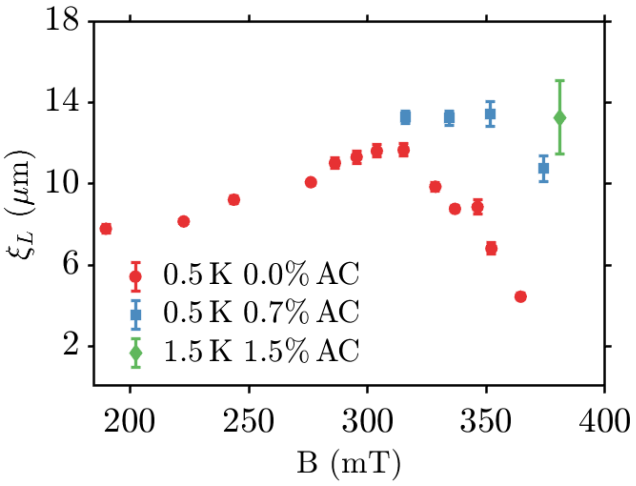

Figure 5.12: The FLL correlation lengths obtained by deconvoluting the instrumental contributions from the experimentally determined rocking curve width. The longitudinal correlation lengths have been estimated as according to Eq. 5.7.

where q is length of the scattering vector. The expression for the longitudinal correlation length can in some cases be observed to be off by a factor of two compared to the expression in Eq. 5.7. For example, the study in Ref. 122 employs the exact same expression as in Eq. 5.7, while the study in Ref. 162 employed the expression $\xi_L = 1/(bq)$. This difference comes down to whether one has related b to a Gaussian or Lorentzian FWHM. Fig. 5.12 displays the correlation lengths calculated based on the rocking curve and diffraction spot widths of Fig. 5.10. The longitudinal correlations decrease as the order-to-disorder transition is approached, indicating a collapse of longitudinal order. Both the 0.7% and 1.5% AC fields are seen to have restoring effects on the longitudinal correlation lengths.

Fig. 5.13 shows an investigation on the effect of changing the amplitude of the applied field. Due to time constraints, the D33 amplitude scan was carried out by just measuring the Bragg peak intensity and not the full rocking curve. The D33 intensities were therefore determined via a 2D Gaussian fit to the diffraction spot on the detector. In the case of both the D33 and SANS-1 data, we see that the intensity initially increases as the AC field amplitude is increased from 0 to 0.6% of the 310 mT main field. At higher AC field amplitudes the intensity starts to decay, indicating that the AC field is inducing disorder in the FLL. The effect is much stronger in the D33 data, which may be related to the differing demagnetization factors between the cylindrical sample of the ILL experiment

and the disk-shaped sample of the D33 experiment. The AC field was also applied along different crystallographic directions, which may play a role, given how Chapter 4 found that the anisotropic nature of low-κ superconductors can influence their dynamic properties. A similar peak was observed in AC amplitude scans by Moreno *et al.* in Ref. 123, cf. right panel of Fig. 5.13. They reason that an optimal AC field amplitude should induce temporary vortex displacements that are comparable to the equilibrium vortex spacing, a_0. The average vortex displacement, $\langle u \rangle$, can be estimated as [123]:

$$\langle u \rangle \approx \frac{1}{2} \frac{H_{AC}}{H_{DC}} r \tag{5.8}$$

where H_{AC} is the oscillating field, H_{DC} the static main field and r the sample radius. With a static applied field of 310 mT, as has been used for the amplitude scan in the right panel of Fig. 5.13, and a sample radius of 2.5 mm, the optimal oscillating field amplitude is in our case just 0.01%. However, the approximation in Eq. (5.8) may underestimate the optimal oscillating field amplitude, seeing as Moreno *et al.* found the optimal experimental value to be 5 times larger than predicted.

5.2.4 Exploring the phase diagram of impure vanadium

To date, there is no general, universally agreed upon vortex phase diagram for all type-II superconductors. The phase diagram of Fig. 2.1 is a commonly used phase diagram [67, 171, 172] in which the Bragg glass, vortex glass and vortex liquid all meet at a tricritical point. An alternative phase diagram was suggested by Menon in Ref. 85, where the Bragg glass and vortex liquid are always separated by a multidomain phase. Schematics of both phase diagrams are presented in Fig. 5.14.

For the sake of further clarifying the phase diagram of the cylindrical vanadium sample, we carried out several temperature scans at low fields to determine the behaviour close to the critical temperature. The measurements were performed at SANS-1 in the parallel geometry. The sample was first cooled down with no oscillating field to 1.2 K below the

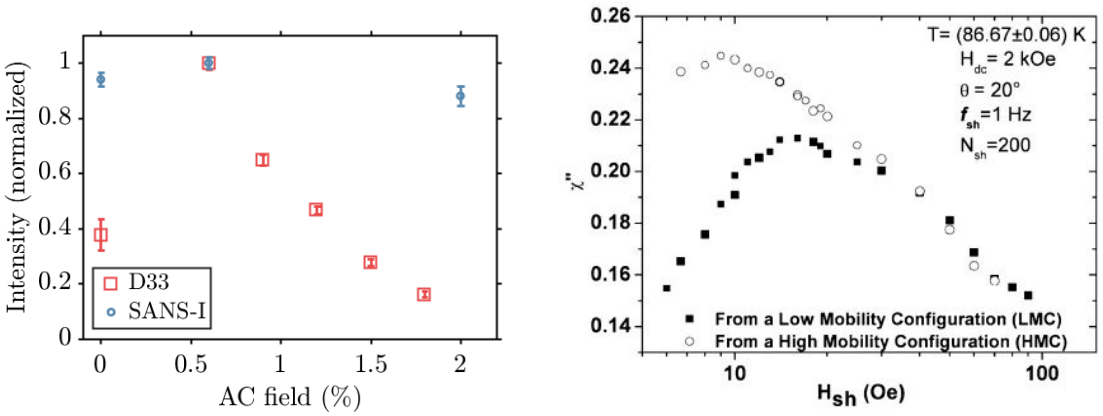

Figure 5.13: Left: Investigation of the effect of the amplitude of the oscillating field with data collected at D33 in the perpendicular geometry and at SANS-1 in the parallel geometry. Both data series have been collected with a sample temperature of 1.5 K and an applied field of 310 mT. A 10 Hz sine-wave was used for the signal generator during the SANS-1 experiment and a 50 Hz sine-wave during the D33 experiment. The data have been normalized with respect to the common point at 0.6% AC field amplitude. **Right:** AC susceptibility of the FLL in single crystal $YBa_2Cu_3O_7$ as a function of the oscillating field amplitude. A low mobility configuration corresponds to a disordered FLL that has been induced by applying an asymmetric AC field, while the high mobility configuration is a well-ordered FLL that has been induced by applying a symmetric AC field. From Ref. [123].

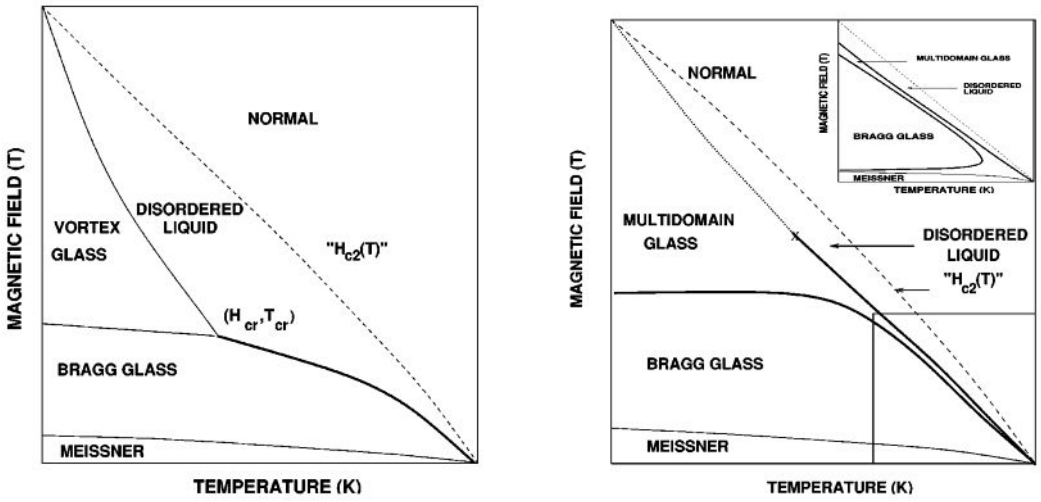

Figure 5.14: Left: The conventional view of the vortex phase diagram of type-II superconductors, similar to the ones presented in Fig. 2.1. Here the Bragg glass transitions directly into the vortex liquid at high temperatures and a multicritical point between the Bragg glass, vortex glass and vortex liquid phase exists at (T_{cr}, H_{cr}). **Right:** The multidomain glass phase diagram proposed as an universal vortex phase diagram by Menon in Ref. 85. According to this phase diagram the Bragg glass transitions to the vortex liquid via a two-step process, where the vortex glass (here interpreted as a multidomain phase) is an intermediate step. Both figures are from Ref. 85.

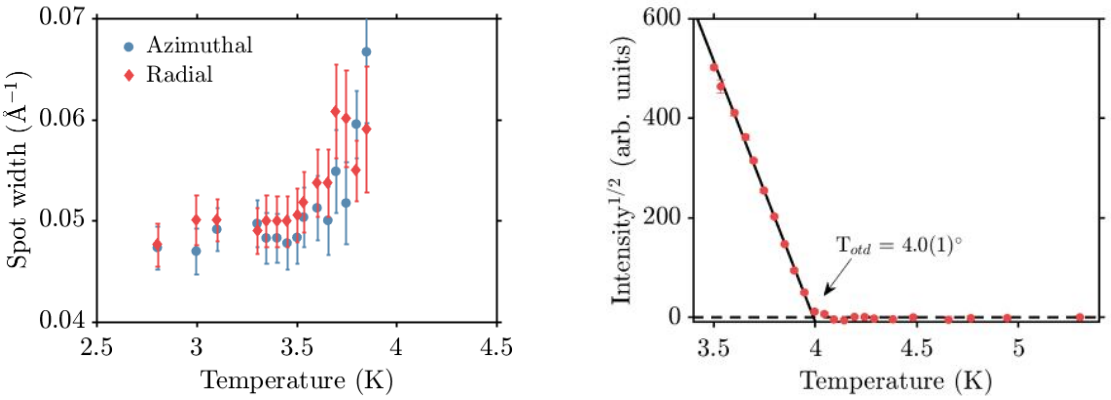

Figure 5.15: Detection of the order-to-disorder transition from warming temperature scans performed at SANS-1 in the parallel geometry. The figure shows data measured while heating with an applied static field of 120 mT and no oscillating field. **Left:** The radial and azimuthal widths of the top diffraction spot (TM), which measure the in-plane vortex correlations. **Right:** The square root of the intensity of the TM Bragg spot as a function of temperature. The sample was warmed up to 7 K. The intensity has been calculated by numerically summing all the intensity in a box enclosing the Bragg spot on the detector plane. The 7 K intensity was used as a background measurements and subtracted from the remaining data points. The solid line is a linear fit to the decaying scattering signal.

expected transition temperature. Subsequently, the sample was slowly warmed back up while measuring the intensity of the top middle Bragg peak (TM). The resulting spot widths were afterwards extracted by performing 2D Gaussian fits to the diffraction spots, while the intensity was found by numerically summing over the TM peak in the detector plane. Correlations lengths cannot be extracted for this data set due to the lack of measurements of full rocking curve widths. The temperature dependences of the spot width and intensity are shown in Fig. 5.15. As was the case for the field scan, the diffraction spot widths are seen to increase as the order-to-disorder line is approached. The transition temperature was determined by plotting the square root of the background-subtracted intensity and fitting a linear function to determine when the intensity reaches zero. The transition temperatures from the field scan are listed in Table 5.2. Based on the combined neutron scattering results from V4 and SANS-1, as well as the magnetometry and neutron scattering results from Ref. 76, a suggested vortex phase diagram has been constructed, cf. Fig. 5.16. The placement of the order-to-disorder phase transi-

$\mu_0 H$ (T)	T_{otd} (K)
0.08	4.4(2)
0.09	4.3(1)
0.1	4.2(2)
0.11	4.1(2)
0.12	4.0(1)
0.14	3.8(1)

Table 5.2: Transition temperatures of the order-to-disorder phase transition, as estimated for different applied fields in Fig. 5.15. Obtained from the SANS-1 experiment.

tion was determined by observing the points at which the SANS intensity went to zero. An equation similar to Eq. (2.5) was fit to the SANS-1 and V4 data to determine the order-to-disorder line. It is immediately apparent that the vortex glass phase takes up a much smaller part of our phase diagram than in Fig. 5.1 [76], despite the fact that both phase diagrams have been constructed from data on the same vanadium sample. At first, one may assume that this difference between new and old data could be caused by the intermittent drop of the sample and a subsequent change of the phase diagram, but the V4 data were collected before the drop and still seem to deviate from the Ref. 76 data. Another possible culprit is the FLL preparation routine employed for each experiment. For both the SANS-1 and V4 experiments, an AC field was applied to help improve the quality of the FLL, which was not done when collecting the Ref. 76 data. However, from our own data, we see that applying an AC field at 0.5 K only lifted the order-to-disorder transition by 20 mT, which is not enough to explain the difference. Especially so, because our experience shows that the AC field becomes less effective at higher temperatures, cf. Figs. 5.6 and 5.7. Another aspect of the preparation of the FLL is the cooling rate. The SANS-1 and V4 experiments were carried out with similar cooling rates, taking about 10-20 min to cool the sample from the normal state at 7 K to the measurement temperature. A different possible explanation is that in the years between the experiments of this thesis and Ref. 76, the sample has essentially been annealed at room temperature (in a time frame of roughly $\approx 2 \cdot 10^8$ s), meaning that the impurity properties might have changed.

In Ref. 85, the following expression is used to describe the Bragg glass-to-multidomain

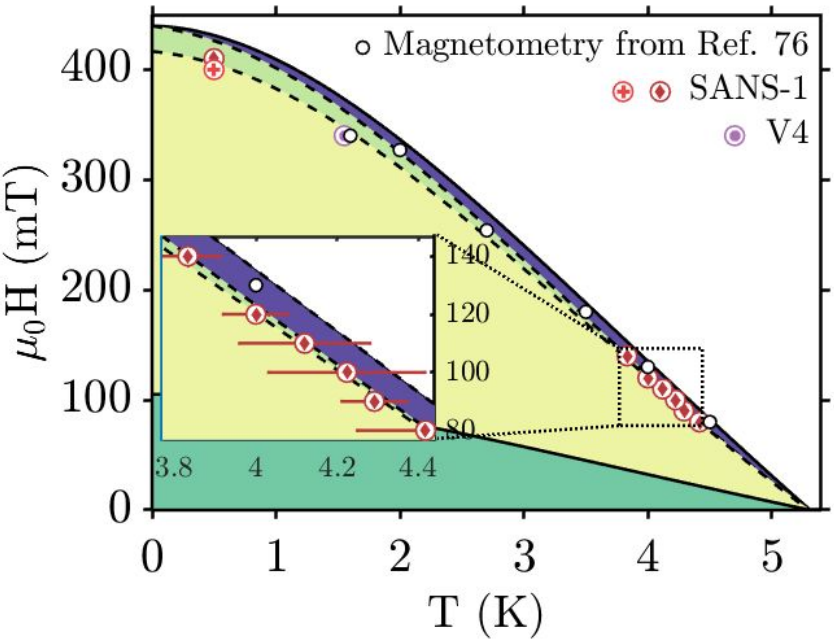

Figure 5.16: Vortex phase diagram of the cylindrical vanadium sample as determined from SANS measurements. Dark red data points depict the order-to-disorder transition as determined from SANS-1 data with an AC field applied during cooling. The one bright red data point depict the order-to-disorder transition as determined from the 0.0% AC field scan. The purple data point is from V4 and the data points with black outlines are magnetometry data from Ref. 76. The solid lines are the upper and lower critical fields. The dashed lines are the Bragg glass-to-vortex glass and vortex glass-to-vortex liquid transitions. The inset zooms in on the high-temperature part of the phase diagram.

transition:

$$\Sigma = \frac{b_M^3(1-t^2)^6}{(1-t^4)^2(1-t^2-b_M)^7} \tag{5.9}$$

where $b_M = B/B_{c2}$ and $t = T/T_c$ are the reduced fields and temperatures. The constant Σ is in Ref. 85 used as a fitting parameter. In the case of our phase diagram, the order-to-disorder phase transition line appears to be very close to the upper critical field at $t = 0$, which results in a large Σ value in Eq. (5.9). Large Σ values translates into almost linear phase transition lines [85], which does not agree with our phase diagram. However, when observing the insets of Fig. 5.16, the error bars from the temperature scan make it unclear whether a tricritical point exists in the phase diagram.

5.3 Muon spin rotation characterization of disordered vanadium vortex states

Muon spin rotational measurements on the cylindrical vanadium sample were collected at the General Purpose Surface-Muon Instrument (GPS) of the Swiss Muon Source of PSI, Switzerland. The μSR data was collected in 2014 and should be comparable to the SANS-1 and V4 SANS data and the vortex phase diagram from Fig. 5.16. The data was collected in the TF geometry, see Section 3.2.2, with the magnetic field applied along the crystallographic [111] direction of the vanadium sample. The experiment was performed by M. Laver, S. Samothrakitis and R. Toft-Petersen, who have provided the field distributions presented below. Therefore, the focus of the next sections will be on the interpretation of the field distributions and how they relate to the SANS measurements of Section 5.2, rather than the experimental procedure itself.

5.3.1 Field distributions

For illustrative purposes, an example of the raw μSR data from one of the positron detector banks is shown in Fig. 5.17. The time-binned data shows an initial spike, defining the

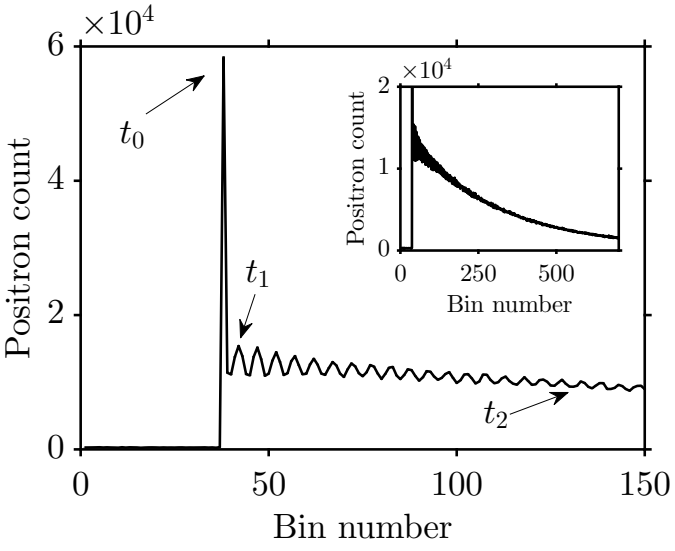

Figure 5.17: The time-binned positron counts recorded in the up detector when measuring with an applied field of 200 mT and a sample temperature of 1.5 K. The variable t_0 defines the time at which the muon enters the sample. Meanwhile t_1 and t_2 define the time period used for subsequent data analysis. The inset displays an out-zoom of the signal to highlight the exponential decay of the counts as a function of time.

time at which the muon enters the sample. Afterwards, an oscillatory signal is observed as a result of the muon precession in the sample. At large time-scales, the signal decays exponentially due to the finite muon lifetime. The two times t_1 and t_2 define a time-interval used for subsequent analysis, which starts after the muon has entered the sample and ends before the signal-to-noise ratio becomes significant. An asymmetry signal, $A(t)$, which is free from the effect of the finite muon lifetime is obtained by either dividing out the exponential decay or calculating the asymmetry between two orthogonal detector banks:

$$A_{UD}(t) = \frac{N_U(t) - N_D(t)}{N_U(t) + N_D(t)} \tag{5.10}$$

where $A_{UD}(t)$ in this case is the asymmetry between the number of counts in the up detector bank, $N_U(t)$, and the down detector bank, $N_D(t)$. Examples of asymmetry signals obtained above and below the critical temperature are depicted in Fig. 5.18. Above T_c all muons should precess coherently around a single uniform field direction, while the decaying features of the asymmetry signal measured below T_c is an indicator of an inhomogeneous internal field distribution. The asymmetry signal is then via an inverse Fourier transform converted into the frequency domain, thereby revealing the internal field distribution of the sample.

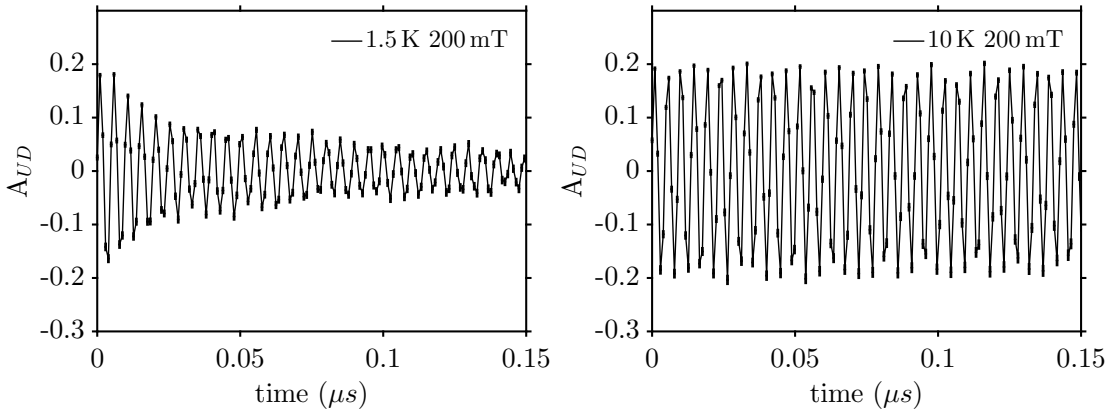

Figure 5.18: Asymmetry μSR signals obtained from the vanadium sample with an applied field of 200 mT and a sample temperature of 1.5 K (left panel) and 10 K (right panel).

Field distributions originating from temperature scans carried out at 30 mT, 110 mT, 200 mT and 290 mT are shown in Fig. 5.19. The skew parameter α, as defined in Chapter 2, has been calculated for each distribution:

$$\alpha = \frac{\langle \Delta B^3 \rangle^{1/3}}{\langle \Delta B^2 \rangle^{1/2}}, \qquad \langle \Delta B^m \rangle = \frac{\sum_j n(B_j)(B_j - \langle B \rangle)^m}{\sum_j n(B_j)} \tag{5.11}$$

Overall, the skew of the distributions appears to decrease with temperature. This indicates a departure from the isotropic equilibrium state with the characteristic field distribution of Fig. 2.3. Based on the skew of the μSR distributions, a new vortex phase diagram can be constructed as shown in Fig. 5.19. From the skew phase diagram, it is evident that the skew has a value of approximately 1 in the Bragg glass phase. Past the Bragg glass-to-vortex glass transition line, the skew rapidly drops and becomes negative. As the normal state is approached, the skew slightly recovers and attains a value of zero within two standard errors. This behaviour is clearly illustrated in Fig. 5.21, where temperature scans of the skew parameter α are shown for applied fields of 30 mT and 200 mT. Negative skewn distributions have already been reported in μSR measurements of the anisotropic superconductor $Bi_{2.15}Sr_{1.85}CaCU_2O_{8+\delta}$ [87]. In this study, the negative skew was argued to be a sign of three-body correlations and a disordered vortex state. A negative skew indicates a more common occurrence of high fields in the field distributions, implying a

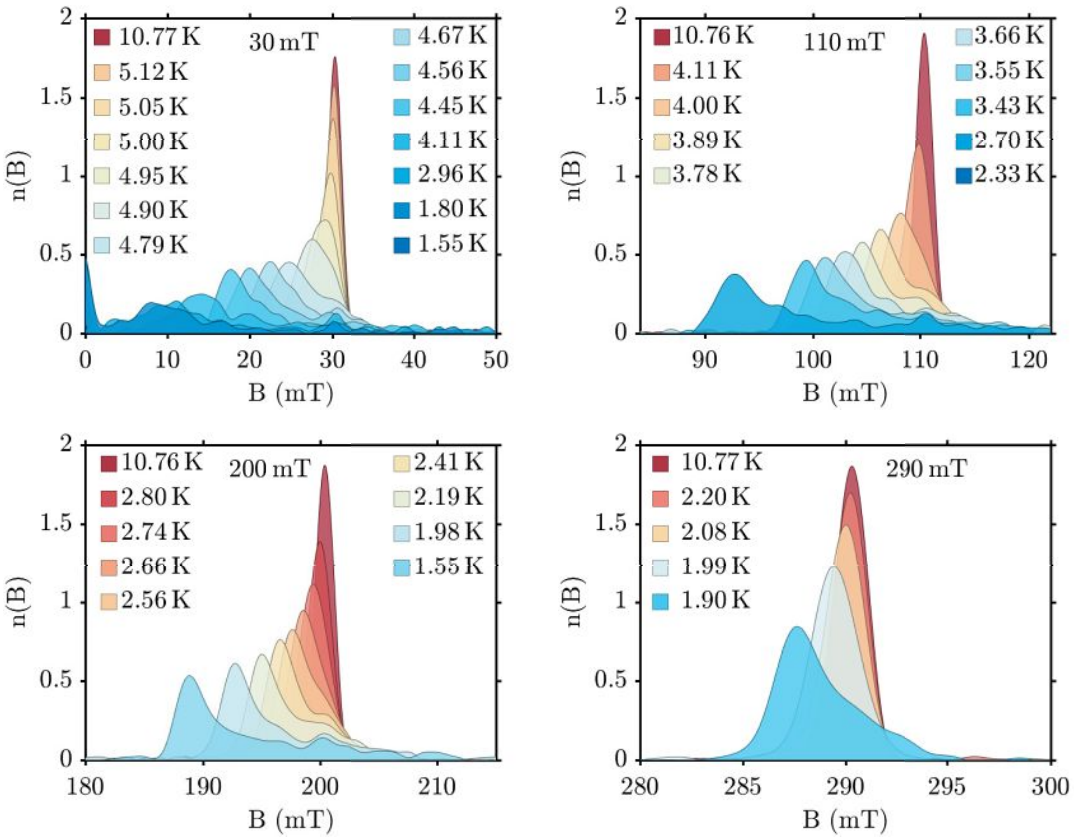

Figure 5.19: Field distributions measured at various fields and temperatures in the TF geometry.

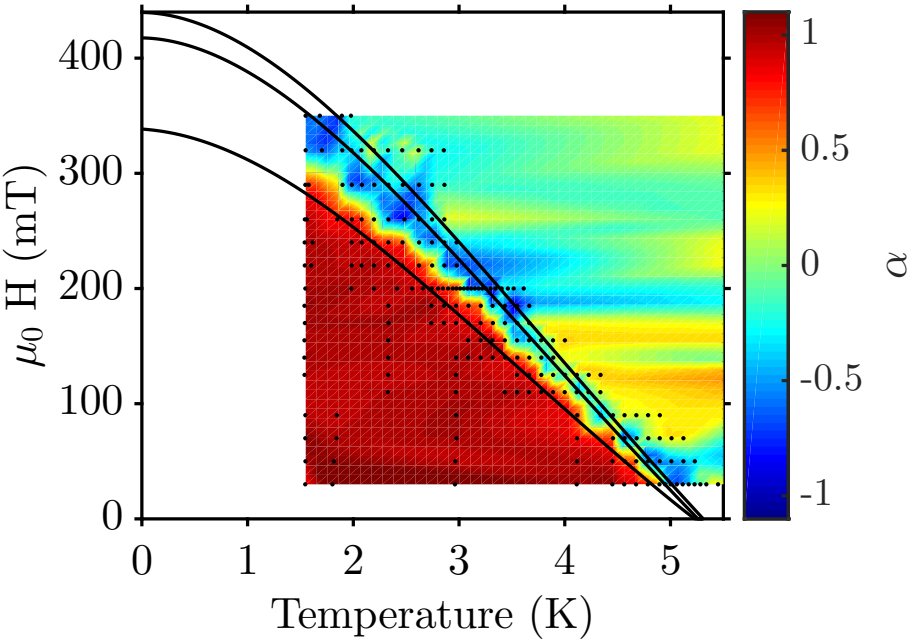

Figure 5.20: Skew μSR phase diagram of the cylindrical vanadium sample. Each black dot mark where a measurement was taken, while the three solid line from top to bottom mark the upper critical field, melting line transition and order-to-disorder transition. These lines are equivalent to the transition lines of Fig. 5.16. The apparent structures in the normal state are an artefact of the colour interpolation routine.

distortion of the vortex cores. The sliver of negative skew in the phase diagram coincides with the peak effect of the vanadium sample, which was observed at an applied field of 335 mT and a temperature of 1.6 K in Ref. 76. The peak effect is in Ref. 76 suspected to be mediated by thermal fluctuations, which locally distort the structure of the vortex cores.

5.4 Summary

SANS and μSR experiments have been used to investigate the vortex phase diagram of an impure vanadium sample. The aim was to explore the general phase diagrams of type-II superconductors. We observed that applying an AC field can help restore longitudinal order at low temperatures. This indicates that the glass state is metastable. Furthermore, we observed that the AC field did not result in significant changes in the rocking curves at temperatures above 1.5 K. Presumably the vortices can at these temperatures transverse

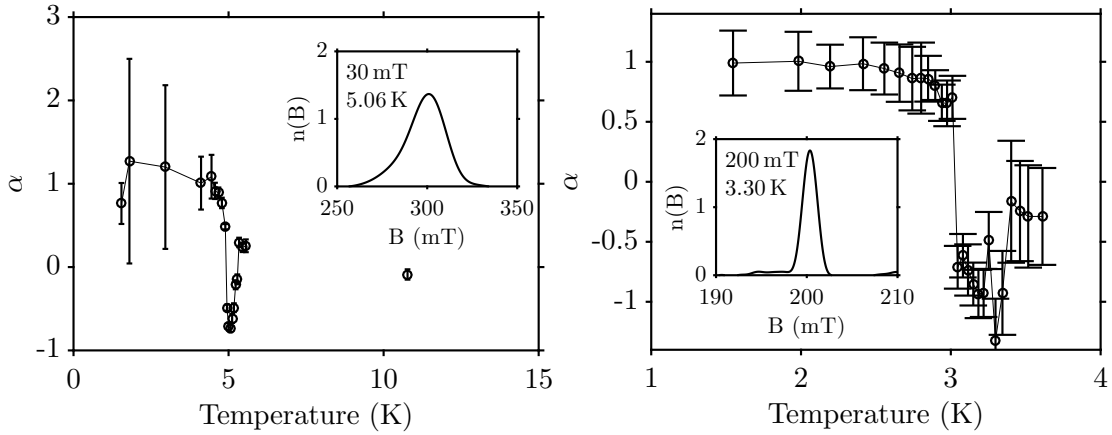

Figure 5.21: Temperature dependence of the skew parameter as calculated from field distributions measured with a static magnetic field of 30 mT (left) and 200 mT (right). The insets show the field distributions with the lowest skew for each applied field.

the pinning barriers via temperature fluctuations, making the AC field superfluous.

FLL correlation lengths were measured as a function of field, showing that the longitudinal correlations declined at high inductions as the order-to-disorder transition was approached. This indicates that the vortex glass is indeed dominated by short-range order correlations. The phase diagram of vanadium was explored more extensively by performing a number of temperature scans at low inductions. Based on our data, it was possible to draw a phase diagram that did not quantitatively resemble the suggested multi-domain vortex phase diagram of Ref. 85. However, the larger error bars on the transition temperatures makes it hard to truly ascertain whether the phase diagram contains a tricritical point.

The μSR results revealed that the asymmetry parameter of the local field distributions, also referred to as the skew, becomes negative deep in the vortex glass region close to the vortex liquid phase. The peak effect measured in Ref. 76 is also observed to coincide with the negative skew region. In the next chapter, we will further investigate the implications of the negative skew.

CHAPTER 6

GINZBURG-LANDAU SIMULATIONS OF THE VORTEX LATTICE

6.1 Introduction

Numerical methods are often employed to investigate pinning effects, especially with the intent of optimizing the critical current via the pinning landscape [173, 110]. In this chapter, we use the time-dependent Ginzburg-Landau (TDGL) equations to numerically continue the investigation of negative skew μSR field distributions initiated in Chapter 5. Instead of modelling realistic pinning landscapes, as is the usual approach, we use the pinning sites as a mean of controlling the vortex positions in our simulations. In this way, we can use the TDGL equations to explore relatively simple systems of just a few vortices and qualitatively observe the behaviour of the vortex cores when exposed to pinning-induced frustration. Through the guided movement of the pinning sites, we explore the necessary conditions for negative skew distributions to occur.

We have implemented the simulations in MATLAB and C. The coupled set of equations from Eq. (1.19) have been employed rather than the infinite-λ approximation of Eq. (2.9), because we are interested in the behaviour of low-κ superconductors. The simulations are carried out on two-dimensional, finite-element, rectangular grids with periodic boundary conditions.

Section 6.2 describes the specific implementation of the TDGL equations used in this work, while Section 6.3 details the result of manipulating the positions of the pinning potentials to achieve a negative skew. We observe negative skews in severely positionally disordered vortex states *as well as* in vortex states that retain their positional disorder while simultaneously exhibiting locally distorted vortex cores.

6.2 Time-dependent Ginzburg-Landau simulations

6.2.1 Implementation of the algorithm

The TDGL equations presented in Section 1.2.4 are first nondimensionalized through the scaling relations [174]:

$$\begin{aligned}
&\mathbf{r} = (x, y) = (\lambda x', \lambda y'), && \psi = \psi_0 \psi' = \sqrt{\frac{a_{\mathrm{GL}}}{b_{\mathrm{GL}}}}\psi', && t = \tau_n t' = \frac{\xi^2}{D} t' \\
&\mathbf{A} = \frac{h}{e^* \xi}\mathbf{A}', && \mathbf{B} = \frac{\hbar}{\lambda \xi e^*}\mathbf{B}' = \sqrt{2}B_c\mathbf{B'}, && \sigma = \sigma_n \sigma' = \frac{1}{\mu_0 D \kappa^2}\sigma', \\
&\mathbf{j}_s = \frac{\hbar}{\mu_0 \lambda^2 \xi e^*}\mathbf{j}_s' &&&&
\end{aligned} \tag{6.1}$$

where the primed variables are unitless. As a reminder from Chapter 1, $\psi(\mathbf{r}) = |\psi(\mathbf{r})|e^{i\theta(\mathbf{r})}$ is the superconducting order parameter, where $|\psi(\mathbf{r})|^2$ is proportional to the Cooper pair density and $\theta(\mathbf{r})$ is the corresponding phase. $\mathbf{A}(\mathbf{r})$ and $\phi(\mathbf{r})$ are the magnetic and electric potentials, $\mathbf{B}(\mathbf{r}) = \nabla \times \mathbf{A}(\mathbf{r})$ is the induced magnetic field, and $\mathbf{j}_s = \nabla \times \nabla \times \mathbf{A}$ is the supercurrent. D is a diffusion constant, σ a field relaxation constant, and e^* is the charge of a Cooper pair. The parameters a_{GL} and b_{GL} are GL parameters that can be calculated through BCS theory [5]. The field relaxation constant affect how fast the simulated FLL respond to perturbations such as changes in the pinning potential. As we are only interested in properties of static vortex configuration, the exact value of the field constant is of less importance and has constantly been kept at a value of $\sigma' = 10$ as in

Ref. 114. Shedding the primes from the variables, the nondimensionalized form of the TDGL equations is [114, 174]:

$$\frac{\partial\psi}{\partial t} + i\phi\psi = \psi - |\psi|^2\psi - \left(i\frac{1}{\kappa}\nabla + \mathbf{A}\right)^2\psi \tag{6.2}$$

$$-\sigma\left(\frac{\partial\mathbf{A}}{\partial t} + \frac{1}{\kappa}\nabla\phi\right) = \nabla\times\nabla\times\mathbf{A} + |\psi|^2\mathbf{A} + \frac{i}{2}\frac{\xi}{\lambda}\left(\psi^*\nabla\psi - \psi\nabla\psi^*\right) \tag{6.3}$$

We chose to work in the often used *zero-electric potential gauge* [175], which further simplifies the equations by eliminating the electric field altogether [174, 41]:

$$\frac{\partial\psi}{\partial t} = \psi - |\psi|^2\psi - \left(i\frac{1}{\kappa}\nabla + \mathbf{A}\right)^2\psi \tag{6.4}$$

$$-\sigma\frac{\partial\mathbf{A}}{\partial t} = \nabla\times\nabla\times\mathbf{A} + |\psi|^2\mathbf{A} + \frac{i}{2}\frac{\xi}{\lambda}\left(\psi^*\nabla\psi - \psi\nabla\psi^*\right) \tag{6.5}$$

These two equations form the basis of our numerical investigations. The essential idea of the simulation scheme is to approach an equilibrium FLL state via iterative time-integrated steps, as is customary for Runge-Kutta schemes. The step from a FLL state k, characterized by the order potential $\psi^k(x,y)$ and vector field components $A_x^k(x,y)$ and $A_y^k(x,y)$, to a new state $k+1$ a time period Δt later, characterized by $\psi^{k+1}(x,y)$, $A_x^{k+1}(x,y)$ and $A_y^{k+1}(x,y)$, is calculated via the equations:

$$\begin{aligned}\psi^{k+1}(x,y) = \psi^k(x,y) + \Delta t\Bigg[&\frac{1}{\kappa^2}\left(\nabla_x^2\psi^k(x,y) + \nabla_y^2\psi^k(x,y)\right) - \frac{i}{\kappa}\left(2A_x^k(x,y)\nabla_x\psi^k(x,y)\right.\\ &+2A_y^k(x,y)\nabla_y\psi^k(x,y) + \psi^k(x,y)\nabla_x A_x^k(x,y) + \psi^k(x,y)\nabla_y A_y^k(x,y)\Big)\\ &-\left((A_x^k(x,y))^2 + (A_y^k(x,y))^2\right)\psi^k(x,y) - \left(|\psi^k(x,y)|^2 - 1\right)\psi^k(x,y)\Bigg]\end{aligned} \tag{6.6}$$

$$\begin{aligned}A_x^{k+1}(x,y) = A_x^k(x,y) - \frac{1}{\sigma}\Delta t\Bigg[&\frac{i}{2\kappa}\left((\psi^k(x,y))^*\nabla_x\psi^k(x,y) - \psi^k(x,y)\nabla_x(\psi^k(x,y))^*\right)\\ &+|\psi^k(x,y)|^2A_x^k(x,y) + \nabla_y\nabla_x A_y^k(x,y) - \nabla_y^2A_x^k(x,y)\Bigg]\end{aligned} \tag{6.7}$$

$$\begin{aligned}A_y^{k+1}(x,y) = A_y^k(x,y) - \frac{1}{\sigma}\Delta t\Bigg[&\frac{i}{2\kappa}\left((\psi^k(x,y))^*\nabla_y\psi^k(x,y) - \psi^k(x,y)\nabla_y(\psi^k(x,y))^*\right)\\ &+|\psi^k(x,y)|^2A_y^k(x,y) + \nabla_x\nabla_y A_x^k(x,y) - \nabla_x^2A_y^k(x,y)\Bigg]\end{aligned} \tag{6.8}$$

which are simply the discretized versions of Eqs. (6.4) and (6.5). Here Δt is the discretized time step, and x and y are the nondimensionalized spatial coordinates. The unit cell of the simulation is defined as a two-dimensional rectangular grid with side lengths L_x and L_y, an area of $|\Omega| = L_x \times L_y$ and $N = N_x \times N_y$ cells. The width of each cell is defined as $\mathrm{d}x$ and $\mathrm{d}y$ in the x- and y-direction, respectively. The spatial derivatives of ψ^k are calculated employing the following gauge-invariant modified Euler scheme [114, 176]:

$$\nabla_x \psi^k(x,y) = \frac{\psi^k(x+\mathrm{d}x,y) - \psi^k(x-\mathrm{d}x,y)}{2\,\mathrm{d}x} \tag{6.9}$$

$$\nabla_y \psi^k(x,y) = \frac{\psi^k(x,y+\mathrm{d}y) - \psi^k(x,y-\mathrm{d}y)}{2\,\mathrm{d}y} \tag{6.10}$$

$$\nabla_x^2 \psi^k(x,y) = \frac{\psi^k(x+\mathrm{d}x,y) + \psi^k(x-\mathrm{d}x,y) - 2\psi^k(x,y)}{\mathrm{d}x^2} \tag{6.11}$$

$$\nabla_y^2 \psi^k(x,y) = \frac{\psi^k(x,y+\mathrm{d}y) + \psi^k(x,y-\mathrm{d}y) - 2\psi^k(x,y)}{\mathrm{d}y^2} \tag{6.12}$$

and similarly so for the spatial derivatives of the vector potential. The mixed second order derivatives appearing in Eqs. (6.7) and (6.8) originate from $\nabla \times \nabla \times \mathbf{A}$. The field is applied perpendicular to the simulation unit cell, meaning that only the z-component of the internal field will be finite, $\mathbf{B} = (0, 0, B)$. As a consequence, the vector potential only possesses finite x- and y-components, and the components of $\nabla \times \mathbf{A}$ and $\nabla \times \nabla \times \mathbf{A}$ are then:

$$\nabla \times \mathbf{A} = \begin{pmatrix} 0 \\ 0 \\ \nabla_x A_y - \nabla_y A_x \end{pmatrix}, \qquad \nabla \times \nabla \times \mathbf{A} = \begin{pmatrix} \nabla_y \nabla_x A_y - \nabla_y^2 A_x \\ \nabla_x \nabla_y A_x - \nabla_x^2 A_y \\ 0 \end{pmatrix} \tag{6.13}$$

Numerically, the mixed second order derivatives $\nabla_x \nabla_y A_x$ and $\nabla_y \nabla_x A_y$ are estimated as:

$$\begin{aligned}\nabla_x \nabla_y A_x^k = \frac{1}{4\,\mathrm{d}x\,\mathrm{d}y} \big[& A_x^k(x+\mathrm{d}x, y+\mathrm{d}y) - A_x^k(x-\mathrm{d}x, y+\mathrm{d}y) \\ & - A_x^k(x+\mathrm{d}x, y-\mathrm{d}y) + A_x^k(x-\mathrm{d}x, y-\mathrm{d}y) \big] \end{aligned} \tag{6.14}$$

$$\begin{aligned}\nabla_y \nabla_x A_y^k = \frac{1}{4\,\mathrm{d}x\,\mathrm{d}y} \big[& A_y^k(x+\mathrm{d}x, y+\mathrm{d}y) - A_y^k(x-\mathrm{d}x, y+\mathrm{d}y) \\ & - A_y^k(x+\mathrm{d}x, y-\mathrm{d}y) + A_y^k(x-\mathrm{d}x, y-\mathrm{d}y) \big] \end{aligned} \tag{6.15}$$

Thus, the presence of the mixed second order derivatives means that the update of each cell requires information from all neighbouring cells, including the diagonal neighbours. To ensure the periodicity of the order parameter, the following boundary conditions are imposed:

$$\boldsymbol{\psi}^k(0, y_{\mathrm{int}}) = \boldsymbol{\psi}^k(N_x, y_{\mathrm{int}}) \cdot \exp\left(-\frac{i \cdot (y_{\mathrm{int}} + 0.5) \cdot \mathrm{d}y \cdot \Phi}{2L_x} \right) \tag{6.16}$$

$$\boldsymbol{\psi}^k(N_x + 1, y_{\mathrm{int}}) = \boldsymbol{\psi}^k(1, y_{\mathrm{int}}) \cdot \exp\left(\frac{i \cdot (y_{\mathrm{int}} + 0.5) \cdot \mathrm{d}y \cdot \Phi}{2L_x} \right) \tag{6.17}$$

$$\boldsymbol{\psi}^k(x_{\mathrm{int}}, 0) = \boldsymbol{\psi}^k(x_{\mathrm{int}}, N_y) \cdot \exp\left(-\frac{i \cdot (x_{\mathrm{int}} + 0.5) \cdot \mathrm{d}x \cdot \Phi}{2L_y} \right) \tag{6.18}$$

$$\boldsymbol{\psi}^k(x_{\mathrm{int}}, N_y + 1) = \boldsymbol{\psi}({}^k x_{\mathrm{int}}, 1) \cdot \exp\left(\frac{i \cdot (x_{\mathrm{int}} + 0.5) \cdot \mathrm{d}x \cdot \Phi}{2L_y} \right) \tag{6.19}$$

Here $x_{\mathrm{int}} = 0, 1, \cdots, N_x + 1$ and $y_{\mathrm{int}} = 0, 1, \cdots, N_y + 1$ are indices used to refer to the various elements stored in $\boldsymbol{\psi}^k$, $\mathbf{A}_x^k$ and $\mathbf{A}_y^k$. Note that the bold font type is used to separate the finite-element matrices used in the simulations from their equivalent scalar functions, i.e. $\boldsymbol{\psi}^k(x_{\mathrm{int}}, y_{\mathrm{int}}) = \psi^k((x_{\mathrm{int}} + 0.5) \cdot dx, (y_{\mathrm{int}} + 0.5) \cdot dy)$. The parameter $\Phi = 2\pi n$ is the reduced magnetic flux, where n is the number of vortices in the sample. The cells $\boldsymbol{\psi}^k(0, y_{\mathrm{int}})$, $\boldsymbol{\psi}^k(N_x + 1, y_{\mathrm{int}})$, $\boldsymbol{\psi}^k(x_{\mathrm{int}}, 0)$, and $\boldsymbol{\psi}^k(x_{\mathrm{int}}, N_y + 1)$ are not included in the simulated unit cell, but instead make up a virtual border, cf. Fig. 6.1. The boundary conditions ensure that the total phase change along the border of the unit cell is $2\pi n$. Thus, since the phase change around every single vortex core is 2π, the number of vortices in the simulation is defined through this boundary condition. Equivalently, the average

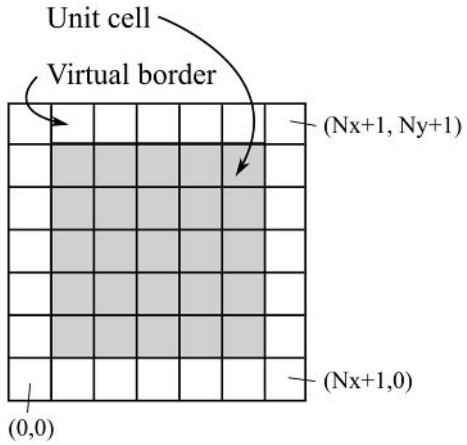

Figure 6.1: Schematic of the basic setup of the simulation space, which is a grid consisting of $(N_y+2)\times(N_x+2)$ cells. The inner set of $N_x \times N_y$ grey cells make out the actual simulation unit cell, while the cells surrounding them are a virtual border, which is used to maintain the periodicity of the unit cell. After each iteration, the virtual border cells are updated as according to Eqs. (6.16)–(6.23).

induced field of the simulation is determined via the boundary conditions on the vector potential, since $\mathbf{B} = \nabla \times \mathbf{A}$. The boundary condition is imposed by adding or subtracting a constant at the boundary:

$$\mathbf{A}_x^k(0, y_{\text{int}}) = \mathbf{A}_x^k(N_x, y_{\text{int}}), \qquad \mathbf{A}_y^k(0, y_{\text{int}}) = \mathbf{A}_y^k(N_x, y_{\text{int}}) - \frac{\Phi}{2\kappa L_y} \tag{6.20}$$

$$\mathbf{A}_x^k(N_x+1, y_{\text{int}}) = \mathbf{A}_x^k(1, y_{\text{int}}), \qquad \mathbf{A}_y^k(N_x+1, y_{\text{int}}) = \mathbf{A}_y^k(1, y_{\text{int}}) + \frac{\Phi}{2\kappa L_y} \tag{6.21}$$

$$\mathbf{A}_x^k(x_{\text{int}}, 0) = \mathbf{A}_x^k(x_{\text{int}}, N_y) + \frac{\Phi}{2\kappa L_x}, \qquad \mathbf{A}_y^k(x_{\text{int}}, 0) = \mathbf{A}_y^k(x_{\text{int}}, N_y) \tag{6.22}$$

$$\mathbf{A}_x^k(x_{\text{int}}, N_y+1) = \mathbf{A}_x^k(x_{\text{int}}, 1) - \frac{\Phi}{2\kappa L_x}, \qquad \mathbf{A}_y^k(x_{\text{int}}, N_y+1) = \mathbf{A}_y^k(x_{\text{int}}, 1) \tag{6.23}$$

Through these boundary conditions the average internal magnetic field is fixed to:

$$\bar{B} = \frac{\Phi}{\kappa|\Omega|} = \frac{2\pi n}{\kappa|\Omega|} \tag{6.24}$$

All simulations were initialized with a constant internal field and a constant order parameter. When running the simulations, inhomogeneities will initially occur along the border as a consequence of applying Eqs. (6.16)-(6.23) to the virtual border of the $\boldsymbol{\psi}^k$, $\mathbf{A}_x^k$, and $\mathbf{A}_y^k$ matrices. Fig. 6.2 contains several time-frames from a simulation of a single vortex, depicting how it gradually emerges from the top right border of the unit cell.

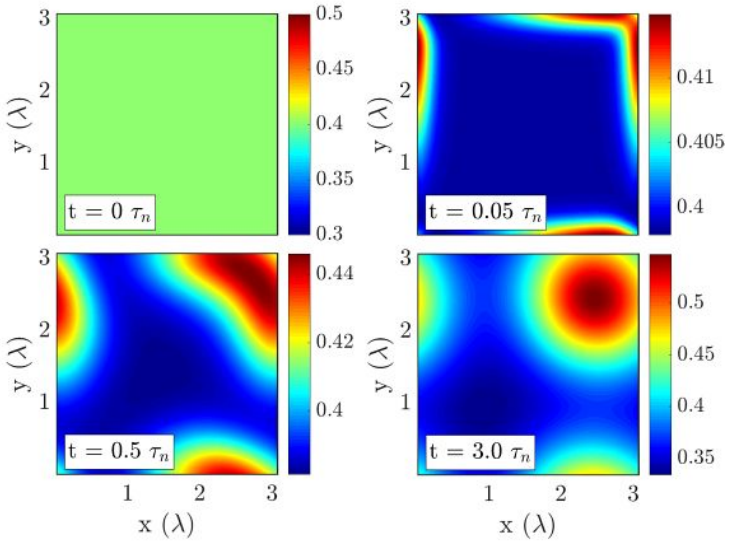

Figure 6.2: Time evolution of the simulated spatial field profile of a single vortex. As time progresses, the vortex gradually emerges from the border grid cells. The simulation was carried out with the parameters $\kappa = 1.3$, $\mathrm{d}x = \mathrm{d}y = 0.05\,\lambda$, $\Delta t = 10^{-4}\,\tau_n$, $\sigma = 10\,\sigma_n$, and an average internal field of $\bar{B} = 0.5\sqrt{2}B_c$.

6.2.2 Geometry effects

Despite the periodic boundary conditions, the size and dimensions of the simulation domain $|\Omega| = L_x L_y$ still plays an important role. The overall simulated vortex morphology is affected by the relative lengths of L_x and L_y. In the absence of pinning and higher-order GL terms, one would expect a traditional hexagonal vortex lattice structure to emerge from the simulations. However, such a morphology will not develop if the unit side lengths do not conform with the hexagonal unit vectors $\mathbf{a}_1 = a_0(1, 0)$ and $\mathbf{a}_2 = a_0 1/2(1, \sqrt{3})$, where a_0 is the unit side length. Fig. 6.3 depicts the results of a simulation carried out with $L_x = L_y$ resulting in geometry-induced frustration and an overall square-looking vortex lattice. To avoid such effects, we have in the rest of the chapter employed unit cells with side lengths having a ratio of $L_y/L_x = n_{\mathrm{int}}\sqrt{3}$, where n_{int} is a positive integer. This ensures that the unpinned vortex state is hexagonal in all subsequent simulations.

6.2.3 Finite-sized spatial mesh effects

It is well known that TDGL simulations can be affected by deceptive numerical effects if the spatial mesh widths, $\mathrm{d}x$ and $\mathrm{d}y$, are chosen to be too large [177]. This section aims to present investigations of the mesh-sensitivity of our implementation of the TDGL

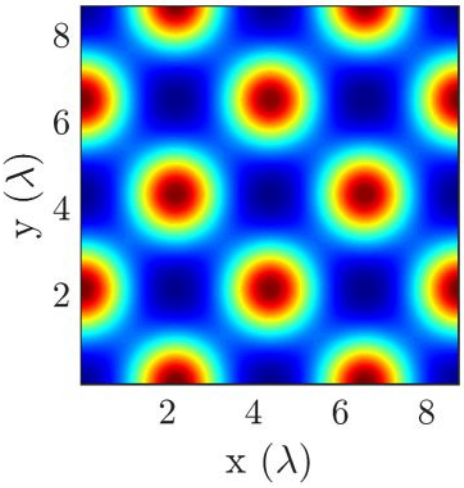

Figure 6.3: The induced field of a vortex lattice simulated with equal side lengths $L_x = L_y$, $\kappa = 1.3$, an average internal field of $\bar{B} = 0.6\sqrt{2}B_c$, $\mathrm{d}x = \mathrm{d}y = 0.05\,\lambda$, $\Delta t = 10^{-4}\,\tau_n$, and $\sigma = 10\,\sigma_n$. The simulation producing this plot ran for 10^6 iterations.

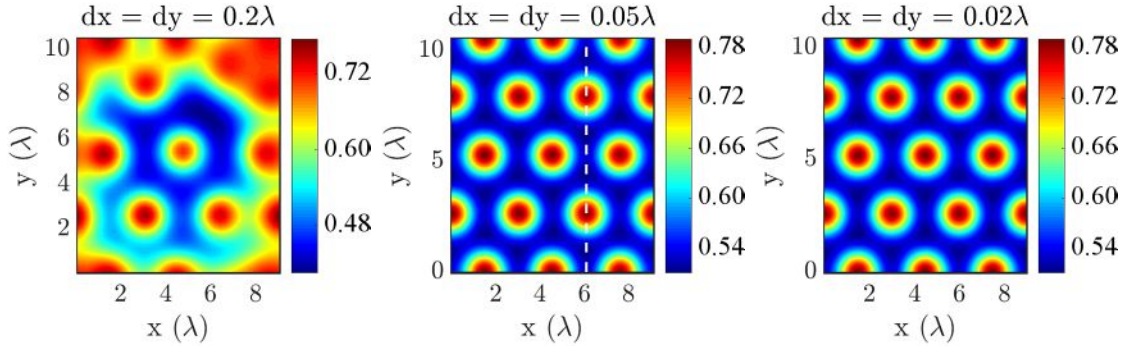

Figure 6.4: Examples of how the choice of mesh width can affect the simulation results. All three plots show the induced field as found with simulations with no pinning, a GL parameter of 1.3, an average internal field of $\bar{B} = 0.6\sqrt{2}B_c$, and varying mesh widths. The dashed white line marks where cuts have been taken to make the 1D-field profiles in Fig. 6.5.

equations. Fig. 6.4 shows the induced field as found in three different instances with identical parameters except for the mesh width, which has been chosen to be $0.2\,\lambda$, $0.05\,\lambda$ and $0.02\,\lambda$. In the case of the $0.2\,\lambda$ simulation, the expected hexagonal symmetry has clearly been broken, seeing as some vortices have accumulated near the border of the unit cell. This behaviour is caused by a too rough spatial resolution, which is incapable of properly resolving the boundary conditions and thus induces an artificial Meissner current in the system. The field plots with $\mathrm{d}x = \mathrm{d}y = 0.05\,\lambda$ and $\mathrm{d}x = \mathrm{d}y = 0.02\,\lambda$ showcase much better hexagonal symmetries. Vertical slices through the field plots are shown in the left panel of Fig. 6.5. The large peaks in these slice plots correspond to the vortex

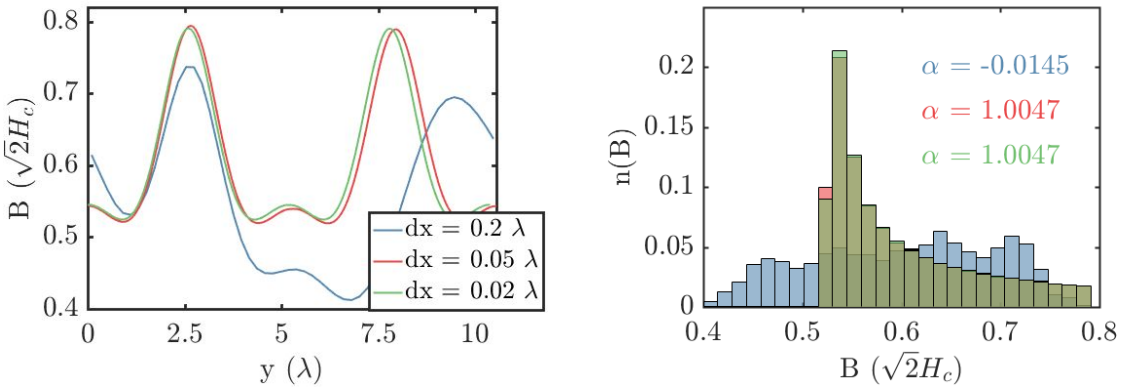

Figure 6.5: Further examples of how inadequate mesh spacings can affect the simulation results. **Left:** Vertical slices through the field distributions presented in Fig. 6.4. **Right:** Histograms of the same field distributions. The skew parameter α has been calculated for each histogram. The two panels share the same colour legend.

cores and should for an hexagonal vortex arrangement have the same maximal field value. It is evident that the $0.2\,\lambda$ vertical slice is asymmetric. The vertical slices of the $0.05\,\lambda$ and $0.02\,\lambda$ field plots are much more symmetric, though the different spatial resolutions still result in slightly differing peak positions. The right panel of Fig. 6.5 shows the different field distributions of the three different simulations. The $0.2\,\lambda$ histogram differ significantly from the $0.05\,\lambda$ and $0.02\,\lambda$ histograms, which are almost identical. This carries into the determined skews, which have been calculated as according to Eq. (2.4).

Choosing the correct values for the parameters $\mathrm{d}x$ and $\mathrm{d}y$ is a trade off between the accuracy of the results and the time and memory needs of the simulation. The $\boldsymbol{\psi}$, $\boldsymbol{A}_x$, and $\boldsymbol{A}_y$ matrices contain seven times more elements for the $\mathrm{d}x = \mathrm{d}y = 0.02\,\lambda$ simulation than the $\mathrm{d}x = \mathrm{d}y = 0.05\lambda$ simulation and the running time is similarly seven times longer. Given the large time difference and the fact that the two runs result in similar distributions with identical skew, the $\mathrm{d}x = \mathrm{d}y = 0.05\,\lambda$ parameters have been used for subsequent simulations with average induced fields of $\bar{B} = 0.6\sqrt{2}B_c$.

Before moving on to negative skew field distributions, one should consider the hexagonal equilibrium vortex configurations. Fig. 6.6 displays the results of simulating systems of

12 vortices with different magnetic fields. Increasing $\bar{B}$ corresponds to decreasing the unit cell size, which is a result of the vortex density having to increase. For each magnetic field, the optimal spatial resolution was optimized as described in Section 6.2.3, resulting in the spatial resolutions $\mathrm{d}x = \mathrm{d}y = 0.05\,\lambda$ for $\bar{B} = 0.4\sqrt{2}B_c$, $\mathrm{d}x = \mathrm{d}y = 0.016\,\lambda$ for $\bar{B} = 0.8\sqrt{2}B_c$ and $\mathrm{d}x = \mathrm{d}y = 0.012\,\lambda$ for $\bar{B} = 1.1\sqrt{2}B_c$. Higher spatial resolutions therefore appear to be required for achieving proper unpinned hexagonal lattices at higher fields. In Fig. 6.6, hexagonal patterns are observed in the induced field and order parameter plots for all three different fields. As is seen from the $|\psi|^2$ plots, the average Cooper pair density is seen to decrease with increased fields. The calculated phase angle, θ from $\psi = |\psi|e^{i\theta}$, is shown for all three fields and it is in all cases evident that there is a total phase change of 2π around each vortex centre. The field distributions all appear similar, with long tails leaning to the right side. The skew has been calculated to be around one for all three equilibrium lattices, though it decreases slightly for higher fields, ostensibly a side-effect of the increasingly overlapping vortex cores.

The equilibrium distributions were obtained by iterating the TDGL equations, Eqs. (6.4)–(6.5), and the boundary conditions, Eqs. (6.16)–(6.23), until the vortex configuration equilibrated. The time evolution of the skewness parameter was used as an equilibrium criterion. For every 1000th iteration the skewness parameter was calculated and compared to the values before it. Once the mean skewness of the 25000 latest iterations differed by less than two standard errors from the mean skewness of the 25000 iterations before them, the simulation was deemed to have equilibriated. This equilibration condition was used for all the remaining simulations of this chapter.

6.3 Investigation of negative skew configurations

In the following section, we proceed with a more careful investigation of spatially perturbed vortex configurations. Past investigations of negative skew distributions are first

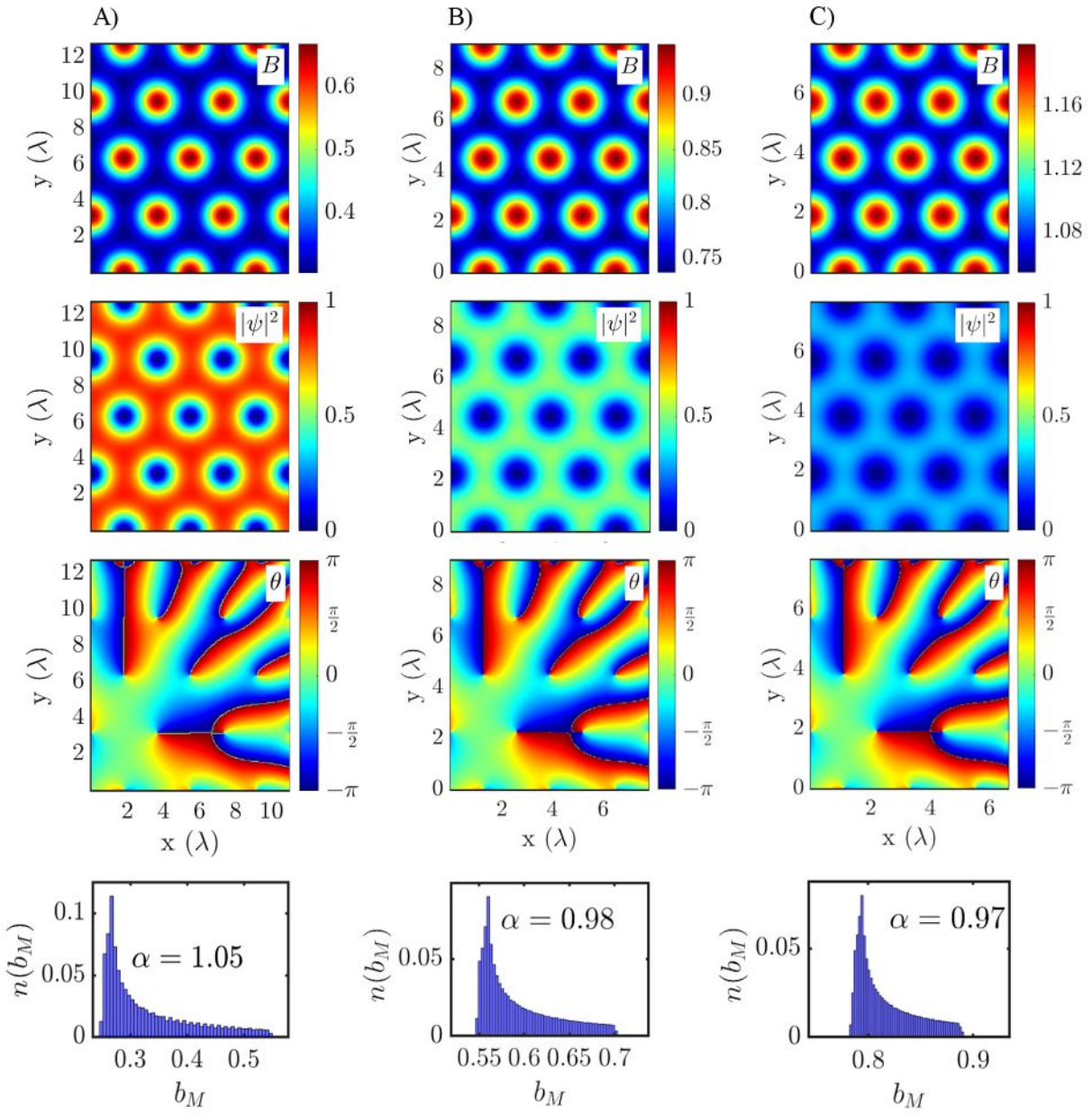

Figure 6.6: The results of simulating 12 vortices with average induced fields of $\bar{B} = 0.4\sqrt{2}B_c$ (column A), $0.8\sqrt{2}B_c$ (column B), and $1.1\sqrt{2}B_c$ (column C). Plots of the induced field $B(\mathbf{r})$, squared order parameter $|\psi|^2(\mathbf{r})$, phase angle $\theta(\mathbf{r})$, and local field distribution are shown for each simulation run. The $\bar{B} = 0.4\sqrt{2}B_c$ results were obtained with the simulations parameters $\mathrm{d}x = \mathrm{d}y = 0.05\,\lambda$ and $\Delta t = 2 \cdot 10^{-4}\,\tau_n$, the $\bar{B} = 0.8\sqrt{2}B_c$ simulation was carried out with $\mathrm{d}x = \mathrm{d}y = 0.016\,\lambda$ and $\Delta t = 1 \cdot 10^{-4}\,\tau_n$, and the $\bar{B} = 1.1\sqrt{2}B_c$ results were obtained with $\mathrm{d}x = \mathrm{d}y = 0.012\,\lambda$ and $\Delta t = 1 \cdot 10^{-5}\,\tau_n$. A κ of 1.3 and a field relaxation constant of $\sigma = 10\,\sigma_n$ was used for all simulations.

reviewed in Section 6.3.1. Afterwards, our own simulation results are presented in Sections 6.3.2–6.3.4, where we try to induce negative skew in several different ways.

6.3.1 Prior investigations of negative skew distributions

Local field distribution with negative skew has previously been observed in μSR investigations of $Bi_{2.15}Sr_{1.85}CaCu_2O_{8+\delta}$ [87] and $La_{1.9}Sr_{0.1}CuO_{4-\delta}$ [178]. The negative skews were in these cases seen to occur deep in the vortex glass and in the vortex liquid phases. In Ref. 178, Menon *et al.* carry out a detailed study of the possible origin of the negative skew distributions. There, the third moment is related to the triplet structure factor, $S^{(3)}$, as:

$$\langle [\Delta B]^3 \rangle \propto \int\int d\mathbf{q}_1 d\mathbf{q}_2 S^{(3)}(\mathbf{q}_1, \mathbf{q}_2) b_F(\mathbf{q}_1) b_F(\mathbf{q}_2) b_F(-\mathbf{q}_1 - \mathbf{q}_2), \tag{6.25}$$

$$S^{(3)}(\mathbf{q}_1, \mathbf{q}_2)) = \frac{1}{N} \langle \delta\rho(\mathbf{q}_1) \delta\rho(\mathbf{q}_2) \delta\rho(-\mathbf{q}_1 - \mathbf{q}_2) \rangle \tag{6.26}$$

where the flux lines are assumed to be rigid and aligned along the field direction. The field of a single flux line in Fourier space is given by $b_F(\mathbf{q})$, and the Fourier components of the deviations of the flux line density is defined as $\delta\rho(\mathbf{q})$. Using Eq. (6.25) as a starting point, Menon argues that a negative third moment cannot be achieved with either a completely uncorrelated, $S^{(3)}(\mathbf{q}_1, \mathbf{q}_2) = 1$, or with a perfectly ordered FLL. In the theoretical calculations of the third moment of the ordered FLL, Menon utilizes the London result of Eq. (3.13) multiplied with a form factor to eliminate the singularity at the vortex core. Eventually it is put forward that non-trivial three-body correlations are needed to achieve a negative third moment and thereby a negative skew. Fig. 6.7 summarizes Menon's results, where experimental μSR estimations of the skew of $La_{1.9}Sr_{0.1}CuO_{4-\delta}$ is compared to the theoretical estimations based on a liquid structure factor with nontrivial three-body correlations and to Monte Carlo simulations results. The simulations were carried out with Gaussian pinning potentials, as used for the MD simulations described in Section 2.2.1, as well as with vortex interaction potential modelled as $\approx K_0(r/\lambda)$. The figure

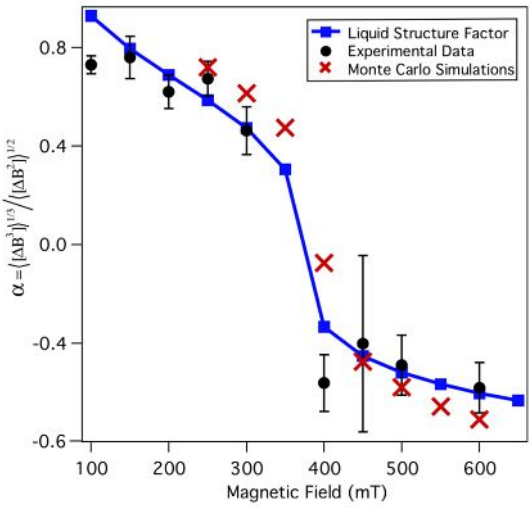

Figure 6.7: The skew α as a function of applied field. The skew has been obtained via experimental μSR measurements on $La_{1.9}Sr_{0.1}CuO_{4-\delta}$ (black circles), a theoretical liquid structure factor (blue squares), and Monte Carlo simulation results (red crosses). The figure is reprinted from Ref. 178.

convincingly shows that three-body correlations can result in a negative skew distribution.

Menon's analysis does not employ GL theory in any way. This is notable, because vortex cores can be non-rigid and deform in the GL description. This is unlike the vortex core behaviour in the typical London model approach, where the form factor is usually fixed to be symmetric. An example of the non-rigid behaviour of the vortex cores is seen in the GL study by Priour and Fertig in Ref. [179], where vortices are observed to deform dramatically in the proximity of impurity defects. The deformed vortex core may affect the overall field distribution, and it is therefore worthwhile to pursue a further GL investigation to determine whether three-body correlations are uniquely responsible for negative skew field distributions.

6.3.2 Inducing negative skew via forced vortex core interactions

The average inter-vortex distance is maximized in the hexagonal equilibrium distribution. A logical first step in the search for unusual vortex states with negative skew distributions is therefore to manually reduce the distance between some of the vortices. We attempt this by first looking at systems with very few vortices and by using the strong pinning model of Ref. 114, $\psi(\mathbf{r}_p) = 0$, to manipulate the position of the vortex cores. The radii

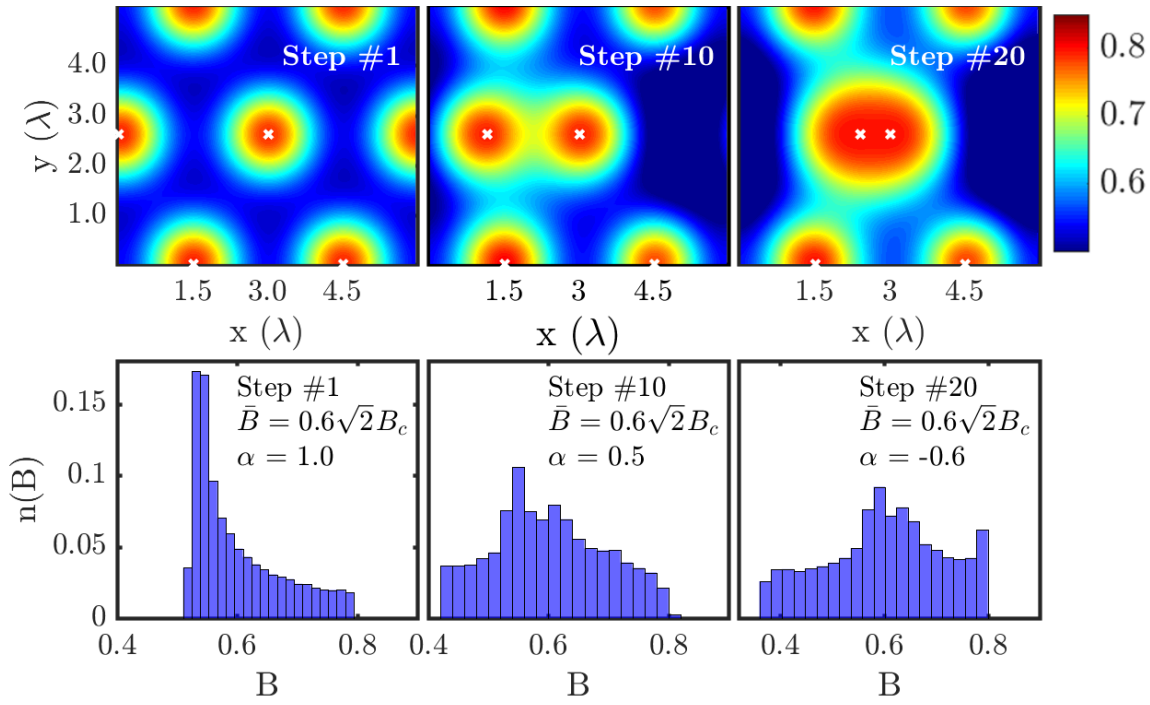

Figure 6.8: TDGL simulations of a system of four vortices with a reduced mean field of $\bar{B} = 0.6\sqrt{2}B_c$. Pinning sites are initially positioned at the hexagonal equilibrium vortex positions. In a step-wise fashion, one of the pinning sites is brought closer to the others in other to see the influence of frustration on the system. The top row shows examples of the field induction profiles of different simulated vortex configuration, while the bottom row displays the corresponding field distributions. The simulations were carried out with the parameters $\mathrm{d}x = \mathrm{d}y = 0.05\,\lambda$, $\Delta t = 2 \cdot 10^{-4}\,\tau_n$, $\sigma = 10\,\sigma_n$.

of the pins were defined to be $0.1\,\xi$. An example of our simulation scheme is shown in Fig. 6.8. The system starts out in the hexagonal equilibrium phase, with pinning sites positioned at each of the vortex centres. In the next step, the leftmost pinning site is brought closer to the middle, and the vortex state is allowed to equilibrate to this new pinning configuration. After equilibration, the pinning site is in the next step brought even closer to the middle and so on. Fig. 6.9 illustrate the simulation process in more detail. Here, the evolution of the skew in between the equilibrium distributions is shown. Initially, the skew is seen to decay exponentially every time the pinning site is moved further to the right. Eventually, as the distance between two of the pins becomes too small, one of the vortices is pushed off its pinning site. At this point, the vortex diffuses back to its equilibrium position to resolve the frustration, and the skew will thereby attain its original equilibrium value.

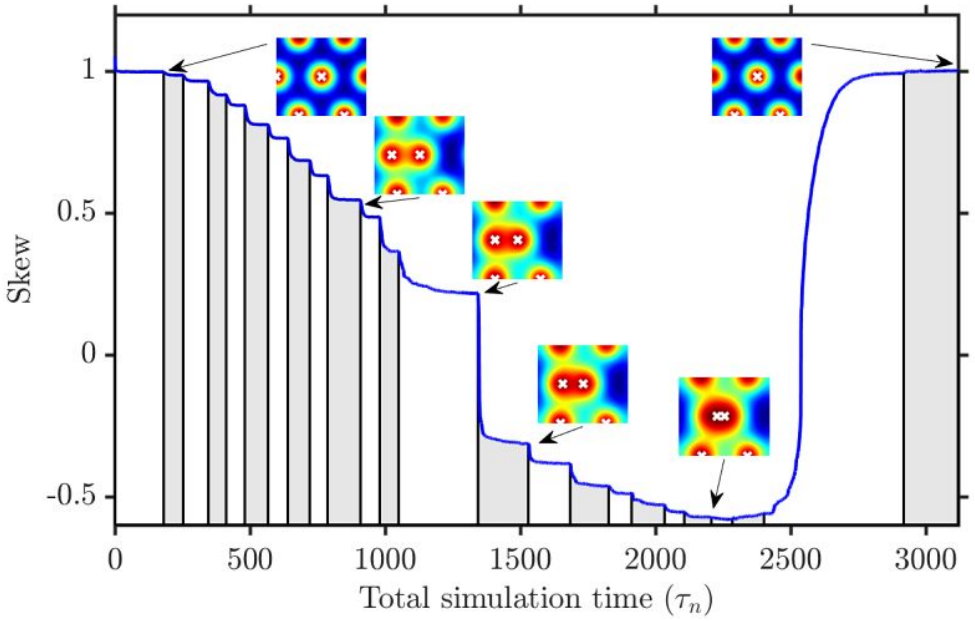

Figure 6.9: The evolution of the skew as the originally leftmost pinning site is gradually moved towards the middle. Each vertical line marks a time in the simulation where the pinning site was moved one step further ahead. The intermediate points between each vertical line show how the FLL relaxes into a new stable configuration after each change to the pinning landscape. The small insets show the induced field at various times in the simulation procedure. The white x marks indicate the position of the pinning sites. In the rightmost inset, only three pinning sites are visible because two of them are overlapping in the middle.

The simulation run with just four vortices per unit cell shows that it is possible to attain a negative skew, provided that enough frustration is induced. The same simulation was also carried out with just two vortices per unit cell, where a negative skew was also observed. Carrying out a distance scan with the same simulation parameters as Fig. 6.8 and just two vortices, we observed a minimum skew of -0.44. Hence, our simulation results go against the notion that three-body correlations are uniquely needed for a negative skew [178].

In Fig. 6.10 the same simulation scheme has been carried out with systems of four vortices and a series of different fields. In all cases, it is evident that the skew decreases as the vortices are brought closer together, though only the simulations with $\bar{B} > 0.5\sqrt{2}B_c$ manage to attain a negative skew value. The distances between the pins originating at vortex A and B, cf. Fig. 6.10, *and* the vortex core positions are continuously tracked. For

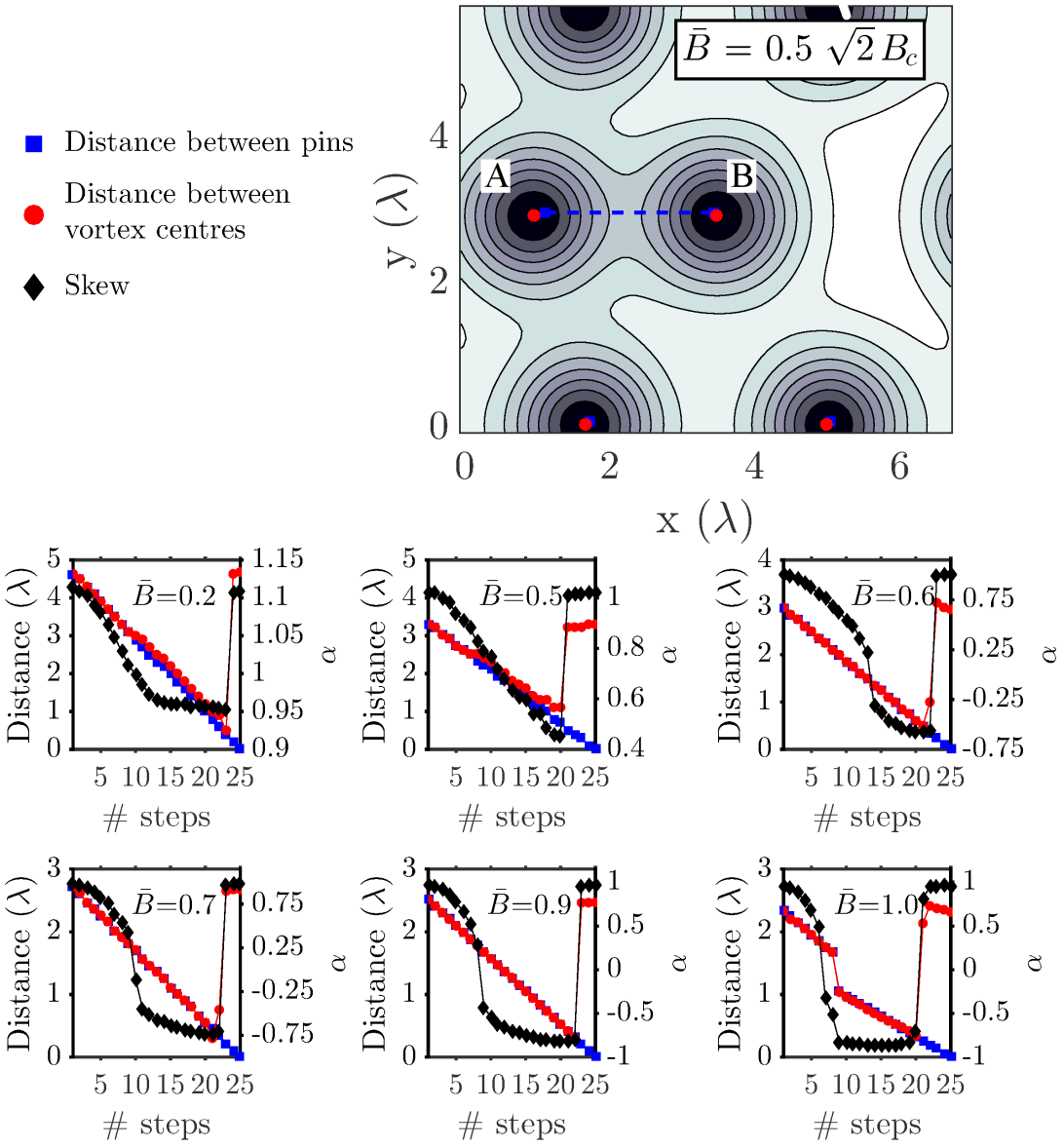

Figure 6.10: Results at different fields $\bar{B}$ of enhancing the core interactions in a system of four vortices by gradually forcing the vortex A towards the vortex B by manipulating the pinning site positions. The strong pinning regime, $\psi(\mathbf{r}_p) = 0$, has been employed. In the top right plot the blue squares are the pinning positions, while the red circles are the vortex centres. The bottom plots show the distance between the A and B pinning sites, the distance between the corresponding vortex centres and the skew, α.

all fields, these two values follow one another until vortex A is pushed off its pin. For all fields, this is seen to occur when the distance between pinning sites is less than $\approx 1\,\lambda$.

6.3.3 Optimization of positional order

In this section we aim to provide a more extended view into how the vortex positioning affects the skew. This is done by including more vortices and by now optimizing their position via a Monte Carlo procedure. The position of the vortices is still controlled through the strong $\psi(\mathbf{r}_p) = 0$ pinning sites. Each Monte Carlo run was started from the hexagonal isotropic state with pins placed at the vortex centres. The following actions were taken during each iteration of the Monte Carlo procedure:

1. Generate a new pinning landscape by moving one of the pins to a new random position, which is within a radius of $0.25\,\lambda$ of its previous position.

2. Let the vortex lattice equilibrate.

3. Calculate the skew of the new vortex configuration and calculate its difference from the old skew: $\Delta\alpha = \alpha_{\text{new}}$ - α_{old}

4. Generate a random number, $0 < x_{\text{rand}} < 1$.

5. Monte Carlo step: Accept the new pinning configuration if $\Delta\alpha < 0$ or $x_{\text{rand}} < \exp(-\Delta\alpha\beta)$. Here β is an effective inverse temperature.

The optimization procedure was carried out on systems with 4, 8, and 12 vortices and periodic boundary conditions. An effective inverse temperature of $\beta = 10^3$ was used for all Monte Carlo runs. In the event that a vortex is pushed off its pin, as was observed in the previous section when two pinning sites get too close, the optimization procedure loses a degree of freedom. To avoid this from happening, all newly generated pinning configurations were required to have a minimum distance of $1\,\xi$ between all pinning sites.

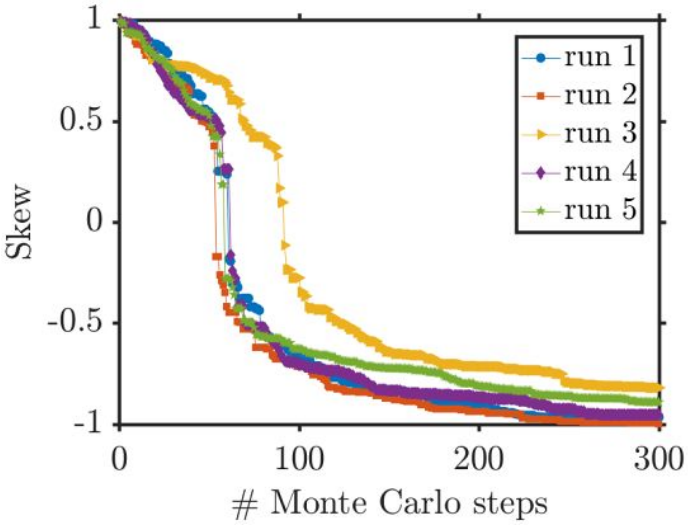

Figure 6.11: The skew as a function of the number of Monte Carlo steps taken in a system with 12 vortices. The optimization procedure was carried out several times with $\kappa = 1.3$, $\mathrm{d}x = \mathrm{d}y = 0.05\,\lambda$, $\bar{B} = 0.6\sqrt{2}B_c$, $\Delta t = 2 \cdot 10^{-4}$, $\sigma = 10\,\sigma_n$.

Fig. 6.11 shows the result of running the optimization procedure on a system with 12 vortices, $\kappa = 1.3$, and $\bar{B} = 0.6\sqrt{2}B_c$. All runs eventually manage to reach a negative skew, resulting in an average skew of $-0.93(6)$ at the 300th Monte Carlo step. The final results of some of the Monte Carlo runs are depicted in Fig. 6.12. These vortex states exhibit a clear distortion compared to their initial equilibrium states. Additionally, the vortex cores no longer appear to have one uniform size, but instead appeas to be deformed due to the pinning-induced frustration.

An unfortunate reality of the Monte Carlo approach is that it is limited to relatively few vortices compared to other simulation methods, which impede the identification of the simulated vortex states as either Bragg or vortex glasses. In Refs. 69 and 76, the Bragg glass is identified by extracting displacement and translational correlation functions from SANS measurements of niobium and vanadium via reverse Monte Carlo methods. In both cases, one has to look at length scales larger than $10a_0$, where a_0 is the equilibrium vortex spacing, to observe specific Bragg glass-like behaviour, i.e. a logarithmic growth of the displacement correlation function and an algebraic decay of the translational correlation function. In our case, the largest investigated system contains 12 vortices and has a periodicity of just $\approx 2a_0$, which is much too short to determine anything about the large-scale nature of the FLL. In Fig. 6.13 we investigate the effect of the number of vortices in our simulations by comparing runs with $N = 12$, 8 and 4 vortices. Systems with fewer

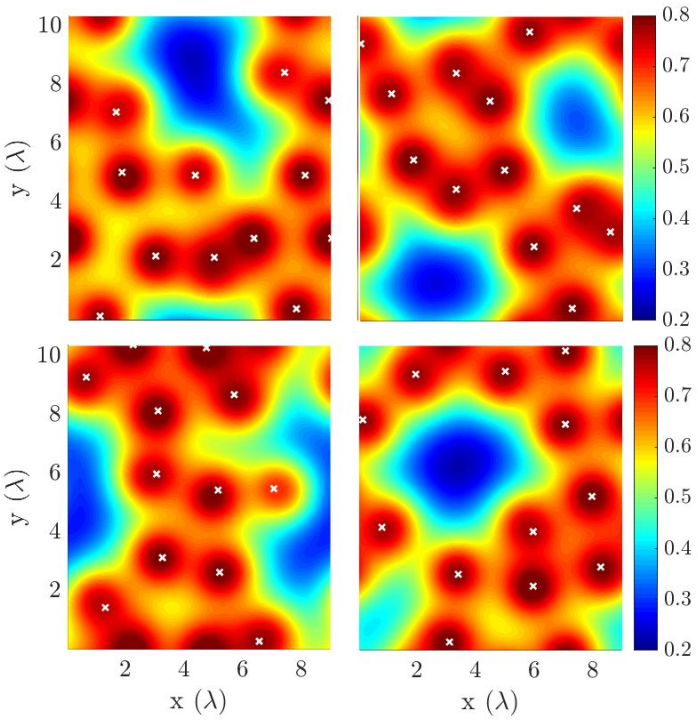

Figure 6.12: Field plots of vortex systems with $\kappa = 1.3$, $\bar{B} = 0.6\sqrt{2}B_c$, and 12 vortices obtained through the Monte Carlo procedure. All of the shown vortex configurations have a skew below -0.7. The color bar indicates the induced field.

vortices are seen to converge faster because they have fewer degrees of freedom. The final average skews, found from 5 runs of each of the three system sizes, are -0.93(7), -0.93(2), and -0.77(5) for $N = 12$, 8 and 4, respectively. There is therefore a slight system size dependence, though the $N = 12$ and $N = 8$ systems ended up finding the same final skew. In the right panel of Fig. 6.13, we attempt to characterize the change of the FLL structure as the skew is decreased through the optimization procedure. The nearest neighbour distance has been calculated for each vortex and averaged over the entire vortex ensemble at every step of the Monte Carlo procedures. It is evident that a decrease of the skew is correlated with a decrease of the average nearest neighbour distance, indicating increasingly distorted structures.

6.3.4 Local distortions of the vortex core

The optimization procedure of the previous section has the built in assumption that negative skew can be obtained through the positional disorder of the lattice. This was shown to be true, though it does not exclude the possibility of local core distortions giving rise

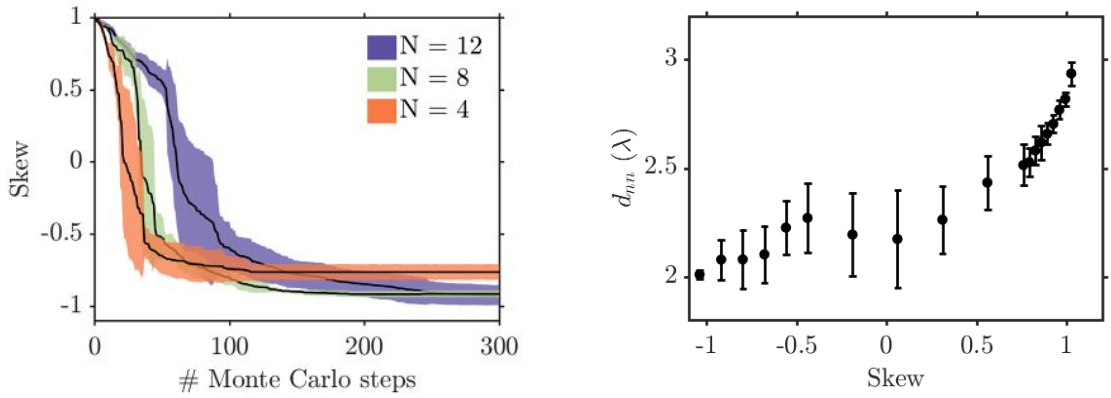

Figure 6.13: Left: The average skew found as a function of the number of Monte Carlo steps, as simulated for three different system sizes. The shaded areas corresponds to ± 1 standard deviation, as determined from 5 Monte Carlo runs for each system size. **Right:** The average distance between nearest neighbour as a function of the skew. The data have been averaged over the results from all the Monte Carlo simulation runs for all three system sizes, $N = 12, 8, 4$.

to negative skew as well. Such a mechanism is interesting to explore, because it has been proposed as a possible explanation for the peak effect [76], especially in the cases where the peak effect is found to occur concurrently with a Bragg glass.

This section documents a small numerical test, where the vortex cores are distorted without changing their "centre of mass" positions. The top panels of Fig. 6.14 show how this is done through the placement of the pinning sites. A random direction is chosen for each vortex, after which a pin is placed on either side of the vortex core in this direction. The pins are placed with the same distance to the vortex centre, meaning that they should exert the same pull. For the result in this section, we have employed the less strong δT_c pinning with $\epsilon(\mathbf{r}) = -1$ as discussed in Section 2.2.2. Each pin has a radius of $1\,\xi$. The local field histograms resulting from these pinning landscapes are also shown in Fig. 6.14. When the pins are placed a distance of $0.5\,\xi$ from the vortex cores, the skew is reduced to 0.73, while a distance of $0.75\,\xi$ results in a negative skew of -0.33. A significant distortion of the vortex cores is therefore necessary to achieve a negative skew if the positional disorder is limited.

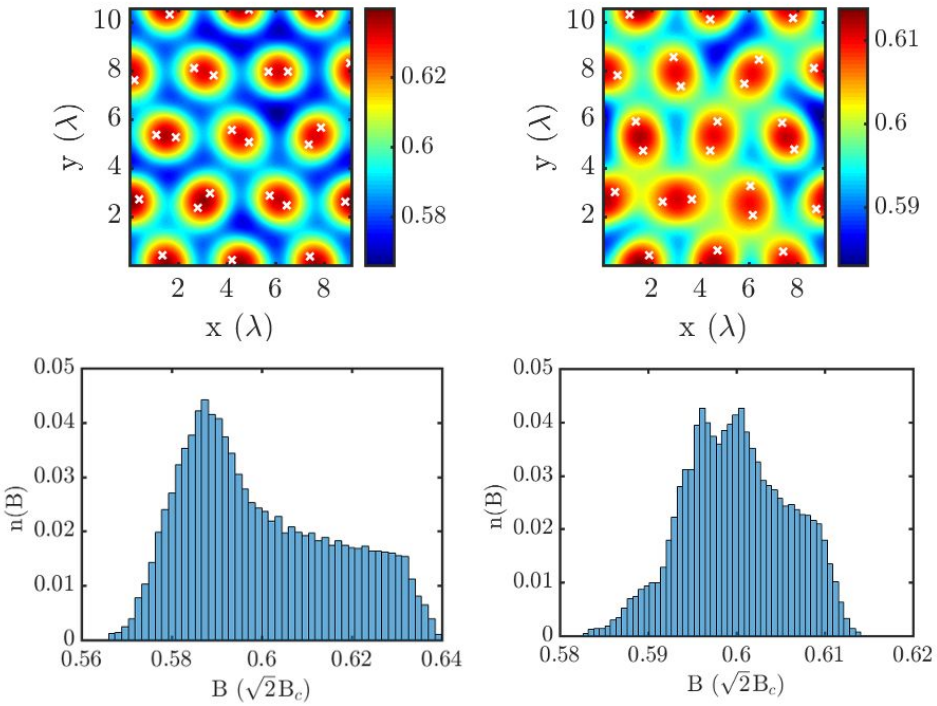

Figure 6.14: The result of distorting the shape of all the vortex cores by placing two equidistant pins near all the vortex cores. The pinning positions are in the top plots marked with white x's. The color bars are used to indicate the value of the induced field. In the top left plot, the pins are placed a distance $0.5\,\xi$ from all vortex cores, resulting in a decreased skew of 0.76. In the right top plot, the pinning sites have been placed a distance $0.75\,\xi$ from the vortex cores, resulting in a skew of -0.33. The lower plots display the field histogram corresponding to the field plots above them. The simulations have been carried out with $\kappa = 1.3$, $\bar{B} = 0.6\sqrt{2}B_c$, $\mathrm{d}x = \mathrm{d}y = 0.05\,\lambda$, $\Delta t = 2 \cdot 10^{-4}\,\tau_n$, and $\sigma = 10\,\sigma_n$.

6.4 Summary

From the investigations of low-κ vortex systems containing 2-12 vortices, we have observed that local field distributions with negative skews can be achieved through both positional disorder and local core deformations. Menon *et al.* convincingly showed that three-body correlations result in a negative skew, though our TDGL simulation results seem to indicate that this relation does not hold the other way: A negative skew can in our simulations be achieved with just two vortices.

In terms of relating the simulations to the experimental situation, high-frustration vortex configurations such as those found from the Monte Carlo optimization procedure, cf. Fig. 6.12, are only realizable in samples with very strong pinning forces. At the same time, we know from Section 6.3.2 that a negative skew is easier to achieve at higher inductions, meaning that less distorted vortex configurations are likely needed at higher induced fields. Still, the simulations show that the negative skew region of the μSR-based phase diagram presented in Chapter 5 (Fig. 5.20) *can* be interpreted as a region with increased disorder. This also fits with the Chapter 5 SANS observation of decaying translational correlation lengths as the order-to-disorder transition is approached.

Temperature fluctuations of individual vortices were in Ref. 76 discussed to be relevant to the peak effect, which also occurs in the negative skew region of the phase diagram. Our results in Section 6.3.4 show that local distortions can indeed contribute to the negative skew.

The simulation method developed for this chapter could be improved in many ways. First of all, optimizing the overall code further so that larger systems can be investigated will help approximate the experimental situation better as well as make it possible to calculate correlation functions. Implementation of temperature fluctuations, anisotropy effects and more realistic pinning potentials will make it possible to continue the exploration of

negative skew distributions.

CONCLUSION

In this thesis, we have explored the flux line lattice of two low-κ superconductors when exposed to either temporal or spatial perturbations.

In Chapter 4, time-resolved SANS was used to investigate the effect of temporal perturbations in a high purity niobium sample, which displayed several different vortex morphologies when the static field was applied along a $\langle 100 \rangle$ crystallographic axis. By tracking the evolution of the characteristic time constants of the FLL as a function of field and temperature, we were able to see that the anisotropic nature of the niobium Fermi surface was expressed in the dynamic behaviour. Our results were to some extent compatible with anisotropic elasticity theory based on the GL equations presented in Section 1.3.2, which predicted decreasing elastic moduli and therefore increasing time scales as a function of increasing field and temperature. However, our data also had indications of non-elastic behaviour, as was observed through the frequency dependence of the measured time constants described in Section 4.4.1, slight differences in the time-constants extracted from different domains shown in Section 4.4.3, as well as diffuse scattering which was either induced or enhanced by the AC field as discussed in Section 4.4.4.

In regards to the structural transitions, we first investigated the dynamic behaviour of the niobium FLL through the scalene-to-isosceles structural transition in Section 4.4.1. The time constants did not change abnormally across the structural transition when employing a uniform perpendicular AC field. However, when employing a constant gradient AC field, the time constants increased more rapidly close to and across the transition. One possible interpretation is that the constant gradient AC field at least partially probes

the c_{66} elastic mode, which is more sensitive to shearing of the unit cell. As a function of field, we investigated the scalene-to-high-field square phase transition in Section 4.4.2. Again, no abnormal behaviour was observed near the structural transition and the time scales were seen to increase with increasing fields.

Spatial perturbations were in Chapter 5 investigated via SANS measurements of an impure vanadium sample. The main result of this investigation was that the correlation lengths decrease significantly as the order-to-disorder transition is approached, indicating that the vortex glass phase is dominated by short-range ordered correlations.
Muon spin rotation measurements of the same vanadium sample resulted in local field distributions, which showed that the skew of the distribution changed from positive to negative in the vortex glass phase. These observations were complemented by Ginzburg-Landau based simulations presented in Chapter 6, that showed that negative skew can be induced by disordered vortex state or in general just by increased vortex core interaction and deformation. We achieved negative skew distributions from simulations with just two vortices, thereby disproving the notion that negative skew is a unique indicator of three-body correlations.

The thesis work demonstrates that low-κ type-II superconductors are far from uninteresting or simple. As a result of their underlying anisotropic nature and relatively large vortex cores, they exhibit a number of complex behaviours. The results from this thesis are currently being written up in a number of papers.

Future work

The study of the dynamic behaviour of niobium could easily be extended further. A more systematic investigation of the influence of the frequency and amplitude of the applied field could help answer important questions about the basic nature of the niobium FLL, i.e. is it fully elastic or better described as a non-Newtonian fluid. The vertical diffuse

streaks have, to our best knowledge, not been reported before and it would therefore be interesting to make a more thorough investigation by carrying out more high-statistic wide-angle rocking curve measurements.

Our investigation of the phase diagram of our impure vanadium sample could benefit from more measurements at intermediate temperatures in order to decide how much the FLL preparation technique affects the exact location of the order-to-disorder transition in this region. Additional full rocking scan measurements with the high-resolution perpendicular setup would facilitate more accurate measurements of the translational correlation lengths.

We have demonstrated that the time dependent Ginzburg-Landau (TDGL) equations can be used in an optimization procedure to obtain negative skew distributions. A reverse Monte Carlo procedure could be attempted to fit specific vortex structures to experimental μSR distributions directly. However, this necessitates high statistics measurements and an optimization of the TDGL code so that more vortices can be included.

APPENDIX A

DYNAMIC MAXWELL COIL DATA

A.1 Introduction

This appendix aims to account for the remaining results from the stroboscopic SANS investigation of the high purity niobium FLL with a Maxwell coil setup. The overall experimental setup is described in Chapter 4. The Maxwell coils induces a constant gradient field. The main motivation for using this setup was that it might induce shearing in the vortex lattice, which we could detect through changes in the detector position of the diffraction spots. Unfortunately, the in-plane resolution of the detector was too poor to capture any shift of the vortices.

A.2 Temperature scan detector images

Fig. A.1 shows the detector images obtained from the field scan performed across the scalene to isosceles phase transition. In Chapter 4, the phase transition temperature was determined as 3.4(1) K. Overall, the detector images are similar to the ones recorded for the Helmholtz setup and one also see features such as the stripes of diffuse scattering between the first order diffraction spots.

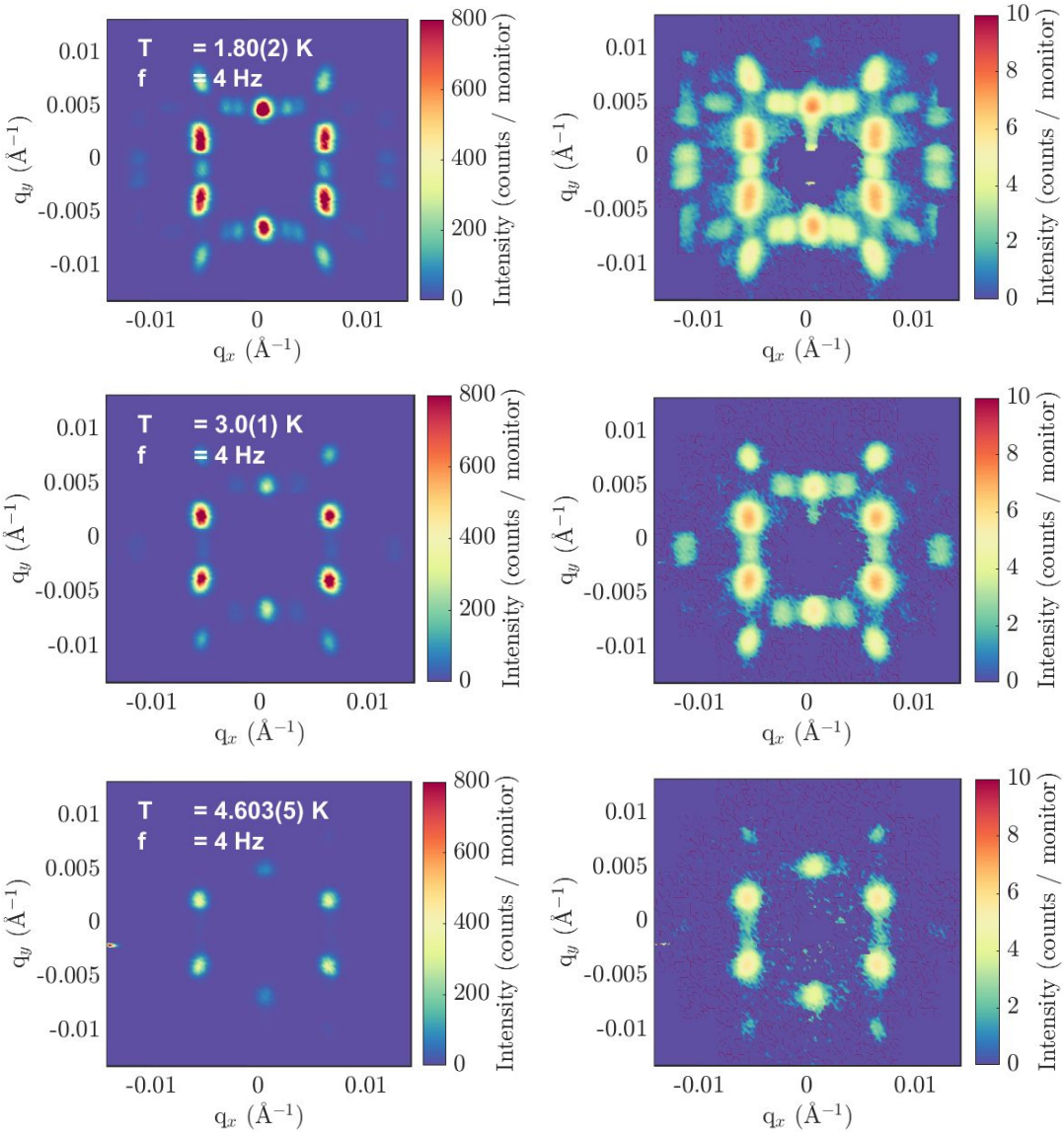

Figure A.1: Images obtained from integrated rocking scans measured with an applied static field of 200 mT and an oscillatory field generated with the Maxwell coil setup with an input voltage of 150 mV_{p2p}. Images in the left column are depicted with a linear colour scales, while the images to the right depict the same data with a logarithmic colour scale. A background measured with a temperature of 10 K and a performed at a temperature of 10 K and a static field of 200 mT was subtracted from the data.

A.3 Rocking curve data

Fig. A.2 shows the time-resolved rocking curve data obtained from a temperature scan measured with the gradient Maxwell configuration. The plots are in many ways reminiscent of the ones presented in Section 4.4.1, with the main difference being that the widths are constant as a function of time. This indicates that the Maxwell configuration perturbs the FLL in a gentler way, such that an angle shift can occur without impacting the order of the lattice. As was the case for the Helmholtz data, the rocking curves of the Maxwell displayed both a long and short range order, which both exhibited time-dependent behaviours.

A.4 Correlations

The radial widths as determined from 2D Gaussian fits to the TM diffraction spot on the detector are shown in Fig. A.3. The radial widths of the Maxwell experiments are similar to those of the Helmholtz experiment. We therefore see that we were not able to detect any in-plane widening as a result of the constant gradient field. The corrected rocking curve widths alongside the corresponding correlations along the flux lines are shown in Fig. A.4, while the corrected $W_{\mathbf{q}}$ width is shown in Fig. A.5. The corrected rocking curve widths have the same order of magnitude between the Helmholtz and Maxwell experiments. As was the case for the Helmholtz experiment, the corrected $W_{\mathbf{q}}$ widths are noisy and almost cannot be separated from 0. This again, is the result of the poor in-plane resolution of the parallel scattering geometry. As was the case for the Helmholtz experiment, the exact values of $W_{\mathbf{q}}$ should be regarded with a certain amount of skepticism. This is because the corrected values are very sensitive to instrument parameters such as the wavelength spread, which likely is not precisely 10%.

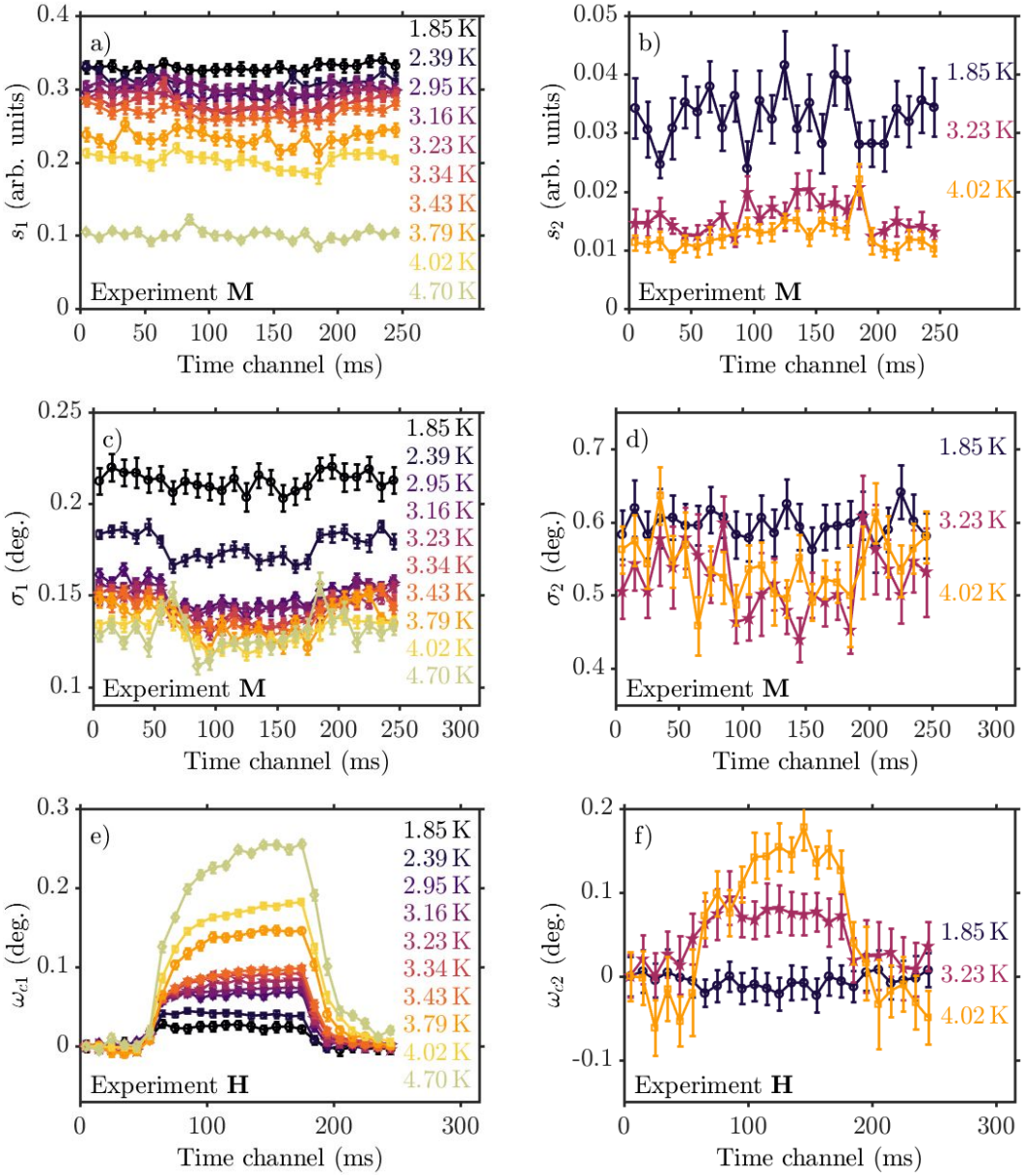

Figure A.2: Time-dependent information extracted from fitting Eq. (4.8) to the rocking curves of the Maxwell coils temperature scan. The plots display **a)** intensity s_1 of the long-range Gaussian peak, **b)** intensity s_2 of the short-range Gaussian peak, **c)** peak width σ_1 of the long-range peak, **d)** peak width σ_2 of the short-range peak, **e)** peak position of the long-range ordered peak, and **f)** peak position of the short-range ordered peak. In subplot **b)**, **d)** and **f)**, only three curves are shown for clarity.

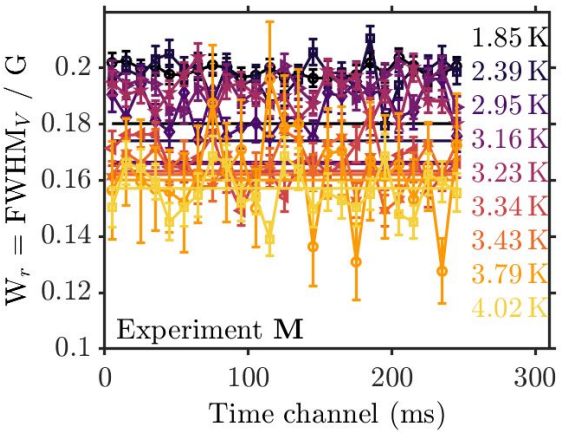

Figure A.3: The radial width of the TM diffraction spot (vertical FWHM) as a function of temperature. The data was collected with the Maxwell coil setup with a static applied field of 200 mT and an oscillating field with a frequency of 4 Hz. The horizontal lines are the expected static values for W_r calculated from Eq. (3.15) assuming $W_{\mathbf{q}} = 0$.

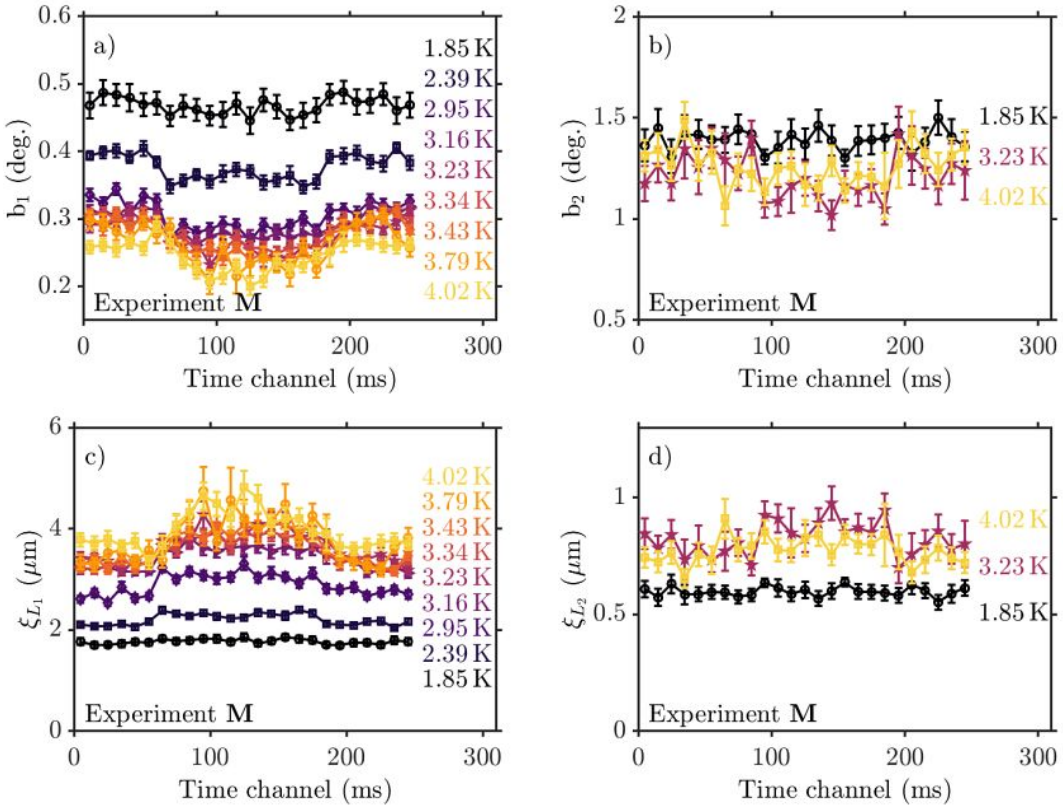

Figure A.4: **a)** and **b)** The resolution corrected rocking curve widths of the the long and short-range order. **c** and **d)** The correlation lengths along the flux lines as calculated from the corrected rocking curve widths. Obtained from the Maxwell coil experiment.

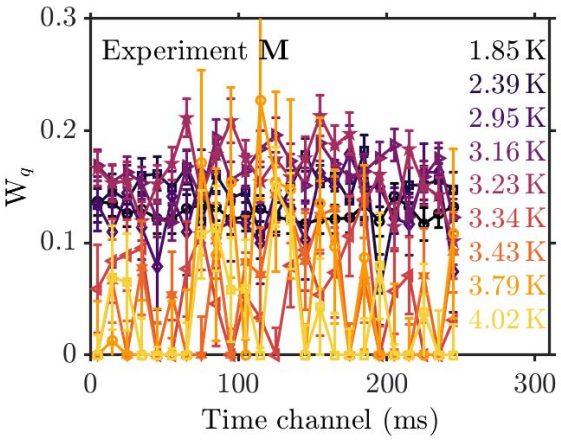

Figure A.5: The width in the direction of scattering, $W_{\mathbf{q}}$, obtained by correcting the radial width, W_r, for the instrumental resolution as a function of time.

Bibliography

[1] Daniel R. Slocombe, Vladimir L. Kuznetsov, Wojciech Grochala, Robert J. P. Williams, and Peter P. Edwards. Superconductivity in transition metals. *Philos. Trans. Royal Soc. A*, **373**(2037), 2015.

[2] W. J. de Haas and F. Jurriaanse. Die Supraleitfähigkeit des Gold-Wismuts. *Naturwissenschaften*, **19**(33):706, 1931.

[3] J. G. Bednorz and K. A. Müller. Possible high Tc superconductivity in the BaLaCuO system. *Zeitschrift für Physik B Condensed Matter*, **64**(2):189, 1986.

[4] Y. Kamihara, T. Watanabe, M. Hirano, and H. Hosono. Iron-Based Layered Superconductor La[$O_{1-x}F_x$]FeAs (x = 0.05–0.12) with T_c= 26 K. *J. Am. Chem. Soc.*, **130**(11):3296, 2008.

[5] J. Bardeen, L. N. Cooper, and J. R. Schrieffer. Theory of Superconductivity. *Phys. Rev.*, **108**:1175, 1957.

[6] J. M. Tranquada. Spins, stripes, and superconductivity in hole-doped cuprates. *AIP Conference Proceedings*, **1550**(1):114, 2013.

[7] J. Kang, X. Wang, A. V. Chubukov, and . M. Fernandes. Interplay between tetragonal magnetic order, stripe magnetism, and superconductivity in iron-based materials. *Phys. Rev. B*, **91**:121104, 2015.

[8] M. Laver, C. J. Bowell, E. M. Forgan, A. B. Abrahamsen, D. Fort, C. D. Dewhurst, S. Mühlbauer, D. K. Christen, J. Kohlbrecher, R. Cubitt, and S. Ramos. Structure and degeneracy of vortex lattice domains in pure superconducting niobium: A small-angle neutron scattering study. *Phys. Rev. B*, **79**:014518, 2009.

[9] E. H. Brandt. The flux-line lattice in superconductors. *Rep. Prog. Phys.*, **58**(11):1465, 1995.

[10] W. Meissner and R. Ochsenfeld. Ein neuer Effekt bei Eintritt der Supraleitfähigkeit. *R. Naturwissenschaften*, **21**:787, 1933.

[11] J. N. Rjabinin and L. W. Shubnikow. Magnetic Properties and Critical Currents of Supra-conducting Alloys. *Nature*, **135**:581, 1935.

[12] F. London and H. London. The electromagnetic equations of the supraconductor. *Proc. Royal Soc. Lond. A*, **149**(866):71, 1935.

[13] V. L. Ginzburg and L. D. Landau. On the theory of superconductivity. *Zh. Eksp. Teor. Fiz.*, **20**:1064, 1950.

[14] A. A. Abrikosov. The magnetic properties of superconducting alloys. *J. Phys. Chem. Solids*, **2**(3):199, 1957.

[15] H. Suderow, I. Guillamón, J. G. Rodrigo, and S. Vieira. Imaging superconducting vortex cores and lattices with a scanning tunneling microscope. *Supercond. Sci. Technol.*, **27**(6):063001, 2014.

[16] H. F. Hess, R. B. Robinson, R. C. Dynes, J. M. Valles, and J. V. Waszczak. Scanning-Tunneling-Microscope Observation of the Abrikosov Flux Lattice and the Density of States near and inside a Fluxoid. *Phys. Rev. Lett.*, **62**:214, 1989.

[17] C. C. Tsuei and J. R. Kirtley. Pairing symmetry in cuprate superconductors. *Rev. Mod. Phys.*, **72**:969, 2000.

[18] H. Hosono and K. Kuroki. Iron-based superconductors: Current status of materials and pairing mechanism. *Physica C*, **514**:399, 2015. Superconducting Materials: Conventional, Unconventional and Undetermined.

[19] D. J. Scalapino. Superconductivity and Spin Fluctuations. *J. Low Temp. Phys.*, **117**(3):179, 1999.

[20] F. Wang and D.-H. Lee. The Electron-Pairing Mechanism of Iron-Based Superconductors. *Science*, **332**(6026):200, 2011.

[21] J. R. Clem. Pancake Vortices. *J. Supercond.*, **17**(5):613, 2004.

[22] P. J. Curran, H. A. Mohammed, S. J. Bending, A. E. Koshelev, Y. Tsuchiya, and T. Tamegai. Tuning the structure of the Josephson vortex lattice in $Bi_2Sr_2CaCu_2O_{8+\delta}$ single crystals with pancake vortices. *Scientific Reports*, **8**:10914, 2018.

[23] P. G. de Gennes. *Superconductivity of Metals and Alloys*. Advanced book classics. Addison-Wesley, Redwood City, Calif. ; Wokingham, 1989.

[24] E. H. Brandt. Vortices in superconductors: ideal lattice, pinning, and geometry effects. *Supercond. Sci. Technol.*, **22**(3):034019, 2009.

[25] J. R. Clem. Simple model for the vortex core in a type II superconductor. *J. Low Temp. Phys.*, **18**(5):427, 1975.

[26] A. B. Pippard. An Experimental and Theoretical Study of the Relation between Magnetic Field and Current in a Superconductor. *Proc. Royal Soc. A*, **216**(1127):547, 1953.

[27] V. G. Kogan. London approach to anisotropic type-II superconductors. *Phys. Rev. B*, **24**:1572, 1981.

[28] L. P. Gorkov. Microscopic derivation of the Ginzburg-Landau equations in the theory of superconductivity. *Zh. Eksp. Teor. Fiz.*, **36**:1364, 1959.

[29] M. R. Eskildsen. *Small Angle Neutron Scattering Studies of the Flux Line Lattices in the Borocarbide Superconductors*. PhD thesis, Risø National Laboratory, 1998.

[30] B. Rosenstein and D. Li. Ginzburg-Landau theory of type II superconductors in magnetic field. *Rev. Mod. Phys.*, **82**:109, 2010.

[31] W. H. Kleiner, L. M. Roth, and S. H. Autler. Bulk Solution of Ginzburg-Landau Equations for Type II Superconductors: Upper Critical Field Region. *Phys. Rev.*, **133**:A1226, 1964.

[32] K. Takanaka. Correlation between Flux-Line Lattice and Crystal Axis in a Mixed State of Superconductors. *Progress of Theoretical Physics*, **50**(2):365, 1973.

[33] P. Miranović, N. Nakai, M. Ichioka, and K. Machida. Microscopic study of low-κ type-II superconductors. *Physica B*, **329-333**:1382, 2003. Proceedings of the 23rd International Conference on Low Temperature Physics.

[34] T. Reimann, S. Mühlbauer, M. Schulz, B. Betz, A. Kaestner, V. Pipich, P. Böni, and C. Grünzweig. Visualizing the morphology of vortex lattice domains in a bulk type-II superconductor. *Nat. Commun.*, **6**:8813, 2015.

[35] S. Mühlbauer. *Vortex Lattices in Superconducting Niobium and Skyrmion Lattices in Chiral MnSi: An Investigation by Neutron Scattering.* PhD thesis, Technische Universität München, 2009.

[36] M. Laver. *A study of the flux line lattice in superconducting niobium by small angle neutron scattering.* PhD thesis, University of Birmingham, 2007.

[37] R. Prozorov. Equilibrium Topology of the Intermediate State in Type-I Superconductors of Different Shapes. *Phys. Rev. Lett.*, **98**:257001, 2007.

[38] L. D. Landau and I. M. Khalatnikov. On the anomalous absorption of a sound near to points of phase transition of the second kind. *Dokl. Akad. Nauk SSSR*, **96**:469, 1954.

[39] J. B. Ketterson and S. N. Song. *Superconductivity.* Cambridge University Press, Cambridge, 1999.

[40] A. Schmid. A time dependent Ginzburg-Landau equation and its application to the problem of resistivity in the mixed state. *Physik der kondensierten Materie*, **5**(4):302, 1966.

[41] W. D. Gropp, H. G. Kaper, G. K. Leaf, D. M. Levine, M. Palumbo, and V. M. Vinokur. Numerical Simulation of Vortex Dynamics in Type-II Superconductors. *J. Comput. Phys.*, **123**(2):254, 1996.

[42] M. Cyrot. Ginzburg-Landau theory for superconductors. *Rep. Prog. Phys.*, **36**(2):103, 1973.

[43] R. L. Frank, C. Hainzl, B. Schlein, and R. Seiringer. Incompatibility of Time-Dependent Bogoliubov–de-Gennes and Ginzburg–Landau Equations. *Letters in Mathematical Physics*, **106**(7):913, 2016.

[44] P.-J. Lin and P. Lipavský. Time-dependent Ginzburg-Landau theory with floating nucleation kernel: Far-infrared conductivity in the Abrikosov vortex lattice state of a type-II superconductor. *Phys. Rev. B*, **80**:212506, 2009.

[45] S. Mühlbauer, C. Pfleiderer, P. Böni, E. M. Forgan, E. H. Brandt, A. Wiedenmann, U. Keiderling, and G. Behr. Time-resolved stroboscopic neutron scattering of vortex lattice dynamics in superconducting niobium. *Phys. Rev. B*, **83**:184502, 2011.

[46] R. Labusch. Elasticity Effects in Type-II Superconductors. *Phys. Rev.*, **170**:470, 1968.

[47] R. Labusch. Elastic Constants of the Fluxoid Lattice Near the Upper Critical Field. *Phys. Status Solidi B*, **32**(1):439, 1969.

[48] E. H. Brandt. Elastic energy of the vortex state in type II superconductors. I. High inductions. *J. Low Temp. Phys.*, **26**(5):709, 1977.

[49] E. H. Brandt. Elastic energy of the vortex state in type II superconductors. II. Low inductions. *J. Low Temp. Phys.*, **26**(5):735, 1977.

[50] R. Labusch. Calculation of the Critical Field Gradient in Type II Superconductors. *Crystal Lattice Defects*, **1**:1, 1969.

[51] L. D. Landau and E. M. Lifshitz. *Theory of elasticity.* Course of theoretical physics; vol. 7. Pergamon Press, London, 1959.

[52] A. I. Larkin and Yu. N. Ovchinnikov. Pinning in type II superconductors. *J. Low Temp. Phys.*, **34**(3):409, 1979.

[53] E. H. Brandt. Elastic and plastic properties of the flux-line lattice in type-II superconductors. *Phys. Rev. B*, **34**:6514, Nov 1986.

[54] D. R. Tilley. The Ginsburg-Landau equations for anisotropic alloys. *Proc. Phys. Soc.*, **86**(2):289, 1965.

[55] A. Houghton, R. A. Pelcovits, and A. Sudbø. Flux lattice melting in high-T_c superconductors. *Phys. Rev. B*, **40**:6763, 1989.

[56] C. P. Bean. Magnetization of Hard Superconductors. *Phys. Rev. Lett.*, **8**:250, 1962.

[57] T. Matsushita. Electromagnetic phenomena and hysteresis losses in superconductors. *Cryogenics*, **30**(4):314, 1990.

[58] D. LeBlanc and M. A. R. LeBlanc. AC-loss valley in type-II superconductors. *Phys. Rev. B*, **45**:5443, 1992.

[59] W. A. Fietz, M. R. Beasley, J. Silcox, and W. W. Webb. Magnetization of Superconducting Nb-25%Zr Wire. *Phys. Rev.*, **136**:A335, 1964.

[60] A. M. Campbell. Flux cutting in superconductors. *Supercond. Sci. Technol.*, **24**(9):091001, 2011.

[61] E. H. Brandt and G. P. Mikitik. Unusual critical states in type-II superconductors. *Phys. Rev. B*, **76**:064526, 2007.

[62] E. H. Brandt, John R. Clem, and D. G. Walmsley. Flux-line cutting in type II superconductors. *J. Low Temp. Phys.*, **37**:43, 1979.

[63] R. Cubitt, E. M. Forgan, G. Yang, S. L. Lee, D. McK. Paul, H. A. Mook, M. Yethiraj, P. H. Kes, T. W. Li, A. A. Menovsky, Z. Tarnawski, and K. Mortensen. Direct observation of magnetic flux lattice melting and decomposition in the high-Tc superconductor $Bi_{2.15}Sr_{1.95}CaCu_2O_{8+x}$. *Nature*, **365**:407, 1993.

[64] T. Bellini, L. Radzihovsky, J. Toner, and N. A. Clark. Universality and scaling in the disordering of a smectic liquid crystal. *Science*, **294**(5544):1074, 2001.

[65] M. Zehetmayer. How the vortex lattice of a superconductor becomes disordered: a study by scanning tunneling spectroscopy. *Sci. Rep.*, **5**(9244), 2015.

[66] Y. Radzyner, A. Shaulov, Y. Yeshurun, K. Kishio, and S. Okayasu. Effects of electron irradiation on the vortex orderdisorder transition in $La_{2-x}Sr_xCuO_4$ crystals. *Physica C Supercond.*, **388-389**:753, 2003. Proceedings of the 23rd International Conference on Low Temperature Physics (LT23).

[67] W.-K. Kwok, U. Welp, A. Glatz, A. E. Koshelev, K. J. Kihlstrom, and G. W. Crabtree. Vortices in high-performance high-temperature superconductors. *Rep. Prog. Phys.*, **79**(11):116501, 2016.

[68] T. Klein, I. Joumard, S. Blanchard, J. Marcus, R. Cubitt, T. Giamarchi, and P. Le Doussal. A Bragg glass phase in the vortex lattice of a type II superconductor. *Nature*, **413**:404, 2001.

[69] M. Laver, E. M. Forgan, A. B. Abrahamsen, C. Bowell, Th. Geue, and R. Cubitt. Uncovering Flux Line Correlations in Superconductors by Reverse Monte Carlo Refinement of Neutron Scattering Data. *Phys. Rev. Lett.*, **100**:107001, Mar 2008.

[70] J. Kierfeld, T. Nattermann, and T. Hwa. Topological order in the vortex-glass phase of high-temperature superconductors. *Phys. Rev. B*, **55**:626, 1997.

[71] A. I. Larkin. Effect of inhomogeneities on the structure of the mixed state of superconductors. *Sov. Phys. JETP 31*, **4**:784, 1970.

[72] V. S. Dotsenko, V. B. Geshkenbein, D. A. Gorokhov, and G. Blatter. Free-energy distribution functions for the randomly forced directed polymer. *Phys. Rev. B*, **82**:174201, 2010.

[73] T. Giamarchi and P. Le Doussal. Elastic theory of flux lattices in the presence of weak disorder. *Phys. Rev. B*, **52**:1242, 1995.

[74] T. Nattermann. Scaling approach to pinning: Charge density waves and giant flux creep in superconductors. *Phys. Rev. Lett.*, **64**:2454, 1990.

[75] D. Cribier, B. Jacrot, L. Madhav Rao, and B. Farnoux. Mise en evidence par diffraction de neutrons d'une structure periodique du champ magnetique dans le niobium supraconducteur. *Physics Letters*, **9**(2):106 – 107, 1964.

[76] R. Toft-Petersen, A. Abrahamsen, S. Balog, L. Porcar, and M. Laver. Decomposing the Bragg glass and the peak effect in a Type-II superconductor. *Nat Commun*, **9**(1):901, 2018.

[77] M. V. Feigel'man, V. B. Geshkenbein, A. I. Larkin, and V. M. Vinokur. Theory of collective flux creep. *Phys. Rev. Lett.*, **63**:2303, 1989.

[78] T. Giamarchi and P. Le Doussal. Elastic theory of pinned flux lattices. *Phys. Rev. Lett.*, **72**:15303, 1994.

[79] A. P. Petrović, Y. Fasano, R. Lortz, C. Senatore, A. Demuer, A. B. Antunes, A. Paré, D. Salloum, P. Gougeon, M. Potel, and Ø. Fischer. Real-Space Vortex Glass Imaging and the Vortex Phase Diagram of $SnMo_6\mathbf{S}_8$. *Phys. Rev. Lett.*, **103**:257001, 2009.

[80] V. Vinokur, B. Khaykovich, E. Zeldov, M. Konczykowski, R.A. Doyle, and P.H. Kes. Lindemann criterion and vortex-matter phase transitions in high-temperature superconductors. *Physica C*, **295**(3):209, 1998.

[81] D. S. Fisher, M. P. A. Fisher, and D. A. Huse. Thermal fluctuations, quenched disorder, phase transitions, and transport in type-II superconductors. *Phys. Rev. B*, **43**:130, 1991.

[82] E. M. Chudnovsky. Hexatic vortex glass in disordered superconductors. *Phys. Rev. B*, **40**:11355, 1989.

[83] G. Blatter, M. V. Feigel'man, V. B. Geshkenbein, A. I. Larkin, and V. M. Vinokur. Vortices in high-temperature superconductors. *Rev. Mod. Phys.*, **66**:1125, 1994.

[84] J. Kierfeld. Topological order in the phase diagram for high-temperature superconductors with point defects. *Physica C: Superconductivity*, **300**(3):171, 1998.

[85] G. I. Menon. Phase behavior of type-II superconductors with quenched point pinning disorder: A phenomenological proposal. *Phys. Rev. B*, **65**:104527, 2002.

[86] U. Divakar, A. J. Drew, S. L. Lee, R. Gilardi, J. Mesot, F. Y. Ogrin, D. Charalambous, E. M. Forgan, G. I. Menon, N. Momono, M. Oda, C. D. Dewhurst, and C. Baines. Direct observation of the flux-line vortex glass phase in a type ii superconductor. *Phys. Rev. Lett.*, **92**:237004, 2004.

[87] D. O. G. Heron, S. J. Ray, S. J. Lister, C. M. Aegerter, H. Keller, P. H. Kes, G. I. Menon, and S. L. Lee. Muon-Spin Rotation Measurements of an Unusual Vortex-Glass Phase in the Layered Superconductor $Bi_{2.15}Sr_{1.85}CaCu_2O_{8+\delta}$. *Phys. Rev. Lett.*, **110**:107004, 2013.

[88] A. Maisuradze, R. Khasanov, A. Shengelaya, and H. Keller. Comparison of different methods for analyzing μSR line shapes in the vortex state of type-II superconductors. *Journal of Physics: Condensed Matter*, **21**(7):075701, 2009.

[89] G. P. Mikitik and E. H. Brandt. Peak effect, vortex-lattice melting line, and order-disorder transition in conventional and high-T_c superconductors. *Phys. Rev. B*, **64**:184514, Oct 2001.

[90] Y. Paltiel, E. Zeldov, Y. Myasoedov, M. L. Rappaport, G. Jung, S. Bhattacharya, M. J. Higgins, Z. L. Xiao, E. Y. Andrei, P. L. Gammel, and D. J. Bishop. Instabilities and Disorder-Driven First-Order Transition of the Vortex Lattice. *Phys. Rev. Lett.*, **85**:3712, Oct 2000.

[91] S. Kokkaliaris, A. A. Zhukov, P. A. J. de Groot, R. Gagnon, L. Taillefer, and T. Wolf. History effects and transition to plastic vortex dynamics in $YBa_2Cu_3O_{7-\delta}$ single crystals. *Physica C*, **332**(1):393, 2000.

[92] P. L. Gammel, U. Yaron, A. P. Ramirez, D. J. Bishop, A. M. Chang, R. Ruel, L. N. Pfeiffer, E. Bucher, G. D'Anna, D. A. Huse, K. Mortensen, M. R. Eskildsen, and P. H. Kes. Structure and Correlations of the Flux Line Lattice in Crystalline Nb through the Peak Effect. *Phys. Rev. Lett.*, **80**:833, Jan 1998.

[93] X. S. Ling, S. R. Park, B. A. McClain, S. M. Choi, D. C. Dender, and J. W. Lynn. Superheating and Supercooling of Vortex Matter in a Nb Single Crystal: Direct Evidence for a Phase Transition at the Peak Effect from Neutron Diffraction. *Phys. Rev. Lett.*, **86**:712, 2001.

[94] H. Safar, P. L. Gammel, D. A. Huse, D. J. Bishop, J. P. Rice, and D. M. Ginsberg. Experimental evidence for a first-order vortex-lattice-melting transition in untwinned, single crystal $YBa_2Cu_3O_7$. *Phys. Rev. Lett.*, **69**:824, 1992.

[95] R. Liang, D. A. Bonn, and W. N. Hardy. Discontinuity of Reversible Magnetization in Untwinned YBCO Single Crystals at the First Order Vortex Melting Transition. *Phys. Rev. Lett.*, **76**:835, 1996.

[96] E. Zeldov, D. Majer, M. Konczykowski, V. B. Geshkenbein, V. M. Vinokur, and H. Shtrikman. Thermodynamic observation of first-order vortex-lattice melting transition in $Bi_2Sr_2CaCu_2O_8$. *Nature*, **375**:373, 1995.

[97] M. Roulin, A. Junod, and E. Walker. Flux Line Lattice Melting Transition in $YBa_2Cu_3O_{6.94}$ Observed in Specific Heat Experiments. *Science*, **273**(5279):1210, 1996.

[98] R. Lortz, F. Lin, N. Musolino, Y. Wang, A. Junod, B. Rosenstein, and N. Toyota. Thermal fluctuations and vortex melting in the Nb_3Sn superconductor from high resolution specific heat measurements. *Phys. Rev. B*, **74**:104502, 2006.

[99] C. J. Bowell, R. J. Lycett, M. Laver, C. D. Dewhurst, R. Cubitt, and E. M. Forgan. Absence of vortex lattice melting in a high-purity Nb superconductor. *Phys. Rev. B*, **82**:144508, 2010.

[100] G. P. Mikitik and E. H. Brandt. Effect of pinning on the vortex-lattice melting line in type-II superconductors. *Phys. Rev. B*, **68**:054509, 2003.

[101] J. Kierfeld and V. Vinokur. Lindemann criterion and vortex lattice phase transitions in type-II superconductors. *Phys. Rev. B*, **69**:024501, 2004.

[102] E. H. Brandt. Precision Ginzburg-Landau Solution of Ideal Vortex Lattices for Any Induction and Symmetry. *Phys. Rev. Lett.*, **78**:2208, 1997.

[103] M. Laulajainen, F. D. Callaghan, C. V. Kaiser, and J. E. Sonier. Muon spin rotation measurements of the vortex state in vanadium: A comparative analysis using iterative and analytical solutions of the Ginzburg-Landau equations. *Phys. Rev. B*, **74**:054511, 2006.

[104] X. B. Xu, H. Fangohr, Z. H. Wang, M. Gu, S. L. Liu, D. Q. Shi, and S. X. Dou. Vortex dynamics for low-κ type-II superconductors. *Phys. Rev. B*, **84**:014515, 2011.

[105] John Bardeen and M. J. Stephen. Theory of the Motion of Vortices in Superconductors. *Phys. Rev.*, **140**:A1197, Nov 1965.

[106] J. S. Watkins and N. K. Wilkin. Extruding the vortex lattice: Two reacting populations of dislocations. *Europhys. Lett.*, **126**(1):16002, 2019.

[107] Wang, J., Zhao, Z. G., Liu, M., Xing, D. Y., and Dong, J. M. Possible inverse melting of vortex lattice in high-T_c superconductors. *Europhys. Lett.*, **65**(1):89, 2004.

[108] S. J. Bending, A. N. Grigorenko, M. J. Van Bael, M. Lange, V. V. Moschalkov, H. Fangohr, and P. A. J. de Groot. Driving force for commensurate vortex domain formation in periodic pinning arrays. *Physica C*, **404**(1):50, 2004. Proceedings of the Third European Conference on Vortex Matter in Superconductors at Extreme Scales and Conditions.

[109] H. J. Jensen, A. Brass, A.-C. Shi, and A. J. Berlinsky. Simulations of the onset of diffusion in a flux-line lattice in a random potential. *Phys. Rev. B*, **41**:6394, 1990.

[110] I. A. Sadovskyy, A. E. Koshelev, W.-K. Kwok, U. Welp, and A. Glatz. Targeted evolution of pinning landscapes for large superconducting critical currents. *Proceedings of the National Academy of Sciences*, **116**(21):10291, 2019.

[111] A. I. Blair and D. P. Hampshire. Time-Dependent Ginzburg-Landau Simulations of the Critical Current in Superconducting Films and Junctions in Magnetic Fields. *IEEE Trans. Appl. Supercond.*, **28**(4):1, 2018.

[112] I. A. Sadovskyy, A. E. Koshelev, A. Glatz, V. Ortalan, M. W. Rupich, and M. Leroux. Simulation of the Vortex Dynamics in a Real Pinning Landscape of $YBa_2Cu_3O_{7-\delta}$ Coated Conductors. *Phys. Rev. Applied*, **5**:014011, 2016.

[113] R. Griessen, Wen Hai-hu, A. J. J. van Dalen, B. Dam, J. Rector, H. G. Schnack, S. Libbrecht, E. Osquiguil, and Y. Bruynseraede. Evidence for mean free path fluctuation induced pinning in $YBa_2Cu_3O_7$ and $YBa_2Cu_4O_8$ films. *Phys. Rev. Lett.*, **72**:1910, 1994.

[114] H.-Y. Liao, S.-P. Zhou, X.-Y. Shi, and B.-H. Zhu. Vortex dynamics in superconductors with periodic pinning arrays. *Physica C*, **408**:603, 2004. Proceedings of the International Conference on Materials and Mechanisms of Superconductivity. High Temperature Superconductors VII – M2SRIO.

[115] Q. Du, M. D. Gunzburger, and J. S. Peterson. Computational simulation of type-II superconductivity including pinning phenomena. *Phys. Rev. B*, **51**:16194, 1995.

[116] R. Wördenweber. Engineering of superconductors and superconducting devices using artificial pinning sites. *Phys. Sci. Rev*, **2**(8), 2017.

[117] L. Horng, T. C. Wu, J. C. Wu, R. Cao, and T. J. Yang. Properties of vortex propagation in a niobium film with spacing-graded density of pinning sites. *Journal of Applied Physics*, **101**(9):09G113, 2007.

[118] K. Yu, M. B. S. Hesselberth, P. H. Kes, and B. L. T. Plourde. Vortex dynamics in superconducting channels with periodic constrictions. *Phys. Rev. B*, **81**:184503, 2010.

[119] C.-H. Sow, K. Harada, A. Tonomura, G. Crabtree, and D. G. Grier. Measurement of the Vortex Pair Interaction Potential in a Type-II Superconductor. *Phys. Rev. Lett.*, **80**:2693, 1998.

[120] Y. Togawa, K. Harada, T. Akashi, H. Kasai, T. Matsuda, F. Nori, A. Maeda, and A. Tonomura. Direct Observation of Rectified Motion of Vortices in a Niobium Superconductor. *Phys. Rev. Lett.*, **95**:087002, 2005.

[121] Mark J. Higgins and S. Bhattacharya. Varieties of dynamics in a disordered flux-line lattice. *Physica C*, **257**(3):232, 1996.

[122] U. Yaron, P. L. Gammel, D. A. Huse, R. N. Kleiman, C. S. Oglesby, E. Bucher, B. Batlogg, D. J. Bishop, K. Mortensen, and K. N. Clausen. Structural evidence for a two-step process in the depinning of the superconducting flux-line lattice. *Nature*, **376**(6543), 1995.

[123] A. J. Moreno, S. O. Valenzuela, G. Pasquini, and V. Bekeris. Oscillatory dynamics of a superconductor vortex lattice in high amplitude ac magnetic fields. *Phys. Rev. B*, **71**:132513, 2005.

[124] Y. Abulafia, A. Shaulov, Y. Wolfus, R. Prozorov, L. Burlachkov, Y. Yeshurun, D. Majer, E. Zeldov, H. Wühl, V. B. Geshkenbein, and V. M. Vinokur. Plastic Vortex Creep in $YBa_2Cu_3O_{7-x}$ Crystals. *Phys. Rev. Lett.*, **77**:1596, 1996.

[125] K. Moon, R. T. Scalettar, and G. T. Zimányi. Dynamical Phases of Driven Vortex Systems. *Phys. Rev. Lett.*, **77**:2778, 1996.

[126] C. J. Olson, C. Reichhardt, and Franco Nori. Superconducting vortex avalanches, voltage bursts, and vortex plastic flow: Effect of the microscopic pinning landscape on the macroscopic properties. *Phys. Rev. B*, **56**:6175, 1997.

[127] E. Olive and J. C. Soret. Chaos and plasticity in superconductor vortices: Low-dimensional dynamics. *Phys. Rev. B*, **77**:144514, 2008.

[128] N. Mangan, C. Reichhardt, and C. J. Olson Reichhardt. Reversible to Irreversible Flow Transition in Periodically Driven Vortices. *Phys. Rev. Lett.*, **100**:187002, 2008.

[129] X. B. Xu, H. Fangohr, S. Y. Ding, F. Zhou, X. N. Xu, Z. H. Wang, M. Gu, D. Q. Shi, and S. X. Dou. Phase diagram of vortex matter of type-II superconductors. *Phys. Rev. B*, **83**:014501, 2011.

[130] G. L. Squires. Introduction to the theory of thermal neutron scattering, 2012.

[131] C. Kittel. *Introduction to solid state physics*. Wiley, New York, Chichester, 7th ed. edition, 1996.

[132] A. Huxley, P. Rodière, P. McK. Donald, N. van Dijk, and R. Cubitt. Realignment of the flux-line lattice by a change in the symmetry of superconductivity in UPt_3. *Nature*, **406**:160, 2000.

[133] R. Cubitt, E.M. Forgan, D.McK. Paul, S.L. Lee, J.S. Abell, H. Mook, and P.A. Timmins. Neutron diffraction by the flux lattice in high-Tc superconductors. *Physica B*, **180-181**:377, 1992.

[134] A.J. Greer and W. J. Kossler. *Low magnetic fields in anisotropic superconductors*. Lecture notes in physics. Springer, Heidelberg, Germany, 1995.

[135] J. E. Sonier. Muon spin rotation studies of electronic excitations and magnetism in the vortex cores of superconductors. *Reports on Progress in Physics*, **70**(11):1717, 2007.

[136] P. Dalmas de Réotier and A. Yaouanc. Muon spin rotation and relaxation in magnetic materials. *J. Phys. Condens. Matter*, **9**(43):9113, 1997.

[137] B. D. Rainford and G. J. Daniell. μSR frequency spectra using the maximum entropy method. *Hyperfine Interactions*, **87**(1):1129, 1994.

[138] E. H. Brandt and M. P. Das. Attractive Vortex Interaction and the Intermediate-Mixed State of Superconductors. *Journal of Superconductivity and Novel Magnetism*, **24**(1):57, 2011.

[139] M. Laver, E. M. Forgan, S. P. Brown, D. Charalambous, D. Fort, C. Bowell, S. Ramos, R. J. Lycett, D. K. Christen, J. Kohlbrecher, C. D. Dewhurst, and R. Cubitt. Spontaneous Symmetry-Breaking Vortex Lattice Transitions in Pure Niobium. *Phys. Rev. Lett.*, **96**:167002, 2006.

[140] S. Mühlbauer, C. Pfleiderer, P. Böni, M. Laver, E. M. Forgan, D. Fort, U. Keiderling, and G. Behr. Morphology of the Superconducting Vortex Lattice in Ultrapure Niobium. *Phys. Rev. Lett.*, **102**:136408, 2009.

[141] B. Obst. Anisotropie in kubischen Supraleitern. *Phys. Status Solidi B*, **45**(2):453, 1971.

[142] U. Yaron, P. L. Gammel, A. P. Ramirez, D. A. Huse, D. J. Bishop, A. I. Goldman, C. Stassis, P. C. Canfield, K. Mortensen, and M. R. Eskildsen. Microscopic coexistence of magnetism and superconductivity in $ErNi_2B_2C$. *Nature*, **382**(6588), 1996.

[143] Y. De Wilde, M. Iavarone, U. Welp, V. Metlushko, A.E. Koshelev, I. Aranson, G.W. Crabtree, P. L. Gammel, D. J. Bishop, and P. C. Canfield. The superconducting energy gap and vortex lattice structure in $LuNi_2B_2C$. *Physica C: Superconductivity*, **282-287**:355, 1997. Materials and Mechanisms of Superconductivity High Temperature Superconductors V.

[144] M. R. Eskildsen, P. L. Gammel, B. P. Barber, A. P. Ramirez, D. J. Bishop, N. H. Andersen, K. Mortensen, C. A. Bolle, C. M. Lieber, and P. C. Canfield. Structural Stability of the Square Flux Line Lattice in YNi_2B_2C and $LuNi_2B_2C$ Studied with Small Angle Neutron Scattering. *Phys. Rev. Lett.*, **79**:487, 1997.

[145] D. McK. Paul, C. V. Tomy, C. M. Aegerter, R. Cubitt, S. H. Lloyd, E. M. Forgan, S. L. Lee, and M. Yethiraj. Nonlocal Effects and Vortex Lattice Transitions in YNi_2B_2C. *Phys. Rev. Lett.*, **80**:1517, 1998.

[146] M. Yethiraj, D. K. Christen, A. A. Gapud, D. McK. Paul, S. J. Crowe, C. D. Dewhurst, R. Cubitt, L. Porcar, and A. Gurevich. Temperature and field dependence of the flux-line-lattice symmetry in V_3Si. *Phys. Rev. B*, **72**:060504, 2005.

[147] A. D. Bianchi, M. Kenzelmann, L. DeBeer-Schmitt, J. S. White, E. M. Forgan, J. Mesot, M. Zolliker, J. Kohlbrecher, R. Movshovich, E. D. Bauer, J. L. Sarrao, Z. Fisk, C. Petrović, and M. R. Eskildsen. Superconducting Vortices in $CeCoIn_5$: Toward the Pauli-Limiting Field. *Science*, **319**(5860):177, 2008.

[148] T. M. Riseman, P. G. Kealey, E. M. Forgan, A. P. Mackenzie, L. M. Galvin, A. W. Tyler, S. L. Lee, C. Ager, D. Mck. Paul, C. M. Aegerter, R. Cubitt, Z. Q. Mao, T. Akima, and Y. Maeno. Observation of a square flux-line lattice in the unconventional superconductor Sr_2RuO_4. *Nature*, **396**(6708), 1998.

[149] R. Gilardi, J. Mesot, A. Drew, U. Divakar, S. L. Lee, E. M. Forgan, O. Zaharko, K. Conder, V. K. Aswal, C. D. Dewhurst, R. Cubitt, N. Momono, and M. Oda. Direct Evidence for an Intrinsic Square Vortex Lattice in the Overdoped High- T_c Superconductor $La_{1.83}Sr_{0.17}CuO_{4+\delta}$. *Phys. Rev. Lett.*, **88**:217003, 2002.

[150] H. W. Weber, E. Seidl, C. Laa, E. Schachinger, M. Prohammer, A. Junod, and D. Eckert. Anisotropy effects in superconducting niobium. *Phys. Rev. B*, **44**:7585, 1991.

[151] N. Nakai, P. Miranović, M. Ichioka, and K. Machida. Reentrant Vortex Lattice Transformation in Fourfold Symmetric Superconductors. *Phys. Rev. Lett.*, **89**:237004, 2002.

[152] H. M. Adachi, M. Ishikawa, T. Hirano, M. Ichioka, and K. Machida. Origin of spontaneous broken mirror symmetry of vortex lattices in Nb. *J. Phys. Soc. Jpn.*, **80**(11):113702, 2011.

[153] U. Keiderling and P. Wiedenmann. New SANS Instrument at the BER-II Reactor in Berlin, Germany. *Physica B*, **213** and **214**:895, 1995.

[154] U. Keiderling. The new BerSANS-PC software for reduction and treatment of small angle neutron scattering data. *Applied Physics A*, **74**(1):s1455, 2002.

[155] J. S. Pedersen, D. Posselt, and K. Mortensen. Analytical treatment of the resolution function for small-angle scattering. *J. Appl. Cryst.*, **23**(4):321, 1990.

[156] H. R. Kerchner, D. K. Christen, and S. T. Sekula. Equilibrium properties of the fluxoid lattice in single-crystal niobium. I. Magnetization measurements. *Phys. Rev. B*, **21**:86, 1980.

[157] S. T. Sekula and R. H. Kernohan. Magnetic Properties of Superconducting Vanadium. *Phys. Rev. B*, **5**:904, 1972.

[158] C. P. Bean and J. D. Livingston. Surface Barrier in Type-II Superconductors. *Phys. Rev. Lett.*, **12**:14, 1964.

[159] C Dewhurst. Grasp: Graphical reduction and analysis SANS program for Matlab. *Institut Laue-Langevin (2001–2007) http://www.ill.eu/fileadmin/users_files/Other_Sites/lss-grasp/grasp_main. html*, 2007.

[160] P. Chaddah. Calculation of spatially resolved energy dissipation in the critical-state model: Supercooling and metastable states. *Phys. Rev. B*, **62**:5361, 2000.

[161] Ernst Helmut Brandt. Penetration of magnetic ac fields into type-II superconductors. *Phys. Rev. Lett.*, **67**:2219, 1991.

[162] U. Yaron, P. L. Gammel, D. A. Huse, R. N. Kleiman, C. S. Oglesby, E. Bucher, B. Batlogg, D. J. Bishop, K. Mortensen, K. Clausen, C. A. Bolle, and F. De La Cruz. Neutron Diffraction Studies of Flowing and Pinned Magnetic Flux Lattices in $2H-NbSe_2$. *Phys. Rev. Lett.*, **73**:2748, 1994.

[163] H. Kraus, J. Jochum, B. Kemmather, M. Gutsche, F.v. Feilitzsch, and R.L. Mssbauer. High resolution X-ray spectroscopy with superconducting tunnel junctions. *Nucl. Instrum. Methods Phys. Res.*, **326**(1):172, 1993.

[164] E. Moser, E. Seidl, and H. W. Weber. Superconductive properties of vanadium and their impurity dependence. *J. Low Temp. Phys.*, **49**(5):585, 1982.

[165] Ray Radebaugh and P. H. Keesom. Low-Temperature Thermodynamic Properties of Vanadium. II. Mixed State. *Phys. Rev.*, **149**:217, 1966.

[166] H. M. Rietveld. A profile refinement method for nuclear and magnetic structures. *J. Appl. Cryst.*, **2**(2):65, 1969.

[167] G. Hölzer, M. Fritsch, M. Deutsch, J. Härtwig, and E. Förster. $K\alpha_{1,2}$ and $K\beta_{1,3}$ x-ray emission lines of the $3d$ transition metals. *Phys. Rev. A*, **56**:4554, 1997.

[168] P. Thompson, D. E. Cox, and J. B. Hastings. Rietveld Refinement of Debye-Scherrer Synchotron X-ray Data from Al_2O_3. *J. Appl. Cryst.*, **20**:79, 1987.

[169] R. Gilardi. *Inelastic and small angle neutron scattering study of the $La_{2-x}Sr_xCuO_4$ high-T_c superconductor in a magnetic field.* PhD thesis, Swiss Federal Institute of Technology Zurich, 2004.

[170] J. Chang, J. S. White, M. Laver, C. J. Bowell, S. P. Brown, A. T. Holmes, L. Maechler, S. Strässle, R. Gilardi, S. Gerber, T. Kurosawa, N. Momono, M. Oda, M. Ido, O. J. Lipscombe, S. M. Hayden, C. D. Dewhurst, R. Vavrin, J. Gavilano, J. Kohlbrecher, E. M. Forgan, and J. Mesot. Spin density wave induced disordering of the vortex lattice in superconducting $La_{2-x}Sr_xCuO_4$. *Phys. Rev. B*, **85**:134520, 2012.

[171] T. Giamarchi and P. Le Doussal. Phase diagrams of flux lattices with disorder. *Phys. Rev. B*, **55**:6577, 1997.

[172] J. Kierfeld, H. Nordborg, and V. M. Vinokur. Theory of Plastic Vortex Creep. *Phys. Rev. Lett.*, **85**:4948–4951, 2000.

[173] A. E. Koshelev, I. A. Sadovskyy, C. L. Phillips, and A. Glatz. Optimization of vortex pinning by nanoparticles using simulations of the time-dependent Ginzburg-Landau model. *Phys. Rev. B*, **93**:060508, Feb 2016.

[174] T. S. Alstrøm, M. P. Sørensen, N. F. Pedersen, and S. Madsen. Magnetic Flux Lines in Complex Geometry Type-II Superconductors Studied by the Time Dependent Ginzburg-Landau Equation. *Acta Appl. Math.*, **115**(1):63, 2011.

[175] J. Fleckinger and Hans Kaper. Gauges for the Ginzburg-Landau equations of superconductivity. *Nonlinear Analysis: Theory, Methods and Applications*, **32**, 08 1997.

[176] Q. Du. Discrete gauge invariant approximations of a time dependent Ginzburg-Landau model of superconductivity. *Math. Comp.*, **67**:965, 1998.

[177] W. B. Richardson, A. L. Pardhanani, G. F. Carey, and A. Ardelea. Numerical effects in the simulation of Ginzburg-Landau models for superconductivity. *International Journal for Numerical Methods in Engineering*, **59**(9):1251, 2004.

[178] G. I. Menon, A. Drew, U. K. Divakar, S. L. Lee, R. Gilardi, J. Mesot, F. Y. Ogrin, D. Charalambous, E. M. Forgan, N. Momono, M. Oda, C. Dewhurst, and C. Baines. Muons as Local Probes of Three-Body Correlations in the Mixed State of Type-II Superconductors. *Phys. Rev. Lett.*, **97**:177004, 2006.

[179] D. J. Priour and H. A. Fertig. Deformation and depinning of superconducting vortices from artificial defects: A Ginzburg-Landau study. *Phys. Rev. B*, **67**:054504, Feb 2003.